Bioinspired Synthesis of Metal Oxides and Sulphide Electrocatalysts for CO_2 and N_2 Conversion to Formate and Ammonia

Thesis Submitted in Partial Fulfilment of the Requirements for the Award of the Degree of

DOCTOR OF PHILOSOPHY

by

Anirban Chowdhury

Department of Chemical Engineering

Indian Institute of Technology Guwahati

Assam-781039, INDIA

April 2023

This page is intentionally left blank


I would like to dedicate my thesis to my family, and my friend, philosopher, and guide - my wife


This page is intentionally left blank

DEPARTMENT OF CHEMICAL ENGINEERING
INDIAN INSTITUTE OF TECHNOLOGY GUWAHATI
GUWAHATI- 781039
ASSAM, INDIA

DECLARATION

I, hereby declare that the content embodied in this thesis entitled **"*Bioinspired Synthesis of Metal Oxides and Sulphide Electrocatalysts for CO_2 and N_2 Conversion to Formate and Ammonia*"** is the result of investigations carried out by me at the Indian Institute of Technology Guwahati, Guwahati— 781039, Assam, under the supervision of Prof. Animes K Golder, Department of Chemical Engineering, IIT Guwahati, and Dr. Nageswara Rao Peela, Department of Chemical Engineering, IIT Guwahati, and is submitted to the Indian Institute of Technology Guwahati, for the award of the degree of Doctor of Philosophy.

In keeping with the general practice of reporting scientific observations, due acknowledgements have been made wherever the work described is based on the findings of other investigators.

Anirban Chowdhury
Roll no. 166107007
Department of Chemical Engineering
Indian Institute of Technology Guwahati

This page is intentionally left blank

DEPARTMENT OF CHEMICAL ENGINEERING
INDIAN INSTITUTE OF TECHNOLOGY GUWAHATI
GUWAHATI- 781039
ASSAM, INDIA

CERTIFICATE

This is to certify that the thesis entitled **"*Bioinspired Synthesis of Metal Oxides and Sulphide Electrocatalysts for CO_2 and N_2 Conversion to Formate and Ammonia*"**, being submitted by ***Mr. Anirban Chowdhury***, to the Indian Institute of Technology Guwahati, India, for the degree of Doctor of Philosophy, has been carried out by him under our guidance and supervision and this work has not been submitted elsewhere for the award of any degree.

Prof. Animes K Golder
(Thesis Supervisor)
Professor
Department of Chemical Engineering
Indian Institute of Technology Guwahati
Guwahati- 781039
Assam, India

Dr. Nageswara Rao Peela
(Thesis Supervisor)
Associate Professor
Department of Chemical Engineering
Indian Institute of Technology Guwahati
Guwahati- 781039
Assam, India

This page is intentionally left blank

Acknowledgement

"Follow the evidence wherever it leads, and question everything."

— Neil deGrasse Tyson

First and foremost, I express my heartfelt gratitude to ***Prof. Animes K Golder*** for the guidance and support throughout my PhD journey. His expertise, encouragement, and mentorship have been invaluable in shaping my academic and professional development. I could not have achieved this milestone without his patient guidance and dedication to my success.

I would like to take this opportunity to express my deepest appreciation to ***Dr. Nageswara Rao Peela*** for his unwavering support and invaluable feedback, which have been crucial in shaping my research and enabling me to achieve my PhD goals.

I would like to extend my gratitude to my doctoral committee members, ***Prof. Bishnupada Mandal***, ***Prof. Kaustubha Mohanty***, and ***Prof. Subhendu Sekhar Bag*** (Department of Chemistry) for their valuable suggestions throughout this journey.

I am deeply thankful to the head of the department of Chemical Engineering, ***Prof. Kaustubha Mohanty***, and former head of the department, ***Prof. Anugrah Singh***, and ***Prof. Bishnupada Mandal*** for their support and guidance and also giving me the opportunity to use the analytical laboratory facility.

"Gravitation is not responsible for people falling in love."

— Albert Einstein

The passion for science that burns within me was ignited by the insightful guidance and captivating teachings of my beloved teachers, ***Mr. Biswajit Roy*** and ***Mr. Tapas Ghosh***.

I am also immensely grateful to my teachers, ***Mrs. Subhanjana Dasgupta***, ***Mr. Vivekananda Roy***, ***Prof. Parameswar De***, ***Prof. Parthasarathi Roy***, ***Prof. Sampa Chakraborti***, ***Dr. Sujay Pattanayak***, and **(Late)** ***Dr. Swaraj Bhusan Maiti*** for their guidance.

I would also like to thank the technical and non-technical staff of our department, for helping me in numerous ways. Specially, I would like to thank ***Mr. Ariful Hoque*** and ***Mr. Deep Jyoti Sinha***, in this regard.

I would like to thank IIT Guwahati for giving me the opportunity to use the facility of the instrument in Central Instruments Facility (CIF).

Special thanks to my lab mates and seniors ***Dr. Raj Kumar Das***, ***Dr. Venkat Narashimha Rao Chelli***, ***Dr. Devipriya Gogoi***, ***Dr. Smruti Ranjan Dash***, ***Dr. Paulomi Bose***, ***Mr. Joy Patar***, ***Mr. Sagar Hareshkumar Shah***, ***Mr. Gautam***, ***Mr. Chandra Bhan***, ***Mr. Anil Kumar***, ***Mr. Ravi***, ***Mr. Pramod Gawal***, ***Mrs. Swagata Patra***, ***Mr. Mrinal Dolai***, ***Mr. Biswajit Bhattacharya***, and ***Mr. Vivek Kumar***.

"When it comes to books and friends, it is best to have only a few but all good ones."

— Guillaume Musso

I would also like to thank my friends ***Mr. Ponnala Rambabu***, ***Dr. Pradeep Sahu***, ***Dr. Bhaskar Jyoti Chowdhury***, ***Mr. Saptarshi Gupta***, ***Dr. Vikki Rajulapati***, ***Mr. Abhradeep Pal***, and ***Dr. Mahesh Nagargoje***. Special thanks to ***Arka***, ***Dipankar***, ***Bhola***, ***Rahul***, ***Pabitra***, ***Sandeep***, ***Bibhas***, and (the late) ***Bikash*** for making my childhood memorable.

"know full well that patience is the best means of success"

—Swami Vivekananda

I owe a debt of gratitude to those who have taught me that patience is the best means of success. Through their guidance and support, I have learned that perseverance and patience are essential for achieving one's goals.

Thanks to ***Kaizen*** art which helped me to focus on small but consistent progress every day, leading to significant improvements in my research and overall productivity. It also helped me develop a more positive and proactive mindset, which was crucial during the challenges of the Ph.D. journey.

"Everything is relative except relatives, and they are absolute."

— Alfred Stieglitz

I am grateful to ***Mr. Biplab Dutta*** (maternal uncle), my in-laws, and ***Dr. Partha Roy*** (brother-in-law) in this regard.

"Happy is the man who finds a true friend, and far happier is he who finds that true friend in his wife."

— Franz Schubert

I am deeply grateful to my wife ***Mrs. Bampi Roy***, who has been my constant source of support, encouragement, and inspiration throughout my Ph.D. journey. She has been my friend, philosopher, and guide, and her unwavering belief in me has kept me going even during the most challenging times. I could not have done this without her love, patience, and understanding.

"Every home is a university and the parents are the teachers."

— Mahatma Gandhi

I would like to express my gratitude to my parents for instilling in me the value of lifelong learning. I am fortunate to have had such wise and dedicated educators in my life. Their teachings have not only helped me succeed academically, but have also shaped my character and values in profound ways.

"Excellence is not a destination; it is a continuous journey that never ends."

— Brain Tracy

I would like to thank all those who have supported me in my pursuit of excellence. Your encouragement and guidance have helped me realize that excellence is not a destination, but a lifelong journey of continuous improvement.

"God gave me nothing I wanted, he gave me everything I needed."

—Swami Vivekananda

I am humbled and grateful for the realization that God's plans for me were far greater than my own desires. His providence has granted me the strength and opportunities to overcome obstacles, learn valuable lessons, and become the best version of myself, and for that, I am forever indebted.

Anirban Chowdhury

Department of Chemical Engineering

IIT Guwahati

April 2023

This page is intentionally left blank

Abstract

Fossil fuel consumption holds 81% of the global primary energy share even in recent years. It directly affects the emission of CO_2 in every corner of the earth. We have seen a rise in CO_2 emissions of 31.79% within a span of 15 years from 2003 to 2018. It results in a meteoric increase in CO_2 concentration in the atmosphere causing the grievous greenhouse effect. Production of various useful chemicals and fuels through direct electrochemical CO_2 reduction reaction (ECO_2RR) owns tremendous opportunities to combat adverse environmental consequences of CO_2 emission. Formic acid (HCOOH) is considered a promising contestant according to the series $CO \approx HCOOH > CH_3OH >> C_2H_4 > CH_4$ among nearly 16 different C_1-C_3 compounds formed through ECO_2RR. Alongside this, the production of NH_3 by N_2 reduction could shift the paradigm of global energy verticals. NH_3 is an effective energy carrier and liquid fuel for developing fuel cells having a high hydrogen capacity (17.8% w/w) and energy density (4.32 $kWhL^{-1}$). In fact, the production of NH_3 through electrochemical nitrogen reduction reaction (ENRR) has garnered significant interest as a potential method of artificial N_2 fixation in ambient conditions.

This doctoral work develops environmentally benign processes for the synthesis of metal oxides and metal sulphide (nano)electrocatalysts. These catalysts are then applied for the electrochemical reduction of CO_2 and N_2 for the formation of value-added chemicals in a semi-batch laboratory electrolyzer.

In the first part, we have synthesized Cu_2O nanoparticles (NPs), denoted, Cu_2O(bio) NPs, using the bioactive compounds present in *Sechium edule* (chayote) vegetal extract. The mechanistic pathways for the formation of the face-centred cubic Cu_2O NPs (37.5−42 nm) and metal-organic (intermediates) ligands leading to the development of its stabilizing cap are investigated in detail. To validate the mechanism of Cu_2O NPs formation, a control synthesis of Cu_2O NPs, using commercially available ascorbic acid (AA) was performed and tested for ECO_2RR. Cu_2O(bio) NPs were decorated on the Toray carbon paper (TCP) for the fabrication of the modified electrode. Cu_2O(bio) NPs/TCP electrode could decrease the charge transfer resistance by 50 folds and catalyze CO_2 reduction to formate ($HCOO^-$), a sole liquid product in

0.5 M $KHCO_3$ electrolyte with a Faradaic efficiency (FE) of 65.3–66.6% in 60 min of reaction at -1.60 V. vs. Ag/AgCl (3MKCl). The predominant (111) facet of Cu_2O(bio) NPs could cause the selective formation of formate. Nevertheless, Cu_2O(bio) NPs underwent oxidation to CuO noted after 100 voltammetric cycles resulting in a decline in CO_2 reduction reaction rate. The stability of Cu_2O(bio) NPs and their delamination from the electrode surface was also studied in this work.

Further, with the aim to improve the efficiency of ECO_2RR to $HCOO^-$, the second study synthesizes SnO_2 NPs, labelled as SnO_2(bio) NPs, using the (bio)analytes present in the aforementioned vegetal extract. A mechanistic route of synthesis of SnO_2 NPs from its inorganic precursor has been proposed. SnO_2(bio) NPs decorated TCP and its calcined counterpart SnO_2(bio)- 800 NPs (800°C) were employed for ECO_2RR. Both SnO_2(bio) NPs and SnO_2(bio)- 800 NPs were active towards ECO_2RR forming $HCOO^-$ as the single product, in the same electrolyte. The maximum FE could reach to 75.6–84.0% in 1 h of chronoamperometric test at -1.50 V. vs. Ag/AgCl (3MKCl) probably because of the predominant (110) crystal facet in SnO_2(bio)- 800 NPs.

This study demonstrates a template-free process of synthesizing 1D Bi_2S_3 nanorods (Bi_2S_3-NRs(bio)) following a simple bio-based route. The morphology of nanorods was controlled via capping of ascorbic acid (AA), a major analyte present in *Sechium edule* fruit. Surface capping of AA on Bi_2S_3-NRs(bio) could reduce the average length of Bi_2S_3 nanorods from 485 to 229.5 nm and diameter from 123 to 31 nm compared with Bi_2S_3-NRs(control), synthesized without bio-extract/reducing agent. The oxidized contaminant, Bi_2O_3 was present in Bi_2S_3-NRs(control). Whereas the surface capping of AA prevented the oxidation of Bi_2S_3-NRs(bio) during its synthesis. A plausible mechanistic route of synthesis of Bi_2S_3-NRs(bio) is also proposed herein. The modified Bi_2S_3-NRs(bio)/TCP electrode also exhibited selective $HCOO^-$ formation with an unprecedented FE of 92.3% against 50.9% for the Bi_2S_3-NRs(control)/TCP electrode at −1.5 V (vs. Ag/AgCl). Higher FE exhibited by the Bi_2S_3-NRs(bio) catalyst was resulted from its compositional and morphological attributes. In-situ electrochemical oxidation of Bi_2S_3-NRs(bio) to $Bi_2O_2CO_3$ also could act as active sites to enhance ECO_2RR towards $HCOO^-$ formation.

Finally, the synthesis of pristine Co_3O_4 nanodiscs (NDs) in an environmentally friendly process using gallic acid was carried out to effectuate catalytic ENRR for the

formation of NH_3. The absorption spectra of Co_3O_4 NDs revealed two peaks at 435 and 735 nm, indicative of O^{2-} to Co^{2+}/Co^{3+} charge transfer. The particles exhibited a distinct propensity for growth along the (311) direction with induced oxygen vacancies. The diameter and thickness of Co_3O_4 NDs were determined to be 240 and 35.5 nm, respectively. FE of NH_3 production of 2.6% was achieved with a yield rate of 17.2 µg h^{-1} $mg_{cat.}^{-1}$ at −1.25 V (vs. Ag/AgCl). Co_3O_4 NDs/TCP electrode showed six times higher FE of NH_3 formation compared to the unmodified and non-catalysed system. However, prolonged electrolysis could result in a reduction in FE due to the sacrifice of active Co(III) sites during ENRR.

Keywords: Bioinspired route; Template-free synthesis; Cu_2O catalysts; SnO_2 nanoparticles; 1D Bi_2S_3 nanorods; pristine Co_3O_4 nanodiscs; Cyclic voltammetry; Linear sweep voltammetry; Impedance spectroscopy; Chronoamperometry; Electrochemical CO_2 reduction; Electrochemical N_2 reduction; Formate formation; NH_3 production

This page is intentionally left blank

Table of Contents

Chapter 2: Materials and methodology

List of Table Captions

List of Figure Captions

This page is intentionally left blank

CHAPTER 1

Introduction and Background of the Work

This chapter presents a general introductory information about various CO_2 sequestration techniques, metal and metal-based nanoparticles, various synthesis approaches and their catalytic properties. A concise overview of the bioinspired approaches of metal oxide and sulphide electrocatalysts synthesis and their applications in electrochemical CO_2 and N_2 reduction to value-added chemicals is presented in this chapter.

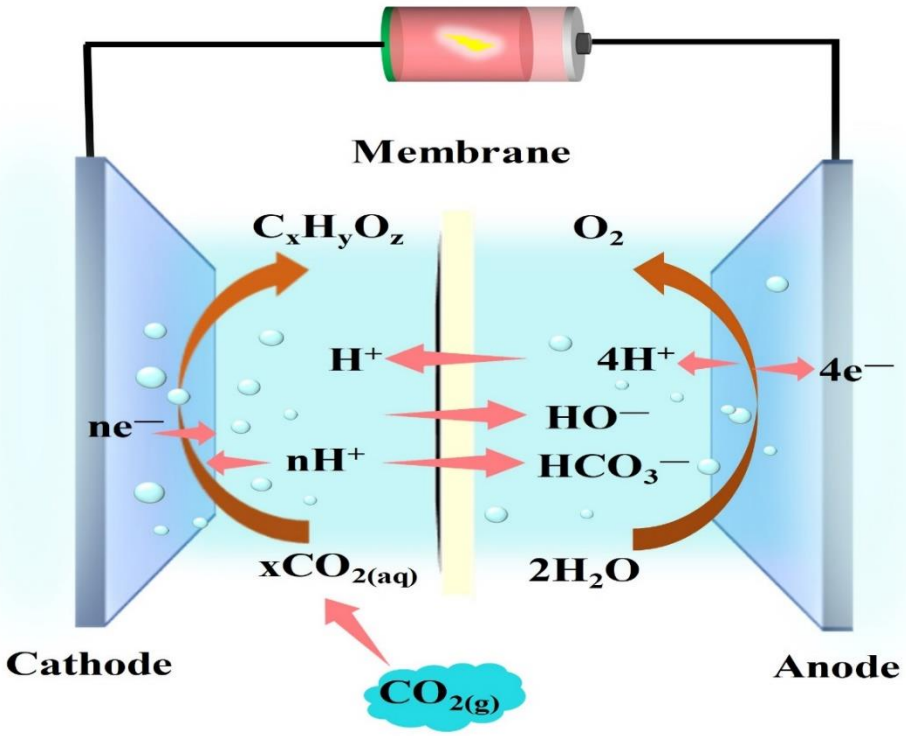

1.1 Introduction and environmental impact of CO_2

Carbon dioxide (CO_2) is an innate product of the combustion of fossil fuels and the respiratory activity of living beings. Photosynthesis by green plants is a biochemical process that reduces the concentration of CO_2 and keeps balancing the atmospheric CO_2 concentration. Human activities have increased the concentration of atmospheric CO_2, a major component of greenhouse gas (GHG) over the past centuries, which causes climate change in association with global warming (Xu and Yang, 2017). According to a report, the world releases about 1 trillion pounds of CO_2 due to the consumption of approximately 1 billion barrels of oil, per 12 days (Varghese et al., 2009). Other than the combustion of fossil fuels, such as oil, coal and gas, deforestation is also a primary cause of CO_2 emission. The various sources of CO_2 emission are illustrated in Figure 1.1. Table 1.1 and Table 1.2 shows the quantitative data of CO_2 emission from different sources and per capita CO_2 emission for major countries, respectively.

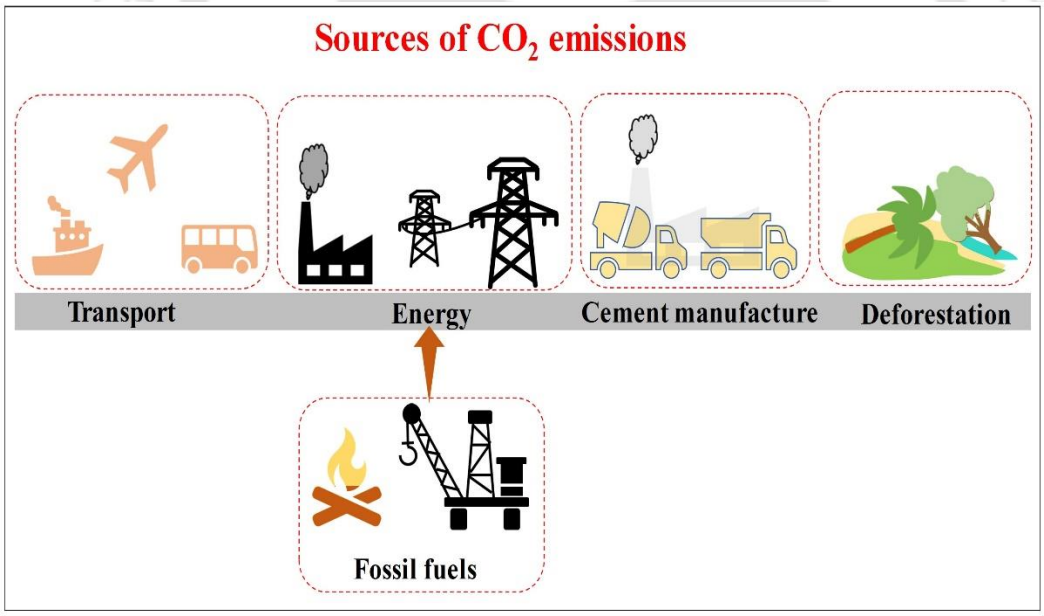

Figure 1.1. Various sources of CO_2 emissions.

Table 1.1. CO_2 emissions from different sources (Ali et al., 2020).

Sources of CO_2 emission	Percentage (%)
Industry	32
Building operations	28
Transportation	23
Building material and construction	11
Other	6

Table 1.2. Per capita CO_2 emission for major countries for the year 2021 [https://ourworldindata.org/co2-emissions].

Country	CO_2 emission (tonnes per capita)
Russia	12.1
Canada	14.3
China	8.05
United States	14.86
Brazil	2.28
Australia	15.09
India	1.93
Argentina	4.12
Kazakhstan	14.41
Saudi Arabia	18.7
Greenland	9.08
Mexico	3.21
Indonesia	2.26
Iran	8.52
South Africa	7.34
Egypt	2.28
Pakistan	0.99
Japan	8.57
Germany	8.09

The effect of climate change includes Arctic sea ice retreat, loss of glaciers, increase in heavy rainfall and the frequent appearance of hurricanes (Solomon et al., 2009). These environmental changes drastically affect human and animal health. Several vector-borne diseases, such as malaria and diarrhea are very much sensitive to climatic conditions, and global warming highly affects the geographical distribution of the vectors and vector-borne diseases. It is also found that the timing and geographical pattern of bird reproduction and migration are altered due to climate change (Corvalan, 2007). A potential solution for reducing the atmospheric concentration of CO_2 is to sequester it (Varghese et al., 2009). As the ability to store several billion tons of carbon emitted in the form of CO_2 is questionable, recycling CO_2 via conversion into value-added hydrocarbons (HCs) is a potential option (Varghese et al., 2009). However, such processes are energy intensive. In this context, electrocatalytic CO_2 conversion into HCs may be considered a viable route.

1.2 Techniques for CO_2 sequestration

There are different methods, both natural and artificial or synthetic for carbon dioxide fixation to avoid its emission into the atmosphere. These methods can broadly be grouped into three categories (Figure 1.2): i) natural sinking process, ii) direct sequestration by artificial processes, and iii) conversion of CO_2 for the synthesis of chemical compounds. The roles of these methods for CO_2 removal and sequestration are outlined in the next sub-sections.

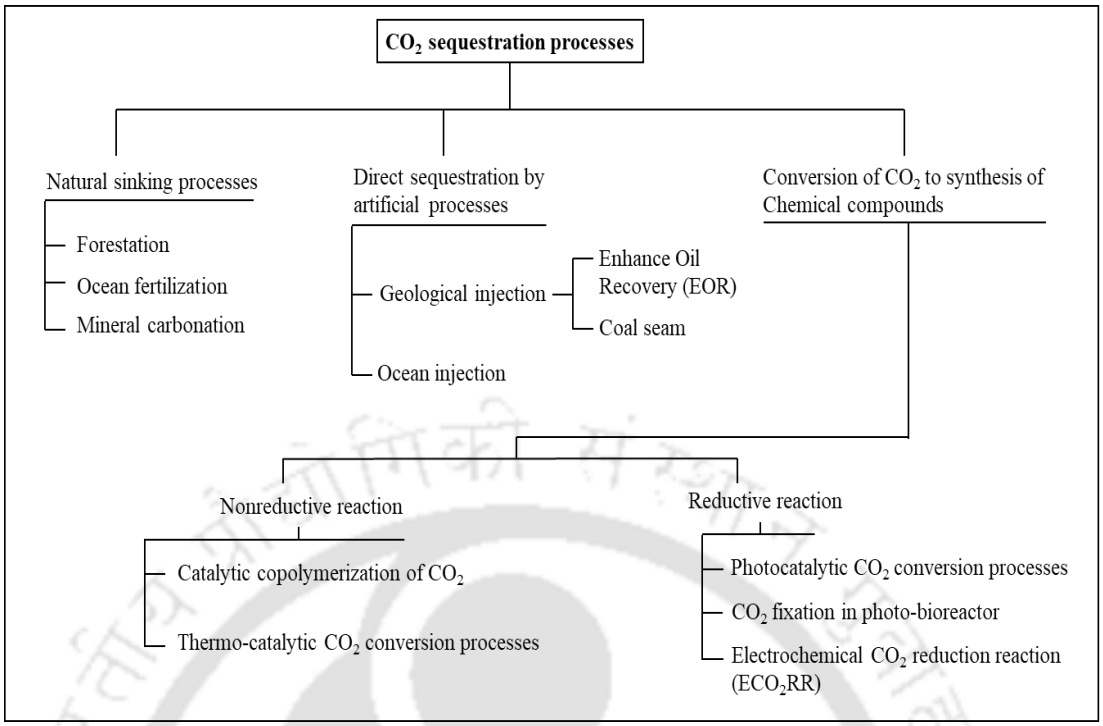

Figure 1.2. Different techniques of CO_2 sequestration.

1.2.1 Natural sinking processes

The natural sinking processes of CO_2 sequestration consist of the formation of fossil fuels via photosynthesis and rock weathering. In these processes, CO_2 is fixed to more stable products such as organic matter of carbonates. The options are forestation, ocean fertilization, and mineral carbonation (Yamasaki, 2003).

1.2.1.1 Forestation

CO_2 capture and storage technology have been expanded to include forestation by the International Energy Agency (IEA), in the year 1991 (Reichle et al., 1999). The carbon flow to the terrestrial vegetation is positive at the beginning of the sequestration process and finally becomes zero. At this stage, a constant amount of CO_2 is sequestrated by the terrestrial system. The terrestrial systems can sequester an estimated amount of 12-169 PgC (1PgC= 10^{15} g carbon) per year (Sha et al., 2022).

1.2.1.2 Ocean fertilization

The biological carbon uptake can be increased by the marine fertilization method. Phytoplankton absorbs CO_2, where bacteria break down organic matter into

inorganic compounds by the process of mineralization. Before the last decade, several experiments on ocean fertilization have been performed (Martin et al., 1994).

In a study, in an area of 100 km^2 of ocean, the sea water is mixed with a micronutrient, iron. During the experiment, a 30 times increase in chlorophyll II is found. Consequently, the plankton biomass is increased by a magnitude through the transformation of 1,00,000 kg of fixed carbon (Martin et al., 1994; Robinson et al., 2014).

1.2.1.3 Mineral carbonation

In a mineral carbonation process, CO_2 forms stable carbonate minerals, such as dolomite ($Ca_{0.5}Mg_{0.5}CO_3$), magnesite ($MgCO_3$), calcite ($CaCO_3$), and siderite ($FeCO_3$) by reacting with calcium and magnesium-containing minerals (Olajire, 2013). This is also known as a chemical weathering process of rocks. The general chemical equation is shown in Equation 1.1 (Maroto-Valer et al., 2005).

$$(Mg,Ca)_xSi_yO_{x+2y} + xCO_2 \rightarrow x(Mg,Ca)CO_3 + ySiO_2 \quad (1.1)$$

The mineral carbonation process stores CO_2 in the form of stable solid mineral carbonate. The energy content of a mineral carbonate is 60 to 180 kJ mol^{-1} lower than that of CO_2 (400 kJ mol^{-1}) (Maroto-Valer et al., 2005). Therefore, the sequestration in the form of mineral carbonation secures a long-term CO_2 fixation.

1.2.2 Direct sequestration by artificial processes

In the direct CO_2 sequestration process, CO_2 emitted from a large point sources (thermal power plant, steel or cement industries) are captured from flue gases and transported to a suitable site, such as ocean or underground, to be injected or sequestered (Yamasaki, 2003).

1.2.2.1 Geological injection

The captured CO_2 is injected into the deep geological formation, sometimes saline aquifers or depleted oil or gas reservoirs. The geological CO_2 injection has a long history of commercialization in terms of EOR (Enhanced oil recovery) and coal seam processes (Yamasaki, 2003).

Enhanced oil recovery (EOR): EOR refers to the process by which oil is recovered from the depleted reservoir by injecting materials that are not naturally present in the reservoir. This method is implemented by thermal injection, chemical injection, and gas injection techniques. In gas injection technique, commonly CO_2 is used, as it reduces the oil viscosity by reducing the interfacial area between oil and water (Blunt et al., 1993). The displacement of oil is dependent on the phase behavior of CO_2 and crude oil mixture. More than 50% of injected gas can be returned with the produced oil in this application (Bondor, 1992), which can be re-injected for minimizing the operational cost.

Coal seam: CO_2 sequestration in coal seam can be one possible route to mitigate the increasing atmospheric CO_2 (Reichle et al., 1999). Adsorption plays main role in coal seam storage at the pressure range of 2067 kPa to 5856 kPa (Das and Dutta, 2017). In the coalification process in coal seam, methane is produced as a main product (70-85 %) (Das and Dutta, 2017), others being water and CO_2. Methane is stored as sorbate in the microporous structure of coal. CO_2 is injected to the coal seam, desorption starts and methane is displaced by CO_2 (Shi and Durucan, 2005).

1.2.2.2 Ocean injection

An estimated 40,000 Gt of carbon is stored in the oceans. While, the terrestrial biosphere and atmosphere contain 2200 and 750 Gt of carbon, respectively (Stewart and Hessami, 2005). Consequently, the change in the carbon concentration in the atmosphere by 2 times, would result in an approximate 2% increase in the carbon concentration in the ocean. Therefore, the ocean can be considered a sink for CO_2. Several injection methods can be applied:

i. Droplet plume: Injection of liquid CO_2 is done by using a manifold below 1000 m, which forms a rising plume.
ii. Dense plume: A mixture of dense CO_2 and seawater, that sinks, is injected between 500 and 1000 m.
iii. Dry ice: Dry ice is dropped from the ships into the ocean for diffusion.
iv. Towed pipe: CO_2 is injected through a towed pipe from moving ship below 1000 m, forming a rising droplet plume.
v. CO_2 lake: CO_2 is released below 4000 m to form a stable deep lake of CO_2.

In natural sinking process, terrestrial plants are capable of atmospheric CO_2 reduction by only 3-6%. Direct sequestration, such as ocean injection, could be unsustainable due to the energy intensive process, high operational and transportation costs, large space required, and furthermore, physical leakage of CO_2 to atmosphere (~15-20% of CO_2 can be leaked over a few hundred years of storage) due to natural disasters like earthquake (Bhola et al., 2014; Farrelly et al., 2013). The ocean acidity is increased by 30% due to absorption of CO_2, which reduces the ability of marine creatures for the construction of their shells and skeletal structure (Farrelly et al., 2013). In case of EOR, the injectivity could be decreased from 10 even up to 100% due to the reservoir compaction, precipitation of minerals, reduction in permeability due to oil emulsification and bacterial growth and moreover ~66% return of CO_2 to the atmosphere along with the produced oil and gas (Xie and Economides, 2009).

In coal seam injection process, the permeability of reservoir could be reduced due to the complexity occurs from the physicochemical alterations in the structure of coal, which in turn affects the injectivity of CO_2 into the seam (Sampath et al., 2020).

While, CO_2 conversion to fuels have prospect of large amount of CO_2 sequestration, approximately 500 Mt $year^{-1}$ (Ghiat and Al-Ansari, 2021). Therefore, about 5-10% of total CO_2 emissions in the atmosphere could be utilized for the production of chemicals and fuels (Cheah et al., 2016). In this context, various CO_2 conversion processes to fuels and chemicals will be discussed in the next section (Section 1.2.3).

1.2.3 Conversion of CO_2 to value-added chemicals

The chemical utilization of CO_2 is considered as another promising route of CO_2 sequestration. The chemical reactions of CO_2 can be classified into two types: i) nonreductive reaction and ii) reductive reaction.

1.2.3.1 Nonreductive reaction

In nonreductive reaction of CO_2, oxygen atoms of CO_2 do not convert and carbon dioxide is fixed to different bonds, such as carbon-carbon, carbon-nitrogen bonds.

Catalytic copolymerization of CO_2: The synthesis of polycarbonates from CO_2 and epoxides has received enormous attention as it consumes CO_2 as a feedstock. The catalysts such as $ZnEt_2/H_2O$, $ZnEt_2$/isophthalic acid, $Zn(OH)_2$/glutaric acid and ZnO/glutaric acid are used to increase the activity (Cooper, 2000). Equation 1.2 represents the general polymerization reaction of such a process (Inoue et al., 1969).

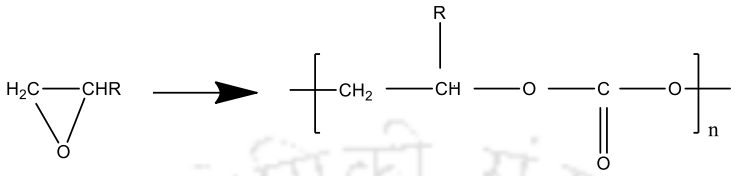

(1.2)

Two steps involve in the copolymerization of CO_2 with epoxide. The first step is the reaction between CO_2 and metal alkoxide, and the second step is the reaction between the epoxide and metal carbonate (Equation 1.3).

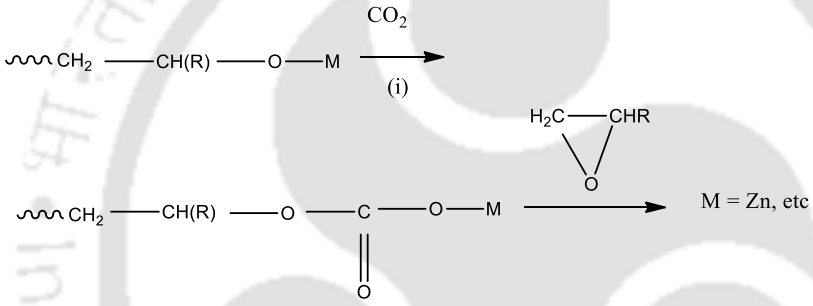

(1.3)

The polymer undergoes thermal degradation (Equation 1.4) upon heating to 200°C for the formation of their corresponding cyclic carbonate (Inoue et al., 1975).

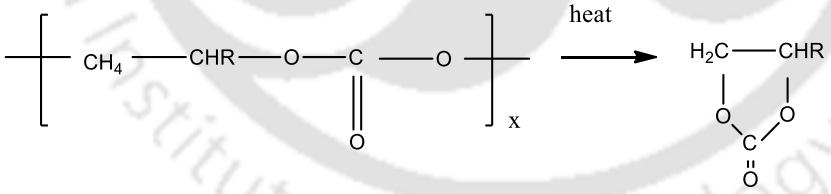

(1.4)

Thermocatalytic CO_2 conversion process: The thermocatalytic conversion of CO_2 combines high-temperature reaction, typically 250-400°C and heterogeneous catalysis to provide a fast reaction rate with large volume of CH_4 production (Das et al., 2020). This is also known as the methanation reaction or the Sabatier reaction after the name of Sabatier and Senderns, who first studied this reaction. Nickel (Ni) and ruthenium (Ru) based catalysts exclusively produce CH_4, while Cu and Ag catalysts mainly produce CH_3OH (Stangeland et al., 2017).

Mattia et al. (2015) reported thermocatalytic CO_2 conversion to HCs, CH_4 and C_2-C_4 alkenes using iron-carbon nanotube, FeCNT, as a catalyst. For the preparation of catalyst, a solution containing ferrocene and toluene is heated at 790°C in a furnace with 450 $cm^3\ min^{-1}$ Ar and 50 $cm^3\ min^{-1}$ H_2 in a quartz reactor. Maximum conversion and selectivity to HCs is found at 370°C and 2.5 bar pressure. The highest selectivity to higher-order HCs is found at 7.5 bar pressure.

1.2.3.2 Reductive reactions

The reductive reaction of CO_2 involves the loss of oxygen atoms of CO_2 or addition of hydrogen atom to form various compounds, such as formic acid, methanol, methane or carbon monoxide. These reactions are generally three types.

Photocatalytic CO_2 conversion (artificial photosynthesis) processes: The term "artificial photosynthesis" was derived by the inspiration from photosynthetic organisms in nature. The common features of natural photosynthetic organisms are that they use antenna system to absorb the energy within the wavelength of light available in the environment and channel this energy to the photosynthetic reaction, called protein-centers. These are the nanoscale devices that transfer electrons from donors to the acceptors by utilizing the excitation energy, which is used to oxidize water and generates sufficient electrons to reduce CO_2 at photocatalytic centers.

The artificial photosynthesis processes mimic the natural system. The basic steps of the reaction associated with artificial photosynthesis involve the dissociation of water into H_2 and O_2, which is a water splitting reaction with a positive Gibbs free energy change (Equation 1.5) (Kibria and Mi, 2016).

$$H_2O \rightarrow \frac{1}{2}O_2 + H_2, \qquad \Delta G = +237.178\ kJmol^{-1} \tag{1.5}$$

The water-splitted hydrogen (H_2) or hydrogen radical ($H\cdot$) can also be used for further reduction of CO_2 into various chemicals, such as formic acid (HCOOH), formaldehyde (HCHO), methanol (CH_3OH), and methane (CH_4). These products are supposed to form via a complex sequential pathway (Equation 1.6) with the formation of several intermediates (McConnell et al., 2010).

$$CO_2 \xrightarrow{+2e^-,\ +2H^+} HCOOH \xrightarrow{+2e^-,\ +2H^+,\ -H_2O} HCHO \xrightarrow{+2e^-,\ +2H^+} CH_3OH \xrightarrow{+2e^-,\ +2H^+,\ -H_2O} CH_4 \tag{1.6}$$

The first experimental demonstration of artificial photocatalysis is done by Fujishima and Honda in 1972 for water splitting in a photoelectrolytic cell composed

of an n-type rutile titanium dioxide (TiO_2) as photoanode and a platinum cathode (Fujishima and Honda, 1972). The primary reactions involved in the processes for the formation of various products by the reduction of CO_2 in an aqueous media at neutral pH 7 are given through Equations 1.7 to 1.14 (Indrakanti et al., 2009). The use of UV light is the primary limitation of a photocatalytic process. Therefore, CO_2 reduction to value-added products by the visible light-responsive photocatalytic process could be an attractive route of CO_2 sequestration.

$$2H^+ + 2e^- \rightarrow H_2 \qquad (E^0 = -0.41 \text{ V vs. NHE}) \qquad (1.7)$$

$$H_2O \rightarrow \frac{1}{2}O_2 + 2H^+ + 2e^- \qquad (E^0 = 0.82 \text{ V vs. NHE}) \qquad (1.8)$$

$$CO_2 + e^- \rightarrow CO_2^{\bullet} \qquad (E^0 = -1.90 \text{ V vs. NHE}) \qquad (1.9)$$

$$CO_2 + H^+ + 2e^- \rightarrow HCO_2^{\bullet} \qquad (E^0 = -0.49 \text{ V vs. NHE}) \qquad (1.10)$$

$$CO_2 + 2H^+ + 2e^- \rightarrow CO + H_2O \qquad (E^0 = -0.53 \text{ V vs. NHE}) \qquad (1.11)$$

$$CO_2 + 4H^+ + 4e^- \rightarrow HCHO + H_2O \qquad (E^0 = -0.48 \text{ V vs. NHE}) \qquad (1.12)$$

$$CO_2 + 6H^+ + 6e^- \rightarrow CH_3OH + H_2O \qquad (E^0 = -0.38 \text{ V vs. NHE}) \qquad (1.13)$$

$$CO_2 + 8H^+ + 8e^- \rightarrow CH_4 + 2H_2O \qquad (E^0 = -0.24 \text{ V vs. NHE}) \qquad (1.14)$$

The bandgaps of some commonly used photocatalysts for CO_2 reduction are shown in Figure 1.3 (Ola and Maroto-Valer, 2015).

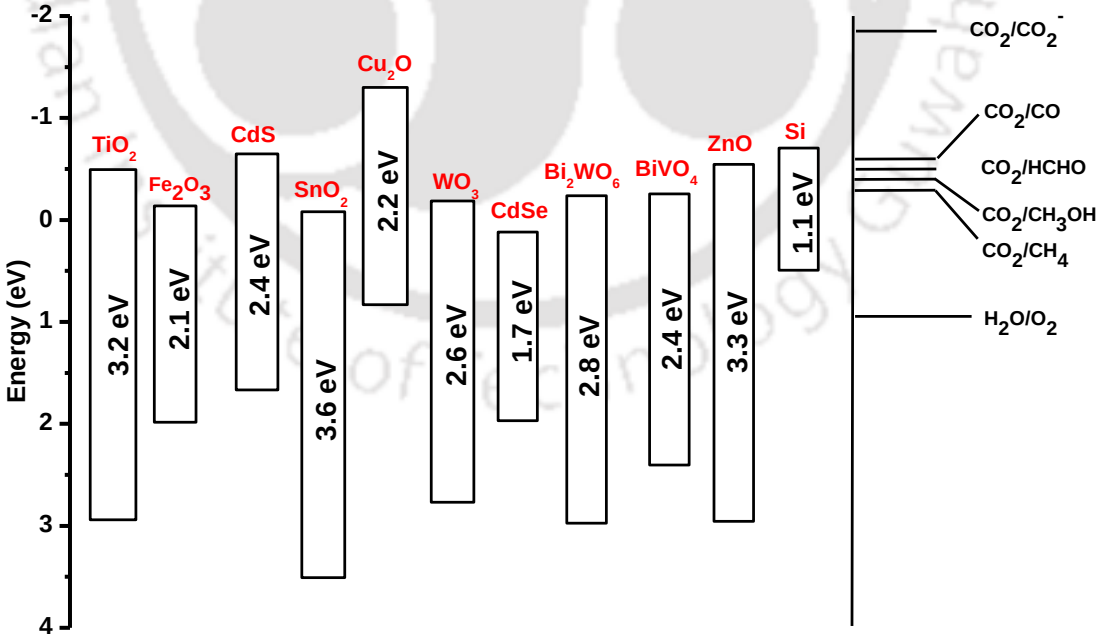

Figure 1.3. Bandgap energies of some commonly used photocatalysts relative to redox potential at pH 7 along with the compounds produced in CO_2 reduction.

CO_2 fixation in (photo) bioprocess: Switching to renewable fuels could be another possible solution for the fixation of anthropogenic CO_2. In this perspective, microalgae have greater photosynthetic effect than other plants (Low et al.,1988), and it can be used to fix CO_2 from three different sources, such as atmospheric CO_2, CO_2 discharge from heavy industry, and CO_2 from soluble carbonate (Brennan and Owende, 2010). Microalgae, including cyanobacteria, *Chlorella sp.*, *Chlamydomonas reinhardtii*, *Scenedesmus sp*., *Nannochloropsis sp.* (Pavlik et al., 2017), etc. are used to perform the photosynthetic reaction. To facilitate uniform microbial growth in photo-bioreactor, light wavelength range of 400-700 nm is usually supplied (Kremer et al., 2008). Photo-bioreactor uses the typical photosynthesis process and converts light, heat, and CO_2 to chemical products (Equation 1.15), like carbohydrate, hydrogen, and oxygen (Stewart and Hessami, 2005).

$$6CO_2(aq) + H_2O(l) + \text{light} + \text{heat} \rightarrow C_6H_{12}O_6 + 6O_2\,(g) \qquad (1.15)$$

In this process, the formation of glucose, the primary product depends on the biological strain used for the conversion reaction.

Mondal et al. (2017) reported CO_2-fixation by *Chlorella sp.* BTA 9031 using a photo-bioreactor. Microalgal cultivation is conducted at pH 7.4 and 25°C under 70 µmol m^{-2} s^{-1} light intensity for 12 h light. Microalgal growth study is performed in BG-11 medium at a low light intensity light of 60 µmol m^{-2} s^{-1} at 25°C for 24 h and continuous aeration with 5 and 15% of CO_2 at a flow rate of 0.25 L min^{-1}. At optimal condition of 28.26°C, 76.64 µmol m^{-2} s^{-1} light intensity, and 4% CO_2, CO_2 bio-fixation rate is found to be 0.235 g L^{-1} d^{-1} with the biomass production and total lipid content of 1.42 g L^{-1} and 22.5%, respectively.

Pavlik et al. (2017) reported CO_2-fixation in a photo-bioreactor using microalga *Chlorella vulgaris* 395 and flue gas at a flow rate of 0.04 m^3 min^{-1} from a power plant as a carbon source (7.6±0.8% v/v of CO_2).

Electrochemical CO_2 reduction: In this process, oxidation of water takes place at the anode surface by releasing electrons and CO_2 reduction takes place at the cathode electrode. The first step of direct conversion of CO_2 is the formation of the $CO_2^{\bullet-}$ radical anion, which is highly unfavorable too. The standard potential of $CO_2/CO_2^{\bullet-}$ couple in aqueous solution is −1.90 V (vs. NHE) (Equation 1.16) (Ganesh,

2014). Depending on the half-cell reaction and the potentials applied, different products can be generated through electrochemical CO_2 reduction reaction (ECO_2RR). The reaction proceeds through -one, -two, -four, -six, -eight, -ten, -twelve, -fourteen, -eighteen electron transfer according to the end product. The required potentials for individual half-cell reactions are calculated from the standard Gibbs free energy. Some of the typical products are listed in Table 1.3, with their equilibrium potential in pH-independent reversible hydrogen electrode (RHE) (Pan and Yang, 2020). The letter in parentheses (g→ gas, l→ liquid) indicates the physical state of the compounds. The slight positive equilibrium potential values for alcohols, aldehyde, and hydrocarbons imply a notably high energy input for their production in ECO_2RR. This is because the minimum equilibrium potential to drive the overall reaction, which is the difference between equilibrium potential of ECO_2RR and the equilibrium potential of oxygen evolution reaction (OER), is larger than 1 V (Nitopi et al., 2019).

$$CO_{2(g)} + e^- \rightarrow CO_2^{\bullet -} \qquad E° = -1.90 \text{ V (vs. NHE)} \qquad (1.16)$$

Table 1.3. Products formed in electrochemical CO_2 reduction reaction at standard potential E^0 vs. RHE.

Products	**Cathode reactions**	**E° (V vs. RHE)**
CO	$CO_2(g) + 2H + e^- \rightarrow CO(g) + H_2O$	−0.11
HCO_2H	$CO_2(g) + 2H + 2e^- \rightarrow HCO_2H(l)$	−0.12
HCHO	$CO_2(g) + 4H^+ + 4e^- \rightarrow HCHO(l) + H_2O(l)$	−0.07
CH_3OH	$CO_2(g) + 6H^+ + 6e^- \rightarrow CH_3OH(l) + H_2O(l)$	0.03
CH_4	$CO_2(g) + 8H^+ + 8e^- \rightarrow CH_4(g) + 2H_2O(l)$	0.17
CH_3CO_2H	$2CO_2(g) + 8H^+ + 8e^- \rightarrow CH_3CO_2H + 2H_2O(l)$	0.11
CH_3CHO	$2CO_2(g) + 10H^+ + 10e^- \rightarrow CH_3CHO(l) + 3H_2O(l)$	0.06
C_2H_4	$2CO_2(g) + 12H^+ + 12e^- \rightarrow C_2H_4(g) + 4H_2O(l)$	0.08
CH_3CH_2OH	$2CO_2(g) + 12H^+ + 12e^- \rightarrow CH_3CH_2OH(l) + 3H_2O(l)$	0.09
C_2H_6	$2CO_2(g) + 14H^+ + 14e^- \rightarrow C_2H_6(g) + 4H_2O(l)$	0.14
C_2H_7OH	$3CO_2(g) + 18H^+ + 18e^- \rightarrow C_2H_7OH(l) + 5H_2O(l)$	0.10

The advantages and disadvantages of different CO_2 sequestration techniques are tabulated below in Table 1.4.

Table 1.4. Advantages and disadvantages of different CO_2 sequestration techniques.

Techniques	Advantages	Disadvantages
Catalytic copolymerization of CO_2	• Ease of catalyst separation (using filtration only 1-2 ppm metal residue) (Lu and Darensbourg, 2012) • No or little side products up to 3.8% (Qin et al., 2015)	• Requires high catalyst loading (epoxy: catalyst= 200-500:1 molar ratio (Lu and Darensbourg, 2012) • Metal sites may be partly active and residual catalyst remains in the polymeric product • Long reaction time (2-19 days) (Qin et al., 2015)
Thermocatalytic CO_2 conversion	• Fast reaction rate (20-40 mol_{CH2} g_{cat}^{-1} h^{-1}) (Rusdan et al., 2022) • Generated CO can be mixed with H_2 to produce syngas, i.e., methanol	• Required hydrogen source is H_2 • Energy-intensive reaction and high temperature (> 2000 K) process (at 5000 K temperature, with 100% conversion, the energy efficiency is 35%) (Snoeckx and Bogaerts, 2017) • High capital cost due high temperature reactor
Photobioreactor	• Cultivation of algae in controlled environment provides higher productivity (e.g., biomass productivity 3.41 $g_{biomass}$ L^{-1} d^{-1} using *Chlorella vulgaris*) (Lim et al., 2021) • Large surface-to-volume ratio (70 m^{-1}) of photobioreactor offers maximum efficiency using light (Singh and Sharma, 2012) • Better control of gas transfer • Uniform temperature distribution in the reactor	• High capital cost ($70 m^{-2}) (Mohler et al., 2019) • Hindrance in algae culture for the specific end-products • Prone to fouling of the reactor (fouling rate 6.9 kPa d^{-1} at 18 h HRT*) (Ding et al., 2022)

Photocatalytic CO_2 reduction	• Operates under ambient conditions • Use of inexhaustible solar energy (5% UV, 95% visible + infrared) (Vu et al., 2019)	• Faster charge-carrier recombination (e.g., for bulk g-C_3N_4: 2.74 ns) (Wen et al., 2017) • Low selectivity and quantum yield (e.g., 9.18% for CH_4 production using Ti-MCM-41 (H. Y. Wu et al., 2014); 0.034% for CO, using N_2-doped TiO_2 nanotube arrays (Delavari et al., 2016)) • Low conversion (5-17%). (Snoeckx and Bogaerts, 2017)
Electrochemical CO_2 reduction	Driven by renewable energy sources; solar, wind, tidal or geothermal for production of energy dense fuels (e.g., ethanol) (Kumar et al., 2016) • Reaction can be controlled by applied electrode potential/ current, cell set-up • Easily scaled up for industrial process (e.g., high current densities (200-600 mA cm^{-2}) for ECO_2RR is achieved by combining gas diffusion electrodes (GDE) and flow-cell configurations) (M. Li et al., 2020) • Use of heterogeneous catalyst leads to easy recovery after reaction	• Relatively low solubility of CO_2 in water (0.03 M at 25°C) (<20% of saturated CO_2 conversion to product) (Burkart et al., 2019) • Faradaic efficiency of the products could be lower due to hydrogen evolution (Hou et al., 2022) • Low product selectivity (Cu exhibited a mixture of 16 products) (Kuhl et al., 2012) • Solvent decomposition at high reduction potential (solvent decomposition starts after -2.5 V Ag/AgCl for Cu electrode in acetonitrile solution) (Figueiredo et al., 2016) • Low catalytic activity and insufficient stability (few hours/days) (Jerome et al., 2022)

*HRT: Hydraulic retention time

1.3 Catalysts for CO_2 conversion and its synthesis routes

The CO_2 is a linear and centrosymmetric molecule having center carbon atom poorly electrophilic in nature. It is considered as a stable molecule due to its C═O

bond dissociation energy higher than 750 kJ mol^{-1}. CO_2 reduction reaction demands the requirement of catalysts preferably in the form of nanoparticles for high energy input to ease CO_2 activation for the desired products (Kumaravel et al., 2020).

The route of nanoparticles synthesis plays a key role in deciding its properties and the domain of applications (Singh et al., 2021). The synthesis of nanoparticles can be achieved both by the conventional and bioinspired methods.

1.3.1 Conventional methods of nanoparticles synthesis

In this section, the typical techniques involved in electrocatalysts synthesis are outlined.

1.3.1.1 Sol-gel method

This is one of the common methods employed for the fabrication of metal oxides, especially the oxides of titanium and silicon. In this method, metal or metalloid elements are used as the precursors for the preparation of colloids. In general, sol-gel method consists of chemical processes, such as hydrolysis, polymerization, gelation, condensation, and densification (Brinker and Scherer, 1990). At first, sol is formed by mechanical mixing of colloidal particles in water at a certain pH to prevent precipitation. A liquid alkoxide precursor is then hydrolyzed with water. The hydrolysis followed by polycondensation reaction eventually results in a metal oxide network and forms sol. The physical properties of the sol particles, such as size and density, depend on pH, temperature, and water content of the solution. The general reaction steps of sol-gel method are shown below in Figure 1.4 (Bokov et al., 2021).

Hasan et al. (2015) reported synthesis of Cu-RGO-TiO_2 nanocomposites using sol-gel method for photoelectrocatalytic CO_2 reduction to formic acid and methanol. The current efficiency of both the products was found to be 32.47% with formation rate of 255 μmol h^{-1} cm^{-2} and 189.06 μmol h^{-1} cm^{-2}, respectively.

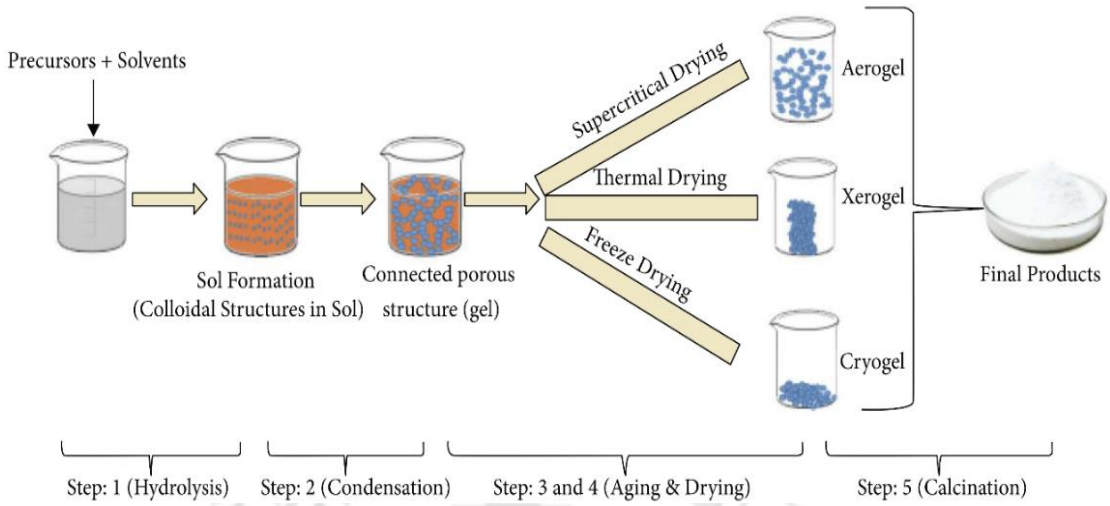

Figure 1.4. Typical steps involved for the synthesis of metal oxides catalysts in sol-gel process. Reprinted from Bokov et al. (2021).

1.3.1.2 Solvothermal method

Solvothermal method involves the use of solvents under moderate to high pressure (typical range 1-100 atm) and temperature (typical range 100-1000°C) to facilitate the interactions between precursors. Figure 1.5 shows the schematic of the synthesis of pristine zeolitic imidazolate framework-8 (ZIF-8) starting from $Zn(NO_3)_2.6H_2O$ precursor, using solvothermal method at 150°C for 5 h (Sharma and Chand, 2022). If water is used as a solvent, it is called "hydrothermal synthesis" (Mandal et al., 2019). In the case of hydrothermal process, the temperature is below the supercritical temperature of water (374°C). Materials including bulk powder, thin film, and nanocrystal are formed in this method.

Chen et al. (2021) synthesized CuS nanoflowers using polyvinylpyrrolidone (PVP, MW 40,000), and ethylene glycol (EG) as solvents for solvothermal method, for electrochemical CO_2 reduction to HCOOH. The electrocatalyst, $Cu_{1.54}S$ (Cu/S atomic ratio 1.54) exhibits ~52% FE of HCOOH formation.

Huang et al. (2022) synthesized Au-Cu gradient alloy (AuCu-g) by following solvothermal method, where hydrazine and polyvinylpyrrolidone are used as Cu^{2+} reducing and stabilizing agents, respectively. The reaction was conducted at 180°C for 4 h to obtain AuCu-g. FE of 20% is obtained for the formation of C_2H_4 at low limiting potential of −0.4 V (vs. RHE).

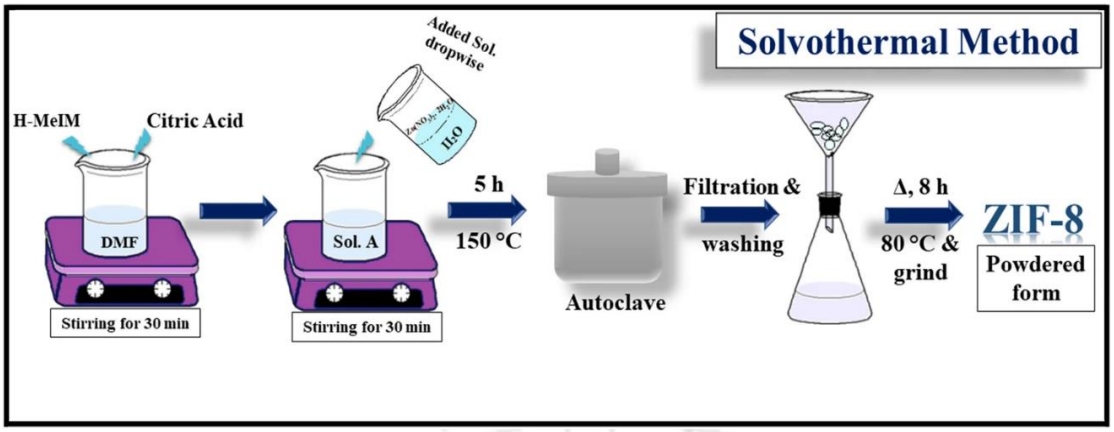

Figure 1.5. Schematic steps of solvothermal synthesis of pure ZIF-8**.** Reprinted with permission from Sharma and Chand (2022). Copyright 2022 Springer Nature.

1.3.1.3 Electrodeposition method

The electrodeposition method is used to coat a thin film of metal on a substrate, using a electroplating cell (Figure 1.6) (Kale et al., 2021). In this method, two metal electrodes are dipped in an electrolyte solution, and a fixed potential is applied, using a direct current (DC) power source to obtain the coating of desired metal on the cathode. In practical application for nanomaterials synthesis, three electrode system (working, reference, and counter electrodes) is employed. By varying the potential and current density, the thickness of the film can be controlled.

Rabiee et al. (2020) reported electrodeposition of Sn on asymmetric porous Cu hollow fiber gas diffusion electrode (HFGDE), at –1 V vs. Ag/AgCl for 15 to 300 s, to enhance ECO_2RR to formate. FE of formate formation was found to be 78% with a current density of 88 mA cm^{-2} at −1.2 V vs. RHE which was two-fold more FE compared to that with pristine Cu-HFGDE.

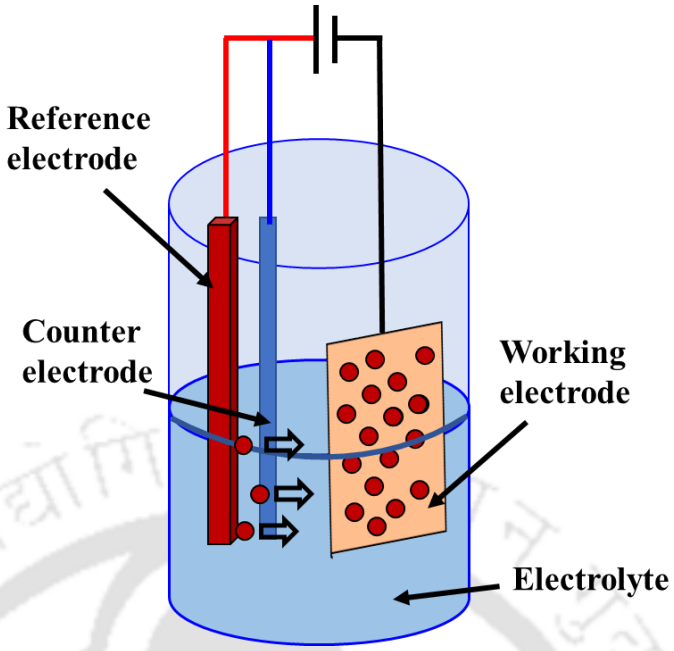

Figure 1.6. Simple schematic of electrochemical deposition setup.

1.3.1.4 Co-precipitation method

In co-precipitation method, soluble metal salts such as hydroxide, carbonate, oxalates or citrates are co-precipitated due to their low solubility. Generally, metal oxides or carbonates are digested with an acid followed by the addition of precipitating agents (e.g., ammonia and sodium bicarbonate). Magnetite and maghemite nanoparticles can be prepared by mixing aqueous $FeCl_2 \cdot 4H_2O$ and $FeCl_3 \cdot 6H_2O$ solution in alkaline pH using sodium hydroxide and ammonium hydroxide as the precipitants. The precipitate obtained is heated in an appropriate temperature (~40°C) for 24 h (Peternele et al., 2014). Figure 1.7 shows cellulose@γ-Fe_2O_3 nanospheres formation using co-precipitation method (Xiong et al., 2014).

Dongare et al. (2021a) synthesized oxide-derived Cu-Zn nanoparticles supported on N-doped graphene ($CuZn_x$/NGN) using co-precipitation method. $CuZn_{20}$/NGN exhibited ethanol selectivity with 34.25% FE at −0.8 V vs. RHE.

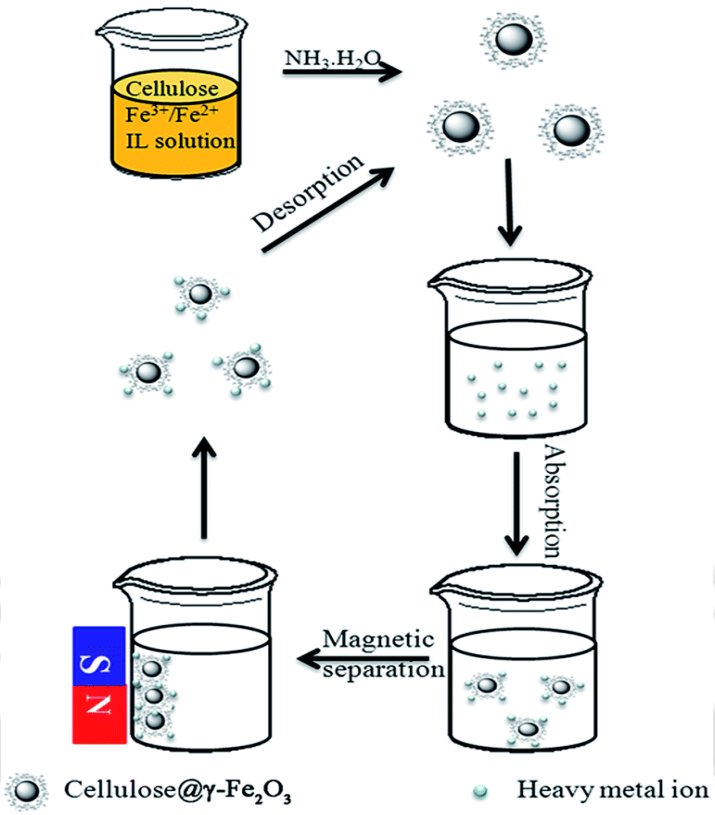

Figure 1.7. Synthesis route of cellulose@γ-Fe_2O_3 nanospheres using co-precipitation method. Reprinted with permission from Xiong et al. (2014). Copyright 2014 The Royal Society of Chemistry.

1.3.1.5 Flame spray pyrolysis

Flame spray pyrolysis (FSP) is one of techniques used for the production of powder materials at an industrial scale (Figure 1.8) (Nunes et al., 2019). This method allows producing powder with high selectivity at a high rate. In a typical FSP process, organic metal compound containing organic solvent and precursor solution is sprayed with high velocity oxygen and ignited with premixed methane-oxygen flame. Solvent and metal compounds are then evaporated and combusted to form atomically dispersed vapors of metal oxides. These metal oxide vapors then form clusters when reach to the cooler part of the flame. By the surface growth mechanism, the clusters formed grow and form non-porous nanoparticles.

Daiyan et al. (2019a) synthesized SnO_2 nanoparticle using FSP method. Tin 2-ethylhexanoate precursor solution in xylene was fed to FSP flame and oxygen was sprayed at 5 L min^{-1}. Oxygen and methane at 3.2 L min^{-1} and 1.5 L min^{-1} flow rate

were used as the supporting flame mixture. The synthesized SnO_2 nanoparticles could catalyze CO_2 reduction to $HCOO^-$ with 85% FE at −1.1 V vs. RHE with a current density of −23.7 mA cm^{-2}.

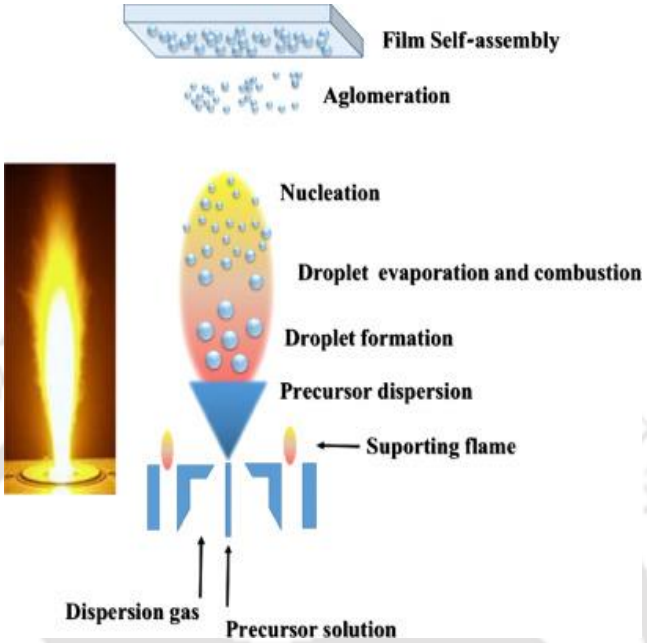

Figure 1.8. Schematic representation of nanoparticles synthesis using flame spray pyrolysis method. Reprinted with permission from Nunes et al. (2019). Copyright 2019 Elsevier.

1.3.1.6 Chemical reduction method

The chemical reduction method is a commonly used technique for synthesizing nanoparticles. This method commonly involves three steps: i) reduction of metal ion precursor using a reducing agent, ii) stabilization of metal-complex, and iii) size controlling and stabilization of nanoparticles by using a capping agent (Figure 1.9).

Z. Zhang et al. (2016) synthesized Bi NPs using the chemical reduction method. Bismuth acetate ($Bi(ac)_3$) precursor solution, 1-octadecene (ODE), 1-dodecanethiol (DDT) as a chelating agent, trioctylphosphine (TOP) as reducing agent, and surfactant were used to synthesize 36 nm of Bi NPs. Bi NPs showed 96.1% FE of CO_2 reduction to CO at −2.0 V vs. Ag/AgCl.

Castillo et al. (2017) synthesized 10-15 nm sized Sn nanoparticles using the chemical reduction method. Polyvinylpyrrolidone (PVP) (molecular weight 55,000) and ethylene glycol (EG) as surfactants, and sodium borohydride ($NaBH_4$) as a

reducing agent for Sn^{2+} were used in the synthesis process. The carbon-supported Sn/GDE (gas diffusion electrode) showed 70% FE of CO_2 reduction to $HCOO^-$ with 150 mA cm^{-2} current density.

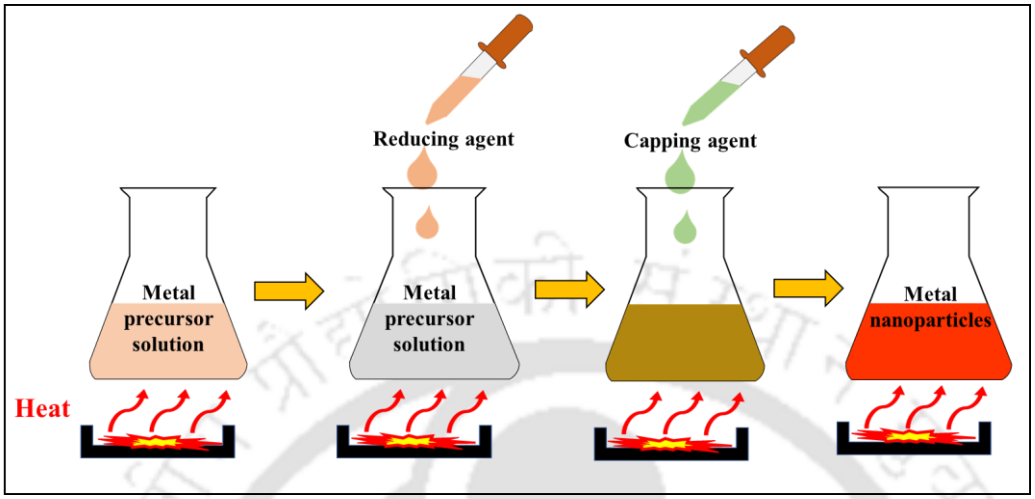

Figure 1.9. Typical steps of nanoparticles synthesis using chemical reduction method.

1.3.1.7 Chemical vapor deposition

Chemical vapor deposition (CVD) is used widely for the formation of solid thin-film coatings on surfaces and the synthesis of bulk materials and powders with high purity along with the fabrication of composite materials. In CVD method, metal is deposited from its vapor phase on a hot solid surface by chemical reactions. The solid materials are in the form of thin film, powder or single crystals. A typical CVD method includes the following steps: (i) a volatile precursor adsorbs onto the substrate in the reactor to liberate supporting ligands, which then desorbs and transports from the reactor and (ii) formation of the stable metal nucleus and subsequent growth by the diffusion of metal atoms (Hampden Smith and Kodas, 1995).

Figure 1.10 shows the schematic of the Au-assisted synthesis of MoS_2 using the CVD method. N_2 at the flow rate of 300 sccm (standard cubic centimetre per minute), was used as a carrier gas and the temperature inside the reactor was in the range of 140°C (temperature zone T1) to 785°C (temperature zone T2) for the growth of monolayer MoS_2 flakes. The method was utilized to form large Monolayer MoS_2 flakes with a lateral size of 20 μm. (Seravalli et al., 2021).

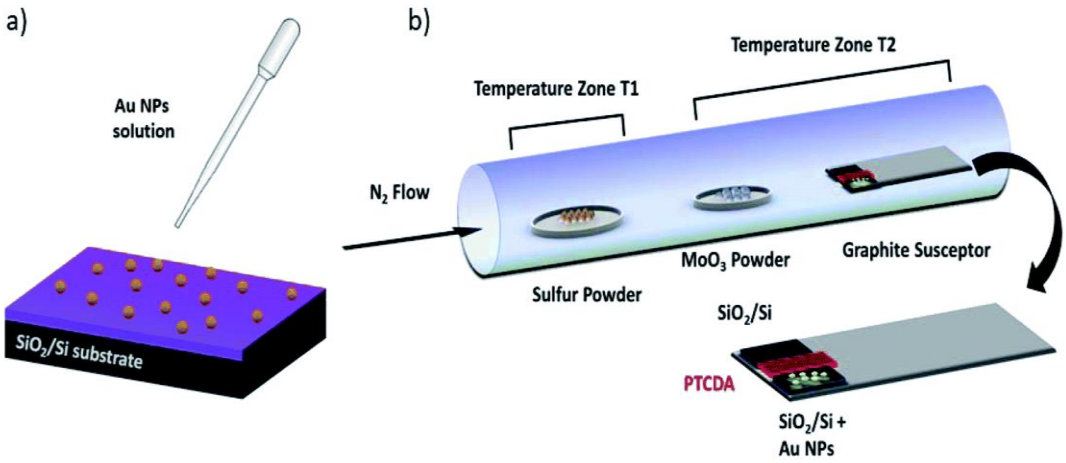

Figure 1.10. (a) Preparation of the AuNPs coated SiO_2/Si substrate. Schematic illustration of the experimental setup and process of the catalyst synthesis using CVD method for growth configuration. Reprinted from Seravalli et al. (2021).

1.3.1.8 Incipient wetness impregnation

Incipient wetness impregnation (IWI) or capillary impregnation method is a common technique for the preparation of heterogeneous catalysts. In a typical IWI method, metal precursor is dissolved in an aqueous or organic solution, which is then added to a catalyst support. The volume of the precursor solution added should be equal to pore volume of the catalyst support. The solution passes through the pores by the capillary action. The catalyst is then dried and calcined to expel the volatile component, which causes deposition of metal on the surface of the catalyst (Figure 1.11) (Y. Zhang et al., 2022).

Zhou et al. (2018) synthesized boron doped Cu catalyst (Cu(B)) using incipient wetness impregnation method. The synthesized catalyst exhibited a good electrochemical CO_2 reduction activity to C2 products with $79 \pm 2\%$ FE.

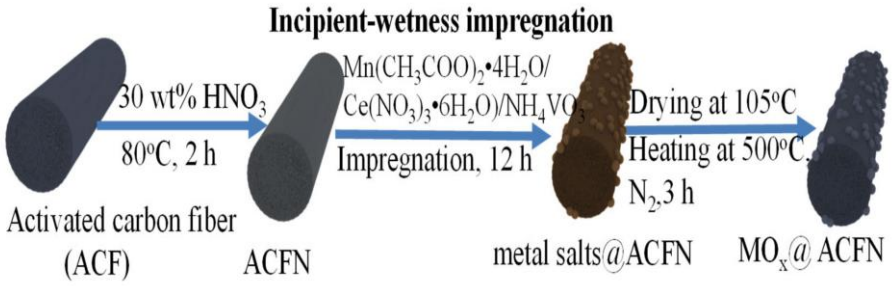

Figure 1.11. Preparation process of metal oxides loaded on activated carbon fiber (MOx@ACFN) via incipient wetness impregnation method. Reprinted from Y. Zhang et al. (2022) with permission from mdpi.com.

Table 1.5 summarizes common advantages and disadvantages of the conventional methods for nanoparticles synthesis discussed in the previous section (1.3.1).

Table 1.5. Advantages and disadvantages of some common fabrication techniques of electrocatalysts.

Methods	Advantages	Disadvantages
Sol-gel method	• High purity and products homogeneity (e.g. monodispersed SnO_2 NPs synthesis 2.8-5.1 nm of size, (Zhang and Gao, 2004); ZnO NPs with high purity (55.38% Zn and 44.62% O), 81.28-84.98 nm particles size (Hasnidawani et al., 2016)) • Better control on structure, and particle size (from zinc acetate to nanorod, zinc chloride to sulphate-nano-prism structure and zinc nitrate-prism flower shape structure) (Hasnidawani et al., 2016) • Low temperature range (20-650 °C)	• Higher cost of organic precursors (alkoxides are much expensive than oxides) (Dislich, 1986) • Film thickness >1 μm is difficult to produce due to large volume shrinkage and cracking during drying (Muromachi et al., 2006)
Solvothermal method	• Cost effective • Moderate temperature range (100-300°C) • Precipitants are not always	• Non-uniformity in both size and shape of nanoparticles • Potentially corrosive slurries (corrosive fluorine sources)

	required • Kinetic control over the phases formed • Precise control of size and shape distribution and highly crystalline products at relatively low temperature (nanorods, triangular plates, hexagonal plates, nanocubes and polyhedron AgNPs were synthesized with 50-90% yield) (Yang et al., 2007)	(Guan et al., 2017) • Expensive autoclave required
Co-precipitation method	• Organic solvents not required (Schwaminger et al., 2017) • Operates at low temperature (<100°C) (Petcharoen and Sirivat, 2012) • Simple direct route of synthesis of metal oxide powders with large surface area (e.g. α-Al_2O_3 nanoparticles synthesized using co-precipitation method with 206.2 m^2g^{-1} surface area compared to sol-gel method 30.72 m^2g^{-1}) (Rajaeiyan and Bagheri-Mohagheghi, 2013)	• High purity and stoichiometric phase cannot be obtained • Contaminants can also be precipitated with products • Reactants having different solubility and precipitate rates are not suitable for this method
Flame spray pyrolysis	• Operating at moderate temperature (100-500°C) (Korotcenkov and Cho, 2017) • Wide variety of low cost precursors (e.g. bismuth nitrate, copper (II) nitrate tri-hydrate, zinc nitrate hexa-hydrate, aluminum nitrate nona-hydrate) (Lee et al., 2015) • Products with high purity and relatively narrow size distribution (e.g. synthesis of $Li_4Ti_5O_{12}$ with >95% (mass) purity and 4-9 nm particles size) (Meierhofer et al., 2017)	• Hazardous gaseous reactants and byproducts (e.g. toxic metalorganics, CO, CO_2) (Leng et al., 2019) • Formation of hard agglomerates in gaseous phase leads to low-quality bulk materials (Meierhofer et al., 2020)
Chemical reduction method	• Desirable particles shape, high yield of nanoparticles (e.g. synthesis of Au nanorods (aspect ratio: 1-5) with ~95% yield)	• Use of toxic and cost chemicals limits large scale production (e.g. hydrazine, hydroquinone, sodium borohydride, hydroxylamine,

	(Jana, 2005; Kim et al., 2004)	$NaBH_4$, phenylenediamine, hydrohalic acid, thiophenol, NH_2OH, N_2H_4, thiocarbamide, etc.) (Kuila et al., 2013)
Chemical vapor deposition (CVD)	• Crystal structure, surface morphology, orientation of product can be manipulated (e.g. direct CVD growth of a graphene pattern using a prepatterned Ni structure) (Reina et al., 2009) • Coating of single layer, multilayer, composite, nanostructured, and well-controlled dimension and unique structure at low temperature (fabrication of large area (~cm^2), 1 to ~12 graphene layer films by CVD method) (Reina et al., 2009) • Usages of wide variety of precursors, namely, halides, hydrides, and organometallics (group 11 and 13 precursors including amidinates, guanidinates, iminopyrrolidinates, etc.) (Koponen et al., 2016)	• High purity gaseous reactants (99.9999%) • Metal oxide reacts with the chalcogen, causing undesirable and uncontrolled changes in the metal vapor flux during the growth (Cohen et al., 2021) • Reactants and products may be hazardous, explosive, and corrosive (metalorganic) • Large number of parameters must be precisely optimized to obtain desirable products (total and partial pressure, substrate temperature, growth time, inlet velocity, inlet mole fraction of H_2) (An et al., 2018; Tummala et al., 2020) • Low material utilization efficiency (1-20%) (Şengül et al., 2008)
Incipient wetness impregnation (IWI)	• Simplest technique • Convenient for scaling up • Highly dispersed metal particles on the surface of support (metal oxide) • Control over the weight of added precursor to the catalyst	• Nonhomogeneous distribution of metal precursor causes metal agglomeration (e.g. synthesis of Co/γ-alumina and Co-Ru/γ-alumina catalysts with 1-20 nm size) (Li et al., 2006) • Strong attraction of oxide of base metal precursor towards silica or alumina causes difficulty to reduce further

1.3.2 Bioinspired routes of synthesis of nanoparticles

As mentioned earlier in Table 1.2, the conventional methods of nanoparticles synthesis involve several toxic reactants, byproducts, and capping/stabilizing agents

which are non-biodegradable (Xu et al., 2021). The conventional methods produce ca. 100,000 kg waste per kg of product, which is 1000 times the waste produced in fine chemicals and pharmaceuticals manufacturing (Patwardhan et al., 2018).

The bioinspired route follows a one-pot process as the bioactive compounds (peptides, amino acids, polyphenols etc.) could simultaneously act as both reducing and capping agents (Xu et al., 2021).

The bioinspired process is cost-effective, environmentally friendly, and non-toxic. The nanoparticles synthesized following this route have been successfully applied in biomedicines for cytotoxicity study, an anti-inflammatory drug, photocatalytic activity, and bioimaging. (Singh et al., 2021). The presence of secondary metabolites, proteins, vitamins, and amino acids in biological sources like bacteria, fungi, and plants could act as capping agents and prevent the agglomeration of nanoparticles during their synthesis, which could further help to synthesize nanoparticles with controlled morphology and shape.

1.3.2.1 Nanoparticles synthesized by bacteria

Bacteria have the unique ability to reduce metal ions (M^{n+}) to metallic nanoparticles (M^0). Bacterial synthesis of metal nanoparticles involves either intracellular or extracellular mechanisms (Figure 1.12). Beveridge and Murray (1980) first reported extracellularly deposition of gold nanoparticles (AuNPs) on *Bacillus subtilis* cell wall (Beveridge and Murray, 1980). Depending on the culture media used, the extracellular method could produce various shapes like hexagonal, triangular, disc, cuboidal nanoparticles (Javaid et al., 2018). Priyadarshini et al. (2013) reported extracellularly triangular-shaped (12-65 nm) AgNPs synthesis using *Bacillus flexus* (Priyadarshini et al., 2013). Whereas extracellular synthesis offers easily purified and retrievable nanoparticles using centrifugation at 10000-12000 rpm (Javaid et al., 2018).

In the contrary, intracellular method of nanoparticles synthesis involves metal ion transport into the bacterial cell facilitated by the enzymes and proteins. The method involves additional steps of nanoparticles separation technique like bacterial cell lysis. In fact, some bacteria, such as *Proteus mirablis*, *Acinetobacter calcoaceticus*, *Bacillus flexus*, *Bacillus cereus* etc., could be able to synthesis AgNPs

both by using extracellular and intracellular methods (Alfryyan et al., 2022). Alfryyan et al. (2022) reported a comparison study on AgNPs synthesized by extracellular and intracellular methods using *Bacillus cereus*. Spherical AgNPs with crystallite size 45.4 nm synthesized by the extracellular method exhibited 100% degradation of methylene blue dye. Polygon AgNPs with crystallite size 90.8 nm synthesized in the latter method, showed 50.6% dye degradation.

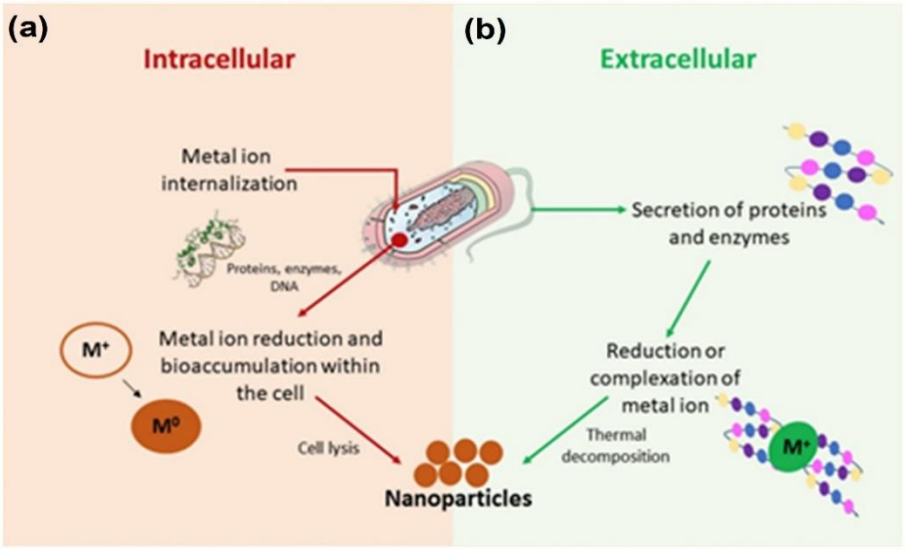

Figure 1.12. Green synthesis of nanoparticles using bacteria cultures. Reprinted with permission from Bandeira et al. (2020). Copyright 2020 Elsevier.

1.3.2.2 Nanoparticles synthesis by fungi

Fungi are the potential source of bioactive compounds that could act as reducing well as stabilizing agents for metal nanoparticles synthesis. Bérdy (2005) reported about 6400 such bioactive compounds using microscopic filamentous fungi, ascomycetes and other such species (Bérdy, 2005). The intracellular synthesis approach involves transportation of metal ions to the cells of microbes and the enzymes produced by the cell walls act as metal reducing agents. While, in an extracellular approach, the nanoparticles synthesis mechanism follows enzymatic reduction of metal ions in the cell wall (Figure 1.13). The extracellular synthesis is potential for major commercial applications due to the ease of nanoparticles separation with high purity.

Nanoparticles synthesis using fungi have advantages over other microorganisms because of the high quantity of enzymes and protein secretion by

fungi, which further amplifies the rate of reaction (Guilger-Casagrande and Lima, 2019). Various fungi species are reported for AgNPs synthesis, namely, *Aspergillus niger*, *Penicillium brevicompactum*, *Phanarochaete chrysosporium*, *Anamorphous Bjerkandera sp.* R1, etc. (Osorio-Echavarría et al., 2021). Osorio-Echavarría et al. (2021) reported intracellular 10-100 nm AgNPs synthesis using *Anamorphous Bjerkandera sp.* R1. Tyagi et al. (2019) reported extracellularly synthesized triangular, circular, and hexagonal shaped AgNPs of 10-50 nm using *Beauveria bassiana*. Chatterjee et al. (2020) reported extracellularly synthesized iron oxide (Fe_3O_4) nanoparticles of 20-40 nm size using *Aspergillus niger* BSC-1 for Cr(VI) removal from water (Chatterjee et al., 2020).

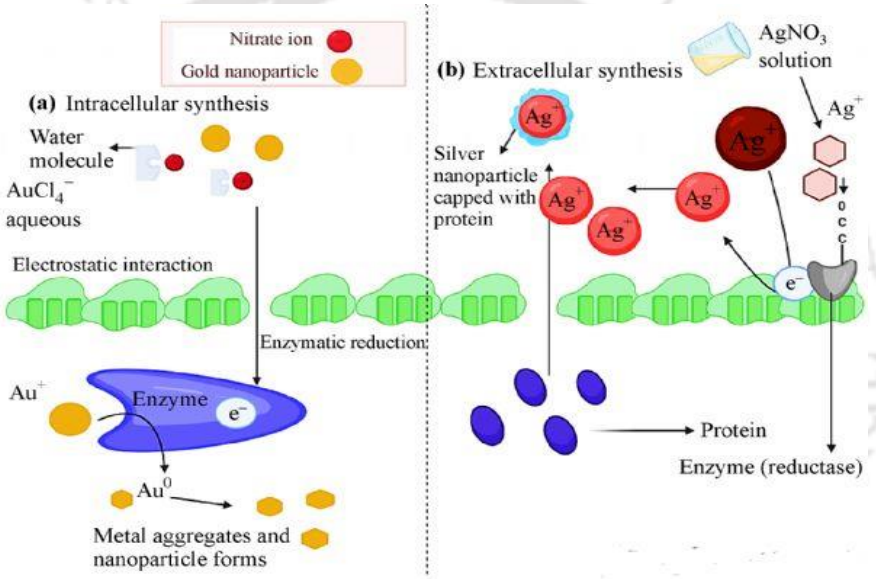

Figure 1.13. Biosynthesis of gold and silver nanoparticles by (a) intracellular and (b) extracellular mechanisms in fungi. Reprinted with permission from Das et al. (2021). Copyright 2021 Springer Nature.

1.3.2.3 Nanoparticles synthesis by plant

The basic step involved in plant-based nanoparticles synthesis, is the preparation of aqueous vegetal extract (leaf, stem, root, fruit/ fruit peel) (Vanlalveni et al., 2021) and conversion of metal ions to metal nanoparticles (Figure 1.14). Different shapes such as spherical, cubic, flower-like, hexagonal, with particle size 20-200 nm, are synthesized using different parts of plants (Vanlalveni et al., 2021). Elia et al. (2014) synthesized hexagonal and truncated triangular AuNPs using *Lippia citriodora* and *Salvia officinalis* leaf extracts, respectively (Figure 1.15).

Plant-based nanoparticles synthesis takes advantage of a greater kinetic rate than that of the other bioinspired routes (Gulia et al., 2022). This method also offers no pathogenic risk as in bacteria/fungi and synthesis of reasonably homogeneous nanoparticles (Alabdallah and Hasan, 2021). Vidhu and Philip (2015) synthesized spherical SnO_2 NPs of 2.2-3.2 nm particles using *Trigonelle foenum-graecum* (commonly known as Fenugreek) seed extract (Figure 1.16). Kumar et al. (2018) synthesized spherical SnO_2 NPs within the particle size range of 8-10 nm using *Psidium Guajava* leaf extract (Kumar et al., 2018). Chelli and Golder (2018) reported a one-pot bioinspired synthesis of Pt, Co and Pt@Co core-shell nanoparticles using *Sechium edule* fruit extract. The size of Pt nanospheres, Co nanoprisms and PtCo core-shell nanoparticles were found to be 28.6, 47.3, and 13.2-26.4 nm with the polydispersity index of 0.18, 0.38, and 0.253-0.307, respectively.

Garibo et al. (2020) synthesized quasi-spherical shaped AgNPs with an average diameter of 5 nm using stem and root extract of *Lysiloma acapulcensis*. The synthesized nanoparticles showed significant antimicrobial activity against *C. albicans*, *E. coli*, *S. aureus* and *P. aeruginosa* compared to AgNPs synthesized utilizing chemical method.

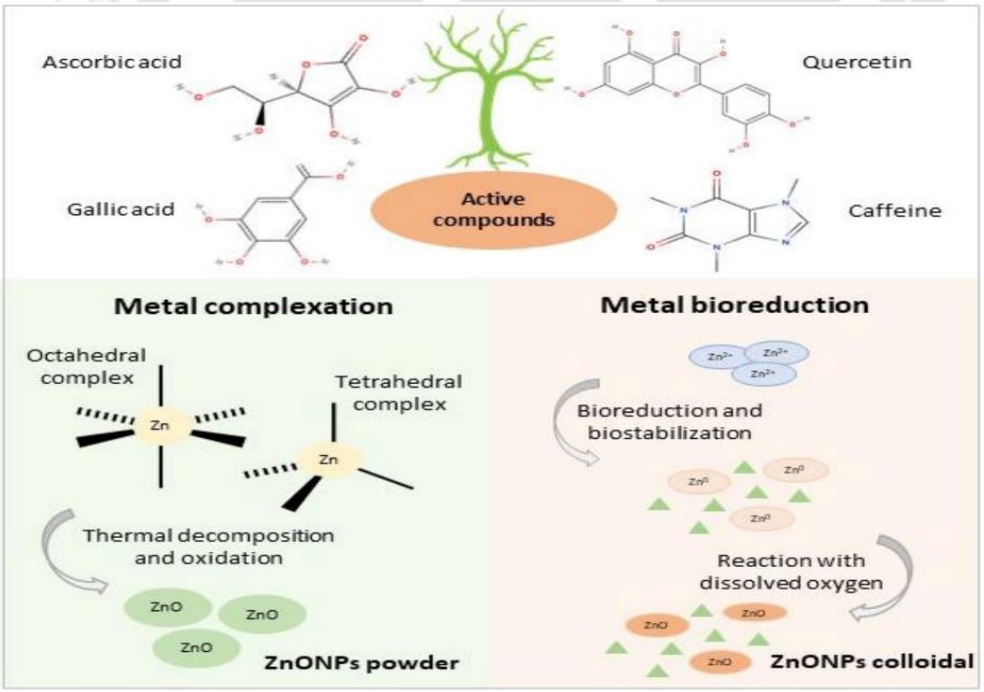

Figure 1.14. Green synthesis of ZnO NPs using plants extracts. Reprinted with permission from Bandeira et al. (2020). Copyright 2020 Elsevier.

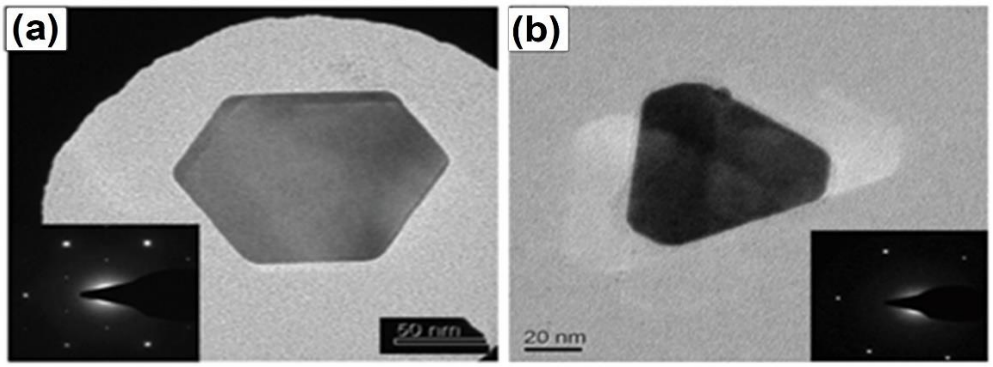

Figure 1.15. TEM images of (B) hexagonal and (C) truncated triangular Au NPs using *Lippia citriodora* and *Salvia officinalis* leaf extracts, respectively. Reprinted from Elia et al. (2014) with prior permission.

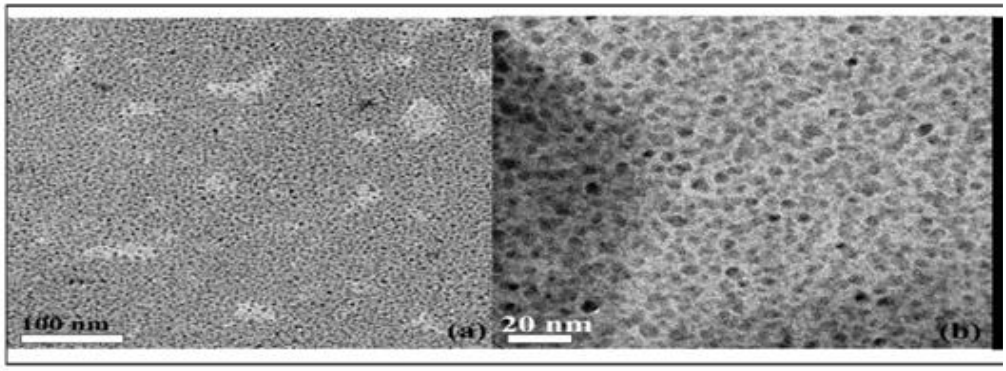

Figure 1.16. TEM images of SnO_2 synthesis using *Trigonella foenum-graecum* (Fenugreek) seeds. Reprinted with permission from Vidhu and Philip (2015). Copyright 2015 Elsevier.

1.4 Electrochemical CO_2 reduction reaction (ECO_2RR) to useful chemicals

1.4.1 Conventional cell configurations for ECO_2RR

To date, the most commonly used conventional lab-scale liquid-phase electrolyzer in ECO_2RR is the H-type reactor. It has gained huge popularity due to operational ease and flexibility of application for different catalysts (Gawel et al., 2022). In this reactor, the working and reference electrodes are placed in the cathodic chamber, and the counter electrode is in the anodic chamber. Both chambers are filled with electrolyte solution separated by a proton-exchange membrane to prevent the reoxidation of the products formed. The whole reactor looks like "H". The working electrode could be catalyst loaded on glassy carbon/ graphite plate/ carbon paper

supported electrodes. CO_2 is continuously bubbled to the catholyte during the electrolysis.

Despite the flexibility in use and cost-effective design of an H-type reactor, the large CO_2 gas diffusion layer (~50 μm) and poor solubility of CO_2 (33 mM) limit the CO_2 mass transport from solution to the catalyst surface, which in turn restricts the current density (<100 mA cm^{-2}) for industrial applications (Song et al., 2019).

To achieve a high rate of reactions in ECO_2RR, the use of semi-batch type H-type reactor is upgraded to the continuous type of reactors, such as microfluidic reactors (MFR), membrane-based flow reactors (MR), and membrane electrode assembly (MEA) electrolyzers (Yang and Li, 2021).

The MFR is membrane-free cells, where the anode and cathode are separated by a very thin channel (<1 mm), filled with the flowing electrolyte. The supply of gaseous CO_2 directly to the GDE reduces the CO_2 solubility restrictions as in an H-type reactor (Figure 1.17) (Yang and Li, 2021). Although, due to the membrane-less design it runs into the product cross-over.

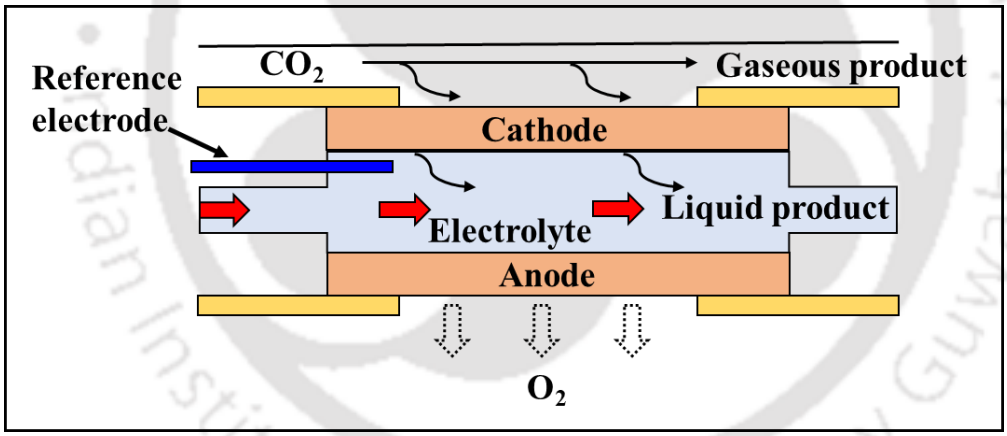

Figure 1.17. Schematic diagram of microfluidic reactor (Yang and Li, 2021).

In MR, the anode and cathode chambers are separated by an ion exchange membrane such as cation-exchange membranes (CEMs)/ anion-exchange membranes (AEMs)/ biopolar membranes (BPMs), to block the product cross-over. However, the over potential experienced due to the extended ohmic loss between anode and cathode and formation of carbonate in alkaline electrolyte increase the capital cost for industrial applications.

To overcome the drawback in MR, the MEA system is designed in such a way that the catalyst layer (CL) of gas diffusion electrode (GDE) is kept in direct contact

with the proton exchange membrane (PEM), in zero-gap mode. The liquid product concentrations are increased by taking out the gas and liquid products from the cathode plate with little diffusion through the membrane.

1.4.2 Factors affecting ECO_2RR

1.4.2.1 Operating conditions

Temperature and pressure: From Henry's law, and acid and bicarbonate (HCO_3^-)/carbonate (CO_3^{2-})/CO_2 buffer equilibria, it is intuitive that CO_2 solubility in aqueous electrolyte could be increased by decreasing temperature or increasing pressure. The rate of H_2 evolution reaction (HER) also could be suppressed at lower temperature (Nitopi et al., 2019). Ahn et al. (2017) reported that on Cu electrode, at 2 °C temperature, FE of CH_4 production was increased to 50%, whereas at elevated temperature, HER dominated with >50% FE (Ahn et al., 2017). Hara et al. (1997) reported selective reduction of CO_2 to CO and formic acid with FE 44 and 30%, respectively, on glassy carbon electrode at 50 mA cm^{-2} under 30 atm pressure. The enhancement in product formation is attributed to the increased CO_2 concentration in the catholyte (Chen and Wang, 2022).

pH: The pH of the electrolyte influences the solubility of CO_2 in an aqueous electrolyte solution. At about pH 6, CO_2 exists as weak carboxylic acid. Whereas, in pH between 6 to 10.3, CO_2 forms HCO_3^- anions, and pH>10.3, CO_2 exists as CO_3^{2-} (Garg et al., 2020). During ECO_2RR, the consumption of H_2O causes the accumulation of OH^- ions, which in turn increases the local pH at the cathode surface (Sikdar et al., 2021). It is well understood from the study reported by Hori et al. (1988) that the lower pH favors the HER and suppresses the formation of C_2H_4 and alcohols at Cu electrode (Hori et al., 1988). The authors suggest that at lower pH (~1), the protonation of CO dominates over the formation of C-C bond (Schouten et al., 2014).

1.4.2.2 Structural engineering of catalyst (nano)particles

Size effects: The size of the nanoparticles has a direct influence on the ratio of atoms at the edge and surface. With decreasing particles size, the coordination number of surface atoms also lowers due to the increase in under coordination sites (Nitopi et

al., 2019). Decreasing coordination numbers leads to alteration in electronic structure on the surface atoms and increases the catalytic activity.

Yang et al. (2020) reported that the particle size of Au trisoctahedron (Au-TOH) has a direct effect on FE of CO formation. A linear decrease in FE of CO formation from 88.80 to 62.13% is noted with the increase in particle size from 50 to 100 nm (Yang et al., 2020). The smaller particles size of Au-TOH has the higher population of edge sites having low coordination. A similar trend of size dependent CO production using PdNPs was reported by Gao et al. (2015). FE of CO production was increased from 5.8% on 10.3 nm NPs to 91.2% on 3.7 nm NPs at −0.89 V (vs. RHE), due to more active edge sites in lower sized NPs.

Shape and facet effects: Nanoparticles with different shapes show a distinct arrangement of atoms on the surface. Moreover, the crystal facet exposed on the metal/ metal-based nanoparticles strongly influence the surface geometry and also the catalytic activity (Liu et al., 2021). For example, the octahedral Cu nanoparticles is more selective towards methane and the cubic Cu towards C_2H_4. While, spherical Cu nanoparticles could not show any selectivity towards ECO_2RR products (Zaza et al., 2022).

Cu crystals with exposed Cu(100) facets could lower the energy dimerization barrier. For example, Cu(100) facets were reported to steer FE of ~57% towards C_2H_4 formation (De Gregorio et al., 2020). Liu et al. (2021) reported Cu_2O octahedral structure with (111) facets for selective production of alcohol with 35.4% FE (Liu et al., 2021). Cu_2O/Cu NPs with abundant (111) facets exhibited 97.7% FE of formate formation at −0.64 V vs. RHE with 5.2 mA cm^{-2} current density. The energy barrier for the intermediate for formate formation (10–20 kJ mol^{-1}) is ten times lower than that of the intermediates for carboxyl (100–350 kJ mol^{-1}) (J. Li et al., 2020).

1.4.3 Performance targets for ECO_2RR forming value-added chemicals

The following key metrics are associated with the catalytic activity, selectivity, and stability of catalysts for the performance evaluation in ECO_2RR processes.

1.4.3.1 Faradaic efficiency (FE)

Faradaic efficiency (FE) is the ratio of the amount of charge required to form a product of interest to the total charge supplied (Garg et al., 2020) (Equation 1.17).

$$FE=\frac{ZnF}{Q} \quad (1.17)$$

Where, Z is the number of electrons required for the product formation, n is the number of moles of the desired product, F is Faradaic constant (96485 C mol^{-1}), and Q is the total charge transfer.

In the assessment of ECO_2RR, FE is a critical factor because of the multiple product formation and simultaneous hydrogen evolution reaction (HER) (L. Li et al., 2020). Catalysts showing high FE could reduce the cost of product separation and increases energy efficiency. Micro-structured Bi catalyst showed 90% FE for $HCOO^-$ formation at −1.45 V vs. SCE (saturated calomel electrode) (Zhang et al., 2017). Whereas hexagonal Bi nanosheet boosted $HCOO^-$ formation with ~100% FE at −1.48 V vs. SCE (Jiang et al., 2021). Ag nanosheet showed 95% FE at −0.7 V vs. RHE (Lee et al., 2017) compared to Ag nanofoam with 97% at −1.2 V vs. RHE of CO formation (Wei et al., 2020).

1.4.3.2 Onset potential

Onset potential is defined as the least negative applied potential at which the product is first formed or faradaic current is detected. More positive onset potential signifies the more effective the catalyst for ECO_2RR, which is highly desirable. For example, ECO_2RR requires an onset potential of at least 1.0 V vs. NHE (normal hydrogen electrode) or more negative when Sn, Bi, Pb, and Cu-based catalysts are used (Masood and Ge, 2022). Bei et al. (2017) reported the onset potential of HCOOH −1.3 V vs. Ag/AgCl by using linear sweep voltammetry. Ordered cone-structured tin (OCSn) exhibited the onset potential of −0.46 V (vs. RHE), compared to Sn-N-60 (synthesized without the Triton X-100), −1.13 V (vs. RHE), for $HCOO^-$ formation (Zhong et al., 2021). RhO_2 showed the onset potential of −0.2 V (vs. RHE) for HCOOH production, while CrO_2 showed −0.3 V (vs. RHE) onset potential for most of the products (Tayyebi et al., 2018).

1.4.3.3 Overpotential (η)

Overpotential (η) is the additional potential applied to cross the kinetic barrier for ECO_2RR (Wu et al., 2020). It is the difference between the applied potential (V_{app}) and equilibrium potential (V_{Eq}) expressed as follows (Equation 1.18).

$$\eta = V_{app} - V_{Eq} \quad (1.18)$$

ECO_2RR is driven with significant overpotentials to overcome the rigid and highly stable CO_2 molecule. For instance, an overpotential of 0.6 V is required for Au catalyst to trigger the reaction at a rate of −5.0 mA cm^{-2} with FE of 87% for CO formation (Suominen and Kallio, 2021). Ag nano-coral structure showed a low overpotential of 0.37 V towards CO production, whereas, the cobalt protoporphyrin/pyrolytic graphite electrode produced CO at a moderate overpotential of 0.5 V (Kumar et al., 2016). Jiang et al. (2021) reported hexagonal Bi nanosheet facilitates $HCOO^-$ formation at 0.65 V of overpotential, which is 0.05 V higher than that of nanostructures Bi/GDE with 0.60 V overpotential (Zhang et al., (2017).

1.4.3.4 Current density (J)

It is used as an important input for designing the electrolyzer and to estimate the rate of CO_2 reduction to the products (Daiyan et al., 2020). Current density is dependent on mass transport, number of active sites and system impedance. It is the total current (I, in Amps) normalized by geometrical area (A, cm^2) of the electrode (cathode) (Equation 1.19).

$$J = \frac{I}{A} \quad (1.19)$$

Porous Zn exhibited −270 mA cm^{-2} current density at −0.95 V vs. RHE (W. Luo et al., 2019b), 54 times higher than that of Zn nanoparticles (−5 mA cm^{-2}) at −1.1 V vs. RHE for CO production (Jeon et al., 2018b). Bi nanotubes could show 24 times higher current density at −0.6 V vs. RHE (Fan et al., 2020), than that of Bi nanoflake (1 mA cm^{-2}) at −1.03 V vs. RHE (Kim et al., 2017).

1.4.3.5 Partial current density ($J_{product}$)

Partial current density ($J_{product}$) is the effective current density that steer the desire products to form. $J_{product}$ for a specific product can be expressed as in Equation 1.20.

$$J_{product}=J\times FE \quad (1.20)$$

In practical applications, an H-type reactor exhibits lower partial current density (<100 mA cm^{-2}) due to the poor solubility of CO_2 in an aqueous electrolyte. A significantly improved $J_{product}$ can be obtained in MEA reactor (> 1 A cm^{-2}) (L. Li et al., 2020). Prism-shaped Cu nanocatalyst exhibited four times higher partial current density (−11.8 mA cm^{-2}) than that of the planar Cu catalyst (−2.8 mA cm^{-2}) (Jeon et al., 2018a). Hierarchical Sn_3O_4 nanosheets had the highest partial current density of 421 mA cm^{-2} at −1.02 V vs. RHE for electrochemical CO_2 reduction to $HCOO^-$ (Liu et al., 2020).

1.4.4 Electrochemical tools for ECO_2RR

1.4.4.1 Cyclic voltammetry (CV)

Voltammetry is a non-destructive electrochemical technique in which varying potential is applied to the working electrode (WE) in an electrochemical system to measure the corresponding current response (Equation 1.21).

$$I=f(E) \quad (1.21)$$

Cyclic voltammetry (CV) is commonly used to investigate the oxidation-reduction reaction functionality of a catalyst. It is a hysteresis graph of current response (I) vs. applied potential (E). Xiang et al. (2014) reported 6,7-dimethyl-4-hydroxy-2-mercaptopteridine (PTE) as an active catalyst on glassy carbon electrode towards ECO_2RR to methanol and formate conversion based on of cyclic voltammetry analysis.

1.4.4.2 Chronoamperometry

Chronoamperometry is a current response (I) vs. time (s) graph at a constant applied potential (E). It is an electrochemical technique employed for measuring the catalytic activity and selectivity of the product(s) formed. The total charge required for Faradaic efficiency calculation is estimated from the current passes during the chronoamperometry measurement. In practical applications, the chronoamperometric potentials are chosen from the voltammograms.

Latiff et al. (2020) reported carbon-based copper(II) phthalocyanine for ECO_2RR. In this study, the potential for chronoamperometry was chosen to be −1.6 V

vs. Ag/AgCl, and the current density is significantly increased beyond −1.5 V vs. Ag/AgCl. The trend in current densities obtained from chronoamperometry is also in line with that of the current densities recorded from CV analysis.

1.4.4.3 Electrochemical impedance spectroscopy (EIS)

Electrochemical impedance spectroscopy (EIS) is a useful non-destructive tool to investigate the kinetic behavior of redox reaction, adsorption-desorption behavior of intermediates on the electrode surface, and the charge transfer and charge transport processes involved in the electrode/electrolyte interface in a electrochemical reaction (Shah et al., 2018). EIS is subjected to the application of AC (alternate current) voltage to the system and study of AC current response as a function of frequency. It is measured by using frequency response analyser (FRA). In EIS study, the response current I (ω,t) of a system is measured by applying a small signal, a sinusoidal voltage [V (ω,t)= Vosin ωt] with the amplitude of Vo and variable frequency f (f= ω/2π, where ω is the angular frequency). By using Ohm's law, the impedance Z(ω,t) of the system can be calculated as follows in Equation 1.22 (Sacco, 2018).

$$Z(\omega,t)= V(\omega,t)/I(\omega,t)= |Z(\omega)|e^{j\theta}= |Z(\omega)|(\cos\theta + j\sin\theta)= Z'(\omega) + jZ''(\omega) \quad (1.22)$$

Where |Z| is the impedance modulus, θ is the impedance phase, j is the imaginary unit, and Z'=|Z|cos θ and Z''= |Z|sinθ are the real and imaginary parts of the impedance, respectively. Z'' is represented as a function of Z' in a complex plane, referred as Nyquist plot.

Latiff et al. (2020) used EIS analysis to study the electrocatalytic activities of carbon based copper(II) phthalocyanine, for ECO_2RR. The results showed the trend of R_{CT} values as CNT-CuPc (20.2 Ω) < carbon black-CuPc (22.9 Ω) < activated carbon-CuPc (192.6 Ω) < graphene oxide-CuPc (250.2 Ω). It was similar to that observed in the CV and chronoamperometry results.

1.4.5 State-of-the-art literature on catalytic ECO_2RR

1.4.5.1 Metal catalysts for ECO_2RR

Noble metal catalysts are categorized mainly into three groups: (i) ability to form CO (Au, Ag, Zn, Pd, Ga), (ii) formic acid (HCOOH)/formate ($HCOO^-$) (Pb, Hg, Tl, In, Sn, Cd, Bi), and (iii) hydrocarbons (Cu) (Wang et al., 2017). As of now,

Sn, In, Hg, Cd, and Pb-based catalysts have demonstrated remarkable selectivity (>75%) for converting CO_2 to formate (B. Zhang et al., 2022). Besides these, a variety of nanostructured zero-dimensional, one-dimensional (nanowires, nanotubes), two-dimensional (nanosheets, nanoflakes), and three-dimensional (nanodendrites, nanoflowers) Bi catalysts have been designed for the reduction of CO_2 (B. Zhang et al., 2022).

Cu stands as a unique electrocatalyst towards ECO_2RR due to its ability to produce hydrocarbons, aldehydes, and alcohols at reasonable current densities (5-10 mA cm^{-2}) (Hori et al., 1986). Hori (2008) reported that Cu electrode with –5.0 mA cm^{-2} current density, could reduce CO_2 to CH_4, C_2H_4, EtOH, PrOH, CO, and $HCOO^-$ with FE (%) of 33.3, 25.5, 5.7, 3.0, 1.3, and 9.4%, respectively, at –1.05 V (vs. RHE) (Hori, 2008).

Kwon and Lee (2010) reported Pb granule electrodes for ECO_2RR to formate ($HCOO^-$) formation with 94% FE at –1.8 V vs. SCE. Porous Pb electrode showed 96.8% FE for $HCOO^-$ formation at –1.7 V vs. SCE (Wang et al., (2015). Kim et al. (2017) reported Bi nanoflakes for $HCOO^-$ formation with ~100 % FE at –0.6 V vs. RHE at ~1 mA cm^{-2}. (X. Zhang et al., 2018) synthesized Bi nanoparticles for $HCOO^-$ production with 94.7% FE at −0.83 V vs. RHE and overpotential of 0.63 V at a current density of ~5 mA cm^{-2}. Nanoporous AuNPs synthesized by electrodeposition exhibited ~99% FE of CO production at 6 mA cm^{-2} (Welch et al., (2019). Guo et al. (2020) reported coral-like porous Ag (CP-Ag) for CO production with 96.38% FE at –0.8 V vs. RHE and current density of 6.36 mA cm^{-2}.

Maimoto et al. (2018) reported Zn electrode for CO production with FE of 62% at –1.09 V vs. RHE and 3.5 mA cm^{-2} current density. Gao et al. (2015) obtained 91.2% FE at –0.89 V vs. RHE and ~6 mA cm^{-2} of current density using PdNPs for CO production. Table 1.6 summarizes some main group metal electrocatalysts towards ECO_2RR.

Table 1.6. Performance comparison of different main group metal electrocatalysts for ECO_2RR.

Catalyst	Synthesis method	Electrolyte	Potential applied (V)	Current density (J, mA cm^{-2})	FE (%)	Reference
Ag nanofoam	Chemical reduction	0.5 M $KHCO_3$	–1.2 V vs. RHE	–33 mA cm^{-2}	97% (CO)	Wei et al. (2020)
Ag nanosheet	Electrodeposition	0.5 M $NaHCO_3$	–0.7 V vs. RHE	–9 mA cm^{-2}	95% (CO)	Lee et al. (2017)
AuNPs	Polyvinyl alcohol method	0.5 M $KHCO_3$	–0.58 vs. RHE	–43.8 mA cm^{-2}	97% (CO)	Ma et al. (2019)
AuNPs	Chemical method	0.1 M $KHCO_3$	–0.8 vs. RHE	~ –11 mA cm^{-2}	100% (CO)	Souza and Lima (2021)
ZnNPs	Inverse micelle encapsulation	0.1 M $KHCO_3$	–1.1 V vs. RHE	–5 mA cm^{-2}	~70% (CO)	Jeon et al. (2018b)
Porous Zn	Electrodeposition	0.1 M $KHCO_3$	–0.95 vs. RHE	–270 mA cm^{-2}	95% (CO)	W. Luo et al. (2019b)
Hexagonal Zn	Electrodeposition	0.5 M KCl	–1.05 V vs. RHE	–7.3 mA cm^{-2}	95.4% (CO)	Won et al. (2016)
Ga single atom catalyst	Chemical method	0.5 M $KHCO_3$	–0.3 V vs. RHE	~ –5 mA cm^{-2}	~92% (CO)	Z. Zhang et al. (2022)
PdNPs	Chemical reduction	1.0 M $KHCO_3$	–0.7 V vs. RHE	–22.9 mA cm^{-2}	93.4% (CO)	Gao et al. (2017)
PdNPs	Chemical reduction	0.1 M $KHCO_3$	–0.89 V vs. RHE	–6 mA cm^{-2}	91.2% (CO)	Gao et al. (2015)
Pd nanosheets	One-pot chemical reduction	0.1 M $KHCO_3$	–0.5 V vs. RHE	–3.2 mA cm^{-2}	94% (CO)	W. Zhu et al. (2018)
Pb granule electrodes	Electrodeposition	0.2 M K_2CO_3	–1.8 V vs. SCE	NA	94% ($HCOO^-$)	Kwon and Lee (2010)
Porous Pb electrode	Electrodeposition	0.5 M $KHCO_3$	-1.7 V vs. SCE	NA	96.8% ($HCOO^-$)	Wang et al. (2015)
Sn electrode	Unipolar pulse electrodeposition (UPED) method	0.1 M $KHCO_3$	–1.7 V vs. Ag/AgCl	–6 mA cm^{-2}	89% (HCOOH)	An et al. (An et al., 2019)
Sn catalyst	Electrodeposition method	0.1 M $KHCO_3$	–1.4 V vs. SCE	–15 mA cm^{-2}	91% ($HCOO^-$)	Zhao and Wang (2016)
Bi nanoflake	Electrodeposition	0.1 M $KHCO_3$	–0.6 V vs. RHE	–1 mA cm^{-2}	~100% ($HCOO^-$)	Kim et al. (2017)

Bi nanotubes	Chemical method	0.5 M $KHCO_3$	–1.03 V vs. RHE	–24 mA cm^{-2}	97% ($HCOO^-$)	Fan et al. (2020)
Ultrathin Bi nanosheets	Electrochemical reduction method	0.5 M $KHCO_3$	–1.0V vs. RHE	–11 mA cm^{-2}	90% ($HCOO^-$)	Su et al. (2018)
3D hierar-chical porous In catalyst	Electrodeposition	0.1 M $KHCO_3$	–1.2 V vs. RHE	–2.5 mA cm^{-2}	90.4% ($HCOO^-$)	W. Luo et al. (2019a)
Dendritic In		0.5 M $KHCO_3$	–0.86 V vs. RHE	–5.8 mA cm^{-2}	86% ($HCOO^-$)	Xia et al. (2018)
In catalyst	Electrodeposition	0.5 M $KHCO_3$	–1.9 V vs. Ag/AgCl	–3.54 mA cm^{-2}	72.5% ($HCOO^-$)	Bohlen et al. (2020)
CuNPs	Chemical method	0.1 M $KHCO_3$	–0.8 V vs. RHE	~ –2.0 mA cm^{-2}	45.4% (HCOOH) 5.84% (EtOH) 1.0% (AcOH) 5.55% (n-propanol)	Dongare et al. (2021b)
Cu nanocrystals	Chemical method	0.1 M $KHCO_3$	–1.1 V vs. RHE	~ –9 mA cm^{-2}	1.0% (CH_3OH) 20% (HCOOH) 5.0% (EtOH) 1.1% (AcOH)	Loiudic et al. (2016)
Cu nanowire	Chemical method	0.1 M $KHCO_3$	–1.1 V vs. RHE	N.A.	7.6% (CO) 17.4% (C_2H_4) 2.4% (C_2H_6) 17.5% ($HCOO^-$) 3.8% (C_2H_5OH) 7.8% (n-propanol)	Ma et al. (2016a)
Cu nanocubes	Electrochemical method	0.25 M $KHCO_3$	–1.01 V vs. RHE	–40 mA cm^{-2}	60% (C_2H_4)	Jiang et al. (2018)

1.4.5.2 Metal-based and metal oxide catalysts for ECO_2RR

To improve the catalytic activity of metal catalysts towards ECO_2RR, several attempts have been made through modification of particle morphology, size, form of oxide, electrode supports (carbon, graphene), etc. (Jung et al., 2019). Such modifications also increase CO_2 adsorption on the metal surface and facilitate C—C coupling for enhanced catalytic performance towards CO_2 reduction (Jiwanti et al., 2021).

Albo and Irabien (2016) showed that Cu^+ can greatly change the selectivity and activity towards CH_3OH production by loading Cu_2O electrocatalyst on the gas diffusion electrode and achieved 42.3% FE for CH_3OH production. Daiyan et al. (2019b) reported that Cu^+/Cu^{2+}, generated on the Cu foam electrode improves the electrocatalytic activity of CuO/Cu_2O on 3D heterostructured Cu foam. FE of CH_3CH_2OH formation was found to be 31% at –0.3 V vs. RHE with a stable current density of –1.25 mA cm^{-2}.

Owing the merit of selective formation of $HCOO^-$/HCOOH in aqueous system, Sn-based catalysts are considered as the potentially most active and commercially viable towards ECO_2RR (Q. Zhang et al., 2018). S. Liu et al. (2019) reported SnO_2 quantum wires of sub-2 nm size, for $HCOO^-$ formation with 80% FE at –1.2 V vs. RHE and 18 mA cm^{-2} current density. Reduced SnO_2 porous nanowires were designed with a high density of grain boundaries (Kumar et al., 2017). HCOOH production was seen to start at a low overpotential of 350 mV and reaches stability at just 0.8 V (vs. RHE).

Bi-based catalysts, such as Bi_2O_3, $Bi_2O_2CO_3$, etc. are explored for ECO_2RR to $HCOO^-$/HCOOH (B. Zhang et al., 2022). However, these compounds eventually transform into metal-based Bi-catalysts, after the reaction. Tran-Phu et al. (2019) observed that β-Bi_2O_3 is transformed to metallic Bi during ECO_2RR. $Bi_2O_2CO_3$ nanosheets exhibited 83% FE of $HCOO^-$ formation at 0.59 V overpotential (Lv et al., 2017). Shi et al. (2022) reported sponge-like $Bi_2O_3$for $HCOO^-$ formation with 93.7% FE. Table 1.7 summarizes some main group metal-based and metal oxides electrocatalysts towards ECO_2RR.

Table 1.7. Performance comparison of different main group metal-based electrocatalysts for ECO_2RR.

Catalyst	Synthesis method	Electrolyte	Potential applied (V)	Current density (J, mA cm^{-2})	FE (%)	Reference
Ag_2O NPs	Electrochemical reduction	0.1 M $KHCO_3$	–0.8 V vs. RHE	–1.15 mA cm^{-2}	89% (CO)	Ma et al. (2016b)
Bi_2O_3 NPs	Hydrothermal method	0.5 M $NaHCO_3$	–1.2 V vs. RHE	–22 mA cm^{-2}	91% ($HCOO^-$)	Miao and Yuan (2018)
Hierarchical SnO_2	Solvothermal method	0.5 M $NaHCO_3$	–0.9 V vs. RHE	–17 mA cm^{-2}	83% ($HCOO^-$)	Han et al. (2019)
SnO_2 porous nanowires	solvo-plasma technique	0.1 M $NaHCO_3$	–0.8 V vs. RHE	–4.8 mA cm^{-2}	80% ($HCOO^-$)	Kumar et al. (2017)
BiO_x	Solvothermal method	1.0 M $KHCO_3$	–1.7 V vs. SCE	–37.8 mA cm^{-2}	89.3% ($HCOO^-$)	X. H. Zhao et al. (2021)
In_2O_3 In_2O_3@C	Coprecipitation and pyrolysis	0.5 M $KHCO_3$	–0.9 V vs. RHE	–2.7 mA cm^{-2} –12.9 mA cm^{-2}	79% ($HCOO^-$) 87.6% ($HCOO^-$)	Mou et al. (2018)
In_2O_3 NPs	Coprecipitation	0.5 M $KHCO_3$	–1.5 V vs. Ag/AgCl	~ –7 mA cm^{-2}	~92% ($HCOO^-$)	White and Bocarsly (2016)
Cu_2O NP/C	Wet-chemical method	0.1 M $KHCO_3$	–1.1 V vs. RHE	–21 mA cm^{-2}	57.3% (C_2H_4) 1.9% (CH_4) 74% (C_2+C_3)	Jung et al. (2019)
Cu/Cu_2O	Electrodeposition method	0.1 M $KHCO_3$	–0.75 V vs. RHE	~ –1.3 mA cm^{-2}	53.6% (CH_3OH) ~28.0% (CH_4) 10% (CO)	Chang et al. (2018)
Cu_2O			–1.39 V vs. Ag/AgCl		42.3% (CH_3OH) 10.1% (C_2H_6O)	

	Commercially available	0.5 M $KHCO_3$			2.4 (C_3H_8O)	Albo and Irabien
Cu_2O/ZnO			–1.16 V vs. Ag/AgCl	–10 mA cm^{-2}	27.5% (CH_3OH) 3.9% (C_2H_6O)	(2016)
Oxide- derived Cu foam	Electrodeposition method	0.5 M $NaHCO_3$	–0.8 V vs. RHE	–6 mA cm^{-2} (C_2H_4 + C_2H_6)	18% (CO) 5% ($HCOO^-$) 20% (C_2H_4) 35% (C_2H_6)	Dutta et al. (2016)
SnO_2 quantum wires	Modified hydrothermal method	0.1 M $KHCO_3$	–1.2 V vs. RHE	–18 mA cm^{-2}	80% ($HCOO^-$)	S. Liu et al. (2019)

* N.A.: Not available

The catalytic activity of Cu-, Sn- and Bi-based, and other electrocatalysts towards ECO_2RR to value-added products are graphically presented in Figures 1.18a1-1.18c2, and Figures 1.18d1-1.18d2, respectively. It is evident that the trend in FE follows as Cu- (41-91.6%) < Sn- (56-99%) < Bi-based catalysts (84-100%) towards the formation of value-added products. Among these three groups of catalysts, only Cu-based catalysts facilitate the formation of mixture of products, whereas the selectivity of $HCOOH/HCOO^-$ follows the trend of Sn-< Bi-based catalysts (Figures 1.18a2, 1.18b2, and 1.18c2).

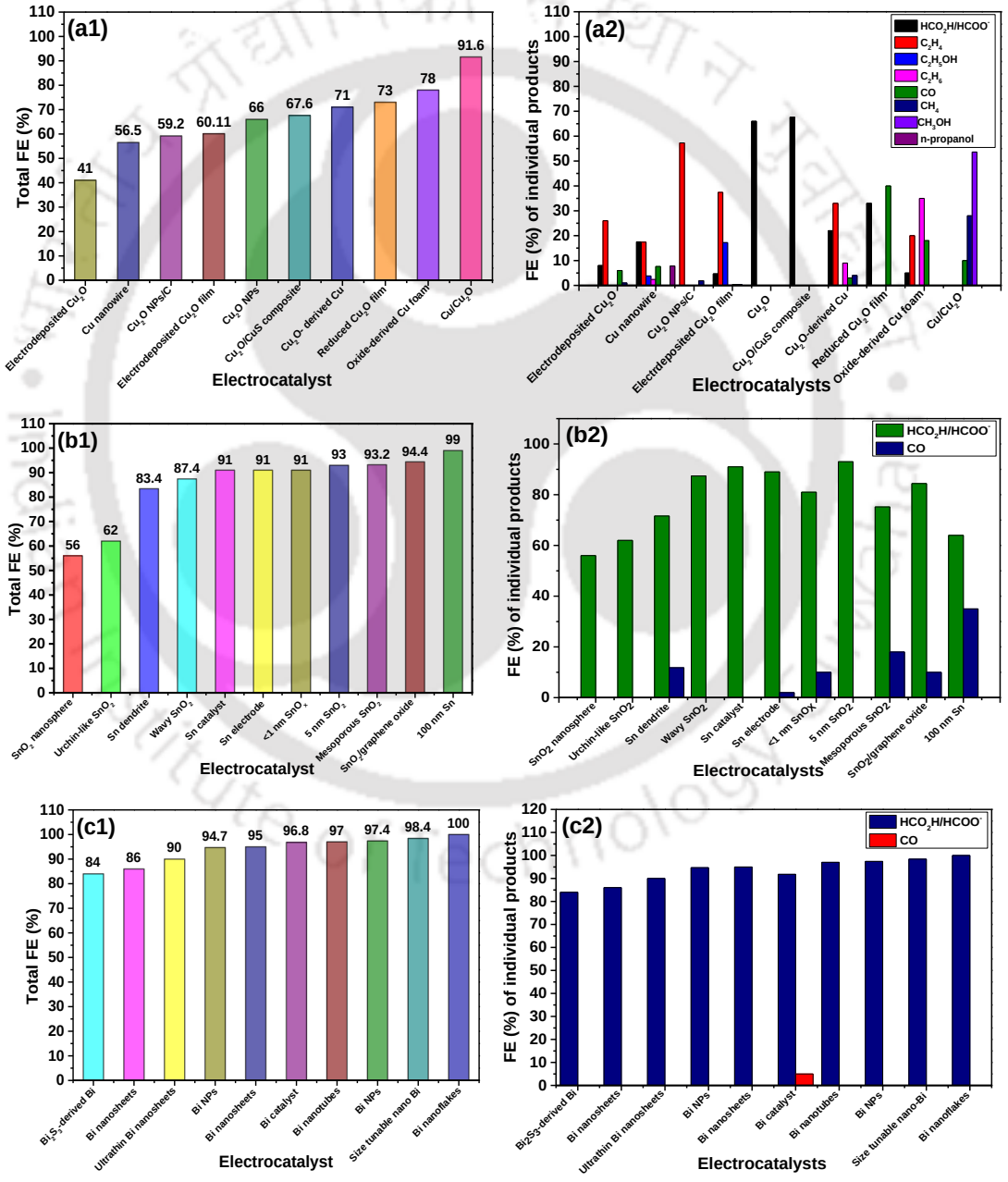

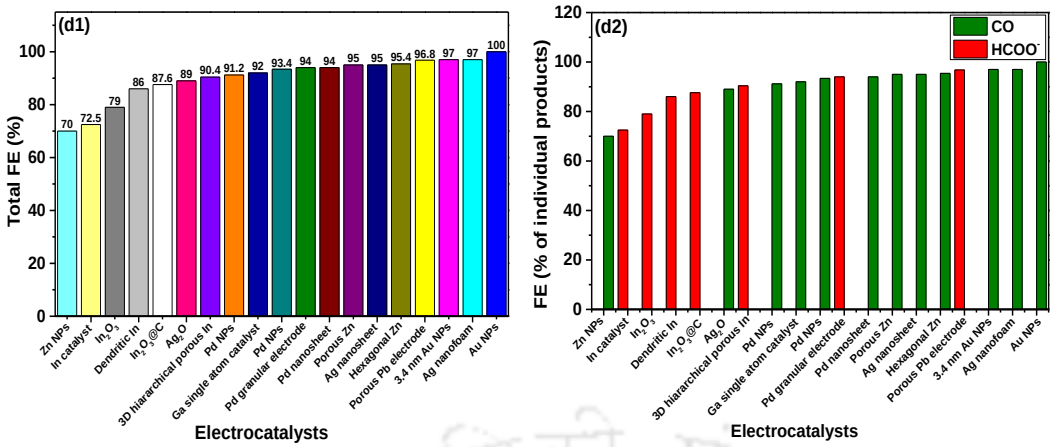

Figure 1.18. Total FE of value-added products formed and FE of individual products using (a1, a2) Cu-based electroctalysts: Electro-deposited Cu_2O (Kim et al., 2015), Cu nanowire (Ma et al., 2016a), Cu_2O NPs/C (Jung et al., 2019), Electro-deposited Cu_2O film (Ren et al., 2015), Cu_2O NPs (X. Zhu et al., 2018), Cu_2O/CuS composite (S. Wang et al., 2021), Cu_2O-derived Cu (Kas et al., 2014), Reduced Cu_2O film (Li and Kanan, 2012), Oxide-derived Cu foam (Dutta et al., 2016), Cu/Cu_2O (Chang et al., 2018); (b1, b2) Sn-based electroctalysts: SnO_2 nanosphere (Fu et al., 2016), Urchin-like SnO_2 (Liu et al., 2017), Sn dendrite (Won et al., 2015), Wavy SnO_2 (Z. Chen et al., 2020), Sn catalyst (Zhao and Wang, 2016), Sn electrode (An et al., 2019), <1 nm SnO_x (Kim et al., 2022), 5 nm SnO_2 (Li et al., 2017), Mesoporous SnO_2 (Daiyan et al., 2018), SnO_2/graphene oxide (Yang et al., 2021), 100 nm Sn (J. Wu et al., 2014); (c1, c2) Bi-based electroctalysts: Bi_2S_3-derived Bi (Y. Zhang et al., 2018), Bi nanosheets (W. Zhang et al., 2018), Ultrathin Bi nanosheets (Su et al., 2018), Bi NPs (X. Zhang et al., 2018), Bi nanosheets (N. Han et al., 2018), Bi catalyst (Li et al., 2021), Bi nanotubes (Fan et al., 2020), Bi NPs (Wei et al., 2022), Size tunable nano-Bi (Qiu et al., 2017), Bi nanoflakes (Kim et al., 2017); (d1, d2) Other electrocatalysts: Zn NPs (Jeon et al., 2018b), In catalyst (Bohlen et al., 2020), In_2O_3 (Mou et al., 2018), Dendritic In (Xia et al., 2018), In_2O_3@C (Mou et al., 2018), Ag_2O (Ma et al., 2016b), 3D hierarchical porous In (W. Luo et al., 2019a), Pd NPs (Gao et al., 2015), Ga single atom catalyst (Z. Zhang et al., 2022), Pd NPs (Gao et al., 2017), Pd granular electrode (Kwon and Lee, 2010), Pd nanosheet (W. Zhu et al., 2018), porous Zn (W. Luo et al., 2019b), Ag nanosheet (Lee et al., 2017), hexagonal Zn (Won et al., 2016), porous Pb electrode (Wang et al., 2015), 3.4 nm AuNPs (Ma et al., 2019), Ag nanofoam (Wei et al., 2020), AuNPs (Souza and Lima, 2021).

Along with ECO_2RR to value-added chemicals and fuels, electrochemical N_2 reduction reaction (ENRR) forming NH_3 is also imperative to meet the current global energy demand. The next section focuses on catalytic ENRR for the production of NH_3.

1.5 Energy harness from ammonia: An alternate to carbon-based fuels

Liquid ammonia (NH_3) has a hydrogen capacity of 17.6% (w/w) and energy density of 4.3 kWh h^{-1}. Its reaction in fuel cells ends with N_2 and H_2O, which are considerably inert products (Qin et al., 2021). It is estimated that the levelized cost of energy (LCOE) for NH_3 in an integrated energy storage system is 251 \$ MW^{-1} h^{-1}, which is competitive with other suggested large-scale storage methods (Elishav et al., 2017). For these reasons, NH_3 could be considered in non-carbon-based energy economy (He et al., 2019). Although, at present industrial NH_3 synthesis relies on Haber–Bosch technique, which need harsh operating conditions (400-600℃ temperature, and 150-350 atm pressure) with a mammoth amount of CO_2 generation (~300 tons / 200 million tons of NH_3 production per year) (He et al., 2019).

Electrochemical N_2 reduction reaction (ENRR) requires suitable catalyst for N_2 adsorption/desorption, cleavage of N≡N bonds of high bond energy (945 kJ mol^{-1} at 298 K) and hydrogenation reaction (Wen et al., 2021). The ENRR under ambient conditions is depicted by the following reactions (Equations 1.23 and 1.24).

at the anode: $3H_2O \rightarrow 3/2O_2 + 6e^- + 6H^+$ (1.23)

at the cathode: $6e^- + 6H^+ + N_2 \rightarrow 2NH_3$ (1.24)

In fact, NH_3 produced in ENRR can be utilized in direct ammonia fuel cell (DAFC) (Figure 1.19) to generate power according to the reactions as follows (Equations 1.25-1.27) (Afif et al., 2016; Trenerry et al., 2021).

at the cathode: $O_2 + 2H_2O + 4e^- \rightarrow 2HO^-$ (1.25)

at the anode: $2NH_3 + 6HO^- \rightarrow N_2 + 2H_2O + 6e^-$ (1.26)

Overall reaction: $4NH_3 + 3O_2 \rightarrow 2N_2 + 6H_2O$ (1.27)

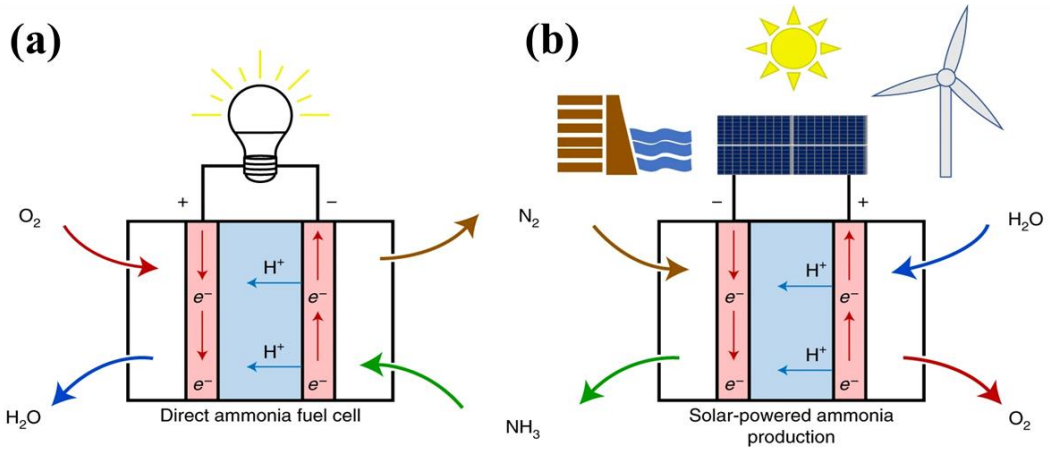

Figure 1.19. Essential components of nitrogen/ammonia economy. a) DAFC and b) Electrochemical ammonia synthesis from air and water. Reprinted with permission from Trenerry et al. (2021). Copyright 2021 Springer Nature.

1.5.1 Measurement standards of catalytic ENRR

The key indicators for the performance evaluation of catalytic ENRR are outlined in the subsequent sub-sections.

1.5.1.1 NH_3 yield

The yield of NH_3 is a measure of the rate of ammonia production over the normalized catalyst loading and time (t) of electrolysis. The rate of ammonia production (r) is calculated using the following Equation 1.28 (X. Zhao et al., 2021).

$$r_{NH_3} = \frac{n \times V}{\Delta \times t} \quad (1.28)$$

Here, n is the concentration of NH_3 in the electrolyte of volume V, Δ is total catalyst loading (cm^2 or $mg_{cat.}$), and t is the electrolysis time. Ag triangular nanoplates exhibited NH_3 yield of 58.5 mg $g_{cat.}^{-1}$ h^{-1} at –0.25 V vs. RHE (Gao et al., 2019). Ag nanosheet showed 4.62×10^{-11} mo1 s^{-1} cm^{-2} at –0.6 V vs. RHE (Huang et al., 2018). Au nanorods catalyzed NH_3 yield of 1.648 µg h^{-1} cm^{-2} at -0.25 V vs. RHE (Bao et al., 2017).

1.5.1.2 Faradaic efficiency (FE)

The process of nitrogen reduction to NH_3 involves six-electron transfer. Therefore, FE can be calculated as follows (Equation 1.29) (X. Zhao et al., 2021).

$$FE_{NH_3}(\%) = \frac{3 \times F \times c \times V}{M_{NH_3} \times Q} \quad (1.29)$$

Where, F is faradaic constant, c and M denote the concentration and molar mass of ammonia, V is the electrolyte volume, and Q is the total charge for the electrochemical reaction.

The yield of NH_3 and FE sometimes have the leverage effect, which is apparent from the low FE with high NH_3 yield or vice-versa (X. Zhao et al., 2021). Therefore, FE could be an important figure of merit for effective ENRR process.

Han et al. (2018) reported the highest FE of 1.9% at −0.3 V vs. RHE, while the maximum NH_3 yield obtained is 29.43 μg h^{-1} $mg_{cat.}^{-1}$ (4.80×10^{-10} mol s^{-1} cm^{-2}) at −0.50 V vs. RHE, using MoO_3 catalysts (J. Han et al., 2018). W. Liu et al. (2019) reported 2D amorphous MoO_{3-x} monolayers for ENRR with FE and NH_3 yield 12% at −0.20 V and 35.83 μg h^{-1} $mg_{cat.}^{-1}$ at −0.40 V vs. RHE, respectively.

1.5.2 Factors affecting ENRR

1.5.2.1 Electrolyte and pH

The effect of electrolyte and pH on ENRR is considered in terms of cations and anions concentration. The proton in acidic electrolyte facilitates NH_3 yield but reduces FE because high proton concentration induces simultaneous ENRR and HER. In alkaline media, the hydroxyl anion improves FE by hindering the HER process. In a neutral electrolyte, the lower proton concentration facilitates the yield by suppressing HER (F. Wang et al., 2021).

FeS@MoS_2/CFC electrode exhibited the highest NH_3 yield rate (8.75 μg h^{-1} cm^{-2}) in 0.1 M HCl than that in 0.1 M Na_2SO_4 (8.45 μg h^{-1} cm^{-2}) and 0.1 M KOH (3.28 μg h^{-1} cm^{-2}) with FE of 0.22, 2.96, and 0.067%, respectively (Guo et al., (2019). The trend in FE is not in line with the reaction mechanism derived by Wang et al. (2021).

1.5.3 State-of-the-art literature on catalytic ENRR forming NH_3

In the past few years, several noble metals (e.g., Au, Ag, Ru, Rh, Pt, Pd) are tested as electrocatalysts for ENRR (Wen et al., 2021). Due to the characteristics of the occupied and empty d orbitals of noble metals, the electrons of N_2 can be accepted

synergistically with the proper energy and symmetry. Through sp hybridization, N atoms in N_2 molecules can provide lone-pair electrons to vacant d orbitals in the transition noble metals. While, the occupied d orbitals of metals can transfer electrons backwards to the π-molecular orbitals of N_2, weakening the N≡N bond and strengthening the metal-nitrogen bond (Q. Chen et al., 2020).

Wang et al. (2018) reported flower-like Au nanoparticles for ENRR with NH_3 yield of 25.57 μg h^{-1} $mg_{cat.}^{-1}$) and 6.05% FE at −0.2 V vs. RHE, in 0.1 M HCl. Ag nanosheets exhibited 4.8% FE with NH_3 production rate of 4.62×10^{-11} mol s^{-1} cm^{-2} at −0.60 V vs. RHE, at 0.1 M HCl (Huang et al., 2018). Ultrathin Rh nanosheets nanoassemblies yielded 23.88 μg h^{-1} $mg_{cat.}^{-1}$ NH_3 with 0.217% FE at −0.2 V vs. RHE, in 0.1 M KOH electrolyte (Liu et al., 2018).

Deng et al. (2019) reported Pd nanoparticles, exhibited 9.49% FE and 24.12 μg h^{-1} $mg_{cat.}^{-1}$ NH_3 yield. Bi-metallic PdRu tripods catalyzed NH_3 production with 1.85% FE and 37.23 μg $mg_{cat.}^{-1}$ h^{-1} yield at −0.2 V vs. RHE (H. Wang et al., 2019a). Chu et al. (2019) reported NiO/G catalyst for ENRR with 7.8% FE of NH_3 production with a yield of 18.6 μg h^{-1} $mg_{cat.}^{-1}$.

Besides the noble metals, non-noble metals (e.g., Fe, Mo, Co, Ni, Ti), and non-metals (e.g., B, C) have also been tested for ENRR. Zhan et al. (2019) synthesized 2D B-nanosheets for ENRR. FE of NH_3 formation was found to be 4.04% with a yield of 13.22 μg h^{-1} mg_{cat}^{-1} at −0.80 V vs. RHE. On the other hand, 2D Multi-layer B nanosheet showed 4.84% FE and 3.12 μg h^{-1} mg^{-1} NH_3 yield at −0.14 V vs. RHE (Fan et al., 2019). Fe/Fe_3O_4 catalyst exhibited 8.29% FE of NH_3 production at −0.3 V vs. RHE (Hu et al., (2018)). Y. Liu et al. (2019) tested Co single atom embedded N-doped porous carbon for ENRR. NH_3 production rate was found to be 0.86 μmol cm^{-2} h^{-1} with 10.5% FE at −0.2 V vs. RHE.

Table 1.8 summarizes some of the metal and metal-based catalysts for ENRR at ambient conditions.

Table 1.8. Performance comparison of different main group metal-based electrocatalysts for ENRR from the literature.

Catalyst	Synthesis method	Electrolyte	Potential (V) (vs. RHE)	NH_3 yield	FE (%)	Reference
Ag triangular nanoplates	Chemical reduction method	0.5 M K_2SO_4	–0.25	58.5 mg g_{cat}^{-1} h^{-1}	25	Liu et al. (2018)
Ag nanosheet	Chemical method	0.1 M HCl	–0.6	4.62×10^{-11} mo1 s^{-1} cm^{-2}	4.8	Huang et al. (2018)
Au nanorods	Seeded growth method	0.1 M KOH	–0.2	1.648 μg h^{-1} cm^{-2}	4.02	Bao et al. (2017)
8 nm monodisperse Au	Chemical method	0.1 M KOH	–0.14	17.49 μg h^{-1} mg_{cat}^{-1}	5.79	C. Chen et al. (2020)
PdNPs	Chemical method	0.1 M Na_2SO_4	–0.45	24.12 μg h^{-1} $mg_{cat.}^{-1}$	9.49	Deng et al. (2019)
Rh nanosheet	Surfactant free chemical method	0.1 M KOH	–0.2	23.88 μg h^{-1} mg_{cat}^{-1}	0.217	Liu et al. (2018)
3D Rh particles	Solvothermal	0.1 M KOH	–0.2	35.58 μg h^{-1} mg_{cat}^{-1}	0.52	T. Chen et al. (2020)
Cu foam	Chemical method	0.1 M HCl	----	2.45×10^{-10} mol s^{-1} cm^{-1} (-0.40 V)	18.0 (–0.35 V)	Ji et al. (2020)
Cu dendrite	Chemical method	0.1 M HCl	–0.4	25.63 μg h^{-1} $mg_{cat.}^{-1}$	15.12	Li et al. (2019)
Sn dendrite	Electrodeposition	Phosphate buffer	–0.6	5.66×10^{11} mol s^{-1} cm^{-2}	3.67	Lv et al. (2020)
Sub-micron SnO_2	Hydrothermal	0.1 M Na_2SO_4	–0.7	4.03 μg h^{-1} mg_{cat}^{-1}	2.17	L. Zhang et al. (2018)
MoO_3	Hydrothermal	0.1 M HCl	–0.3	29.43 μg h^{-1} m g_{cat}^{-1}	1.9	J. Han et al. (2018)

Mn_3O_4	Hydrothermal	0.1 M Na_2SO_4	–0.8	11.6 μg h^{-1} mg_{cat}^{-1}	3.0	Wu et al. (2018)
NiO nanosheet	Hydrothermal, plasma	0.1 M Na_2SO_4	–0.5	29.1 μg h^{-1} mg_{cat}^{-1}	10.8	Y. Li et al. (2020)
Co_3O_4@NC	Chemical method	0.05 M H_2SO_4	–0.2	42.58 μg h^{-1} mg_{cat}^{-1}	8.49	S. Luo et al. (2019)
CuO/RGO	Chemical method	0.1 M Na_2SO_4	–0.75	1.8×10^{-10} mol s^{-1} cm^{-2}	3.9	F. Wang et al. (2019)
PdRu nanorods	Chemical method	0.1 M HCl	–0.2	34.2 μg h^{-1} mg_{cat}^{-1}	2.4	H. Wang et al. (2019b)
Pd/TiO_2	Hydrothermal	0.1 M NaOH	–0.1	1847.3 μg h^{-1} mg_{cat}^{-1}	2.63	Lv et al. (2019)
Fe_2O_3 nanorods	Hydrothermal	0.1 M Na_2SO_4	–0.8	15.9 μg h^{-1} mg_{cat}^{-1}	0.94	Xiang et al. (2018)

Figure 1.20 shows the performance graph in terms of FE of NH_3 production on different metal-based electrocatalysts. From the graph, it is clearly evident that Ag triangle NPs showed the maximum FE of 25% compared to Rh nanosheets with 0.22% FE. The literatures on metal-based electrocatalysts employed for both ECO_2RR and ENRR are summarized in Table 1.9.

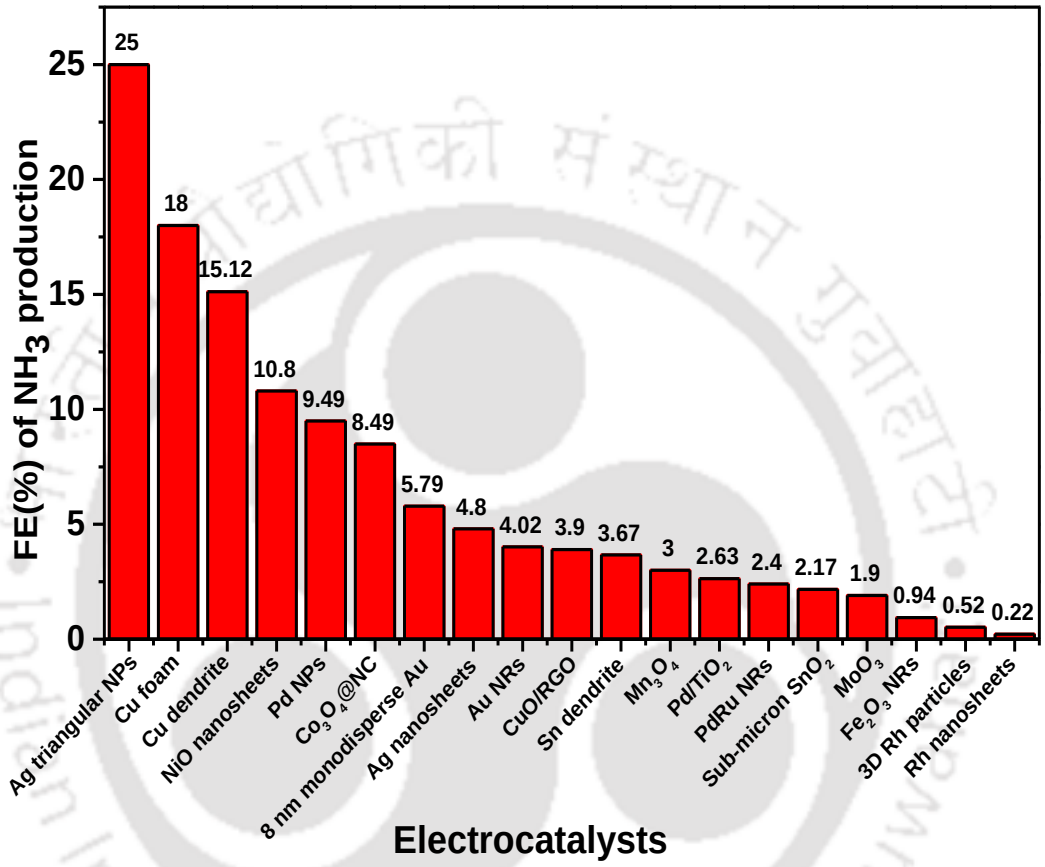

Figure 1.20. FE of NH_3 production on different metal-based electrocatalysts.

Table 1.9. A few selected metal-based electrocatalysts tested for both ECO_2RR and ENRR.

Catalyst group	**Catalyst type**	**Electrolyte**	**Potential (V) (**vs. RHE**)**	**FE (%) @ ECO_2RR**	**FE (%) @ NH_3**	**Reference**
Ag-based	Ag nanofoam	0.5 M $KHCO_3$	–1.2	97 (CO)	N.A.*	Wei et al. (2020)
	Ag nanosheet	0.5 M $NaHCO_3$	–0.7	95 (CO)	N.A.	Lee et al. (2017)
	Ag_2O NPs	0.1 M $KHCO_3$	–0.8	89 (CO)	N.A.	Ma et al. (2016b)
	Ag triangular nanoplates	0.5 M K_2SO_4	–0.25	N.A.	25	Gao et al. (2019)
	Ag nanosheet	0.1 M HCl	–0.6	N.A.	4.8	Huang et al. (2018)
Au-based	3.4 nm Au NPs	0.5 M $KHCO_3$	–0.58	97 (CO)	N.A.	Ma et al. (2019)
	Au NPs	0.1 M $KHCO_3$	–0.8	100 (CO)	N.A.	Souza and Lima (2021)
	Au nanorods	0.1 M KOH	–0.2	N.A.	4.02	Bao et al. (2017)
	8 nm monodisperse Au	0.1 M KOH	–0.14	N.A.	5.79	C. Chen et al. (2020)
Pd-based	Pd nanoparticles	1.0 M $KHCO_3$	–0.7	93.4 (CO)	N.A.	Gao et al. (2017)
	Pd nanosheets	0.1 M $KHCO_3$	–0.5	94 (CO)	N.A.	W. Zhu et al. (2018)
	Pd nanoparticles	0.1 M Na_2SO_4	–0.45	N.A.	9.49	Deng et al. (2019)
Sn-based	Sn electrode	0.1 M $KHCO_3$	–1.47	89 (HCOOH)	N.A.	An et al. (2019)
	SnO_2 quantum wires	0.1 M $KHCO_3$	–1.2	80 ($HCOO^-$)	N.A.	S. Liu et al. (2019)
	Sn dendrites	Phosphate buffer	–0.60	N.A.	3.67	Lv et al. (2020)
	Sub-micron SnO_2	0.1 M Na_2SO_4	–0.7	N.A.	2.17	L. Zhang et al. (2018)
Cu-based	Cu nanowires	0.1 M $KHCO_3$	–1.1	7.6 (CO) 17.4 (C_2H_4)	N.A.	Ma et al. (2016a)
	Cu nanocubes	0.25 M $KHCO_3$	–1.01	60 (C_2H_4)	N.A.	Jiang et al. (2018)
	Cu foam	0.1 M HCl	–0.35	N.A.	18.0	Ji et al. (2020)
	Cu dendrite	0.1 M HCl	–0.4	N.A.	15.12	Li et al. (2019)

* N.A.: Not Applicable

1.6 Knowledge gap and objectives of the proposed work

The studies on the horizon of facile bioinspired green routes are not focused both at international and national levels apart from the recent works mostly from our research group (Chelli and Golder, 2016; Dash et al., 2018; El-Shobaky and Turky, 2000). Das and Golder (2017) reported spinel Co_3O_4 NPs synthesis using *Sechium edule* fruit extract for electrochemical H_2O_2 sensing with a limit of detection (LoD) of 0.0217 μM and sensitivity 65.32 nA μM^{-1} cm^{-2}. Dash et al. (2018) reported a one-pot microwave-assisted formation of AgNPs using *Psidium guajava* for electrocatalytic sensing of ascorbic acid. The limit of detection and sensitivities of AgNPs (pH 9.5)/GPE are found to be 14.63 μM, 0.719 (diffusion control) and 0.390 (activation control) μA cm^{-2} μM^{-1}.

As discussed earlier in this thesis (section 1.3.2), the waste generated in the conventional method of synthesizing nanoparticles has an E-factor (waste to product ratio) as high as in the range of 100 to 100,000. Further, the use of (toxic/strong) reducing agents (hydrazine, sodium borohydride, etc.) and organic solvents (toluene, xylene, etc.) in nanoparticles synthesis land up with the generation of a considerable amount of liquid wastes. For example, the synthesis of AuNPs using the chemical reduction method, stabilized by thiols and ionic liquids suffers a setback with an E-factor value of 99,400 (García-Quintero and Palencia, 2021). On the other hand, nanoparticles synthesized using bacteria and fungi could be costly due to the additional separation and purification steps along with associated potential safety issues. With the above considerations in mind, this thesis focuses on the development of environmentally benign processes for the synthesis of metal oxides and metal sulphide nanoparticles.

This technique would use the organs of plants, weeds, and leftovers of edible plants rich in (bio)analytes such as glycosides, polyphenolic compounds, and ascorbic acid. It is envisaged that such analytes can be extracted out and applied for the synthesis of catalysts for ECO_2RR to value-added chemicals along with the production of NH_3 which is going to open a new domain of research for the development of electrocatalysts in bioinspired and bio-based routes. *Sechium edule* (commonly known as Chayote), a vegetable fruit belongs to the family Cucurbitaceae. The fruit contains abundant flavonoids (193.0 mg g^{-1} (dry basis)), carbohydrate (35-

84 mg g^{-1} (dry basis)), ascorbic acid (AA), 0.294 mg g^{-1} (dry basis), gallic acid, caffeic acid, isoquercetin, etc. (Das, 2018; Rao and Golder, 2016). Therefore, with the above knowledge gap and selected vegetal source, the following objectives are considered in the doctoral work.

i. To synthesize Cu_2O NPs using *Sechium edule* fruit extract and to fabricate Cu_2O NPs/carbon electrode for electrocatalytic CO_2 reduction to formate (**Chapter 3**)
ii. To develop a tunable bioinspired process of SnO_2 NPs synthesis for electrocatalytic CO_2 into formate conversion (**Chapter 4**)
iii. To develop a template-free bioinspired route for 1D Bi_2S_3 nanorods synthesis for the enhancement of electrocatalytic CO_2 reduction to formate (**Chapter 5**)
iv. To synthesize shape-controlled 2D Co_3O_4 spinel nanodiscs using gallic acid for electrocatalytic N_2 reduction to NH_3 (**Chapter 6**)

1.7 Organization of the thesis

The thesis is divided into seven chapters. These are outlined as follows:

CHAPTER 1: Introduction and background of the work

This chapter presents a general introduction about the adverse effects of CO_2 in the environment, different technologies for CO_2 sequestration, different conventional methods for catalysts synthesis, and their advantages and disadvantages are also described. The fundamentals of electrochemical CO_2 reduction reaction (ECO_2RR) and literature review on metal and metal-based nanoparticles for the ECO_2RR are discussed. Ammonia (NH_3) as a prospect of non-carbon-based fuel, is also discussed with literature review. At the end of the chapter, knowledge gap and the research objectives are composed.

CHAPTER 2: Materials and methodology

This chapter discusses the experimental methods, the reagents used, and the equipment utilized to characterize and analyze the bio-analytes, catalysts, electrochemical systems. This chapter also describes the details of the general theory and instructions of all the electrochemical experiments involved this study. The important experimental steps and methodologies involved: (i) Preparation of bio-extract, (ii) Bioinspired synthesis of Cu_2O nanoparticles, (iii) Bioinspired synthesis of SnO_2 nanoparticles, (iv) Bioinspired synthesis of Bi_2S_3 nanorods, and (v) Synthesis of Co_3O_4 nanodiscs in a green route.

CHAPTER 3: Synthesis of Cu_2O NPs using bioanalytes present in *Sechium edule*: Mechanistic insights and application in electrocatalytic CO_2 reduction to formate

This chapter focuses on the synthesis of metal-organic capped Cu_2O NPs, labeled as Cu_2O(bio) NPs using the bioactive compounds present in *Sechium edule* fruit. The elucidated mechanism of formatlon of Cu_2O(bio) NPs and metal-organic intermediates leading to capping of NPs are also discussed. Moreover, the utilization of Cu_2O(bio) NPs decorated carbon paper towards electrochemical CO_2 reduction to formate, are also discussed.

CHAPTER 4: A tunable bioinspired process of SnO_2 NPs synthesis for electrocatalytic CO_2 into formate conversion

The work in this chapter discusses the development of a tunable bioinspired process of SnO_2 NPs synthesis, labeled as SnO_2(bio) NPs using the bio-analytes present in the *S. edule* fruit. The discussion covers the mechanistic insights of the formation of SnO_2 NPs, and utiliztion of the as-synthesized SnO_2(bio) NPs and its calcined counterpart, namely SnO_2(bio)- 800 (800°C) NPs towards electrochemical CO_2 reduction to formate formation.

CHAPTER 5: A simple template-free bioinspired route of 1D Bi_2S_3 nanorods synthesis for electrocatalytic CO_2 reduction to formate

In this chapter, a template-free process of synthesizing 1D Bi_2S_3 nanorods, (Bi_2S_3-NRs(bio) is developed in a simple bioinspired route using *Sechium edule* fruit extract. The role of bio-active compounds forming Bi_2S_3-NRs(bio) with controlled morphology and size and their functionality for the capping of nanorods are also investigated. Subsequently, the Bi_2S_3-NRs(bio) modified carbon paper electrode was fabricated by simple drop-casting, and were assessed in a semi-batch reactor to determine its effectiveness and selectivity towards ECO_2RR.

CHAPTER 6: Environmentally benign synthesis of shape-controlled 2D Co_3O_4 spinel nanodiscs using gallic acid for formation of NH_3 by electrocatalytic N_2 reduction

The bioinspired Cu_2O, SnO_2, and Bi_2S_3 had been successful for CO_2 conversion to formate. This chapter further investigates for the development of environmentally benign route using gallic acid for the synthesis of Co_3O_4 nanodiscs

(Co_3O_4-NDs). After that the Co_3O_4-NDs were modified using carbon paper electrode in electrocatalyzing N_2 reduction reaction (ENRR) for NH_3 formation.

CHAPTER 7: Conclusions and scopes for future studies

In this chapter, the salient outcomes of the overall work are documented. The recommendation and future perspective of the work, based on the knowledge of the present study are also included.

Table 1.10 shows the timeline of the work conducted during the course of the thesis work.

Table 1.10. Timeline of the work conducted during the course of the thesis work.

Work components	Timeline (months)										
	Jul-Dec 2017	Jan-Jun 2018	Jul-Dec 2018	Jan-Jun 2019	Jul-Dec 2019	Jan-Jun 2020	Jul-Dec 2020	Jan-Jun 2021	Jul-Dec 2021	Jan-Jun 2022	Jun 2022-April 2023
Literature review											
Selection of (bio-) analytes and synthesis of Cu_2O NPs											
Electrodes fabrication for electrochemical studies											
Synthesis of Cu_2O NPs and electrochemical CO_2 reduction											
Synthesis of SnO_2 NPs and electrochemical CO_2 reduction											
Synthesis of Bi_2S_3 NRs and electrochemical CO_2 reduction											
Synthesis of Co_3O_4 NDs and electrochemical N_2 reduction											
Documentation											

References

Afif, A., Radenahmad, N., Cheok, Q., Shams, S., Kim, J.H., Azad, A.K., 2016. Ammonia-fed fuel cells: A comprehensive review. Renew. Sustain. Energy Rev. 60, 822–835. https://doi.org/10.1016/j.rser.2016.01.120

Ahn, S.T., Abu-Baker, I., Palmore, G.T.R., 2017. Electroreduction of CO_2 on polycrystalline copper: Effect of temperature on product selectivity. Catal. Today 288, 24–29. https://doi.org/10.1016/j.cattod.2016.09.028

Alabdallah, N.M., Hasan, M.M., 2021. Plant-based green synthesis of silver nanoparticles and its effective role in abiotic stress tolerance in crop plants. Saudi J. Biol. Sci. 28, 5631–5639. https://doi.org/10.1016/j.sjbs.2021.05.081

Albo, J., Irabien, A., 2016. Cu_2O-loaded gas diffusion electrodes for the continuous electrochemical reduction of CO_2 to methanol. J. Catal. 343, 232–239. https://doi.org/10.1016/j.jcat.2015.11.014

Alfryyan, N., Kordy, M.G.M., Abdel-Gabbar, M., Soliman, H.A., Shaban, M., 2022. Characterization of the biosynthesized intracellular and extracellular plasmonic silver nanoparticles using *Bacillus cereus* and their catalytic reduction of methylene blue. Sci. Rep. 12, 12495. https://doi.org/10.1038/s41598-022-16029-1

Ali, K.A., Ahmad, M.I., Yusup, Y., 2020. Issues, impacts, and mitigations of carbon dioxide emissions in the building sector. Sustainability 12. https://doi.org/10.3390/SU12187427

An, L., Liu, C., Liu, Y., 2018. Optimization of operating parameters in polysilicon chemical vapor deposition reactor with response surface methodology. J. Cryst. Growth 489, 11–19. https://doi.org/10.1016/j.jcrysgro.2018.02.030

An, X., Li, S., Yoshida, A., Wang, Z., Hao, X., Abudula, A., Guan, G., 2019. Electrodeposition of tin-based electrocatalysts with different surface tin species distributions for electrochemical reduction of CO_2 to HCOOH. ACS Sustain. Chem. Eng. 7, 9360–9368. https://doi.org/10.1021/acssuschemeng.9b00515

Bandeira, M., Giovanela, M., Roesch-Ely, M., Devine, D.M., da Silva Crespo, J., 2020. Green synthesis of zinc oxide nanoparticles: A review of the synthesis methodology and mechanism of formation. Sustain. Chem. Pharm. 15, 100223. https://doi.org/10.1016/j.scp.2020.100223

Bao, D., Zhang, Q., Meng, F.L., Zhong, H.X., Shi, M.M., Zhang, Y., Yan, J.M., Jiang, Q., Zhang, X.B., 2017. Electrochemical reduction of N_2 under ambient conditions for artificial N_2 fixation and renewable energy storage using N_2/NH_3 cycle. Adv. Mater. 29, 1–5. https://doi.org/10.1002/adma.201604799

Bei, J., Zhang, R., Chen, Z., Lv, W., Wang, W., 2017. Efficient reduction of CO_2 to formate using in situ prepared nano-sized Bi electrocatalyst. Int. J. Electrochem. Sci. 12, 2365–2375. https://doi.org/10.20964/2017.03.72

Bérdy, J., 2005. Bioactive Microbial Metabolites. J. Antibiot. (Tokyo). 58, 1–26. https://doi.org/10.1038/ja.2005.1

Beveridge, T.J., Murray, R.G.E., 1980. Sites of metal deposition in the cell wall of *Bacillus subtilis*. J. Bacteriol. 141, 876–887. https://doi.org/10.1128/jb.141.2.876-887.1980

Bhola, V., Swalaha, F., Ranjith Kumar, R., Singh, M., Bux, F., 2014. Overview of the potential of microalgae for CO_2 sequestration. Int. J. Environ. Sci. Technol. 11, 2103–2118. https://doi.org/10.1007/s13762-013-0487-6

Blunt, M., Fayers, F.J., Orr Jr., F.M., 1993. Carbon dioxide in enhanced oil recovery. Energy Convers. Manag. 34, 1197–1204. https://doi.org/10.1016/0196-8904(93)90069-M

Bohlen, B., Wastl, D., Radomski, J., Sieber, V., Vieira, L., 2020. Electrochemical CO_2 reduction to formate on indium catalysts prepared by electrodeposition in deep eutectic solvents. Electrochem. commun. 110, 106597. https://doi.org/10.1016/j.elecom.2019.106597

Bokov, D., Turki Jalil, A., Chupradit, S., Suksatan, W., Javed Ansari, M., Shewael, I.H., Valiev, G.H., Kianfar, E., 2021. Nanomaterial by sol-gel method: synthesis and application. Adv. Mater. Sci. Eng. 2021. https://doi.org/10.1155/2021/5102014

Bondor, P.L., 1992. Applications of carbon dioxide in enhanced oil recovery. Energy Convers. Manag. 33, 579–586. https://doi.org/10.1016/0196-8904(92)90059-6

Brennan, L., Owende, P., 2010. Biofuels from microalgae—a review of technologies for production, processing, and extractions of biofuels and co-products. Renew. Sustain. Energy Rev. 14, 557–577. https://doi.org/10.1016/j.rser.2009.10.009

Burkart, M.D., Hazari, N., Tway, C.L., Zeitler, E.L., 2019. Opportunities and challenges for catalysis in carbon dioxide utilization. ACS Catal. 9, 7937–7956.

https://doi.org/10.1021/acscatal.9b02113

Chang, X., Wang, T., Zhao, Z., Yang, P., Greeley, J., Mu, R., Zhang, G., Gong, Z., Luo, Z., Chen, J., Cui, Y., Ozin, G.A., Gong, J., 2018. Tuning Cu/Cu_2O interfaces for the reduction of carbon dioxide to methanol in aqueous solutions. Angew. Chemie Int. Ed. 57, 15415–15419. https://doi.org/10.1002/anie.201805256

Chatterjee, S., Mahanty, S., Das, P., Chaudhuri, P., Das, S., 2020. Biofabrication of iron oxide nanoparticles using manglicolous fungus *Aspergillus niger* BSC-1 and removal of Cr(VI) from aqueous solution. Chem. Eng. J. 385, 123790. https://doi.org/10.1016/j.cej.2019.123790

Cheah, W.Y., Ling, T.C., Juan, J.C., Lee, D.J., Chang, J.S., Show, P.L., 2016. Biorefineries of carbon dioxide: From carbon capture and storage (CCS) to bioenergies production. Bioresour. Technol. 215, 346–356. https://doi.org/10.1016/j.biortech.2016.04.019

Chelli, V.R., Golder, A.K., 2018. One pot green synthesis of Pt, Co and Pt@Co core-shell nanoparticles using Sechium edule. J. Chem. Technol. Biotechnol. 94, 911–918. https://doi.org/10.1002/jctb.5838

Chelli, V.R., Golder, A.K., 2016. pH dependent size control, formation mechanism and antimicrobial functionality of bio-inspired AgNPs. RSC Adv. 6, 95483–95493. https://doi.org/10.1039/C6RA16475G

Chen, C., Liang, C., Xu, J., Wei, J., Li, X., Zheng, Y., Li, Junrui, Tang, H., Li, Junsheng, 2020. Size-dependent electrochemical nitrogen reduction catalyzed by monodisperse Au nanoparticles. Electrochim. Acta 335, 135708. https://doi.org/10.1016/j.electacta.2020.135708

Chen, J., Tu, Y., Zou, Y., Li, X., Jiang, J., 2021. Morphology and composition-controllable synthesis of copper sulfide nanocrystals for electrochemical reduction of CO_2 to HCOOH. Mater. Lett. 284, 128919. https://doi.org/10.1016/j.matlet.2020.128919

Chen, J., Wang, L., 2022. Effects of the catalyst dynamic changes and influence of the reaction environment on the performance of electrochemical CO_2 reduction. Adv. Mater. 34, 2103900. https://doi.org/10.1002/adma.202103900

Chen, Q., Zhang, X., Jin, Y., Zhou, X., Yang, Z., Nie, H., 2020. An overview on noble metal (Group VIII)-based heterogeneous electrocatalysts for nitrogen

reduction reaction. Chem. - An Asian J. 15, 4131–4152. https://doi.org/10.1002/asia.202000969

Chen, T., Liu, S., Ying, H., Li, Z., Hao, J., 2020. Reactive ionic liquid enables the construction of 3D Rh particles with nanowire subunits for electrocatalytic nitrogen reduction. Chem. - An Asian J. 15, 1081–1087. https://doi.org/10.1002/asia.202000008

Chen, Z., Fan, T., Zhang, Y.Q., Xiao, J., Gao, M., Duan, N., Zhang, J., Li, J., Liu, Q., Yi, X., Luo, J.L., 2020. Wavy SnO_2 catalyzed simultaneous reinforcement of carbon dioxide adsorption and activation towards electrochemical conversion of CO_2 to HCOOH. Appl. Catal. B Environ. 261, 118243. https://doi.org/10.1016/j.apcatb.2019.118243

Chu, K., Liu, Y.P., Wang, J., Zhang, H., 2019. NiO nanodots on graphene for efficient electrochemical N_2 reduction to NH_3. ACS Appl. Energy Mater. 2, 2288–2295. https://doi.org/10.1021/acsaem.9b00102

Cohen, A., Patsha, A., Mohapatra, P.K., Kazes, M., Ranganathan, K., Houben, L., Oron, D., Ismach, A., 2021. Growth-etch metal-organic chemical vapor deposition approach of WS_2 atomic layers. ACS Nano 15, 526–538. https://doi.org/10.1021/acsnano.0c05394

Cooper, A.I., 2000. Polymer synthesis and processing using supercritical carbon dioxide. J. Mater. Chem. 10, 207–234.

Corvalan, C., 2007. WHO news Climate change and human health. WHO news 85, 830–833.

Daiyan, R., Lovell, E.C., Bedford, N.M., Saputera, W.H., Wu, K., Lim, S., Horlyck, J., Ng, Y.H., Lu, X., Amal, R., 2019a. Modulating activity through defect engineering of tin oxides for electrochemical CO_2 reduction. Adv. Sci. 6, 1–9. https://doi.org/10.1002/advs.201900678

Daiyan, R., Lu, X., Saputera, W.H., Ng, Y.H., Amal, R., 2018. Highly selective reduction of CO_2 to formate at low overpotentials achieved by a mesoporous tin oxide electrocatalyst. ACS Sustain. Chem. Eng. 6, 1670–1679. https://doi.org/10.1021/acssuschemeng.7b02913

Daiyan, R., Saputera, W.H., Masood, H., Leverett, J., Lu, X., Amal, R., 2020. A disquisition on the active sites of heterogeneous catalysts for electrochemical reduction of CO_2 to value-added chemicals and fuel. Adv. Energy Mater. 10, 1–

36. https://doi.org/10.1002/aenm.201902106

Daiyan, R., Saputera, W.H., Zhang, Q., Lovell, E., Lim, S., Ng, Y.H., Lu, X., Amal, R., 2019b. 3D heterostructured copper electrode for conversion of carbon dioxide to alcohols at low overpotentials. Adv. Sustain. Syst. 3, 1–10. https://doi.org/10.1002/adsu.201800064

Das, B.S., Das, A., Mishra, A., Arakha, M., 2021. Microbial cells as biological factory for nanoparticle synthesis. Front. Mater. Sci. 15, 177–191. https://doi.org/10.1007/s11706-021-0546-8

Das, R.K., 2018. Bio-inspired synthesis of Co_3O_4 and NiO Nanoparticles for Electrocatalytic H_2O_2 generation and sensing. Indian Institiute Technol. Guwahati. Indian Institiute of Technology Guwahati.

Das, R.K., Golder, A.K., 2017. Co_3O_4 spinel nanoparticles decorated graphite electrode: Bio-mediated synthesis and electrochemical H_2O_2 sensing. Electrochim. Acta 251, 415–426. https://doi.org/10.1016/j.electacta.2017.08.122

Das, S., Dutta, P., 2017. Preliminary understanding of CO_2 sequestration and enhanced methane recovery in raniganj coalfield of india by reservoir simulation. Energy Procedia 114, 4643–4657. https://doi.org/10.1016/j.egypro.2017.03.1267

Das, S., Pérez-Ramírez, J., Gong, J., Dewangan, N., Hidajat, K., Gates, B.C., Kawi, S., 2020. Core–shell structured catalysts for thermocatalytic, photocatalytic, and electrocatalytic conversion of CO 2. Chem. Soc. Rev. 49, 2937–3004. https://doi.org/10.1039/C9CS00713J

Dash, S.R., Bag, S.S., Golder, A.K., 2018. Synergized AgNPs formation using microwave in a bio-mediated route: studies on particle aggregation and electrocatalytic sensing of ascorbic acid from biological entities. J. Electroanal. Chem. 827, 181–192. https://doi.org/10.1016/j.jelechem.2018.09.023

De Gregorio, G.L., Burdyny, T., Loiudice, A., Iyengar, P., Smith, W.A., Buonsanti, R., 2020. Facet-dependent selectivity of Cu catalysts in electrochemical CO_2 reduction at commercially viable current densities. ACS Catal. 10, 4854–4862. https://doi.org/10.1021/acscatal.0c00297

Del Castillo, A., Alvarez-Guerra, M., Solla-Gullón, J., Sáez, A., Montiel, V., Irabien, A., 2017. Sn nanoparticles on gas diffusion electrodes: synthesis, characterization and use for continuous CO_2 electroreduction to formate. J. CO2 Util. 18, 222–228. https://doi.org/10.1016/j.jcou.2017.01.021

Delavari, S., Amin, N.A.S., Ghaedi, M., 2016. Photocatalytic conversion and kinetic study of CO_2 and CH_4 over nitrogen-doped titania nanotube arrays. J. Clean. Prod. 111, 143–154. https://doi.org/10.1016/j.jclepro.2015.07.077

Deng, G., Wang, T., Alshehri, A.A., Alzahrani, K.A., Wang, Y., Ye, H., Luo, Y., Sun, X., 2019. Improving the electrocatalytic N_2 reduction activity of Pd nanoparticles through surface modification. J. Mater. Chem. A 7, 21674–21677. https://doi.org/10.1039/c9ta06523g

Ding, M., Wang, C., Woo Bae, S., Yong Ng, H., 2022. Enhanced nutrient removal and bioenergy production in microalgal photobioreactor following anaerobic membrane bioreactor for decarbonized wastewater treatment. Bioresour. Technol. 364, 128120. https://doi.org/10.1016/j.biortech.2022.128120

Dislich, H., 1986. Sol-gel: Science, processes and products. J. Non. Cryst. Solids 80, 115–121. https://doi.org/10.1016/0022-3093(86)90384-4

Dongare, S., Singh, N., Bhunia, H., 2021a. Oxide-derived Cu-Zn nanoparticles supported on N-doped graphene for electrochemical reduction of CO_2 to ethanol. Appl. Surf. Sci. 556, 149790. https://doi.org/10.1016/j.apsusc.2021.149790

Dongare, S., Singh, N., Bhunia, H., 2021b. Electrocatalytic reduction of CO_2 to useful chemicals on copper nanoparticles. Appl. Surf. Sci. 537, 148020. https://doi.org/10.1016/j.apsusc.2020.148020

Dutta, A., Rahaman, M., Luedi, N.C., Mohos, M., Broekmann, P., 2016. Morphology matters: Tuning the product distribution of CO_2 electroreduction on oxide-derived Cu foam catalysts. ACS Catal. 6, 3804–3814. https://doi.org/10.1021/acscatal.6b00770

El-Shobaky, G.A., Turky, A.E.M.M., 2000. Catalytic decomposition of H2O2 on Co3O4 doped with MgO and V2O5. Colloids Surfaces A Physicochem. Eng. Asp. 170, 161–172. https://doi.org/10.1016/S0927-7757(00)00496-9

Elia, P., Zach, R., Hazan, S., Kolusheva, S., Porat, Z., Zeiri, Y., 2014. Green synthesis of gold nanoparticles using plant extracts as reducing agents. Int. J. Nanomedicine 38, 4007–4021. https://doi.org/10.2147/IJN.S57343

Elishav, O., Lewin, D.R., Shter, G.E., Grader, G.S., 2017. The nitrogen economy: Economic feasibility analysis of nitrogen-based fuels as energy carriers. Appl. Energy 185, 183–188. https://doi.org/10.1016/j.apenergy.2016.10.088

Fan, K., Jia, Y., Ji, Y., Kuang, P., Zhu, B., Liu, X., Yu, J., 2020. Curved surface

boosts electrochemical CO_2 reduction to formate via bismuth nanotubes in a wide potential window. ACS Catal. 10, 358–364. https://doi.org/10.1021/acscatal.9b04516

Fan, Q., Choi, C., Yan, C., Liu, Y., Qiu, J., Hong, S., Jung, Y., Sun, Z., 2019. High-yield production of few-layer boron nanosheets for efficient electrocatalytic N_2 reduction. Chem. Commun. 55, 4246–4249. https://doi.org/10.1039/c9cc00985j

Farrelly, D.J., Everard, C.D., Fagan, C.C., McDonnell, K.P., 2013. Carbon sequestration and the role of biological carbon mitigation: A review. Renew. Sustain. Energy Rev. 21, 712–727. https://doi.org/10.1016/j.rser.2012.12.038

Figueiredo, M.C., Ledezma-Yanez, I., Koper, M.T.M., 2016. In situ spectroscopic study of CO_2 electroreduction at copper electrodes in acetonitrile. ACS Catal. 6, 2382–2392. https://doi.org/10.1021/acscatal.5b02543

Fu, Y., Li, Y., Zhang, X., Liu, Y., Zhou, X., Qiao, J., 2016. Electrochemical CO_2 reduction to formic acid on crystalline SnO_2 nanosphere catalyst with high selectivity and stability. Chinese J. Catal. 37, 1081–1088. https://doi.org/10.1016/S1872-2067(15)61048-8

FUJISHIMA, A., HONDA, K., 1972. Electrochemical Photolysis of Water at a Semiconductor Electrode. Nature 238, 37–38. https://doi.org/10.1038/238037a0

Ganesh, I., 2014. Conversion of carbon dioxide into methanol - A potential liquid fuel: Fundamental challenges and opportunities (a review). Renew. Sustain. Energy Rev. 31, 221–257. https://doi.org/10.1016/j.rser.2013.11.045

Gao, D., Zhou, H., Cai, F., Wang, D., Hu, Y., Jiang, B., Cai, W.-B., Chen, X., Si, R., Yang, F., Miao, S., Wang, J., Wang, G., Bao, X., 2017. Switchable CO_2 electroreduction via engineering active phases of Pd nanoparticles. Nano Res. 10, 2181–2191. https://doi.org/10.1007/s12274-017-1514-6

Gao, D., Zhou, H., Wang, Jing, Miao, S., Yang, F., Wang, G., Wang, Jianguo, Bao, X., 2015. Size-dependent electrocatalytic reduction of CO_2 over Pd nanoparticles. J. Am. Chem. Soc. 137, 4288–4291. https://doi.org/10.1021/jacs.5b00046

Gao, W.Y., Hao, Y.C., Su, X., Chen, L.W., Bu, T.A., Zhang, N., Yu, Z.L., Zhu, Z., Yin, A.X., 2019. Morphology-dependent electrocatalytic nitrogen reduction on Ag triangular nanoplates. Chem. Commun. 55, 10705–10708. https://doi.org/10.1039/c9cc04691g

García-Quintero, A., Palencia, M., 2021. A critical analysis of environmental sustainability metrics applied to green synthesis of nanomaterials and the assessment of environmental risks associated with the nanotechnology. Sci. Total Environ. 793, 148524. https://doi.org/10.1016/j.scitotenv.2021.148524

Garg, S., Li, M., Weber, A.Z., Ge, L., Li, L., Rudolph, V., Wang, G., Rufford, T.E., 2020. Advances and challenges in electrochemical CO_2 reduction processes: An engineering and design perspective looking beyond new catalyst materials. J. Mater. Chem. A 8, 1511–1544. https://doi.org/10.1039/c9ta13298h

Garibo, D., Borbón-Nuñez, H.A., de León, J.N.D., García Mendoza, E., Estrada, I., Toledano-Magaña, Y., Tiznado, H., Ovalle-Marroquin, M., Soto-Ramos, A.G., Blanco, A., Rodríguez, J.A., Romo, O.A., Chávez-Almazán, L.A., Susarrey-Arce, A., 2020. Green synthesis of silver nanoparticles using *Lysiloma acapulcensis* exhibit high-antimicrobial activity. Sci. Rep. 10, 12805. https://doi.org/10.1038/s41598-020-69606-7

Gawel, A., Jaster, T., Siegmund, D., Holzmann, J., Lohmann, H., Klemm, E., Apfel, U.P., 2022. Electrochemical CO_2 reduction - the macroscopic world of electrode design, reactor concepts & economic aspects. iScience 25, 104011. https://doi.org/10.1016/j.isci.2022.104011

Ghiat, I., Al-Ansari, T., 2021. A review of carbon capture and utilisation as a CO_2 abatement opportunity within the EWF nexus. J. CO2 Util. 45, 101432. https://doi.org/10.1016/j.jcou.2020.101432

Guan, Q., Cheng, J., Li, X., Ni, W., Wang, B., 2017. Porous CoF_2 spheres synthesized by a one-pot solvothermal method as high capacity cathode materials for lithium-ion batteries. Chinese J. Chem. 35, 48–54. https://doi.org/10.1002/cjoc.201600229

Guilger-Casagrande, M., Lima, R. de, 2019. Synthesis of silver nanoparticles mediated by fungi: a review. Front. Bioeng. Biotechnol. 7, 1–16. https://doi.org/10.3389/fbioe.2019.00287

Gulia, K., James, A., Pandey, S., Dev, K., Kumar, D., Sourirajan, A., 2022. Bio-inspired smart nanoparticles in enhanced cancer theranostics and targeted drug delivery. J. Funct. Biomater. 13. https://doi.org/10.3390/jfb13040207

Guo, W., Shim, K., Ngome, F.O.O., Moon, Y.H., Choi, S.Y., Kim, Y.T., 2020. Highly active coral-like porous silver for electrochemical reduction of CO_2 to

CO. J. CO2 Util. 41, 101242. https://doi.org/10.1016/j.jcou.2020.101242

Guo, Y., Yao, Z., Timmer, B.J.J., Sheng, X., Fan, L., Li, Y., Zhang, F., Sun, L., 2019. Boosting nitrogen reduction reaction by bio-inspired FeMoS containing hybrid electrocatalyst over a wide pH range. Nano Energy 62, 282–288. https://doi.org/10.1016/j.nanoen.2019.05.051

Hampden-Smith, M.J., Kodas, T.T., 1995. Chemical vapor deposition of metals: Part 1. An overview of CVD processes. Chem. Vap. Depos. 1, 8–23. https://doi.org/10.1002/cvde.19950010103

Han, J., Ji, X., Ren, X., Cui, G., Li, L., Xie, F., Wang, H., Li, B., Sun, X., 2018. MoO_3 nanosheets for efficient electrocatalytic N_2 fixation to NH_3. J. Mater. Chem. A 6, 12974–12977. https://doi.org/10.1039/c8ta03974g

Han, N., Wang, Y., Deng, J., Zhou, J., Wu, Y., Yang, H., Ding, P., Li, Y., 2019. Self-templated synthesis of hierarchical mesoporous SnO_2 nanosheets for selective CO_2 reduction. J. Mater. Chem. A 7, 1267–1272. https://doi.org/10.1039/c8ta10959a

Han, N., Wang, Y., Yang, H., Deng, J., Wu, J., Li, Yafei, Li, Yanguang, 2018. Ultrathin bismuth nanosheets from in situ topotactic transformation for selective electrocatalytic CO_2 reduction to formate. Nat. Commun. 9, 1320. https://doi.org/10.1038/s41467-018-03712-z

Hara, K., Kudo, A., Sakata, T., 1997. Electrochemical CO_2 reduction on a glassy carbon electrode under high pressure. J. Electroanal. Chem. 421, 1–4. https://doi.org/10.1016/S0022-0728(96)01028-5

Hasan, M.R., Abd Hamid, S.B., Basirun, W.J., Meriam Suhaimy, S.H., Che Mat, A.N., 2015. A sol–gel derived, copper-doped, titanium dioxide–reduced graphene oxide nanocomposite electrode for the photoelectrocatalytic reduction of CO_2 to methanol and formic acid. RSC Adv. 5, 77803–77813. https://doi.org/10.1039/C5RA12525A

Hasnidawani, J.N., Azlina, H.N., Norita, H., Bonnia, N.N., Ratim, S., Ali, E.S., 2016. Synthesis of ZnO nanostructures using sol-gel method. Procedia Chem. 19, 211–216. https://doi.org/10.1016/j.proche.2016.03.095

He, C., Wu, Z.Y., Zhao, L., Ming, M., Zhang, Y., Yi, Y., Hu, J.S., 2019. Identification of FeN_4 as an efficient active site for electrochemical N_2 reduction. ACS Catal. 9, 7311–7317. https://doi.org/10.1021/acscatal.9b00959

Hori, Y., 2008. Electrochemical CO_2 reduction on metal electrodes, in: Modern Aspects of Electrochemistry. Springer New York, New York, NY, pp. 89–189. https://doi.org/10.1007/978-0-387-49489-0_3

Hori, Y., Kikuchi, K., Murata, A., Suzuki, S., 1986. Production of methane and ethylene in electrochemical reduction of carbon dioxide at copper electrode in aqueous hydrogencarbonate solution. Chem. Lett. 15, 897–898. https://doi.org/10.1246/cl.1986.897

Hori, Y., Murata, A., Takahashi, R., Suzuki, S., 1988. Enhanced formation of ethylene and alcohols at ambient temperature and pressure in electrochemical reduction of carbon dioxide at a copper electrode. J. Chem. Soc. Chem. Commun. 17–19. https://doi.org/10.1039/C39880000017

Hou, M., Shi, Y. xia, Li, J. jun, Gao, Z., Zhang, Z., 2022. Cu-based organic-inorganic composite materials for electrochemical CO_2 reduction. Chem. – An Asian J. 17, 1–20. https://doi.org/10.1002/asia.202200624

Hu, L., Khaniya, A., Wang, J., Chen, G., Kaden, W.E., Feng, X., 2018. Ambient electrochemical ammonia synthesis with high selectivity on Fe/Fe oxide catalyst. ACS Catal. 8, 9312–9319. https://doi.org/10.1021/acscatal.8b02585

Huang, H., Xia, L., Shi, X., Asiri, A.M., Sun, X., 2018. Ag nanosheets for efficient electrocatalytic N_2 fixation to NH_3 under ambient conditions. Chem. Commun. 54, 11427–11430. https://doi.org/10.1039/c8cc06365f

Huang, J., Dai, J., Zhu, J., Chen, R., Fu, X., Liu, H., Li, G., 2022. Bimetallic Au-Cu gradient alloy for electrochemical CO_2 reduction into C_2H_4 at low overpotential. J. Catal. 415, 134–141. https://doi.org/10.1016/j.jcat.2022.09.033

Indrakanti, V.P., Kubicki, J.D., Schobert, H.H., 2009. Photoinduced activation of CO_2 on Ti-based heterogeneous catalysts: current state, chemical physics-based insights and outlook. Energy Environ. Sci. 2, 745. https://doi.org/10.1039/b822176f

Inoue, S., Koinuma, H., Tsuruta, T., 1969. Copolymerisation of carbon dioxide and epoxide. J. Polym. Sci. Part B Polym. Lett. 7, 287–292. https://doi.org/10.1002/pol.1969.110070408

Jana, N.R., 2005. Gram-scale synthesis of soluble, near-monodisperse gold nanorods and other anisotropic nanoparticles. Small 1, 875–882. https://doi.org/10.1002/smll.200500014

Javaid, A., Oloketuyi, S.F., Khan, M.M., Khan, F., 2018. Diversity of bacterial synthesis of silver nanoparticles. Bionanoscience 8, 43–59. https://doi.org/10.1007/s12668-017-0496-x

Jeon, H.S., Kunze, S., Scholten, F., Roldan Cuenya, B., 2018a. Prism-Shaped Cu Nanocatalysts for Electrochemical CO_2 Reduction to Ethylene. ACS Catal. 8, 531–535. https://doi.org/10.1021/acscatal.7b02959

Jeon, H.S., Sinev, I., Scholten, F., Divins, N.J., Zegkinoglou, I., Pielsticker, L., Cuenya, B.R., 2018b. Operando evolution of the structure and oxidation state of size-controlled Zn nanoparticles during CO_2 electroreduction. J. Am. Chem. Soc. 140, 9383–9386. https://doi.org/10.1021/jacs.8b05258

Jerome, M.P., Alahmad, F.A., Salem, M.T., Tahir, M., 2022. Layered double hydroxide (LDH) nanomaterials with engineering aspects for photocatalytic CO_2 conversion to energy efficient fuels: fundamentals, recent advances, and challenges. J. Environ. Chem. Eng. 10, 108151. https://doi.org/10.1016/j.jece.2022.108151

Ji, X., Wang, T., Liu, Q., Luo, Y., Lu, S., Chen, G., Gao, S., Asiri, A.M., Sun, X., 2020. Oxidation-etching induced morphology regulation of Cu catalysts for high-performance electrochemical N_2 reduction. EcoMat 2, 1–7. https://doi.org/https://doi.org/10.1002/eom2.12026

Jiang, H., Wang, L., Li, Y., Gao, B., Guo, Y., Yan, C., Zhuo, M., Wang, H., Zhao, S., 2021. High-selectivity electrochemical CO_2 reduction to formate at low overpotential over Bi catalyst with hexagonal sheet structure. Appl. Surf. Sci. 541, 148577. https://doi.org/10.1016/j.apsusc.2020.148577

Jiang, K., Sandberg, R.B., Akey, A.J., Liu, X., Bell, D.C., Nørskov, J.K., Chan, K., Wang, H., 2018. Metal ion cycling of Cu foil for selective C-C coupling in electrochemical CO_2 reduction. Nat. Catal. 1, 111–119. https://doi.org/10.1038/s41929-017-0009-x

Jiwanti, P.K., Sultana, S., Wicaksono, W.P., Einaga, Y., 2021. Metal modified carbon-based electrode for CO_2 electrochemical reduction: A review. J. Electroanal. Chem. 898, 115634. https://doi.org/10.1016/j.jelechem.2021.115634

Jung, H., Lee, S.Y., Lee, C.W., Cho, M.K., Won, D.H., Kim, C., Oh, H.-S., Min, B.K., Hwang, Y.J., 2019. Electrochemical fragmentation of Cu_2O nanoparticles enhancing selective C–C coupling from CO_2 reduction reaction. J. Am. Chem.

Soc. 141, 4624–4633. https://doi.org/10.1021/jacs.8b11237

Kale, M.B., Borse, R.A., Gomaa Abdelkader Mohamed, A., Wang, Y., 2021. Electrocatalysts by electrodeposition: recent advances, synthesis methods, and applications in energy conversion. Adv. Funct. Mater. 31. https://doi.org/10.1002/adfm.202101313

Kas, R., Kortlever, R., Milbrat, A., Koper, M.T.M., Mul, G., Baltrusaitis, J., 2014. Electrochemical CO_2 reduction on Cu_2O-derived copper nanoparticles: Controlling the catalytic selectivity of hydrocarbons. Phys. Chem. Chem. Phys. 16, 12194–12201. https://doi.org/10.1039/c4cp01520g

Kibria, M.G., Mi, Z., 2016. Artificial photosynthesis using metal/nonmetal-nitride semiconductors: current status, prospects, and challenges. J. Mater. Chem. A 4, 2801–2820. https://doi.org/10.1039/C5TA07364B

Kim, D., Lee, S., Ocon, J.D., Jeong, B., Lee, J.K., Lee, J., 2015. Insights into an autonomously formed oxygen-evacuated Cu_2O electrode for the selective production of C_2H_4 from CO_2. Phys. Chem. Chem. Phys. 17, 824–830. https://doi.org/10.1039/c4cp03172e

Kim, K. Do, Han, D.N., Kim, H.T., 2004. Optimization of experimental conditions based on the taguchi robust design for the formation of nano-sized silver particles by chemical reduction method. Chem. Eng. J. 104, 55–61. https://doi.org/10.1016/j.cej.2004.08.003

Kim, M.K., Lee, H., Won, J.H., Sim, W., Kang, S.J., Choi, H., Sharma, M., Oh, H.S., Ringe, S., Kwon, Y., Jeong, H.M., 2022. Design of less than 1 nm scale spaces on SnO_2 nanoparticles for high-performance electrochemical CO_2 reduction. Adv. Funct. Mater. 32, 1–10. https://doi.org/10.1002/adfm.202107349

Kim, S., Dong, W.J., Gim, S., Sohn, W., Park, J.Y., Yoo, C.J., Jang, H.W., Lee, J.L., 2017. Shape-controlled bismuth nanoflakes as highly selective catalysts for electrochemical carbon dioxide reduction to formate. Nano Energy 39, 44–52. https://doi.org/10.1016/j.nanoen.2017.05.065

Koponen, S.E., Gordon, P.G., Barry, S.T., 2016. Principles of precursor design for vapour deposition methods. Polyhedron 108, 59–66. https://doi.org/10.1016/j.poly.2015.08.024

Korotcenkov, G., Cho, B.K., 2017. Spray pyrolysis deposition of undoped SnO_2 and In_2O_3 films and their structural properties. Prog. Cryst. Growth Charact. Mater.

63, 1–47. https://doi.org/10.1016/j.pcrysgrow.2016.12.001

Kremer, G., Vis, M., Prudich, M., Bayless, D., n.d. Practical Photosynthetic Carbon Dioxide Mitigation. Biofouling. https://doi.org/10.1.1.580.7494

Kuhl, K.P., Cave, E.R., Abram, D.N., Jaramillo, T.F., 2012. New insights into the electrochemical reduction of carbon dioxide on metallic copper surfaces. Energy Environ. Sci. 5, 7050. https://doi.org/10.1039/c2ee21234j

Kuila, T., Mishra, A.K., Khanra, P., Kim, N.H., Lee, J.H., 2013. Recent advances in the efficient reduction of graphene oxide and its application as energy storage electrode materials. Nanoscale 5, 52–71. https://doi.org/10.1039/C2NR32703A

Kumar, B., Atla, V., Brian, J.P., Kumari, S., Nguyen, T.Q., Sunkara, M., Spurgeon, J.M., 2017. Reduced SnO_2 porous nanowires with a high density of grain boundaries as catalysts for efficient electrochemical CO_2-into-HCOOH conversion. Angew. Chemie - Int. Ed. 56, 3645–3649. https://doi.org/10.1002/anie.201612194

Kumar, B., Brian, J.P., Atla, V., Kumari, S., Bertram, K.A., White, R.T., Spurgeon, J.M., 2016. New trends in the development of heterogeneous catalysts for electrochemical CO_2 reduction. Catal. Today 270, 19–30. https://doi.org/10.1016/j.cattod.2016.02.006

Kumar, M., Mehta, A., Mishra, A., Singh, J., Rawat, M., Basu, S., 2018. Biosynthesis of tin oxide nanoparticles using *Psidium Guajava* leave extract for photocatalytic dye degradation under sunlight. Mater. Lett. 215, 121–124. https://doi.org/10.1016/j.matlet.2017.12.074

Kumaravel, V., Bartlett, J., Pillai, S.C., 2020. Photoelectrochemical conversion of carbon dioxide (CO_2) into fuels and value-added products. ACS Energy Lett. 486–519. https://doi.org/10.1021/acsenergylett.9b02585

Kwon, Y., Lee, J., 2010. Formic acid from carbon dioxide on nanolayered electrocatalyst. Electrocatalysis 1, 108–115. https://doi.org/10.1007/s12678-010-0017-y

Latiff, N.M., Fu, X., Mohamed, D.K., Veksha, A., Handayani, M., Lisak, G., 2020. Carbon based copper(II) phthalocyanine catalysts for electrochemical CO_2 reduction: Effect of carbon support on electrocatalytic activity. Carbon N. Y. 168, 245–253. https://doi.org/10.1016/j.carbon.2020.06.066

Lee, C.Y., Zhao, Y., Wang, C., Mitchell, D.R.G., Wallace, G.G., 2017. Rapid

formation of self-organised Ag nanosheets with high efficiency and selectivity in CO_2 electroreduction to CO. Sustain. Energy Fuels 1, 1023–1027. https://doi.org/10.1039/c7se00069c

Lee, S., Schneider, K., Schumann, J., Mogalicherla, A.K., Pfeifer, P., Dittmeyer, R., 2015. Effect of metal precursor on $Cu/ZnO/Al_2O_3$ synthesized by flame spray pyrolysis for direct DME production. Chem. Eng. Sci. 138, 194–202. https://doi.org/10.1016/j.ces.2015.08.021

Leng, J., Wang, Z., Wang, J., Wu, H.H., Yan, G., Li, X., Guo, H., Liu, Y., Zhang, Q., Guo, Z., 2019. Advances in nanostructures fabricated *via* spray pyrolysis and their applications in energy storage and conversion. Chem. Soc. Rev. 48, 3015–3072. https://doi.org/10.1039/c8cs00904j

Li, C., Mou, S., Zhu, X., Wang, F., Wang, Y., Qiao, Y., Shi, X., Luo, Y., Zheng, B., Li, Q., Sun, X., 2019. Dendritic Cu: a high-efficiency electrocatalyst for N_2 fixation to NH_3 under ambient conditions. Chem. Commun. 55, 14474–14477. https://doi.org/10.1039/c9cc08234d

Li, C.W., Kanan, M.W., 2012. CO_2 reduction at low overpotential on Cu electrodes resulting from the reduction of thick Cu_2O films. J. Am. Chem. Soc. 134, 7231–7234. https://doi.org/10.1021/ja3010978

Li, J., Kuang, Y., Meng, Y., Tian, X., Hung, W.-H., Zhang, X., Li, A., Xu, M., Zhou, W., Ku, C.-S., Chiang, C.-Y., Zhu, G., Guo, J., Sun, X., Dai, H., 2020. Electroreduction of CO_2 to formate on a copper-based electrocatalyst at high pressures with high energy conversion efficiency. J. Am. Chem. Soc. 142, 7276–7282. https://doi.org/10.1021/jacs.0c00122

Li, Jiayu, Li, Jinxia, Liu, X., Chen, J., Tian, P., Dai, S., Zhu, M., Han, Y.F., 2021. Probing the role of surface hydroxyls for Bi, Sn and In catalysts during CO_2 reduction. Appl. Catal. B Environ. 298, 120581. https://doi.org/10.1016/j.apcatb.2021.120581

Li, L., Huang, Y., Li, Y., 2020. Carbonaceous materials for electrochemical CO_2 reduction. EnergyChem 2, 100024. https://doi.org/10.1016/j.enchem.2019.100024

Li, M., Wang, H., Luo, W., Sherrell, P.C., Chen, J., Yang, J., 2020. Heterogeneous single-atom catalysts for electrochemical CO_2 reduction reaction. Adv. Mater. 32, 2001848. https://doi.org/10.1002/adma.202001848

Li, P., Liu, J., Nag, N., Crozier, P.A., 2006. In situ synthesis and characterization of Ru promoted Co/Al_2O_3 Fischer-Tropsch catalysts. Appl. Catal. A Gen. 307, 212–221. https://doi.org/10.1016/j.apcata.2006.03.051

Li, Q., Wang, Z., Zhang, M., Hou, P., Kang, P., 2017. Nitrogen doped tin oxide nanostructured catalysts for selective electrochemical reduction of carbon dioxide to formate. J. Energy Chem. 26, 825–829. https://doi.org/10.1016/j.jechem.2017.08.010

Li, Y., Liu, Y., Wang, J., Guo, Y., Chu, K., 2020. Plasma-engineered NiO nanosheets with enriched oxygen vacancies for enhanced electrocatalytic nitrogen fixation. Inorg. Chem. Front. 7, 455–463. https://doi.org/10.1039/C9QI01133A

Lim, Y.A., Chong, M.N., Foo, S.C., Ilankoon, I.M.S.K., 2021. Analysis of direct and indirect quantification methods of CO_2 fixation via microalgae cultivation in photobioreactors: A critical review. Renew. Sustain. Energy Rev. 137, 110579. https://doi.org/10.1016/j.rser.2020.110579

Liu, B., Yao, X., Zhang, Z., Li, C., Zhang, J., Wang, P., Zhao, J., Guo, Y., Sun, J., Zhao, C., 2021. Synthesis of Cu_2O nanostructures with tunable crystal facets for electrochemical CO_2 reduction to alcohols. ACS Appl. Mater. Interfaces 13, 39165–39177. https://doi.org/10.1021/acsami.1c03850

Liu, H.M., Han, S.H., Zhao, Y., Zhu, Y.Y., Tian, X.L., Zeng, J.H., Jiang, J.X., Xia, B.Y., Chen, Y., 2018. Surfactant-free atomically ultrathin rhodium nanosheet nanoassemblies for efficient nitrogen electroreduction. J. Mater. Chem. A 6, 3211–3217. https://doi.org/10.1039/c7ta10866d

Liu, L.X., Zhou, Y., Chang, Y.C., Zhang, J.R., Jiang, L.P., Zhu, W., Lin, Y., 2020. Tuning Sn_3O_4 for CO_2 reduction to formate with ultra-high current density. Nano Energy 77, 105296. https://doi.org/10.1016/j.nanoen.2020.105296

Liu, S., Xiao, J., Lu, X.F., Wang, J., Wang, X., Lou, X.W. (David), 2019. Efficient electrochemical reduction of CO_2 to HCOOH over Sub-2 nm SnO_2 quantum wires with exposed grain boundaries. Angew. Chemie Int. Ed. 58, 8499–8503. https://doi.org/10.1002/anie.201903613

Liu, W., Li, C., Xu, Q., Yan, P., Niu, C., Shen, Y., Yuan, P., Jia, Y., 2019. Anderson localization in 2D amorphous MoO_{3-x} monolayers for electrochemical ammonia synthesis. ChemCatChem 11, 5412–5416. https://doi.org/10.1002/cctc.201901171

Liu, Y., Fan, M., Zhang, X., Zhang, Q., Guay, D., Qiao, J., 2017. Design and engineering of urchin-like nanostructured SnO2 catalysts via controlled facial hydrothermal synthesis for efficient electro-reduction of CO2. Electrochim. Acta 248, 123–132. https://doi.org/10.1016/j.electacta.2017.07.140

Liu, Y., Xu, Q., Fan, X., Quan, X., Su, Y., Chen, S., Yu, H., Cai, Z., 2019. Electrochemical reduction of N_2 to ammonia on Co single atom embedded N-doped porous carbon under ambient conditions. J. Mater. Chem. A 7, 26358–26363. https://doi.org/10.1039/c9ta10382a

Loiudice, A., Lobaccaro, P., Kamali, E.A., Thao, T., Huang, B.H., Ager, J.W., Buonsanti, R., 2016. Tailoring copper nanocrystals towards C_2 products in electrochemical CO_2 reduction. Angew. Chemie Int. Ed. 55, 5789–5792. https://doi.org/10.1002/anie.201601582

Lu, X.-B., Darensbourg, D.J., 2012. Cobalt catalysts for the coupling of CO_2 and epoxides to provide polycarbonates and cyclic carbonates. Chem. Soc. Rev. 41, 1462–1484. https://doi.org/10.1039/C1CS15142H

Luo, S., Li, X., Zhang, B., Luo, Z., Luo, M., 2019. MOF-derived Co_3O_4@NC with core-shell structures for N_2 electrochemical reduction under ambient conditions. ACS Appl. Mater. Interfaces 11, 26891–26897. https://doi.org/10.1021/acsami.9b07100

Luo, W., Xie, W., Li, M., Zhang, J., Züttel, A., 2019a. 3D hierarchical porous indium catalyst for highly efficient electroreduction of CO_2. J. Mater. Chem. A 7, 4505–4515. https://doi.org/10.1039/c8ta11645h

Luo, W., Zhang, J., Li, M., Züttel, A., 2019b. Boosting CO production in electrocatalytic CO_2 reduction on highly porous Zn catalysts. ACS Catal. 9, 3783–3791. https://doi.org/10.1021/acscatal.8b05109

Lv, J., Tian, Z., Dai, K., Ye, Y., Liang, C., 2019. Interface and defect engineer of titanium dioxide supported palladium or platinum for tuning the activity and selectivity of electrocatalytic nitrogen reduction reaction. J. Colloid Interface Sci. 553, 126–135. https://doi.org/10.1016/j.jcis.2019.05.105

Lv, W., Bei, J., Zhang, R., Wang, Wenjuan, Kong, F., Wang, L., Wang, Wei, 2017. $Bi_2O_2CO_3$ nanosheets as electrocatalysts for selective reduction of CO_2 to formate at low overpotential. ACS Omega 2, 2561–2567. https://doi.org/10.1021/acsomega.7b00437

Lv, X., Wang, F., Du, J., Liu, Q., Luo, Y., Lu, S., Chen, G., Gao, S., Zheng, B., Sun, X., 2020. Sn dendrites for electrocatalytic N_2 reduction to NH_3 under ambient conditions. Sustain. Energy Fuels 4, 4469–4472. https://doi.org/10.1039/d0se00828a

Ma, L., Hu, W., Pan, Q., Zou, L., Zou, Z., Wen, K., Yang, H., 2019. Polyvinyl alcohol-modified gold nanoparticles with record-high activity for electrochemical reduction of CO<sub>2</sub to CO. J. CO2 Util. 34, 108–114. https://doi.org/10.1016/j.jcou.2019.06.002

Ma, M., Djanashvili, K., Smith, W.A., 2016a. Controllable hydrocarbon formation from the electrochemical reduction of CO_2 over Cu nanowire arrays. Angew. Chemie - Int. Ed. 55, 6680–6684. https://doi.org/10.1002/anie.201601282

Ma, M., Trześniewski, B.J., Xie, J., Smith, W.A., 2016b. Selective and efficient reduction of carbon dioxide to carbon monoxide on oxide-derived nanostructured silver electrocatalysts. Angew. Chemie Int. Ed. 55, 9748–9752. https://doi.org/10.1002/anie.201604654

Mandal, S.K., Dutta, K., Pal, S., Mandal, S., Naskar, A., Pal, P.K., Bhattacharya, T.S., Singha, A., Saikh, R., De, S., Jana, D., 2019. Engineering of ZnO/rGO nanocomposite photocatalyst towards rapid degradation of toxic dyes. Mater. Chem. Phys. 223, 456–465. https://doi.org/10.1016/j.matchemphys.2018.11.002

Maroto-Valer, M.M., Fauth, D.J., Kuchta, M.E., Zhang, Y., Andrésen, J.M., 2005. Activation of magnesium rich minerals as carbonation feedstock materials for CO_2 sequestration. Fuel Process. Technol. 86, 1627–1645. https://doi.org/10.1016/j.fuproc.2005.01.017

Martin, J.H., Coale, K.H., Johnson, K.S., Fitzwater, S.E., Gordon, R.M., Tanner, S.J., Hunter, C.N., Elrod, V. a., Nowicki, J.L., Coley, T.L., Barber, R.T., Lindley, S., Watson, A.J., Van Scoy, K., Law, C.S., Liddicoat, M.I., Ling, R., Stanton, T., Stockel, J., Collins, C., Anderson, A., Bidigare, R., Ondrusek, M., Latasa, M., Millero, F.J., Lee, K., Yao, W., Zhang, J.Z., Friederich, G., Sakamoto, C., Chavez, F., Buck, K., Kolber, Z., Greene, R., Falkowski, P., Chisholm, S.W., Hoge, F., Swift, R., Yungel, J., Turner, S., Nightingale, P., Hatton, A., Liss, P., Tindale, N.W., 1994. Testing the iron hypothesis in ecosystems of the equatorial Pacific Ocean. Nature. https://doi.org/10.1038/371123a0

Masood, Z., Ge, Q., 2022. Electrochemical reduction of CO_2 at the earth-abundant

transition metal-oxides/copper interfaces. Catal. Today 409, 53–62. https://doi.org/10.1016/j.cattod.2022.05.013

Mattia, D., Jones, M.D., O'Byrne, J.P., Griffiths, O.G., Owen, R.E., Sackville, E., McManus, M., Plucinski, P., 2015. Towards carbon-neutral CO_2 conversion to hydrocarbons. ChemSusChem 8, 4064–4072. https://doi.org/10.1002/cssc.201500739

McConnell, I., Li, G., Brudvig, G.W., 2010. Energy conversion in natural and artificial photosynthesis. Chem. Biol. 17, 434–447. https://doi.org/10.1016/j.chembiol.2010.05.005

Meierhofer, F., Li, H., Gockeln, M., Kun, R., Grieb, T., Rosenauer, A., Fritsching, U., Kiefer, J., Birkenstock, J., Mädler, L., Pokhrel, S., 2017. Screening precursor–solvent combinations for Li_4 Ti_5 O_{12} energy storage material using flame spray pyrolysis. ACS Appl. Mater. Interfaces 9, 37760–37777. https://doi.org/10.1021/acsami.7b11435

Meierhofer, F., Mädler, L., Fritsching, U., 2020. Nanoparticle evolution in flame spray pyrolysis—Process design via experimental and computational analysis. AIChE J. 66, 1–14. https://doi.org/10.1002/aic.16885

Miao, C.C., Yuan, G.Q., 2018. Morphology-controlled Bi_2O_3 nanoparticles as catalysts for selective electrochemical reduction of CO_2 to formate. ChemElectroChem 5, 3741–3747. https://doi.org/10.1002/celc.201801036

Mohler, D.T., Wilson, M.H., Fan, Z., Groppo, J.G., Crocker, M., 2019. Beneficial reuse of industrial CO_2 emissions using a microalgae photobioreactor: Waste heat utilization assessment. Energies 12, 18–21. https://doi.org/10.3390/en12132634

Mondal, M., Ghosh, A., Gayen, K., Halder, G., Tiwari, O.N., 2017. Carbon dioxide bio-fixation by Chlorella sp. BTA 9031 towards biomass and lipid production: Optimization using Central Composite Design approach. J. CO2 Util. 22, 317–329. https://doi.org/10.1016/j.jcou.2017.10.008

Morimoto, M., Takatsuji, Y., Hirata, K., Fukuma, T., Ohno, T., Sakakura, T., Haruyama, T., 2018. Visualization of catalytic edge reactivity in electrochemical CO_2 reduction on porous Zn electrode. Electrochim. Acta 290, 255–261. https://doi.org/10.1016/j.electacta.2018.09.080

Mou, K., Chen, Z., Yao, S., Liu, L., 2018. Enhanced electrochemical reduction of

carbon dioxide to formate with in-situ grown indium-based catalysts in an aqueous electrolyte. Electrochim. Acta 289, 65–71. https://doi.org/10.1016/j.electacta.2018.09.026

Muromachi, T., Tsujino, T., Kamitani, K., Maeda, K., 2006. Application of functional coatings by sol-gel method. J. Sol-Gel Sci. Technol. 40, 267–272. https://doi.org/10.1007/s10971-006-8386-7

Nitopi, S., Bertheussen, E., Scott, S.B., Liu, X., Engstfeld, A.K., Horch, S., Seger, B., Stephens, I.E.L., Chan, K., Hahn, C., Nørskov, J.K., Jaramillo, T.F., Chorkendorff, I., 2019. Progress and perspectives of electrochemical CO_2 reduction on copper in aqueous electrolyte. Chem. Rev. 119, 7610–7672. https://doi.org/10.1021/acs.chemrev.8b00705

Nunes, D., Pimentel, A., Santos, L., Barquinha, P., Pereira, L., Fortunato, E., Martins, R., 2019. Synthesis, design, and morphology of metal oxide nanostructures, in: Metal Oxide Nanostructures. Elsevier, pp. 21–57. https://doi.org/10.1016/B978-0-12-811512-1.00002-3

Ola, O., Maroto-Valer, M.M., 2015. Review of material design and reactor engineering on TiO_2 photocatalysis for CO_2 reduction. J. Photochem. Photobiol. C Photochem. Rev. 24, 16–42. https://doi.org/10.1016/j.jphotochemrev.2015.06.001

Olajire, A.A., 2013. A review of mineral carbonation technology in sequestration of CO_2. J. Pet. Sci. Eng. 109, 364–392. https://doi.org/10.1016/j.petrol.2013.03.013

Osorio-Echavarría, Jerónimo, Osorio-Echavarría, Juliana, Ossa-Orozco, C.P., Gómez-Vanegas, N.A., 2021. Synthesis of silver nanoparticles using white-rot fungus Anamorphous *Bjerkandera* sp. R1: influence of silver nitrate concentration and fungus growth time. Sci. Rep. 11, 3842. https://doi.org/10.1038/s41598-021-82514-8

Pan, F., Yang, Y., 2020. Designing CO_2 reduction electrode materials by morphology and interface engineering. Energy Environ. Sci. 13, 2275–2309. https://doi.org/10.1039/d0ee00900h

Patwardhan, S. V., Manning, J.R.H., Chiacchia, M., 2018. Bioinspired synthesis as a potential green method for the preparation of nanomaterials: Opportunities and challenges. Curr. Opin. Green Sustain. Chem. 12, 110–116. https://doi.org/10.1016/j.cogsc.2018.08.004

Pavlik, D., Zhong, Y., Daiek, C., Liao, W., Morgan, R., Clary, W., Liu, Y., 2017. Microalgae cultivation for carbon dioxide sequestration and protein production using a high-efficiency photobioreactor system. Algal Res. 25, 413–420. https://doi.org/10.1016/j.algal.2017.06.003

Petcharoen, K., Sirivat, A., 2012. Synthesis and characterization of magnetite nanoparticles via the chemical co-precipitation method. Mater. Sci. Eng. B 177, 421–427. https://doi.org/10.1016/j.mseb.2012.01.003

Peternele, W.S., Monge Fuentes, V., Fascineli, M.L., Rodrigues da Silva, J., Silva, R.C., Lucci, C.M., Bentes de Azevedo, R., 2014. Experimental investigation of the coprecipitation method: an approach to obtain magnetite and maghemite nanoparticles with improved properties. J. Nanomater. 2014, 1–10. https://doi.org/10.1155/2014/682985

Priyadarshini, S., Gopinath, V., Meera Priyadharsshini, N., MubarakAli, D., Velusamy, P., 2013. Synthesis of anisotropic silver nanoparticles using novel strain, *Bacillus flexus* and its biomedical application. Colloids Surfaces B Biointerfaces 102, 232–237. https://doi.org/10.1016/j.colsurfb.2012.08.018

Qin, B., Li, Y.H., Zhang, Q., Yang, G., Wang, H., Zhang, Y., Peng, F., 2021. Mechanistic insights into the electrochemical reduction of CO_2 and N_2 on the regulation of a boron nitride defect-derived two-dimensional catalyst using density functional theory calculations. J. Phys. Chem. Lett. 12, 7151–7158. https://doi.org/10.1021/acs.jpclett.1c01920

Qin, Y., Wang, X., Wang, F., 2015. Recent advances in carbon dioxide based copolymer. J. CO2 Util. 11, 3–9. https://doi.org/10.1016/j.jcou.2014.10.003

Qiu, Y., Du, J., Dong, W., Dai, C., Tao, C., 2017. Selective conversion of CO_2 to formate on a size tunable nano-Bi electrocatalyst. J. CO_2 Util. 20, 328–335. https://doi.org/10.1016/j.jcou.2017.05.024

Rabiee, H., Zhang, X., Ge, L., Hu, S., Li, M., Smart, S., Zhu, Z., Yuan, Z., 2020. Tuning the product selectivity of the Cu hollow fiber gas diffusion electrode for efficient CO_2 reduction to formate by controlled surface Sn electrodeposition. ACS Appl. Mater. Interfaces 12, 21670–21681. https://doi.org/10.1021/acsami.0c03681

Rajaeiyan, A., Bagheri-Mohagheghi, M.M., 2013. Comparison of sol-gel and co-precipitation methods on the structural properties and phase transformation of γ

and α-Al_2O_3 nanoparticles. Adv. Manuf. 1, 176–182. https://doi.org/10.1007/s40436-013-0018-1

Rao, C.V., Golder, A.K., 2016. Development of a bio-mediated technique of silver-doping on titania. Colloids Surfaces A Physicochem. Eng. Asp. 506, 557–565. https://doi.org/10.1016/j.colsurfa.2016.07.031

Reichle, D., Houghton, J., Kane, B., Ekmann, J., and others, 1999. Carbon sequestration research and development, Ecosystems. https://doi.org/10.2172/810722

Reina, A., Jia, X., Ho, J., Nezich, D., Son, H., Bulovic, V., Dresselhaus, M.S., Kong, J., 2009. Large area, few-layer graphene films on arbitrary substrates by chemical vapor deposition. Nano Lett. 9, 30–35. https://doi.org/10.1021/nl801827v

Ren, D., Deng, Y., Handoko, A.D., Chen, C.S., Malkhandi, S., Yeo, B.S., 2015. Selective electrochemical reduction of carbon dioxide to ethylene and ethanol on copper(I) oxide catalysts. ACS Catal. 5, 2814–2821. https://doi.org/10.1021/cs502128q

Robinson, J., Popova, E.E., Yool, A., Srokosz, M., Lampitt, R.S., Blundell, J.R., 2014. How deep is deep enough? Ocean iron fertilization and carbon sequestration in the Southern Ocean. Geophys. Res. Lett. 41, 2489–2495. https://doi.org/10.1002/2013GL058799

Rusdan, N.A., Timmiati, S.N., Isahak, W.N.R.W., Yaakob, Z., Lim, K.L., Khaidar, D., 2022. Recent application of core-shell nanostructured catalysts for CO_2 thermocatalytic conversion processes. Nanomaterials 12. https://doi.org/10.3390/nano12213877

Sampath, K.H.S.M., Ranjith, P.G., Perera, M.S.A., 2020. A comprehensive review of structural alterations in CO_2-interacted coal: Insights into CO_2 sequestration in coal. Energy and Fuels 34, 13369–13383. https://doi.org/10.1021/acs.energyfuels.0c02782

Schouten, K.J.P., Pérez Gallent, E., Koper, M.T.M., 2014. The influence of pH on the reduction of CO and CO_2 to hydrocarbons on copper electrodes. J. Electroanal. Chem. 716, 53–57. https://doi.org/10.1016/j.jelechem.2013.08.033

Schwaminger, S.P., Bauer, D., Fraga-García, P., Wagner, F.E., Berensmeier, S., 2017. Oxidation of magnetite nanoparticles: impact on surface and crystal properties.

CrystEngComm 19, 246–255. https://doi.org/10.1039/c6ce02421a

Şengül, H., Theis, T.L., Ghosh, S., 2008. Toward sustainable nanoproducts: an overview of nanomanufacturing methods. J. Ind. Ecol. 12, 329–359. https://doi.org/10.1111/j.1530-9290.2008.00046.x

Seravalli, L., Bosi, M., Fiorenza, P., Panasci, S.E., Orsi, D., Rotunno, E., Cristofolini, L., Rossi, F., Giannazzo, F., Fabbri, F., 2021. Gold nanoparticle assisted synthesis of MoS_2 monolayers by chemical vapor deposition. Nanoscale Adv. 3, 4826–4833. https://doi.org/10.1039/d1na00367d

Sha, Z., Bai, Y., Li, R., Lan, H., Zhang, X., Li, J., Liu, X., Chang, S., Xie, Y., 2022. The global carbon sink potential of terrestrial vegetation can be increased substantially by optimal land management. Commun. Earth Environ. 3, 1–10. https://doi.org/10.1038/s43247-021-00333-1

Shah, A.H., Wang, Y., Woldu, A.R., Lin, L., Iqbal, M., Cahen, D., He, T., 2018. Revisiting electrochemical reduction of CO_2 on Cu electrode: where do we stand about the intermediates? J. Phys. Chem. C 122, 18528–18536. https://doi.org/10.1021/acs.jpcc.8b05348

Sharma, S., Chand, P., 2022. Effect of calcination temperature on electrochemical behavior of pristine zeolitic imidazolate framework-8. Ionics (Kiel). 28, 5395–5404. https://doi.org/10.1007/s11581-022-04783-1

Shi, J.Q., Durucan, S., 2005. CO_2 storage in deep unminable coal seams. Oil Gas Sci. Technol. 60, 547–558. https://doi.org/10.2516/ogst:2005037

Shi, Y., Wen, C.F., Wu, X., Zhao, J.Y., Mao, F., Liu, P.F., Yang, H.G., 2022. In situ reconstruction of vegetable sponge-like Bi_2O_3 for efficient CO_2 electroreduction to formate. Mater. Chem. Front. 6, 1091–1097. https://doi.org/10.1039/d1qm01557e

Sikdar, N., Junqueira, J.R.C., Dieckhöfer, S., Quast, T., Braun, M., Song, Y., Aiyappa, H.B., Seisel, S., Weidner, J., Öhl, D., Andronescu, C., Schuhmann, W., 2021. A metal–organic framework derived $Cu_xO_yC_z$ catalyst for electrochemical CO_2 reduction and impact of local pH change. Angew. Chemie Int. Ed. 60, 23427–23434. https://doi.org/10.1002/anie.202108313

Singh, K.R., Nayak, V., Singh, J., Singh, A.K., Singh, R.P., 2021. Potentialities of bioinspired metal and metal oxide nanoparticles in biomedical sciences. RSC Adv. 11, 24722–24746. https://doi.org/10.1039/D1RA04273D

Singh, R.N., Sharma, S., 2012. Development of suitable photobioreactor for algae production - A review. Renew. Sustain. Energy Rev. 16, 2347–2353. https://doi.org/10.1016/j.rser.2012.01.026

Snoeckx, R., Bogaerts, A., 2017. Plasma technology – a novel solution for CO_2 conversion? Chem. Soc. Rev. 46, 5805–5863. https://doi.org/10.1039/C6CS00066E

Solomon, S., Plattner, G.-K., Knutti, R., Friedlingstein, P., 2009. Irreversible climate change due to carbon dioxide emissions. Proc. Natl. Acad. Sci. U. S. A. 106, 1704–9. https://doi.org/10.1073/pnas.0812721106

Song, J.T., Song, H., Kim, B., Oh, J., 2019. Towards higher rate electrochemical CO_2 conversion: From liquid-phase to gas-phase systems. Catalysts 9. https://doi.org/10.3390/catal9030224

Souza, M.L., Lima, F.H.B., 2021. Dibenzyldithiocarbamate-functionalized small gold nanoparticles as selective catalysts for the electrochemical reduction of CO_2 to CO. ACS Catal. 11, 12208–12219. https://doi.org/10.1021/acscatal.1c00591

Stangeland, K., Kalai, D., Li, H., Yu, Z., 2017. CO2 Methanation: The Effect of Catalysts and Reaction Conditions. Energy Procedia 105, 2022–2027. https://doi.org/10.1016/j.egypro.2017.03.577

Stewart, C., Hessami, M.-A., 2005. A study of methods of carbon dioxide capture and sequestration—the sustainability of a photosynthetic bioreactor approach. Energy Convers. Manag. 46, 403–420. https://doi.org/10.1016/j.enconman.2004.03.009

Su, P., Xu, W., Qiu, Y., Zhang, T., Li, X., Zhang, H., 2018. Ultrathin bismuth nanosheets as a highly efficient CO_2 reduction electrocatalyst. ChemSusChem 11, 848–853. https://doi.org/10.1002/cssc.201702229

Suominen, M., Kallio, T., 2021. What we currently know about carbon-supported metal and metal oxide nanomaterials in electrochemical CO_2 reduction. ChemElectroChem 8, 2397–2406. https://doi.org/10.1002/celc.202100345

Tayyebi, E., Hussain, J., Abghoui, Y., Skúlason, E., 2018. Trends of electrochemical CO_2 reduction reaction on transition metal oxide catalysts. J. Phys. Chem. C 122, 10078–10087. https://doi.org/10.1021/acs.jpcc.8b02224

Trenerry, M.J., Wallen, C.M., Brown, T.R., Park, S. V., Berry, J.F., 2021. Spontaneous N_2 formation by a diruthenium complex enables electrocatalytic and aerobic oxidation of ammonia. Nat. Chem. 13, 1221–1227.

https://doi.org/10.1038/s41557-021-00797-w

Tummala, P., Lamperti, A., Alia, M., Kozma, E., Nobili, L.G., Molle, A., 2020. Application-oriented growth of a molybdenum disulfide (MoS_2) single layer by means of parametrically optimized chemical vapor deposition. Materials (Basel). 13, 1–13. https://doi.org/10.3390/ma13122786

Tyagi, S., Tyagi, P.K., Gola, D., Chauhan, N., Bharti, R.K., 2019. Extracellular synthesis of silver nanoparticles using entomopathogenic fungus: characterization and antibacterial potential. SN Appl. Sci. 1, 1545. https://doi.org/10.1007/s42452-019-1593-y

Vanlalveni, C., Lallianrawna, S., Biswas, A., Selvaraj, M., Changmai, B., Rokhum, S.L., 2021. Green synthesis of silver nanoparticles using plant extracts and their antimicrobial activities: a review of recent literature. RSC Adv. 11, 2804–2837. https://doi.org/10.1039/D0RA09941D

Varghese, O.K., Paulose, M., Latempa, T.J., Grimes, C.A., 2009. High-rate solar photocatalytic conversion of CO_2 and water vapor to hydrocarbon fuels. Nano Lett. 9, 731–737.

Vidhu, V.K., Philip, D., 2015. Phytosynthesis and applications of bioactive SnO_2 nanoparticles. Mater. Charact. 101, 97–105. https://doi.org/10.1016/j.matchar.2014.12.027

Vu, N.N., Kaliaguine, S., Do, T.O., 2019. Critical aspects and recent advances in structural engineering of photocatalysts for sunlight-driven photocatalytic reduction of CO_2 into fuels. Adv. Funct. Mater. 29. https://doi.org/10.1002/adfm.201901825

Wang, F., Liu, Y., Zhang, H., Chu, K., 2019. CuO/graphene nanocomposite for nitrogen reduction reaction. ChemCatChem 11, 1441–1447. https://doi.org/10.1002/cctc.201900041

Wang, F., Mao, L., Xie, H., Mao, J., 2021. Graphene derivatives and graphene composite electrocatalysts for N_2 reduction reaction. Small Struct. 2, 2000075. https://doi.org/10.1002/sstr.202000075

Wang, H., Li, Y., Li, C., Deng, K., Wang, Z., Xu, Y., Li, X., Xue, H., Wang, L., 2019a. One-pot synthesis of bi-metallic PdRu tripods as an efficient catalyst for electrocatalytic nitrogen reduction to ammonia. J. Mater. Chem. A 7, 801–805. https://doi.org/10.1039/c8ta09482a

Wang, H., Li, Y., Yang, D., Qian, X., Wang, Z., Xu, Y., Li, X., Xue, H., Wang, L., 2019b. Direct fabrication of bi-metallic PdRu nanorod assemblies for electrochemical ammonia synthesis. Nanoscale 11, 5499–5505. https://doi.org/10.1039/c8nr10398d

Wang, J., Wang, H., Han, Z., Han, J., 2015. Electrodeposited porous Pb electrode with improved electrocatalytic performance for the electroreduction of CO_2 to formic acid. Front. Chem. Sci. Eng. 9, 57–63. https://doi.org/10.1007/s11705-014-1444-8

Wang, S., Kou, T., Varley, J.B., Akhade, S.A., Weitzner, S.E., Baker, S.E., Duoss, E.B., Li, Y., 2021. Cu_2O/CuS nanocomposites show excellent selectivity and stability for formate generation via electrochemical reduction of carbon dioxide. ACS Mater. Lett. 3, 100–109. https://doi.org/10.1021/acsmaterialslett.0c00520

Wang, Yuhang, Liu, J., Wang, Yifei, Al-Enizi, A.M., Zheng, G., 2017. Tuning of CO_2 reduction selectivity on metal electrocatalysts. Small 13, 1701809. https://doi.org/10.1002/smll.201701809

Wang, Z., Li, Y., Yu, H., Xu, Y., Xue, H., Li, X., Wang, H., Wang, L., 2018. Ambient electrochemical synthesis of ammonia from nitrogen and water catalyzed by flower-like gold microstructures. ChemSusChem 11, 3480–3485. https://doi.org/10.1002/cssc.201801444

Wei, L., Li, H., Chen, J., Yuan, Z., Huang, Q., Liao, X., Henkelman, G., Chen, Y., 2020. Thiocyanate-modified silver nanofoam for efficient CO_2 reduction to CO. ACS Catal. 10, 1444–1453. https://doi.org/10.1021/acscatal.9b04633

Wei, X., Zhang, W., Liu, Depei, Liu, Duanduan, Yan, Y., Zhang, J., Yang, Y., Yan, S., Zou, Z., 2022. Bi particles with exposed (012) facet on 3D substrate as highly active and durable electrode for CO_2 reduction to formate. J. CO2 Util. 55, 101797. https://doi.org/10.1016/j.jcou.2021.101797

Welch, A.J., Duchene, J.S., Tagliabue, G., Davoyan, A., Cheng, W.H., Atwater, H.A., 2019. Nanoporous gold as a highly selective and active carbon dioxide reduction catalyst. ACS Appl. Energy Mater. 2, 164–170. https://doi.org/10.1021/acsaem.8b01570

Wen, J., Xie, J., Chen, X., Li, X., 2017. A review on g-C_3N_4-based photocatalysts. Appl. Surf. Sci. 391, 72–123. https://doi.org/10.1016/j.apsusc.2016.07.030

Wen, J., Zuo, L., Sun, H., Wu, X., Huang, T., Liu, Z., Wang, J., Liu, L., Wu, Y., Liu,

X., van Ree, T., 2021. Nanomaterials for the electrochemical nitrogen reduction reaction under ambient conditions. Nanoscale Adv. 3, 5525–5541. https://doi.org/10.1039/D1NA00426C

White, J.L., Bocarsly, A.B., 2016. Enhanced carbon dioxide reduction activity on indium-based nanoparticles. J. Electrochem. Soc. 163, H410–H416. https://doi.org/10.1149/2.0681606jes

Won, D.H., Choi, C.H., Chung, J., Chung, M.W., Kim, E.H., Woo, S.I., 2015. Rational design of a hierarchical tin dendrite electrode for efficient electrochemical reduction of CO2. ChemSusChem 8, 3092–3098. https://doi.org/10.1002/cssc.201500694

Won, D.H., Shin, H., Koh, J., Chung, J., Lee, H.S., Kim, H., Woo, S.I., 2016. Highly efficient, selective, and stable CO_2 electroreduction on a hexagonal Zn catalyst. Angew. Chemie Int. Ed. 55, 9297–9300. https://doi.org/10.1002/anie.201602888

Wu, H.Y., Bai, H., Wu, J.C.S., 2014. Photocatalytic reduction of CO_2 using Ti-MCM-41 photocatalysts in monoethanolamine solution for methane production. Ind. Eng. Chem. Res. 53, 11221–11227. https://doi.org/10.1021/ie403742j

Wu, J., Risalvato, F.G., Ma, S., Zhou, X.D., 2014. Electrochemical reduction of carbon dioxide III. the role of oxide layer thickness on the performance of Sn electrode in a full electrochemical cell. J. Mater. Chem. A 2, 1647–1651. https://doi.org/10.1039/c3ta13544f

Wu, X., Xia, L., Wang, Y., Lu, W., Liu, Q., Shi, X., Sun, X., 2018. Mn_3O_4 nanocube: an fficient electrocatalyst toward artificial N_2 fixation to NH_3. Small 14. https://doi.org/10.1002/smll.201803111

Wu, Y., Cao, S., Hou, J., Li, Z., Zhang, B., Zhai, P., Zhang, Y., Sun, L., 2020. Rational design of nanocatalysts with nonmetal species modification for electrochemical CO_2 reduction. Adv. Energy Mater. 10, 1–31. https://doi.org/10.1002/aenm.202000588

Xia, Z., Freeman, M., Zhang, D., Yang, B., Lei, L., Li, Z., Hou, Y., 2018. Highly selective electrochemical conversion of CO_2 to HCOOH on dendritic indium foams. ChemElectroChem 5, 253–259. https://doi.org/10.1002/celc.201700935

Xiang, D., Magana, D., Dyer, R.B., 2014. CO_2 reduction catalyzed by mercaptopteridine on glassy carbon. J. Am. Chem. Soc. 136, 14007–14010. https://doi.org/10.1021/ja5081103

Xiang, X., Wang, Z., Shi, X., Fan, M., Sun, X., 2018. Ammonia synthesis from electrocatalytic N_2 reduction under ambient conditions by Fe_2O_3 nanorods. ChemCatChem 10, 4530–4535. https://doi.org/10.1002/cctc.201801208

Xie, X., Economides, M.J., 2009. The impact of carbon geological sequestration. J. Nat. Gas Sci. Eng. 1, 103–111. https://doi.org/10.1016/j.jngse.2009.06.002

Xiong, R., Wang, Y., Zhang, X., Lu, C., 2014. Facile synthesis of magnetic nanocomposites of cellulose@ultrasmall iron oxide nanoparticles for water treatment. RSC Adv. 4, 22632–22641. https://doi.org/10.1039/C4RA01397B

Xu, L., Zhu, Z., Sun, D.W., 2021. Bioinspired nanomodification strategies: Moving from chemical-based agrosystems to sustainable agriculture. ACS Nano 15, 12655–12686. https://doi.org/10.1021/acsnano.1c03948

Xu, Z., Yang, Z.-L., 2017. Relative impacts of increased greenhouse gas concentrations and land cover change on the surface climate in arid and semi-arid regions of china. Clim. Change 144, 491–503. https://doi.org/10.1007/s10584-017-2025-x

Yamasaki, A., 2003. An overview of CO_2 mitigation options for global warming-emphasizing CO_2 sequestration options. J. Chem. Eng. Japan 36, 361–375. https://doi.org/10.1252/jcej.36.361

Yang, D.R., Liu, L., Zhang, Q., Shi, Y., Zhou, Y., Liu, C., Wang, F. Bin, Xia, X.H., 2020. Importance of Au nanostructures in CO_2 electrochemical reduction reaction. Sci. Bull. 65, 796–802. https://doi.org/10.1016/j.scib.2020.01.015

Yang, Y., Li, F., 2021. Reactor design for electrochemical CO_2 conversion toward large-scale applications. Curr. Opin. Green Sustain. Chem. 27, 100419. https://doi.org/10.1016/j.cogsc.2020.100419

Yang, Y., Matsubara, S., Xiong, L., Hayakawa, T., Nogami, M., 2007. Solvothermal synthesis of multiple shapes of silver nanoparticles and their SERS properties. J. Phys. Chem. C 111, 9095–9104. https://doi.org/10.1021/jp068859b

Yang, Z., Yang, C., Han, J., Zhao, W., Shao, S., Li, S., Gao, H., Xie, H., Zhang, X., 2021. Boosting electrochemical CO_2 reduction to formate using SnO_2/graphene oxide with amide linkages. J. Mater. Chem. A 9, 19681–19686. https://doi.org/10.1039/d1ta02780h

Zaza, L., Rossi, K., Buonsanti, R., 2022. Well-defined copper-based nanocatalysts for selective electrochemical reduction of CO_2 to C_2 products. ACS Energy Lett. 7,

1284–1291. https://doi.org/10.1021/acsenergylett.2c00035

Zhang, B., Wu, Y., Zhai, P., Wang, C., Sun, L., Hou, J., 2022. Rational design of bismuth-based catalysts for electrochemical CO_2 reduction. Chinese J. Catal. 43, 3062–3088. https://doi.org/10.1016/s1872-2067(22)64132-9

Zhang, J., Gao, L., 2004. Synthesis and characterization of nanocrystalline tin oxide by sol-gel method. J. Solid State Chem. 177, 1425–1430. https://doi.org/10.1016/j.jssc.2003.11.024

Zhang, L., Ren, X., Luo, Y., Shi, X., Asiri, A.M., Li, T., Sun, X., 2018. Ambient NH_3 synthesis via electrochemical reduction of N_2 over cubic sub-micron SnO_2 particles. Chem. Commun. 54, 12966–12969. https://doi.org/10.1039/c8cc06524a

Zhang, Q., Xu, W., Xu, J., Liu, Y., Zhang, J., 2018. High performing and cost-effective metal/metal oxide/metal alloy catalysts/electrodes for low temperature CO_2 electroreduction. Catal. Today 318, 15–22. https://doi.org/10.1016/j.cattod.2018.03.029

Zhang, W., Hu, Y., Ma, L., Zhu, G., Zhao, P., Xue, X., Chen, R., Yang, S., Ma, J., Liu, J., Jin, Z., 2018. Liquid-phase exfoliated ultrathin Bi nanosheets: Uncovering the origins of enhanced electrocatalytic CO_2 reduction on two-dimensional metal nanostructure. Nano Energy 53, 808–816. https://doi.org/10.1016/j.nanoen.2018.09.053

Zhang, X., Hou, X., Zhang, Q., Cai, Y., Liu, Y., Qiao, J., 2018. Polyethylene glycol induced reconstructing Bi nanoparticle size for stabilized CO_2 electroreduction to formate. J. Catal. 365, 63–70. https://doi.org/10.1016/j.jcat.2018.06.019

Zhang, X., Lei, T., Liu, Y., Qiao, J., 2017. Enhancing CO_2 electrolysis to formate on facilely synthesized Bi catalysts at low overpotential. Appl. Catal. B Environ. 218, 46–50. https://doi.org/10.1016/j.apcatb.2017.06.032

Zhang, X., Wu, T., Wang, H., Zhao, R., Chen, H., Wang, T., Wei, P., Luo, Y., Zhang, Y., Sun, X., 2019. Boron nanosheet: An elemental two-dimensional (2D) material for ambient electrocatalytic N_2-to-NH_3 fixation in neutral media. ACS Catal. 9, 4609–4615. https://doi.org/10.1021/acscatal.8b05134

Zhang, Y., Li, F., Zhang, X., Williams, T., Easton, C.D., Bond, A.M., Zhang, J., 2018. Electrochemical reduction of CO_2 on defect-rich Bi derived from Bi_2S_3 with enhanced formate selectivity. J. Mater. Chem. A 6, 4714–4720.

https://doi.org/10.1039/C8TA00023A

Zhang, Y., Zhu, M., Wei, Q., Wang, M., 2022. Removing chlorobenzene via the synergistic effects of adsorption and catalytic oxidation over activated carbon fiber loaded with transition metal oxides. Atmosphere (Basel). 13. https://doi.org/10.3390/atmos13122074

Zhang, Z., Chi, M., Veith, G.M., Zhang, P., Lutterman, D.A., Rosenthal, J., Overbury, S.H., Dai, S., Zhu, H., 2016. Rational design of Bi nanoparticles for efficient electrochemical CO_2 reduction: the elucidation of size and surface condition effects. ACS Catal. 6, 6255–6264. https://doi.org/10.1021/acscatal.6b01297

Zhang, Z., Zhu, J., Chen, S., Sun, W., Wang, D., 2022. Liquid fluxional ga single atom catalysts for efficient electrochemical CO_2 reduction. Angew. Chemie - Int. Ed. https://doi.org/10.1002/anie.202215136

Zhao, C., Wang, J., 2016. Electrochemical reduction of CO_2 to formate in aqueous solution using electro-deposited Sn catalysts. Chem. Eng. J. 293, 161–170. https://doi.org/10.1016/j.cej.2016.02.084

Zhao, X., Hu, G., Chen, G.F., Zhang, H., Zhang, S., Wang, H., 2021. Comprehensive understanding of the thriving ambient electrochemical nitrogen reduction reaction. Adv. Mater. 33, 1–46. https://doi.org/10.1002/adma.202007650

Zhao, X.H., Chen, Q.S., Zhuo, D.H., Lu, J., Xu, Z.N., Wang, C.M., Tang, J.X., Sun, S.G., Guo, G.C., 2021. Oxygen vacancies enriched Bi based catalysts for enhancing electrocatalytic CO_2 reduction to formate. Electrochim. Acta 367, 137478. https://doi.org/10.1016/j.electacta.2020.137478

Zhong, H., Qiu, Y., Li, X., Pan, L., Zhang, H., 2021. Ordered cone-structured tin directly grown on carbon paper as efficient electrocatalyst for CO_2 electrochemical reduction to formate. J. Energy Chem. 55, 236–243. https://doi.org/10.1016/j.jechem.2020.06.058

Zhou, Y., Che, F., Liu, M., Zou, C., Liang, Z., De Luna, P., Yuan, H., Li, J., Wang, Z., Xie, H., Li, H., Chen, P., Bladt, E., Quintero-Bermudez, R., Sham, T.-K., Bals, S., Hofkens, J., Sinton, D., Chen, G., Sargent, E.H., 2018. Dopant-induced electron localization drives CO_2 reduction to C_2 hydrocarbons. Nat. Chem. 10, 974–980. https://doi.org/10.1038/s41557-018-0092-x

Zhu, W., Zhang, L., Yang, P., Hu, C., Luo, Z., Chang, X., Zhao, Z., Gong, J., 2018. Low-coordinated edge sites on ultrathin palladium nanosheets boost carbon

dioxide electroreduction performance. Angew. Chemie Int. Ed. 57, 11544–11548. https://doi.org/10.1002/anie.201806432

Zhu, X., Gupta, K., Bersani, M., Darr, J.A., Shearing, P.R., Brett, D.J.L., 2018. Electrochemical reduction of carbon dioxide on copper-based nanocatalysts using the rotating ring-disc electrode. Electrochim. Acta 283, 1037–1044. https://doi.org/10.1016/j.electacta.2018.07.025

This page is intentionally left blank

CHAPTER 2

Materials and Methodology

This chapter describes the experimental details including the synthesis processes of Cu_2O, SnO_2, Bi_2S_3, and Co_3O_4 NPs, preparation of modified carbon paper electrodes, experimentation on electrochemical CO_2 reduction reaction (ECO_2RR) and electrochemical N_2 reduction reaction (ENRR). This chapter also describes the reagents details, the equipment utilized for characterizing and analyzing the catalysts, and the target analytes. Any particular modification or deviation from what is discussed in this chapter is indicated in the relevant Section(s)/Chapter(s).

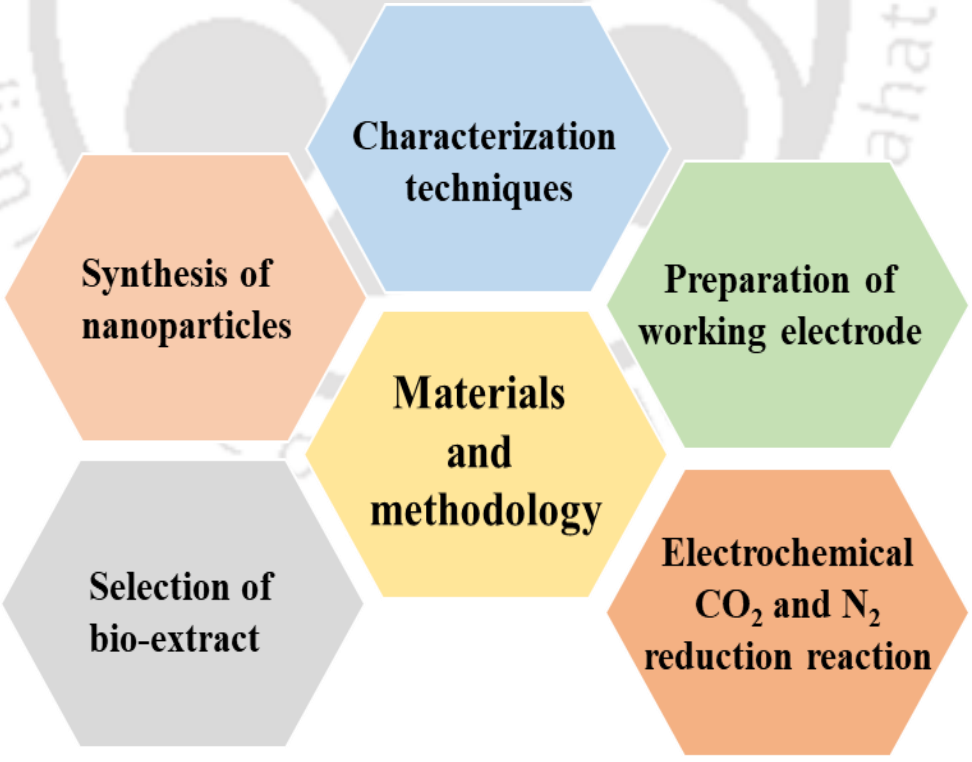

2.1 Reagents and chemicals

2.1.1 Analytical reagents

Chemicals, reagents, and materials (Table 2.1) were used as received without further purification unless otherwise mentioned. All the solutions were prepared using deionized water (resistivity: 18.2 MΩ.cm) from Millipore water synthesis unit (Elix-3, USA).

Table 2.1. List of chemicals and reagents used in this doctoral work.

Reagents/chemicals	Purity	Grade	CAS/ Catalogue no.	Make
Copper(II) sulphate pentahydrate [$CuSO_4.5H_2O$]	99.0% (w/w)	ACS	7758-99-8	Merck, India
Ethanol (C_2H_5OH)	98.0% (v/v)	ACS	64-17-5	
Sodium hydroxide [NaOH] pellets	99.0% (w/w)	AR	1310-73-2	
Sodium sulphate [Na_2SO_4]	>99.0%	EMSURE®	7757-82-6	
Potassium bromide [KBr]	99.5% (w/w	GR	7758-02-3	
Barium sulphate [$BaSO_4$]	99.9%	---	7727-43-7	
Potassium hydrogen carbonate [$KHCO_3$]	99.0% (w/w)	EMPLURA®	298-14-6	
2-Propanol [$(CH_3)_2CHOH$]	99.9%	HPLC	67-63-0	
Bismuth nitrate [$Bi(NO_3)_3{\cdot}5H_2O$]	99.9%	EMSURE®	10035-06-0	
polyethylene glycol 6000 [$HO(C_2H_4O)_nH$]	---	Molecular Biology	25322-68-3	
Sulphuric acid [H_2SO_4]	98.0%	AR	7664-93-9	
Thiourea [CH_4N_2S]	>99.0%	ACS	62-56-6	
Co(II) nitrate hexahydrate [$Co(NO_3)_2.6H_2O$]	>99.0%	AR	10026-22-9	
Salicylic acid [$C_7H_6O_3$]	>99.0%	ACS	69-72-7	

Sodium citrate tribasic dehydrate [HOC(COONa)(CH_2 COONa)$_2$·2H_2O]	>99.0%	ACS	6132-04-3	
Ammonium chloride [NH_4Cl]	>99.8%	EMSURE® ACS	12125-02-9	
Sodium hypochlorite solution [NaOCl]	6-14% active chlorine	EMPLURA®	7681-52-9	
Nafion® D-521 dispersion	5% (w/w) in water and 1-propanol	---	31175-20-9	Alfa Aesar, USA
Toray carbon paper [TCP]	---	---	TCP, TGP-H-60	
Nafion N-115 proton exchange membrane (>0.90 meq g^{-1} exchange capacity)	---	---	31175-20-9	
Tin(IV) chloride pentahydrate [$SnCl_4$·5H_2O]	>98.0%	---	10026-06-9	Acros Organics, India
Potassium formate (HCO_2K)	99.0%	Reagent Plus®	590-29-4	Sigma Aldrich, USA
Deuterium oxide (D_2O)	99.9 atom % D	---	7789-20-0	
Gallic acid ($C_7H_6O_5$)	>99.0%	ACS	149-91-7	
Sodium nitroferricyanide dehydrate [$C_5FeN_6Na_2O$·2H_2O]	>99.0%	ACS	13755-38-9	
Nitrogen (N_2)	99.9%	---	---	Assam Air Products Pvt. Ltd., India.
Carbon dioxide (CO_2)	99.9%	---	---	
Carbon coated TEM grid 300 mesh (PK/25)	---	---	9012	EMS/ProSciTech, Australia
Conductive double sided carbon tape, 8 mm	---	---	50-285-81	Fisher Scientific, US

2.2 Biomass and bio-extract

2.2.1 Selection of *Sechium edule* fruit extract

Fresh *Sechium edule* fruit was purchased from the market complex situated at Indian Institute of Technology Guwahati, Assam, India. The fruit contains bioanalytes

such as alkaloids, flavonoids, phenols, and polyphenols; gallic acid, caffeic acid and isoquercetin (Andrés et al., 2018). The fruit is also enriched with ascorbic acid (294 mg kg^{-1} dry fruit) (Chelli and Golder, 2018). The reducing property of bio-extract simultaneously utilized as metal ion reduction and capping of metal nanoparticles. In recent years, synthesis of metal nanoparticles, such as Ag, Pt, and Co NPs (Chelli and Golder, 2018), and metal oxides, such as Co_3O_4 (Das and Golder, 2017) and NiO NPs (Das and Golder, 2018) in my research group provided the foundation of selecting *Sechium edule* fruit for the synthesis of Cu_2O nanoparticles NPs (Cu_2O(bio) NPs), SnO_2 nanoparticles (SnO_2(bio) NPs), Bi_2S_3 nanorods (Bi_2S_3 NRs) for ECO_2RR, in the present work.

Additionally, taking into consideration that the ability of bio-analytes such as ascorbic acid, gallic acid, caffeic acid and isoquercetin, etc. to act as reducing/capping agents, present in the fruit extract, we have further selected commercially available gallic acid to synthesize Co_3O_4 nanodiscs (Co_3O_4 NDs) for ENRR. Table 2.2 shows the chemical compositions of different parts of *Sechium edule* fruit.

Table 2.2. Chemical composition of different parts of *Sechium edule* fruit (Chelli V. R., 2017, Bio-inspired route of metal nanoparticles synthesis and photocatalysis doping (PhD thesis, Indian Institute of Technology Guwahati).

Composition	**Leaf**	**Fruit**	**Root**
Ascorbic acid, mg	16	29.8	19
Flavonoid content, g	35	19.3	30.5
Energy, cal	60	26-30	79
Protein, g	4	0.9-1.1	2
Carbohydrates, g	4.7	3.5-8.4	17.8
Phosphorus, µg	108	20-27	34
Calcium, mg	21.7-69.5	6.1-19	6.1-17.5
Nitrogen, g	0.49-0.778	0.95-0.156	0.332
Thiamine, mg	0.043-0.0119	0.03-0.33	0.041-0.08
Riboflovin, mg	0.124-0.208	0.03-0.37	0.05-0.028
Niacin, mg	0.919-1.19	0.35-1.1	0.7-1.04

2.2.2 Preparation of *Sechium edule* fruit extract

The fruit was rigorously washed in running water followed by DI water. After removing the peel and seed, an amount of 125 g of the fruit was sliced into small pieces (~5 mm × 5 mm × 5 mm) (Figure 2.1). The fruit-pieces were then added into 500 mL DI water and kept on stirring at 350 rpm on a magnetic stirrer at 90°C temperature for about 12 h. The extract was then kept to cool at room temperature and filtered using a 0.2 µm filter paper. The fresh, nearly colourless and clear solution was obtained which was used every time for the synthesis of various nanoparticles. The synthesis of nanoparticles was performed during May-July month to minimize the effect of seasonal changes in the chemical compositions of *Sechium edule*. Further, a fixed ascorbic acid equivalent (AAE) (Senguttuvan et al., 2014) of 2 mg L^{-1} was used for each batch of experiment by diluting the concentrated bio-extract.

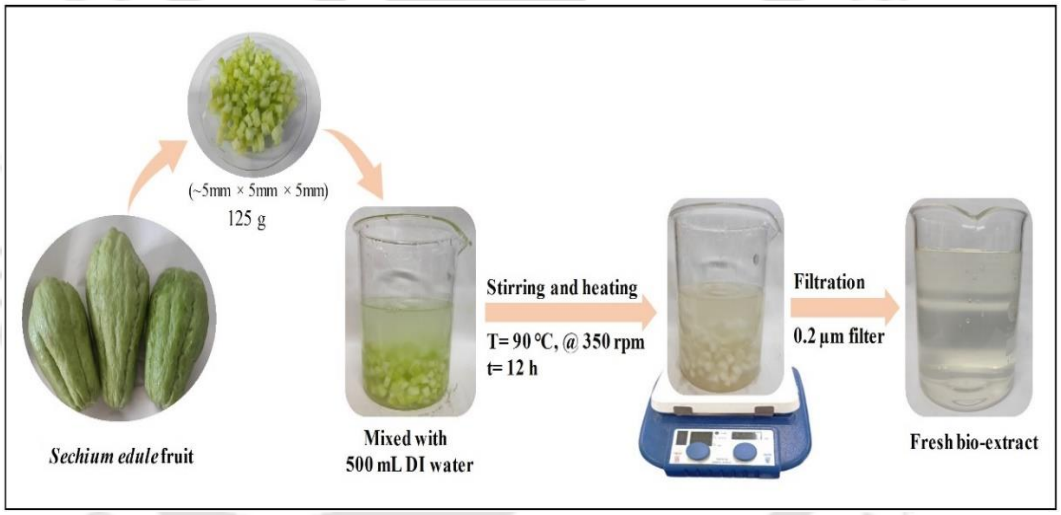

Figure 2.1. Preparation of bio-extract.

2.2.3 DPPH assay of bio-extract

For the 1,1-diphenyl-2-picrylhydrazyl (DPPH) assay, a volume of 0.2 mL of bio-extract was mixed with 1.8 mL of 50 µM DPPH solution followed by an incubation time for 30 min. The absorbance was measured at 592 nm (λ_{max}) in the UV-vis spectrophotometer. Furthermore, 10-50 mg L^{-1} of ascorbic acid was used instead of bio-extract and the absorbance values were fitted linearly to obtain the calibration graph (Figure 2.2) and the calibration equation. The ascorbic acid content in bio-extract was calculated by using the calibration equation expressed as AAE, mg L^{-1} (Senguttuvan et al., 2014).

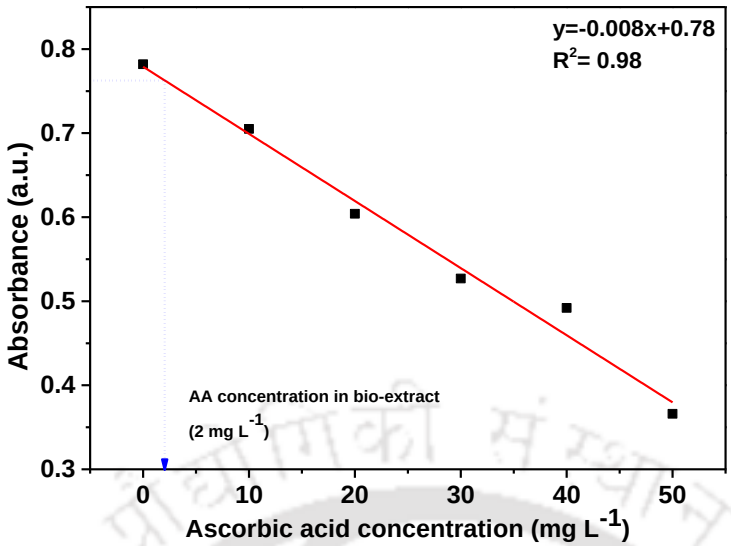

Figure 2.2. Determination of ascorbic acid equivalent (AAE) of prepared *Sechium edule* fruit extract using DPPH assay.

2.3 Methodologies of electrocatalysts synthesis

2.3.1 Bioinspired synthesis of Cu_2O(bio) NPs

2.3.1.1 Using Sechium edule fruit extract

For the synthesis of Cu_2O(bio) NPs, 20 mM $CuSO_4 \cdot 5H_2O$ solution and freshly prepared bio-extract was mixed in 1:1 (v/v) ratio and kept on stirring at 350 rpm. The initial pH of the mixture was noted as 4.06, which was adjusted to 12 by dropwise addition of 2 M NaOH solution. The colour of the mixture was changed to dark blue which was turned into the pale green after 2 h and yellow after 4 h (Figure 2.3). The colour of the solution was dark orange after about 6 h which is indicative of the formation of Cu_2O(bio) NPs (Salek et al., 2015). Formations of Cu-complexes/Cu_2O(bio) NPs with the progress of reaction is also shown in Figure 2.3 (bottom panel). The resulting solution was then centrifuged at 4900 RCF (2−16 P, Sigma, Germany) for 10 min. The residue was collected and washed three times with DI water followed by water-ethanol mixture (1:1 v/v). The final Cu_2O(bio) NPs were obtained after overnight drying in a hot air oven at 100°C.

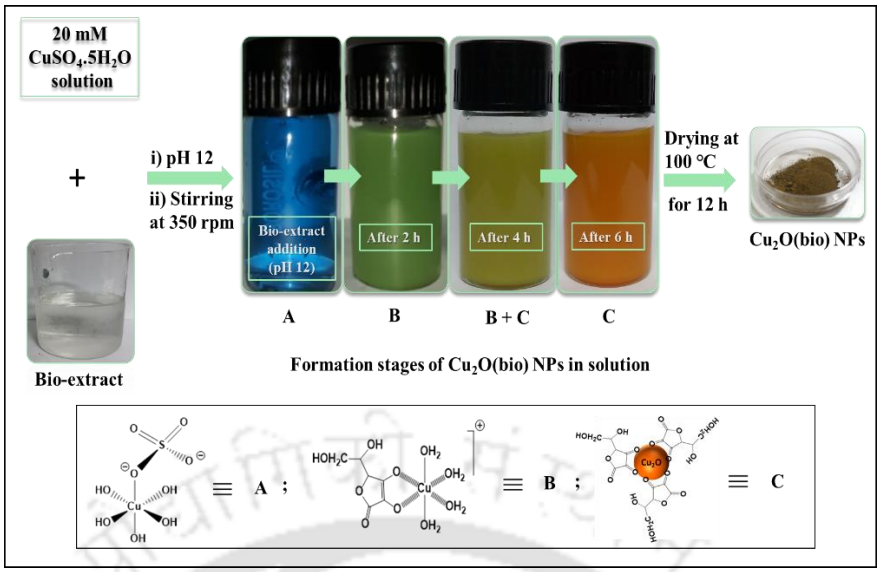

Figure 2.3. Steps of formation of Cu_2O(bio) NPs using bioactive compounds (bottom panel shows formations of Cu-complexes/Cu_2O(bio) NPs with the progress of reaction).

2.3.1.2 Using commercially available ascorbic acid (AA)

Synthesis of Cu_2O NPs using AA (Cu_2O-AA NPs) was done by applying the method described as: typically, 0.06 g of $CuSO_4 \cdot 5H_2O$ and 0.2 g NaOH were separately dissolved into 100 mL and 20 mL DI water, respectively. After mixing, 15 mL solution containing 0.39 g AA was poured into the mixture. After 10 min, the change in colour of the solution from deep blue to orange indicates the formation of Cu_2O-AA NPs. It was then dried in a hot air oven for overnight to get Cu_2O-AA NPs powder.

2.3.2 Bioinspired synthesis of SnO_2 NPs

Typically, 50 mM $SnCl_4 \cdot 5H_2O$ precursor solution was sonicated for 20 min before mixing with the bio-extract (3:1 v/v). pH of the solution was measured to be 4.5. The mixture was then stirred at 400 rpm at 75°C for 18 h. Nanoparticles thus formed are collected after centrifugation for 10 min at 5000 RCF followed by washing with (1:1) v/v ethanol-deionized water mixture three times and dried in a hot-air oven at 80°C for 12 h. This sample was designated as SnO_2(bio) NPs. SnO_2(bio) NPs sample was divided in 03 parts, and it was then calcined at 380, 550, and 800°C for 2 h. These samples were designated as SnO_2(bio)- 380 NPs, SnO_2(bio)- 550 NPs,

and SnO_2(bio)- 800 NPs, respectively (Figure 2.4). The dried samples were then collected and stored in air-tight containers for further physicochemical characterizations and electrochemical applications.

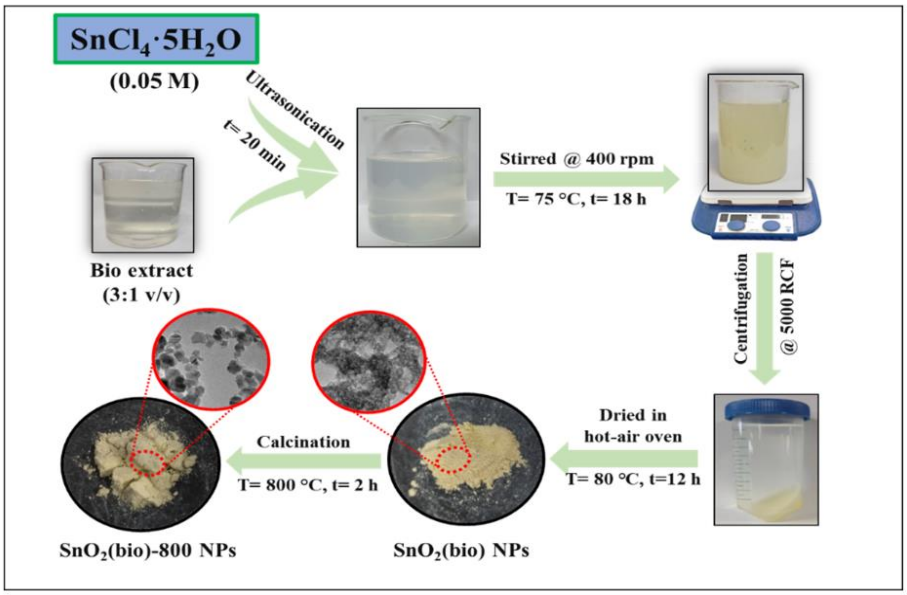

Figure 2.4. Different steps for SnO_2 NPs synthesis using *Sechium edule* fruit extract.

2.3.3 Bioinspired synthesis of template free 1D Bi_2S_3 NRs

2.3.3.1 Synthesis of Bi_2S_3-NRs(bio)

An amount of 0.125 M $Bi(NO_3)_3 \cdot 5H_2O$ was ultrasonicated for 20 min and mixed with bio-extract (3:1 v/v), and 0.71 g of thiourea. pH of the reaction mixture was maintained at 3 by using 1 M HNO_3 solution. The mixture was then stirred (400 rpm) on a magnetic stirrer at 75°C for 18 h. The suspension was then centrifuged at 6000 RCF. The residue was collected and dispersed in 1:1 (v/v) water:ethanol solution. The process was repeated three times. The dark-brown precipitate obtained, was dried in a hot air oven (Universal Hot Air Oven, Navyug, Kolkata, India) at 80°C for 5 h. The powder material was marked as Bi_2S_3-NRs(bio) (Figure 2.5).

Similarly, three more samples were prepared using the bio-extract: i) an equal proportion of precursor and bio-extract (125 g in 500 mL) at pH 3, named as Bi_2S_3-NRs-(bio0); ii) an equal proportion of precursor and bio-extract (150 g in 200 mL) at pH 3, denoted as Bi_2S_3NRs(bio1); and iii) conditions same as in Bi_2S_3-NRs(bio), except the pH, at 9. This sample is marked as Bi_2S_3-NRs(bio2).

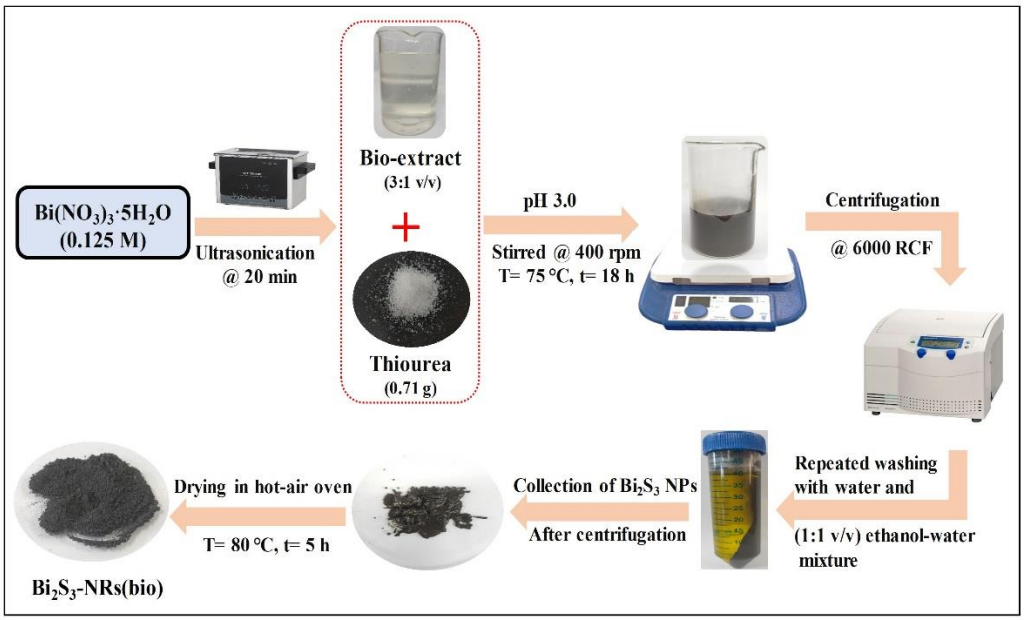

Figure 2.5. Steps involved in synthesizing Bi_2S_3NRs(bio) using *Sechium edule* fruit extract.

2.3.3.2 Synthesis of Bi_2S_3-NRs(control)

A control experiment was also carried out using the same volume of DI water instead of bio-extract keeping other conditions unaltered. The material formed was marked as Bi_2S_3-NRs(control). The dried materials were then powdered using a mortar pestle and stored in an air-sealed container for characterization and electrocatalytic applications.

2.3.4 Synthesis procedure of Co_3O_4 NDs using gallic acid

In a typical process, 10 mM of $Co(NO_3)_2 \cdot 6H_2O$ precursor solution was mixed with an equimolar gallic acid solution. The pH of the solution was maintained at 11 with the dropwise addition of 3 M NaOH solution. After that, the green suspended solution was moved to a Teflon-coated steel autoclave of 150 mL capacity. The temperature of the autoclave was maintained at 180°C for 48 h. It was then cooled to room temperature prior to the collection of residue. It was thoroughly washed using deionized water and subsequently washed with a mixture of water and ethanol (1:1 v/v), and dried in a hot air oven at 80°C for 12 h. The dried residue was calcined at 700°C for 6 h (Das and Golder, 2017) (Figure 2.6).

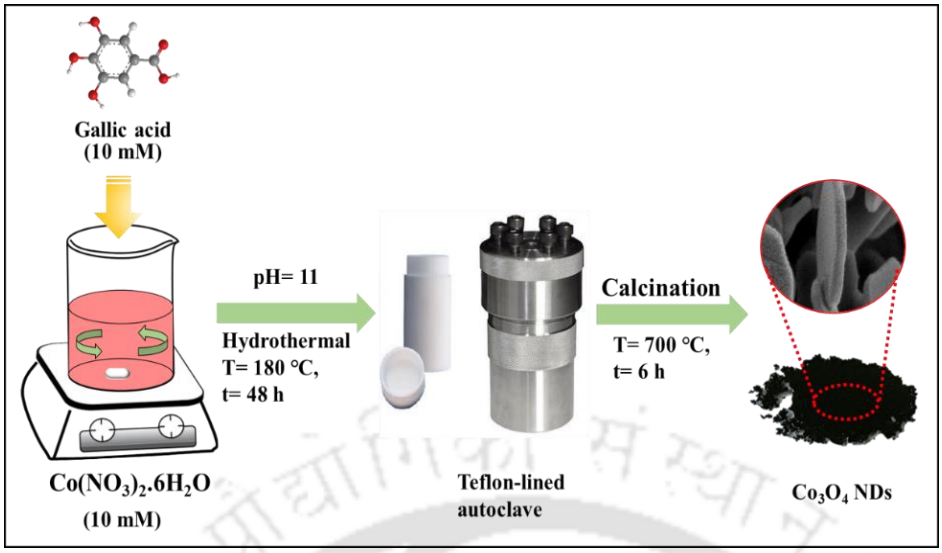

Figure 2.6. Different steps involved in Co_3O_4 NDs synthesis.

2.4 Characterizations of electrocatalysts

2.4.1 UV-vis spectroscopy

A UV-Vis spectrophotometer from Shimadzu, Japan (UV-2600 with ISR 2600 attachment) was used to record the optical absorbance spectra of Cu_2O(bio), SnO_2, Bi_2S_3, and Co_3O_4 nanomaterials synthesized under different experimental conditions. Depending on the experiments, the incident light's wavelength was scanned between 200 and 700 nm to record the absorbance. For this analysis, a small amount of $BaSO_4$ powder was pilled followed by spreading the powder sample into a thin uniform layer, where $BaSO_4$ was used as a standard.

2.4.2 High-resolution mass spectrometry

Mass spectrometry (MS) is an analytical technique used to elucidate the chemical structure of various molecules. In the initial step of the analysis, the sample undergoes gas phase ionization by the electron ionization process and produces fragmented ions. The mass spectrometer differentiates the fragmented ions based on their mass-to-charge (m/z) ratio and measures their abundance proportionally. Finally, mass spectrum of the molecule is represented by a graphical plot of ion abundance against the m/z. This study involved recording the mass spectra of liquid samples (Dash, 2021).

Mass spectroscopy studies of the *Sechium edule* fruit extracts were conducted in ESI negative ion mode, using a mass spectrometer (Q-Tof Premier, Waters, USA). For this analysis, bio-extract was mixed with HPLC-grade methanol and filtered with a 0.2 μm membrane filter before the analysis. The active components present in *Sechium edule* fruit extract were analyzed using this technique, and the reaction mechanism of Cu_2O(bio) NPs formation was proposed (Chapter 3).

2.4.3 X-ray diffraction

The phase and crystallinity of the synthesized nanoparticles were investigated using X-ray diffraction (XRD) analysis. The basic principle of X-ray diffraction involves the constructive interference of monochromatic X-rays with a sample of crystalline material. X-ray diffraction involves generating a beam of X-rays using a cathode ray tube, which is then filtered to monochromatic wavelength, collimated to concentrate, and targeted at the sample. The diffraction peaks are obtained only when Bragg's law is satisfied with the Equation 2.1, through constructive interference from the angle of diffraction with the spacing between planes of atoms in the crystal lattice.

$$n\lambda = 2d \sin\theta \quad (2.1)$$

Where λ is the wavelength of the incident X-rays, d is the spacing between the planes of atoms in the crystal lattice, and θ is Bragg's angle, also known as the angle of incidence. The diffracted X-rays are then detected, processed and recorded. The bioinspired nanoparticles were characterized by employing this phenomenon, which aids in identifying the material present in the sample. Briefly, 20 mg of dried material was inserted into the sample holder, and the XRD patterns between 10 and 90° angle were then recorded. The X-ray diffraction was studied by acquiring the diffractogram (SmartLab9KW, Rigaku, Japan) at λ = 0.15406 nm of CuKα radiation at a 20° min^{-1} scan rate.

2.4.4 Field emission scanning electron microscopy

Surface morphology and elemental composition of the synthesized NPs were analyzed using a Field emission scanning electron microscope (FESEM). This microscopic technique is used to visualize topographic details on a surface at the nanometer scale. A high-energy electron beam is generated by an electron source, which is heated to create thermionic emission of electrons. FESEM can magnify the

samples beyond the 10 KX range. A carbon tape kept on a metal stub, is used as a substrate for mounting the sample during the analysis. In this work, FESEM (Sigma, Zeiss, Germany) was used to investigate the morphology of the synthesized nanoparticles, and the nanoparticles coated on the working electrode surface. A small piece of carbon tape was used to mount the sample of interest for this analysis.

2.4.5 Field emission transmission electron microscopy

Field emission transmission electron microscopy (FETEM) is a type of imaging technique that involves passing a high-energy electron beam through an extremely thin sample. The resulting images are produced based on the transmission and attenuation of electrons and are then magnified for analysis on the micro- and nano-levels. To prepare the sample, approximately 1 mg of it was dispersed in 1 mL solution of ethanol and water (1:1 v/v). The sample was then dropped cast over a carbon-coated copper- TEM grid. Finally, the TEM grid containing the sample was dried in an oven for analysis (Make: JEOL, model: JEM 21006 Tokyo, Japan). The FETEM analysis also provided the details of the nanoparticles about their fringe width, as well as their crystallinity, which was determined from SAED (Selected Area Electron Diffraction) data.

2.4.6 Energy-dispersive X-ray spectroscopy

Energy-dispersive X-ray spectroscopy (EDX) is an analytical technique employed for the elemental analysis or chemical composition of the sample. In this technique, an X-ray is produced by directing an electron beam onto a specimen. The X-rays produced are determined by the unique characteristics and composition of the elements present in the sample. The method of sample preparation is comparable to that used in FESEM/FETEM, depending on the parent equipment employed. In this study, EDX spectra, elemental mapping and the percentage elemental compositions of the synthesized nanoparticles and the modified working electrodes were examined. The EDX spectra of the synthesized nanoparticles were acquired either using FESEM (Make: Zeiss, model: Sigma, Jena, Germany) or FETEM (Make: JEOL, model: JEM 2100F, Tokyo, Japan) (Dash, 2021).

2.4.7 Thermogravimetric analysis

The thermal stability of synthesized NPs and traces of bio-analytes present onto NPs were analyzed by thermogravimetric analysis (TG 209 F1, Netzsch, Germany). A 10 mg sample was used for the analysis at the temperature range of 25 to 900°C. The analysis was conducted using a N_2 flow rate of 20 mL min^{-1} and a heating rate of 10°C min^{-1}.

2.4.8 BET surface area analysis

The specific surface area of NPs was determined using a BET analyzer (SA 3100, Beckman Coulter, Switzerland) by the N_2 adsorption-desorption isotherm. The sample was degassed in N_2 at 150°C for 4 h before the analysis. A heating rate of 10°C min^{-1} with an N_2 flow rate of 20 mL min^{-1} was employed.

2.4.9 X-ray photon spectroscopy analysis

X-ray photoelectron spectroscopy (XPS) is a quantitative technique of surface analysis to determine the elemental compositions and chemical state of natural and synthetic materials. This information is particularly useful for the analysis of thin films, coatings, and surfaces of materials used in a wide range of applications, including catalysis, semiconductors, and electronics.

The basic principle of XPS involves the use of a monochromatic X-ray beam to eject photoelectrons from the surface of a material. These photoelectrons are then analyzed to provide information about the atomic composition and chemical state of the materials.

Typically, an X-ray source like a monochromator or an X-ray tube produces the X-ray beam. The beam is then directed at the sample and the interaction between the X-rays and the electrons in the material results in the ejection of photoelectrons from the top few nanometers of the material surface.

A detector then analyses the energy of the expelled photoelectrons to create an energy spectrum. By analysing the energy of the photoelectrons, the chemical state of the elements present in the sample is determined.

In this work, the oxidation states of metal ions in the synthesized nanomaterials (Cu_2O(bio) NPs, SnO_2 NPs, Bi_2S_3 NRs, and Co_3O_4 NDs) were determined using X-ray photoelectron spectroscopy (XPS) (ESCALAB Xi+, Thermo

Fisher Scientific Pvt. Ltd., UK) equipped with a monochromatic X-ray source of Al Kα (1486.6 eV). The generated XPS spectra were processed using XPSPEAK 4.1 software.

2.4.10 Fabrication of working electrode

For the electrode fabrication, an amount of 4 mg of catalysts were dispersed in a 100 µL mixture of Nafion dispersion (5% w/w) and 2-propanol (IPA) solution (1:5 ratio). After 30 min of ultrasonication, the catalyst ink was drop-coated on both sides of 2 × 1 cm^2 TCP (TGP-H-60) and left for 12 h to evaporate the remaining solvent (Figure 2.7). This led to the catalyst loading of about 1 mg cm^{-2} on the TCP electrode. The modified electrodes were then used for ECO_2RR and ENRR.

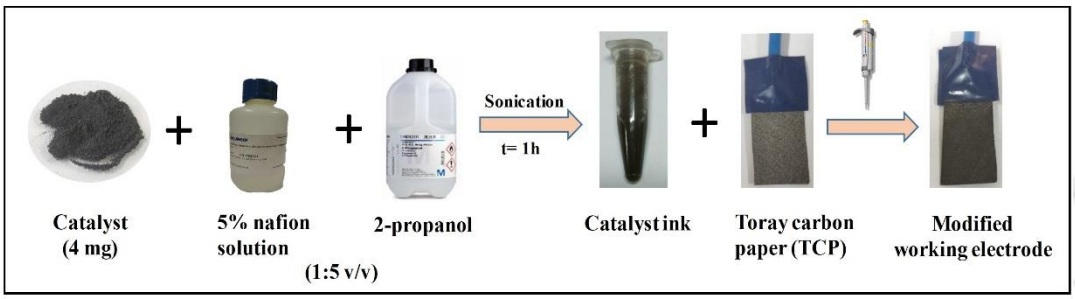

Figure 2.7. Different steps for electrode fabrication.

2.5 Electrochemical reactor set-up for CO_2 reduction reaction

Electrochemical experiments were conducted in an H-cell glass reactor (Figure 2.8). Two compartments of the reactor were separated by a proton exchange membrane (Nafion N-115) having an exchange capacity of >0.90 meq g^{-1}. Both the cells of the reactor were filled with 100 mL 0.5 M $KHCO_3$ electrolyte. The electrolyte solution was first purged with N_2 for 15 min to free the electrolyte solution from dissolved oxygen. After that, CO_2 at a flow rate of 100 mL min^{-1} was bubbled continuously starting from 30 min before the ECO_2RR for its pre-saturation. pH of the electrolyte solution was measured to be ~7 after CO_2 saturation. The CO_2 flow rate was maintained at 40 mL min^{-1} using a rotameter. A platinum (Pt) wire (ϕ 1 mm) and a silver/silver chloride (Ag/AgCl) (3 M KCl) were mounted as the counter (CE), and reference electrodes (RE), respectively. Catalyst-coated modified carbon paper electrodes were employed as the working electrode (WE).

The electrochemical measurements were carried out by using a high-performance Potentiostat/Galvanostat (AUTOLAB 302 N, Metrohm Autolab B.V., Netherlands), and the data acquisition were done using NOVA 1.11 software which was supplied by the manufacturer. The cyclic voltammetry (CV) sweep both in inert condition (with N_2 purging) and CO_2-saturated aqueous solution containing 0.5 M $KHCO_3$, were conducted at a scan rate of 50 mV s^{-1} in the applied potential range of 0 to −2 V vs. Ag/AgCl. The chronoamperometric study of ECO_2RR was performed at different potentials from −1.55 to −1.80 V vs. Ag/AgCl for 3600 s at atmospheric pressure and room temperature.

The possible electrochemical reactions in the H-type reactor are as follows (Rumayor et al., 2018).

Cathodic reaction: $CO_2 + H_2O + 2e^- \rightarrow HCOO^- + HO^-$ (2.2)

$2H_2O + 2e^- \rightarrow H_2 + HO^-$ (2.3)

Anodic reaction: $H_2O \rightarrow 2H^+ + 2e^- + 1/2\ O_2$ (2.4)

Overall reaction: $CO_2 + 2H_2O \rightarrow HCOOH + O_2 + H_2$ (2.5)

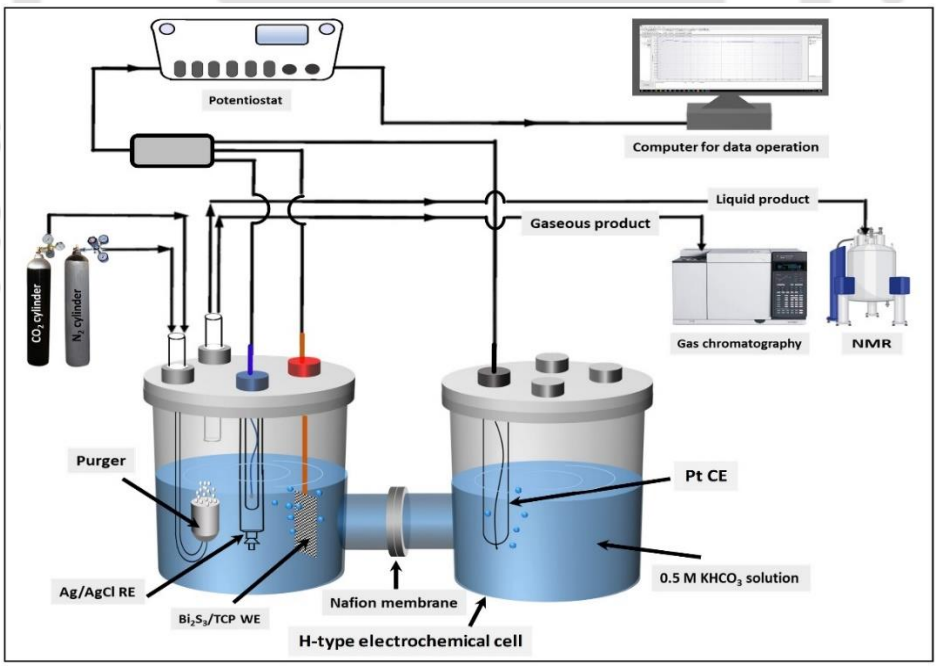

Figure 2.8. H-type reactor for electrochemical CO_2 reduction reaction.

2.6 Electrochemical reactor set-up for N_2 reduction reaction

The electrochemical tests were also carried out by using an H-type three-electrode cell. A precision Potentiostat/Galvanostat (AUTOLAB 302 N, Metrohm Autolab B.V., Netherlands) was employed for this work (Chowdhury et al., 2021). A Pt wire (diameter 1 mm), an Ag/AgCl (3 M KCl), and Co_3O_4 NDs/TCP were mounted as the counter, reference, and working electrodes, respectively. Each compartment of the reactor, containing 100 mL of 0.1 M Na_2SO_4 solution, was separated by Nafion N-115 proton exchange membrane. High-purity Ar (used as a control) and N_2 (purity >99.9%) were purged through 2 M H_2SO_4 electrolyte stock to remove NH_3 or O_2 contamination from the feed gas or atmosphere before its introduction to the electrolysis cell (Wen et al., 2021). Figure 2.9 shows a similar schematic of the electrochemical setup employed for ENRR. The electrolyte solution was further purged with Ar or N_2 for 30 min before the start of electrochemical measurements. A flow rate of 40 mL min^{-1} was maintained with the help of a rotameter during ENRR. Polarization curves were obtained by linear sweep voltammetry (LSV), performed in Ar- and N_2-bubbled 0.1 M Na_2SO_4 electrolyte at 20 mV s^{-1}. The formation of NH_3 during ENRR was monitored through the chronoamperometric tests subjected to a range of potentials (−1.2 to −1.55 V vs. Ag/AgCl) for a duration of 1 h.

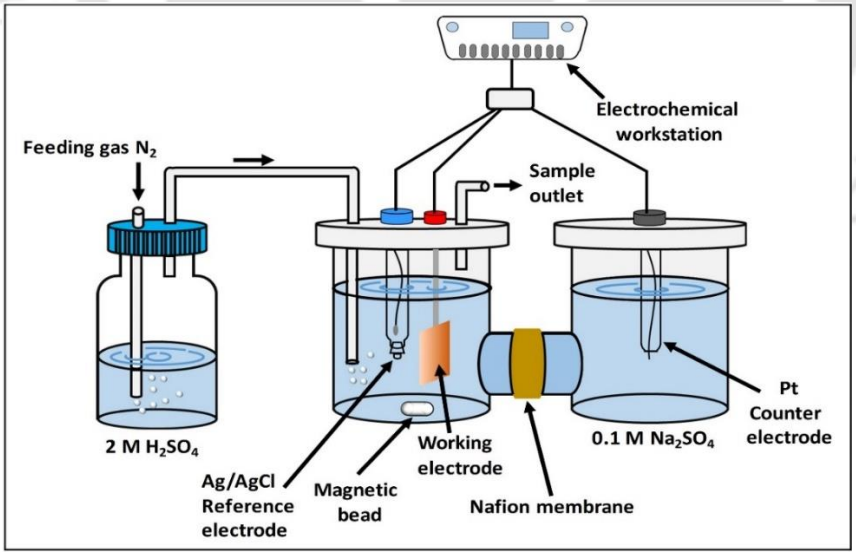

Figure 2.9. H-type reactor for electrochemical N_2 reduction.

2.7 Product analysis

2.7.1 Products formed during ECO_2RR

2.7.1.1 Gas chromatography analysis

The gaseous sample was analyzed in Gas chromatography (Trace GC 1000, Thermofisher, Germany) equipped with a 60/80 Carboxen-1000 column and a TCD detector. Figure 2.10 shows the calibration curve of standard H_2 gas, where the peak area is in a good linear relationship with the H_2 concentration (y= 134.49x, R^2= 0.996).

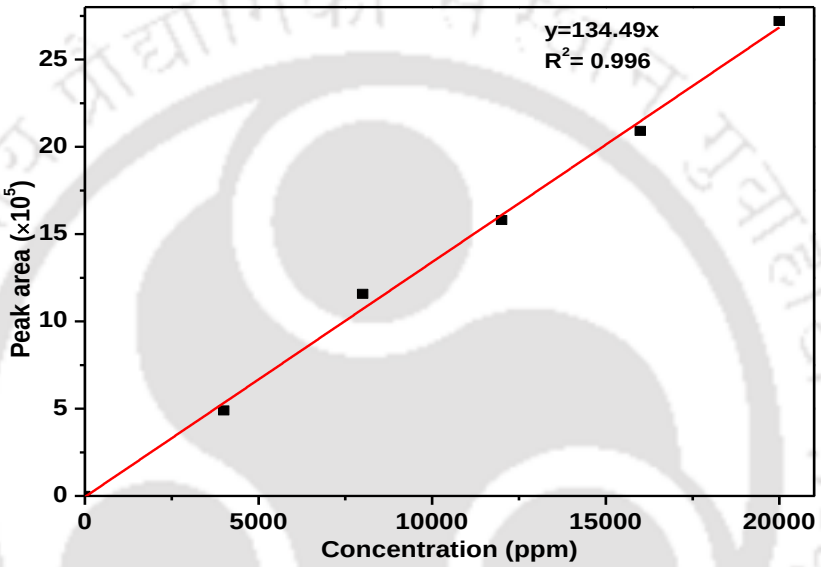

Figure 2.10. Calibration curve of standard H_2 gas.

2.7.1.2 H^1 Nuclear magnetic resonance

The liquid product formed during ECO_2RR was analyzed in a 600 MHz H^1 NMR (Nuclear magnetic resonance) spectrometer (ASCEND 600, Bruker, Germany).

NMR identification and quantification of liquid product was carried out as follows (Figures 2.11a and 2.11b). A volume of 2 mL of catholyte was collected after 60 minutes of reaction. It was then mixed with 100 µL internal standard (50 mM phenol, 99.5 %). An aliquot of 250 µL of this mixture was then added to 350 µL D_2O (99.9 %, Sigma Aldrich) and transferred into an NMR tube (Ren et al., 2015). 1D ^1H NMR spectroscopy of the prepared sample was performed in a 600 MHz spectrometer using the solvent suppression method. The concentration of the liquid product was calculated using the standard calibration curve (Figure 2.11c) made using the internal standards mentioned previously.

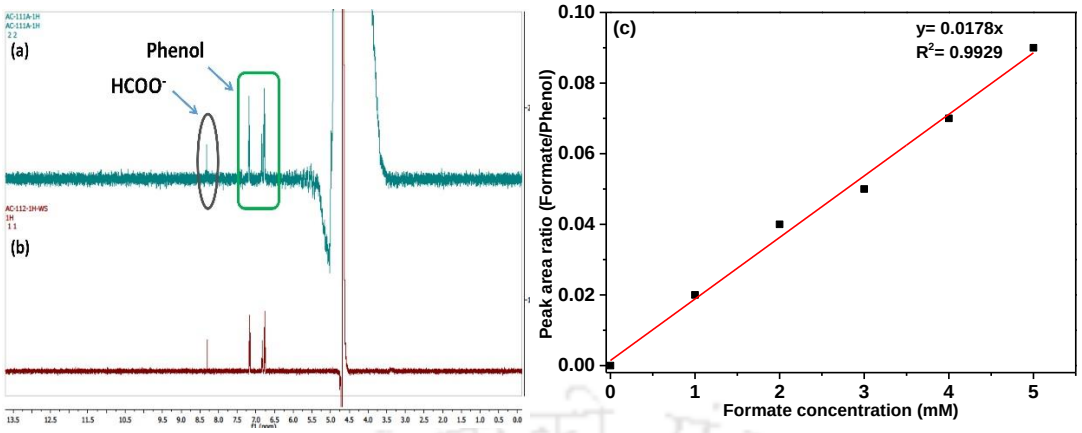

Figure 2.11. NMR spectra of (a) standard 3 mM formate solution and (b) catholyte after 3600 s of CO_2 reduction, and (c) Calibration curve for formate (phenol as an internal standard (IS)).

2.7.2 Determination of products from ENRR

Determination of NH_3: The concentration of NH_3 produced was determined spectrophotometrically by the indophenol blue method (Zhao et al., 2018). A volume of 2 mL of aliquot was mixed with 2 mL of 1 M NaOH containing 5 (% w/w) of each salicylic acid and sodium citrate, followed by 1 mL of 0.05 M NaClO solution. The mixture was then added with 0.2 mL of 1% (w/w) $C_5FeN_6Na_2O{\cdot}2H_2O$ (sodium nitroferricyanide dihydrate) solution. The UV-vis absorption spectrum was determined after 2 h of incubation at room temperature. The wavelength at 659 nm was used to measure the formation of indophenol blue. The concentration vs. absorbance curve was calibrated using standard NH_4Cl solution with NH_3 concentrations of 0.0, 0.2, 0.4, 0.6, 0.8, 1.0, 1.5, 2.0, 2.5, 3.0, 4.0, and 5.0 μg mL^{-1} in 0.1 M Na_2SO_4. The UV-vis absorbance values were found to have a good linear relationship with NH_3 ($y=0.1405x + 0.0345$, $R^2 = 0.996$, Figure 2.12).

The calculation of FE for NH_3 production was determined using Equation 2.6 (Jang and Choi, 2020). Where n is the number of electrons needed for the reduction of N_2 to form NH_3 (here 3), F is Faraday's constant (96485.33 C mol^{-1}), and Q is the total amount of charge passed during ENRR.

$$\text{FE}\ (\%) = \frac{n \times \text{mol of } NH_3 \times F\ (\text{C mol}^{-1})}{Q\ (\text{C})} \times 100 \qquad (2.6)$$

Determination of N_2H_4: The hydrazine present in the electrolyte was measured by the method of Watt and Chrisp (Watt and Chrisp, 1952; Zhang et al., 2018). A colour reagent was prepared by using p-(dimethylamino) benzaldehyde (5.99 g), conc. hydrochloric acid (30 mL) and ethanol (300 mL). An aliquot of 5 mL of this mixture was added to 5 mL of electrolyte solution collected after the chronoamperometric experiment. The solution obtained was stirred for 10 min at room temperature. Finally, UV-vis spectroscopy was employed to measure the absorbance of the solution at a wavelength of 460 nm.

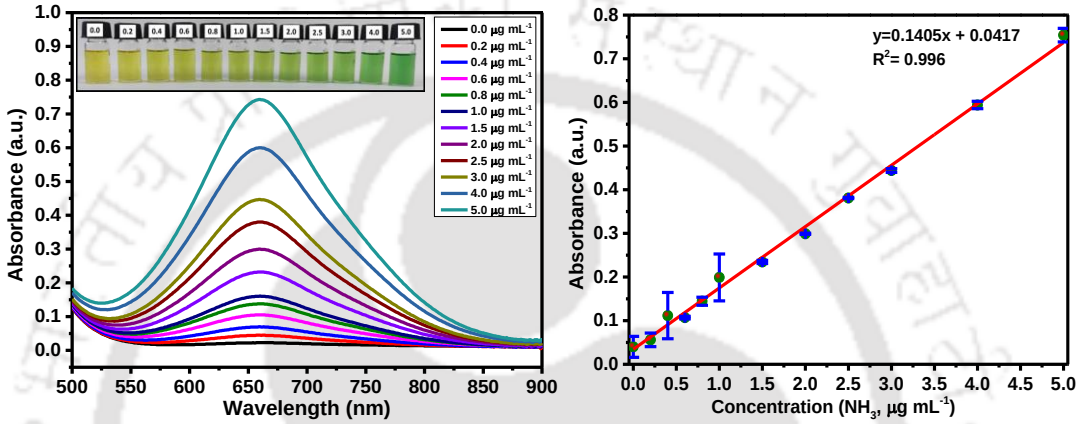

Figure 2.12. (a) UV-vis absorption spectra of NH_4^+ ions using indophenol blue method, after 2 h of incubation at ambient conditions and (b) Calibration curve obtained from UV-vis spectra for the calculation of NH_3 concentration.

References

Andrés, O., Ángel, D., León-garcía, E., Vela-gutiérrez, G., Cruz, J. De, García-varela, R., García, H.S., 2018. Chayote (*Sechium edule* (Jacq.) Swartz), in: Yahia, E.M. (Ed.), Fruit and Vegetable Phytochemicals: Chemistry and Human Health. John Wiley & Sons, Ltd., pp. 979–992. https://doi.org/10.1002/9781119158042.ch47

Chelli, V.R., Golder, A.K., 2018. One pot green synthesis of Pt, Co and Pt@Co core-shell nanoparticles using Sechium edule. J. Chem. Technol. Biotechnol. 94, 911–918. https://doi.org/10.1002/jctb.5838

Chowdhury, A., Peela, N.R., Golder, A.K., 2021. Synthesis of Cu_2O NPs using bioanalytes present in *Sechium edule*: Mechanistic insights and application in electrocatalytic CO_2 reduction to formate. J. CO2 Util. 51, 101622. https://doi.org/10.1016/j.jcou.2021.101622

Das, R.K., Golder, A.K., 2018. Use of plant based analytes for the synthesis of NiO nanoparticles in catalyzing electrochemical H_2O_2 production. J. Electroanal. Chem. 823, 9–19. https://doi.org/10.1016/j.jelechem.2018.05.029

Das, R.K., Golder, A.K., 2017. Co_3O_4 spinel nanoparticles decorated graphite electrode: Bio-mediated synthesis and electrochemical H_2O_2 sensing. Electrochim. Acta 251, 415–426. https://doi.org/10.1016/j.electacta.2017.08.122

Dash, S.R., 2021. Bioinspired engineering of nanomaterials for electrocatalytic sensing of heavy metals and organic analytes. Indian Institute of Technology Guwahati.

Jang, Y.J., Choi, K.S., 2020. Enabling electrochemical N_2 reduction to NH_3 in the low overpotential region using non-noble metal Bi electrodes: Via surface composition modification. J. Mater. Chem. A 8, 13842–13851. https://doi.org/10.1039/d0ta02550j

Ren, D., Deng, Y., Handoko, A.D., Chen, C.S., Malkhandi, S., Yeo, B.S., 2015. Selective electrochemical reduction of carbon dioxide to ethylene and ethanol on copper(I) oxide catalysts. ACS Catal. 5, 2814–2821. https://doi.org/10.1021/cs502128q

Rumayor, M., Dominguez-Ramos, A., Irabien, A., 2018. Formic Acid manufacture: Carbon dioxide utilization alternatives. Appl. Sci. 8, 1–12. https://doi.org/10.3390/app8060914

Salek, G., Tenailleau, C., Dufour, P., Guillemet-Fritsch, S., 2015. Room temperature inorganic polycondensation of oxide (Cu_2O and ZnO) nanoparticles and thin films preparation by the dip-coating technique. Thin Solid Films 589, 872–876. https://doi.org/10.1016/j.tsf.2015.04.082

Senguttuvan, J., Paulsamy, S., Karthika, K., 2014. Phytochemical analysis and evaluation of leaf and root parts of the medicinal herb, *Hypochaeris radicata* L. for in vitro antioxidant activities. Asian Pac. J. Trop. Biomed. 4, S359–S367. https://doi.org/10.12980/APJTB.4.2014C1030

Watt, G.W., Chrisp, J.D., 1952. Spectrophotometric Method for Determination of Hydrazine. Anal. Chem. 24, 2006–2008. https://doi.org/10.1021/ac60072a044

Wen, J., Chang, H., Huang, T., Hossain, M., Liu, Z., Sun, H., Zhu, Y., Chen, Y., Huang, Q., Wu, Y., 2021. A simple synthesis of Co_3O_4@CNT to boost electrochemical nitrogen fixation. Electrochim. Acta 367, 137421. https://doi.org/10.1016/j.electacta.2020.137421

Zhang, L., Ji, X., Ren, X., Luo, Y., Shi, X., Asiri, A.M., Zheng, B., Sun, X., 2018. Efficient electrochemical N_2 reduction to NH_3 on MoN nanosheets array under ambient conditions. ACS Sustain. Chem. Eng. 6, 9550–9554. https://doi.org/10.1021/acssuschemeng.8b01438

Zhao, X., Lan, X., Yu, D., Fu, H., Liu, Z., Mu, T., 2018. Deep eutectic-solvothermal synthesis of nanostructured Fe_3S_4 for electrochemical N_2 fixation under ambient conditions. Chem. Commun. 54, 13010–13013. https://doi.org/10.1039/c8cc08045c

CHAPTER 3

Synthesis of Cu_2O NPs using Bioanalytes Present in *Sechium edule*: Mechanistic Insights and Application in Electrocatalytic CO_2 Reduction to Formate

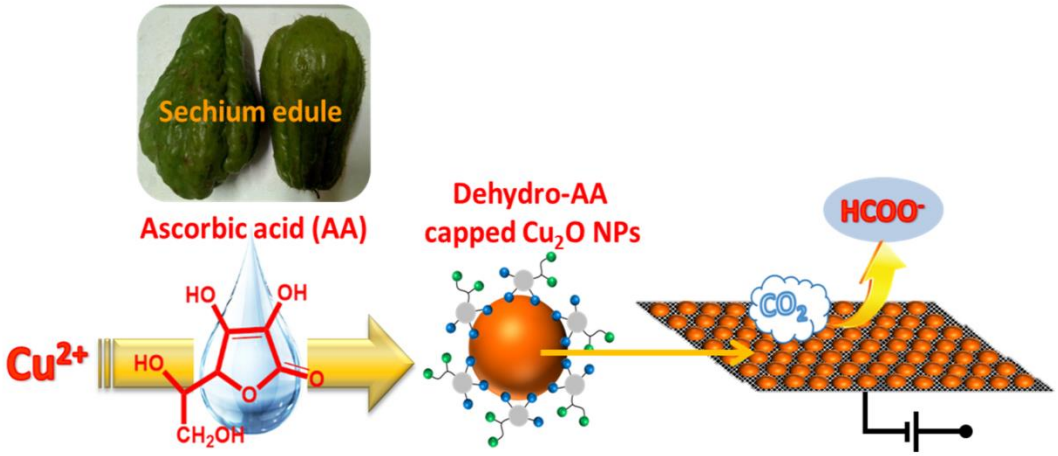

Highlights

- Metal-organic ligand capped Cu_2O(bio) NPs synthesis using analytes present in *Sechium edule*
- Cu_2O NPs reduced charge transfer resistance by 98%
- Elucidated mechanism of formation of Cu_2O(bio) NPs and metal-organic intermediates leading to capping of NPs
- Cu_2O(bio) NPs electrocatalyzed CO_2 reduction to $HCOO^-$ and improved product specificity
- Bioinspired and chemically synthesized Cu_2O NPs exhibited similar Faradaic efficiency in CO_2 reduction

3.1 Background and executive motivation

Carbon dioxide (CO_2) is an innate product of combustion of fossil fuels and respiratory activity of living-beings. CO_2 is one of the major contributors of the greenhouse effect (An et al., 2014). To control the atmospheric CO_2 concentration, the plausible ways of transforming the energy production from fossil fuel to sustainable CO_2-reduction processes include the conversion of CO_2 into (i) carbon-neutral fuel and (ii) other value-added inorganic/organic chemicals (Ahn et al., 2017).

Different CO_2 reduction products from C_1 to C_3 are carbon monoxide (CO), methane (CH_4), formic acid (HCOOH)/ formate ($HCOO^-$), formaldehyde (HCHO), methanol (CH_3OH), ethanol (C_2H_5OH), ethane (C_2H_6), ethylene (C_2H_4), and propanol (C_3H_7OH) (Han et al., 2017; Zhao et al., 2017). The major CO_2 reduction processes include photocatalytic, biochemical, thermochemical, and electrochemical techniques (An et al., 2014; Nitopi et al., 2019; Shaughnessy et al., 2020). Among them, electrochemical reduction of CO_2 attracts special attention because it (i) could utilize electrical power from the intermittent renewable energy sources (like solar, tidal, wind, etc.) (Shaughnessy et al., 2020), (ii) could be operated under atmospheric temperature and pressure, (iii) is tunable in the context of applied voltage and type of electrolytes (Ahn et al., 2017), and (iv) could recover electrolytes with low cost depending on products quality and its concentration.

CO_2 is a thermodynamically stable molecule ($\Delta G° = -394$ kJ mol^{-1}) having a linear and symmetrical structure with the C and O atoms, where C=O bonds are relatively stronger (783 kJ mol^{-1}) (Snoeckx and Bogaerts, 2017). Consequently, the conversion of CO_2 to value-added chemicals is required substantial energy input, optimized reaction conditions and a suitable catalyst.

Towards this goal, several metals (Bi, In, etc.), noble metals (Au, Ag, Pd, etc.), transition metals (Cu, Co, Ni, Zn, Hg, Sn, Pb, etc.), and metal-oxide catalysts (Cu_2O(bio), ZnO, SnO_2, etc.) are applied to improve the product selectivity and its yield through electrochemical CO_2 reduction reaction (ECO_2RR) (Yin et al., 2019; Zhang et al., 2019).

Out of the metal-based catalysts mentioned earlier, Cu and Cu-based catalysts stand uniquely for ECO_2RR as it could produce aldehydes, alcohols, and hydrocarbons having higher-order carbon (or $>2e^-$ C products) with considerable Faradaic efficiencies (FE) (Nitopi et al., 2019; Ren et al., 2020). It could catalyze

ECO_2RR to various chemicals with high FE (even up to overall FE ~98.7%) (Han et al., 2017) and selectivity (>90%) (Xia et al., 2019).

Cu-based bimetallic Cu-Au electrocatalyst was used for the selective reduction of CO_2 to formate with 81% FE at −0.8 V vs. reversible hydrogen electrode (RHE) (Tao et al., 2019). Cu_2O/CuS nanocomposite exhibited formate formation with FE of 67.6% at −0.9 V vs. RHE (Wang et al., 2021). Liu et al. (2021) reported 77.1% FE for formate at −0.9 V vs. RHE, on porous Cu hollow fiber catalyst. Gupta et al. (2016) reported 61% FE for formate formation on CuO (111) nanoparticles at −1.40 V vs. Ag/AgCl. Zhu et al. (2018) reported selective formate formation (FE 66%) on Cu_2O NPs coated on rotating disk electrode at −0.8 V vs. RHE. The study reported by Wang et al. (2021) supports the selective formation of formate over Cu_2O (111), where the (111) plane of Cu (I) facilitates the formation of bidentate *OCHO intermediate by lowering the energy barrier.

It is evident from Chapter 1 that in recent years, bioinspired synthesis route for metal and metal oxide nanoparticles has received immense success in the context of the simplicity of the procedures and use of environmentally benign chemicals (Chelli and Golder, 2018; Das and Golder, 2017). *Sechium edule* fruit extract has been successfully tested for metal doping and synthesis of transition metal oxides nanoparticles (NPs) (Chelli and Golder, 2018; Das and Golder, 2017). The fruit contains flavonoids, reducing sugars, ascorbic acid (AA) which are capable of reducing metal ions forming various metal NPs such as Cu_2O NPs.

The standard electrode potential (E°) of AA/ dehydroascorbic acid (DHA) system is +0.1 V vs. standard hydrogen electrode (SHE) (Holade et al., 2016), which is lower than that of the Cu^{2+}/Cu^{+} system (E°= +0.155 V vs. SHE (Lemishko and Lemishko, 2017). The work in this chapter aims at the synthesis of Cu_2O(bio) NPs using *Sechium edule* fruit extract being rich in AA content (294 mg kg^{-1} dry fruit). The mechanisms of formation of Cu_2O(bio) NPs play crucial roles on the understanding the kinetics of its synthesis, structural morphology, and particles stability. Therefore, the mechanistic pathways to understand the formation of intermediates and metal-organic (intermediates) ligand leading to the formation of Cu_2O(bio) NPs and its protective cap using both bio-extract and commercial AA are proposed and validated through mass spectroscopic analyses. The optical absorption property, crystallinity, structural morphology, and bulk property of Cu_2O(bio) NPs are

studied thoroughly using various analytical tools such as X-ray diffraction, X-ray photoelectron spectroscopy, electron microscopy, etc. The electrode (Cu_2O(bio) NPs/TCP electrode) was fabricated by the drop-coating of Cu_2O(bio) NPs on Toray carbon paper (TCP) and tested for highly selective electrocatalytic CO_2 reduction to formate. Further, the loss of catalytic activity and delamination of Cu_2O(bio) NPs from the Cu_2O(bio) NPs/TCP electrode due to CO_2 reduction reaction were investigated in details.

3.2 Results and discussions

3.2.1 Physiochemical characteristics of Cu_2O(bio) NPs

3.2.1.1 UV-Vis diffused reflectance spectrum

Figure 3.1a shows the UV-Vis spectrum of the synthesized Cu_2O(bio) NPs with a characteristic broadband absorbance peak at λ_{max}= 450 nm. This broadband transition is attributed to the electronic transition in Cu atom from $3d^9 4s^1$ to $3d^{10}$ electronic configuration (Valodkar et al., 2011). The bandgap of the Cu_2O(bio) NPs was calculated from UV-Vis absorbance spectrum according to Tauc's formula, using the Equation 3.1 (Bhaumik et al., 2014).

$$\alpha = \frac{B(h\nu - E_g)^n}{h\nu} \quad (3.1)$$

Where, hν is the photon energy, B is a constant, E_g is the optical bandgap energy, n is a constant and its value of 1/2 signifies to the direct allowed transition, and α is the absorption coefficient (Odling et al., 2018). The $(\alpha h\nu)^2$ vs. hν plot in Figure 3.1b shows the E_g value of 1.98 eV, which is in between the values reported for bulk Cu_2O particles (E_g= 2.0-2.17 eV) (Zhang et al., 2010) and Cu_2O NPs (E_g= 1.93-1.97 eV) because of the particles morphology (Zhao et al., 2008).

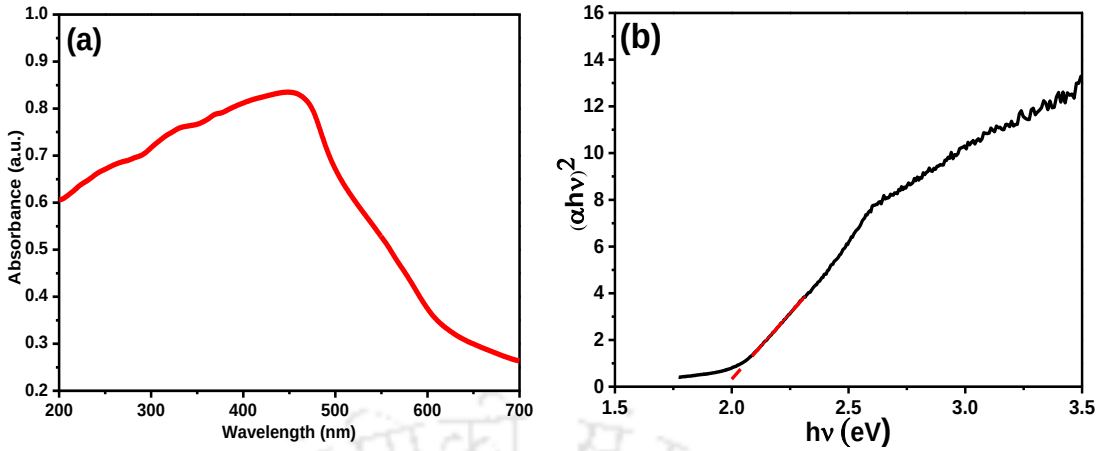

Figure 3.1. (a) UV-Vis diffused reflectance spectra of Cu_2O(bio) NPs and (b) Bandgap calculation of Cu_2O(bio) NPs using the Tauc's plot.

3.2.1.2 XRD analysis

The diffraction pattern depicts the formation of highly crystalline single phase cubic Cu_2O(bio) NPs (Figure 3.2a). The diffraction pattern corresponding to the face-centered cubic (fcc) lattice structure is supported by those of Cu_2O(bio) from JCPDS database (05-0667). The peaks with 2θ values of 29.60º, 36.52º, 42.44º, 61.34º, 73.69º, and 77.6º correspond to the crystal planes with Miller indices of (110), (111), (200), (220), (311), and (222), respectively (Bhosale and Bhanage, 2016). The XRD diffraction pattern clearly infers that the sample is rich in (111) oriented plane of Cu_2O(bio). The crystal size was determined using the Scherrer's relation (Equation 3.2).

$$L=\frac{K\lambda}{\beta\cos\theta} \qquad (3.2)$$

Where, L is the crystallite size (nm), K is the Scherrer constant (its value is 0.9), λ is the X-ray wavelength (= 0.154 nm), β is the breadth of the diffraction pattern, i.e. the full width at the half maxima (FWHM), and θ is the diffraction angle for the (111) peak of Cu_2O(bio) NPs. The lattice constant (a) was calculated using the following relation (Equation 3.3). Where, d is the interplanar distance and (hkl) are Miller indices.

$$a=d\sqrt{h^2+k^2+l^2} \qquad (3.3)$$

The calculated average lattice constant was found to be 4.26 Å. The inter-planar distance corresponding to the 2θ values are found to be 3.00, 2.46, 2.13, 1.50,

1.28, and 1.23 nm, respectively. The crystallite size determined was as 23.2 nm. Figure 3.2b shows the diffraction pattern of Cu_2O-AA NPs (Cu_2O NPs synthesized using commercial AA). The peaks with 2θ values of 29.90°, 36.80°, 42.74°, 61.92°, 73.96°, and 77.94° correspond to the crystal planes of (110), (111), (200), (220), (311), and (222), respectively. The average lattice constant is calculated as a=4.23 Å. The inter-planar distance corresponding to the 2θ values are 2.981, 2.439, 2.113, 1.497, 1.280, and 1.222 nm, respectively, with an average crystallite size of 15.9 nm. The crystalline nature of both the Cu_2O(bio) NPs, synthesized using *Sechium edule* fruit extract and commercial AA are found to be in accordance with the literature (Bhosale and Bhanage, 2016). A typical XRD pattern of CuO in (Figure 3.2c) was observed from the control experiment which was carried out without using *Sechium edule* fruit extract. The XRD pattern is a good agreement with the literature reported value (JCPDS no. 41-0254) (Nikam et al., 2014).

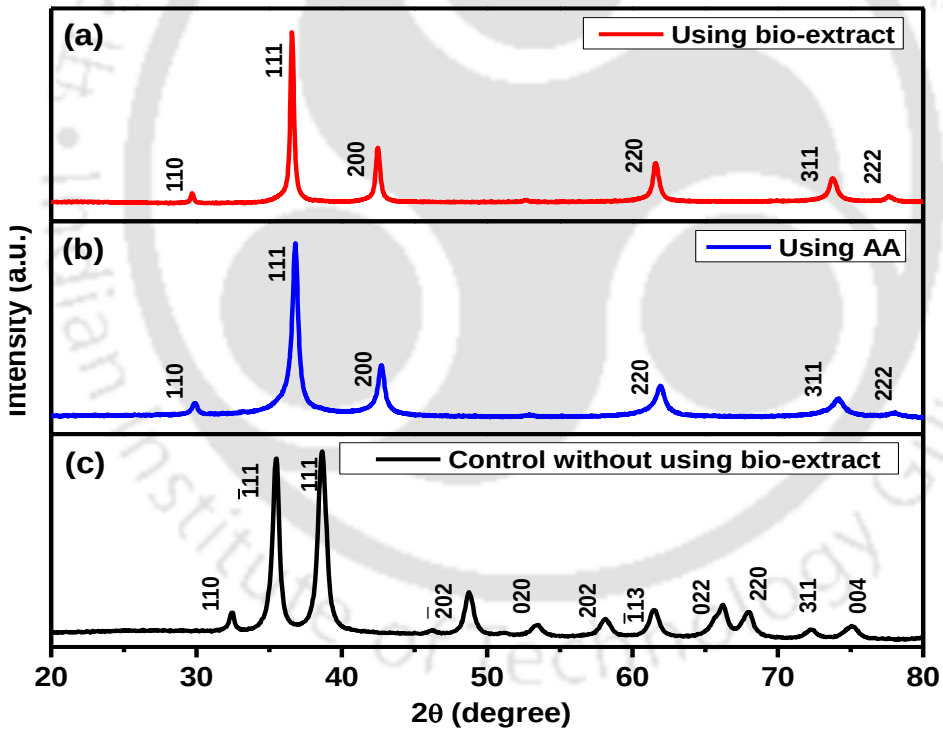

Figure 3.2. X-ray diffraction pattern of (a) Cu_2O(bio) NPs synthesized using *Sechium edule* bio-extract, (b) Cu_2O NPs synthesized using AA, and (c) CuO formed without using of bio-extract (control experiment).

3.2.1.3 Morphological properties of Cu_2O(bio) NPs

The FESEM micrograph of synthesized Cu_2O(bio) NPs is shown in Figures 3.3a-3.3b from two different batches of the experiments under the identical condition. The morphology of particles was mostly uniform with particle size ranging from 30.3 to 49.9 nm with an average diameter of 37.5 nm. It implies that the composition of *Sechium edule* collected during May-July 2020 didn't affect much the quality of synthesized Cu_2O(bio) NPs. The energy dispersive X-ray analyses of Cu_2O(bio) NPs are shown in Figures 3.3c-3.3f. The elemental spectrum (Figure 3.3c) reveals the existence of Cu and O atoms. The presence of C atom in this spectrum is due to the carbon tape used in the sample preparation technique and existence of a trace quantity of biomolecules acting as a capping agent which could arrest the particles agglomeration (Sahai et al., 2016).

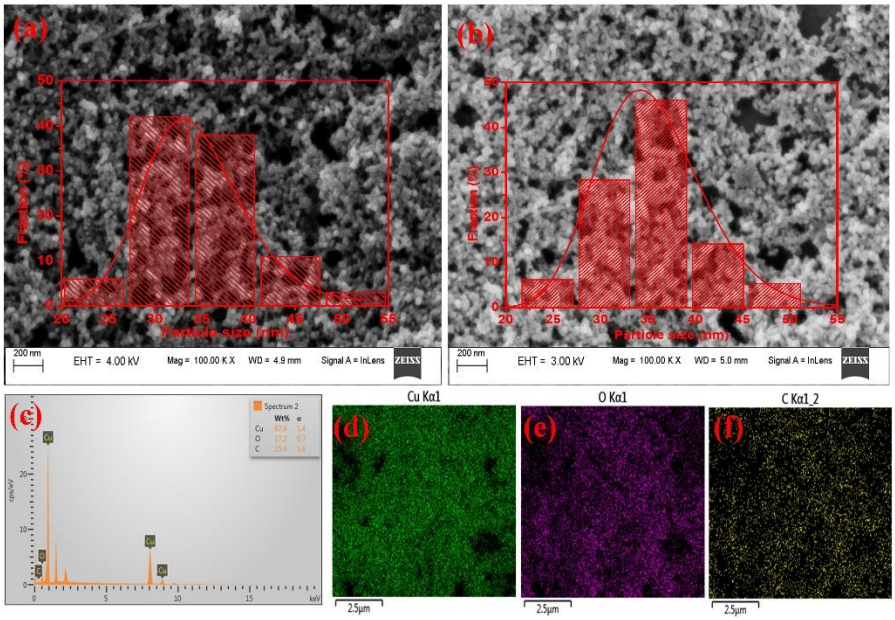

Figure 3.3. (a-b) FESEM micrographs of Cu_2O(bio) NPs synthesized under identical condition, (c) EDX spectrum, and (d-f) EDX image mapping of Cu_2O(bio) NPs.

FETEM micrographs of Cu_2O(bio) NPs are shown in Figure 3.4. The micrograph shows that the particles are bit agglomerated and oblate in shape (Figure 3.4a). The average particle size was measured to be 42 nm (Figure 3.4b) which is slightly larger than the particles sizes recorded in FESEM. The lattice fringe with an interplaner distance of 0.245 nm (Figure 3.4c) is a good agreement with the d(hkl) (111) plane of Cu_2O NPs (Zhou et al., 2014). The diffraction spots from the selected

area electron diffraction (SAED) pattern (Figure 3.4d) indicate the crystalline planes corresponding to Miller indices of (111), (202), (200), and (311), which are in accordance with the XRD pattern. Both the XRD and HRTEM analyses infer that the synthesized Cu_2O(bio) NPs could electrocatalyze CO_2 reduction for selective formation of formate because of the predominant presence of (111) crystal plane. However, the faint diffuse rings in the SAED pattern might be an indication of the presence of amorphous CuO on the surface of crystalline Cu_2O(bio) NPs.

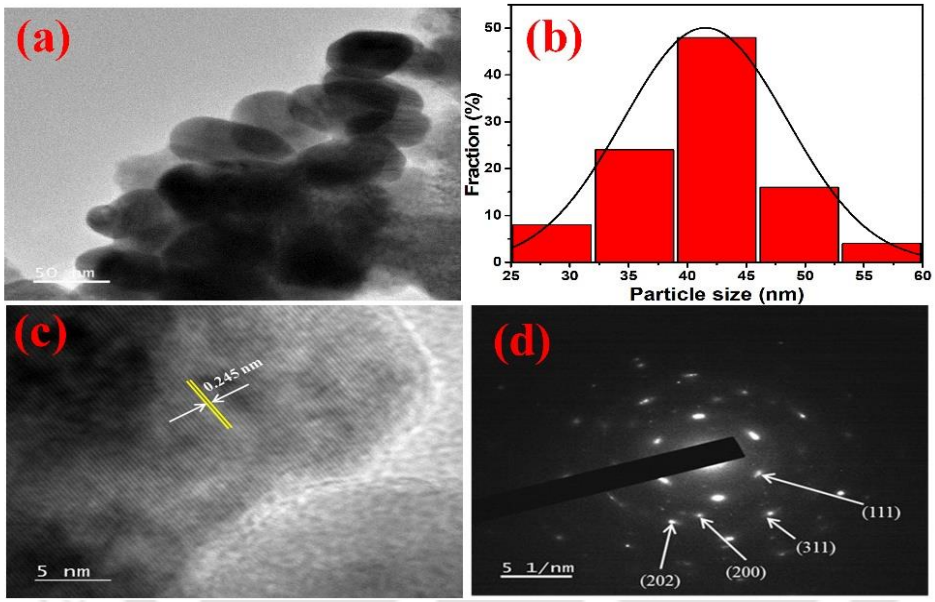

Figure 3.4. (a) FETEM micrograph, (b) HRTEM micrograph, c) histogram of the particle size distribution, and (d) SAED pattern of Cu_2O(bio) NPs.

3.2.1.4 XPS analysis

The Cu $2p_{3/2}$ core level spectra were studied using XPS analysis to investigate the surface oxidation state of Cu. The survey spectra of Cu_2O(bio) NPs is shown in Figure 3.5. It reveals the characteristic peaks of Cu 2p, O 1s, and C 1s. The doublet peaks in Figure 3.6a at approximately 932.1 and 952.1 eV attribute to the Cu $2p_{3/2}$ and Cu $2p_{1/2}$ in Cu_2O(bio), respectively. Whereas, the Cu $2p_{3/2}$ and Cu $2p_{1/2}$ peaks at 934 and 954.1 eV signify the presence of CuO. The peak at 934 eV is higher than the reported energy value for CuO (933.7 eV) depicting that the binding energy was shifted from 933.7 to 934 eV due to the small amount of CuO present on the surface (Teo et al., 2006). This could be due to the formation of amorphous CuO on the

Cu_2O(bio) surface. Also, the shake-up satellites at 943.2 and 962.9 eV are for Cu $2p_{3/2}$ and Cu $2p_{1/2}$ of unfield 3d or 3d9 shell of Cu(II) (Brookshier et al., 1999). Further, Cu_2O(bio) could be oxidized to amorphous CuO on the surface of NPs, which was not seen in the XRD (Figure 3.2) and SAED (Figure 3.4d) analyses. The core-level XPS spectra of O 1s is shown in Figure 3.6b. The peak located at 530.6 eV could be due to the lattice oxygen. O^{2-} presents in Cu_2O(bio) (Teo et al., 2006), and the second peak at 531.8 eV attributes to the presence of adsorbed oxygen onto the surface of Cu_2O(bio) NPs (Wang et al., 2002). The peak area at 531.8 eV is higher than the peak area at 530.6 eV. It implies that more oxygen was adsorbed onto the Cu_2O(bio) surface due to its unstable nature and eases its oxidation in the presence of air. The binding energy, FWHM, and peak area of Cu $2p_{3/2}$ of Cu_2O(bio) NPs are summarized in Table 3.1. From the peak area calculation, the CuO percentage was found to be 49.7%. The survey spectra of the Cu_2O(bio)-NPs/TCP electrode after 100 cycles of CV analysis, is shown in Figure 3.7. It depicts the characteristic peaks correspond to C 1s, F 1s, O 1s, Cu 2p, and, S 2p. A sharp peak appeared in C 1s region at 292.7 eV which was absent in the case of XPS survey analysis of powder Cu_2O(bio) NPs (Figure 3.5). It could be due to the residual bioactive components and adsorbed CO_2, onto the surface (Favaro et al., 2017). The source of F and S was Nafion, which was used as a binder for the coating of Cu_2O(bio) NPs onto TCP. The binding energies of 933.15, 935.08, and 942.62 eV attributed to the presence of CuO on the surface of the Cu_2O(bio) NPs (Figure 3.8a). From the peak area calculation (Table 3.2) it was found that the surface of Cu_2O(bio)-NPs/TCP electrode contains 71.4% CuO. It implies that after successive CV, the Cu_2O(bio) NPs was oxidized to CuO. The core level XPS spectra of O 1s is shown in Figure 3.8b. The presence of chemisorbed CO_2, C-O(H), and formate ($HCOO^-$) could be identified by the peak overlapped at 530.9 eV (Figure 3.8b). The peak appeared at high binding energy (532.2 eV) is attributed to adsorbed H_2O (Favaro et al., 2017). The peak appeared at 535.2 eV could be attributed to the oxygen bonded to the ether configuration in nafion (Schulze et al., 1999).

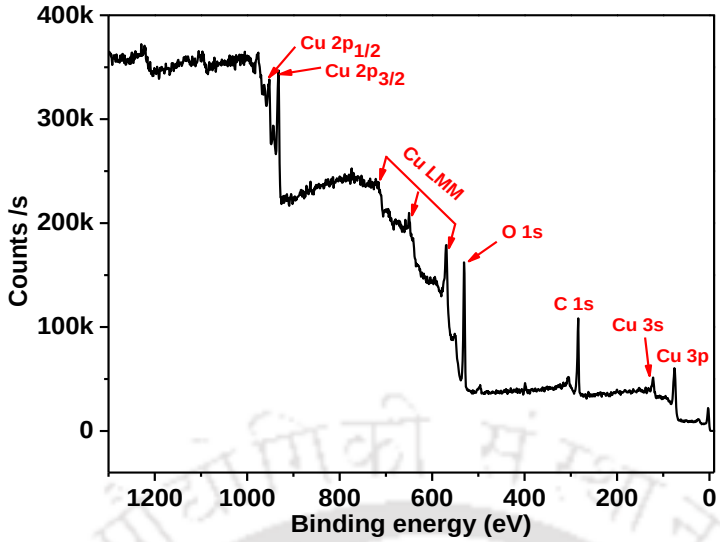

Figure 3.5. XPS survey of the Cu_2O(bio) NPs.

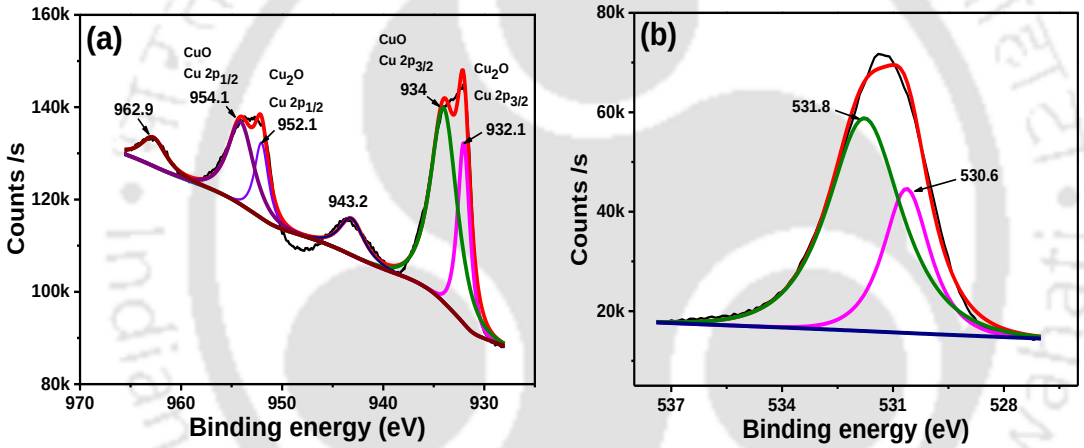

Figure 3.6. core-level XPS of (a) Cu 2p, (b) O 1s of the Cu_2O(bio) NPs.

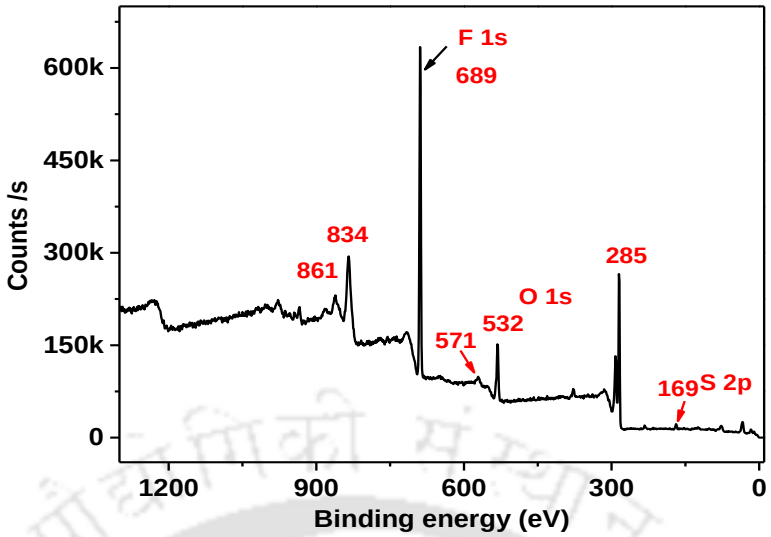

Figure 3.7. XPS survey of the Cu_2O(bio) NPs/TCP electrode after 100 scans of CV at 50 mV s^{-1}.

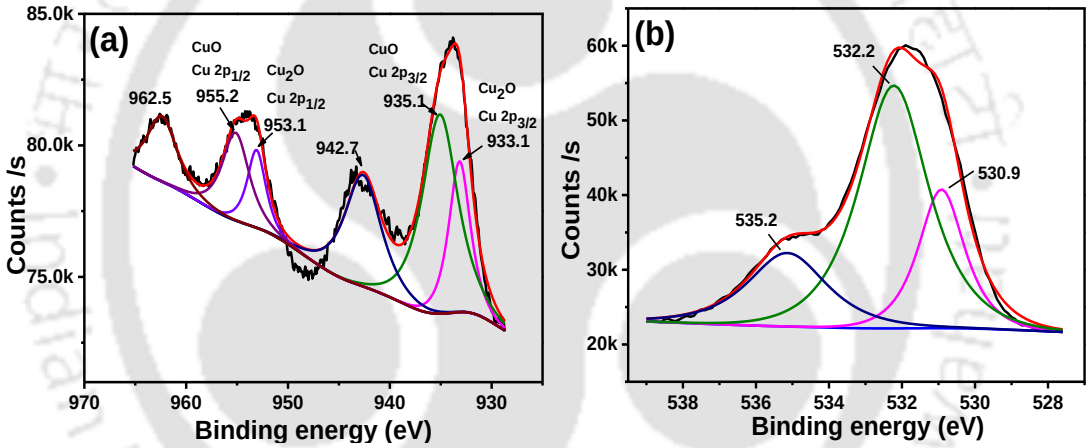

Figure 3.8. Core-level XPS of (a) Cu 2p, and (b) O 1s of the Cu_2O(bio) NPs/TCP electrode after 100 scans of CV at 50 mV s^{-1}.

Table 3.1. Results of deconvolution of XPS Cu 2p3/2 peaks of Cu_2O(bio) NPs.

Peak	Binding energy (eV)	Cu phase	Area	FWHM	Percentage (%)
1	932.03	Cu_2O(bio)	66615.24	1.42	18.32
2	934.00	CuO	153987.6	3.05	42.35
3	943.14	CuO	26575.3	2.79	7.31

Table 3.2. The results of deconvolution of XPS Cu 2p3/2 peaks of Cu_2O(bio) NPs/TCP electrode after 100 cycles CV analysis.

Peak	Binding energy (eV)	Cu phase	Area	FWHM	Percentage (%)
1	933.15	CuO	17085.84	2.49	16.15
2	935.08	CuO	37052.08	4.09	35.01
3	942.62	CuO	21441.34	4.23	20.26

3.2.1.5 BET surface area and NPs purity from thermogravimetric analysis

Figure 3.9 shows that the as-synthesized Cu_2O(bio) NPs exhibited an type-II isotherm suggesting a typical nature of a mesoporous material (Nguyen et al., 2017). The BET surface was calculated to be 16.1 $m^2 g^{-1}$. Mesoporous materials are widely used for the application in gas adsorption via physisorption interaction, and the as-synthesized Cu_2O(bio) NPs could be a potential electrocatalyst in the ECO_2RR process (Zhao et al., 2019). Further, the pore size distribution was determined by using the Barrett-Joyner-Halenda (BJH) model. According to the distribution curve (inset Figure 3.9), the average pore size was 3.7 nm.

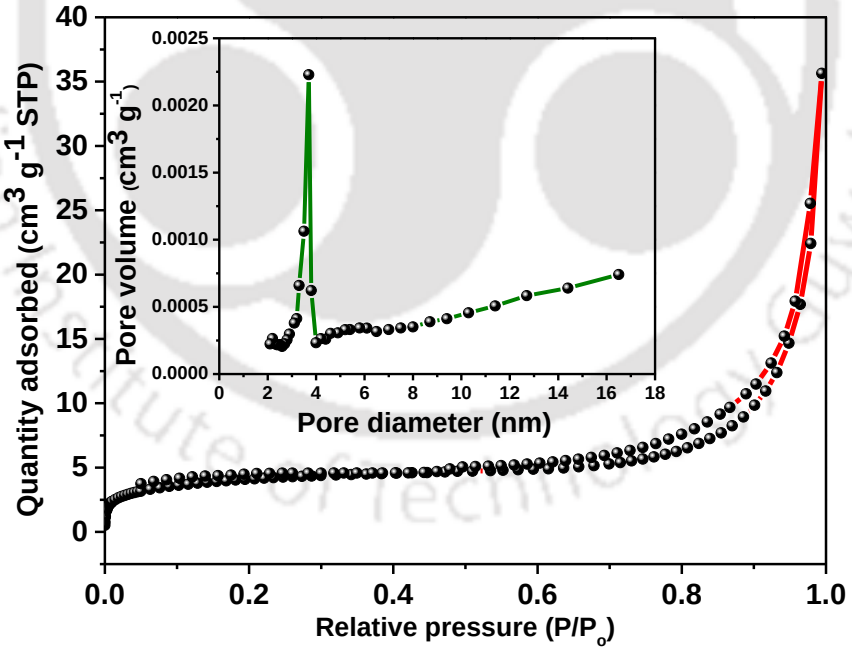

Figure 3.9. N_2 adsorption-desorption isotherm and (inset) Barrett-Joyner-Halenda (BJH) pore size distribution plot of Cu_2O(bio) NPs from BET analysis.

Figure 3.10 shows the TGA curve of Cu_2O(bio) NPs. The weight loss from 50 to 100ºC was <1% due to the removal of moisture (Bhosale and Bhanage, 2016). The

second weight loss was barely 5% from 130 to 400°C owing to the thermal decomposition of bio-moieties present on the NPs. Further, a mass gain (<1%) was noted in the temperature range from 450 to 695°C (inset of Figure 3.10). It could be due to the oxidation of Cu_2O(bio) to CuO (Equation 3.4) (Firmansyah et al., 2009). In fact, a trace amount of oxygen present as an impurity in the N_2 gas employed for TGA is sufficient for this oxidation in this temperature range (Bhosale and Bhanage, 2016; Firmansyah et al., 2009). The mass loss of 3% beyond 700°C is attributed to the decomposition of carbonaceous residue. It indicates that the proposed bioinspired method could synthesize Cu_2O(bio) NPs reasonably in pure form, and the biomolecules present on Cu_2O(bio) NPs is not more than 8%.

$$Cu_2O+\frac{1}{2}O_2 \rightarrow 2CuO \qquad (3.4)$$

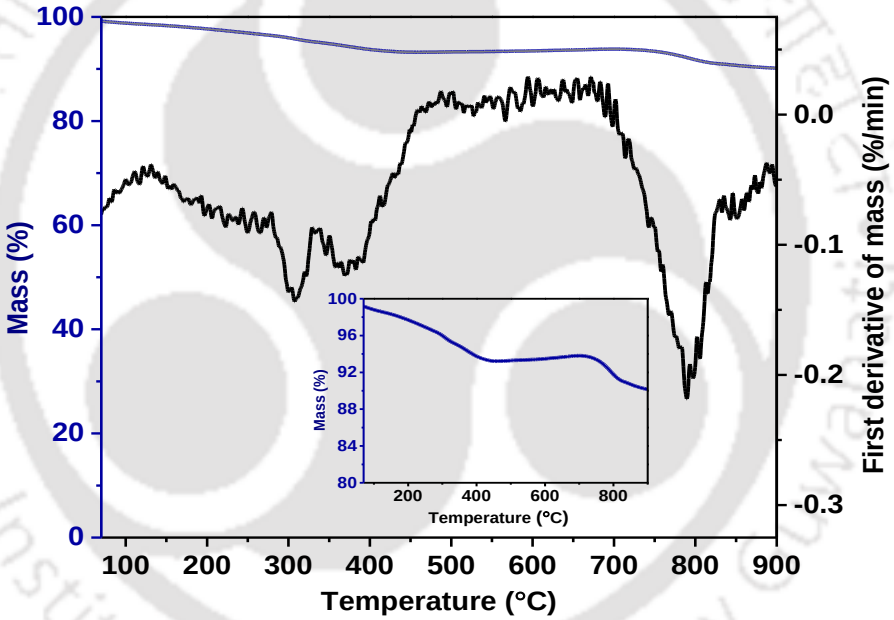

Figure 3.10. TGA and DTG profiles of Cu_2O(bio) NPs (inset: A selected part of TGA profile of Cu_2O(bio) NPs).

3.3 Mechanism of formation of Cu_2O(bio) NPs

The mass spectra of the anlaytes present in *Sechium edule* fruit extract at the experimental conditions are shown in Figures 3.11a-3.11c. From these spectra, several peaks could be identified based on the mass number (m/z) of the compounds reported in the literature (Szultka et al., 2014). The fruit is enriched with AA (Chelli and Golder, 2018). AA was identified at m/z= 175.12 (Figure 3.11a). The proposed

pathway of reaction for the synthesis of Cu_2O(bio) NPs was developed using AA as a leading reducing agent, and the peaks of the intermediate compounds were identified in the mass spectra (Figure 3.11c). The schematic reaction pathway for the synthesis of Cu_2O(bio) NPs is shown in Figure 3.12. The reactions involved for the formation various intermediate products are presented in Figure 3.14. In an alkaline medium, the first ionization –OH group of AA takes place at –O(3)H, (structure I in Figure 3.14), followed by the second ionization of –O(2)H at pH 12 and forms a comparatively stable ascorbyl radical, $A^{\bullet-}$ (VII) (Zu, 2006). Like other transition metal ions, AA forms chelate complex with Cu^{2+}, making a five-membered ring with the ene-diol (O-2 and O-3) fragment of AA molecule. The ascorbate anion (structure III) forms complex (structure IV) with the Cu^{2+} ion, which is further attacked by the dissolve O_2 molecule and forms Cu^{+}-ascorbate-O_2 complex (structure V-VI) (Khan and Martell, 1967). Electron transfer from ascorbate anion to molecular oxygen occurs through the Cu^{2+} ion. The transfer of an electron of oxygen of ascorbate to metal ion takes place from the 2p orbital of an oxygen atom to a t_{2g} (nonbonding orbital) or an e_g (antibonding orbital) orbital of Cu^{2+} ion. Then the electron is further transferred to a $\pi_y^*(2p)$ (or $\pi_z^*(2p)$) antibonding orbital of the O_2 molecule. The orbital overlap of Cu^{2+} ion could be thought of as similar to that of the overlap of π orbital of ethylene to pd or d^2sp^3 orbital of the metal ion. The ascorbyl radical (structure VII) formed, is stabilized by several resonance structures (structure VII-1 to VII-5), known as the captodative effect (Avendaño and Menéndez, 2015). The ascorbyl radical then reacts with Cu^{2+} ion to produce DHA, an oxidation product of AA (structure VIII) with m/z= 173.01 and Cu^{2+} ion reduces to Cu^{+}. In an alkaline condition, DHA is known to decompose in oxalic acid (m/z= 90.98) and trihydroxybutyric acid (m/z= 135.02) (Figure 3.8) (Ünaleroğlu et al., 1997). The $HO_2^{\bullet}$ radical (structure IX) formed, reacts with the Cu^{+} ion and produces CuOOH (structure X). CuOOH decomposes to $CuO^{\bullet}$ (structure XI) and $HO^{\bullet}$ radicals. $CuO^{\bullet}$ further reacts with Cu^{+} ion and Cu_2O(bio) is formed. Furthermore, the Cu_2O(bio) NPs formed were stabilized by DHA. Xiao et al. (2011) used DHA as a stabilizing cum capping agent to synthesize iron oxide NPs. According to the hard soft acid base (HSAB) principle, carbonyl (–CO) groups in DHA, a soft ligand, has the tendency to coordinate with the soft metal ion (here Cu^{+}) (Eslami et al., 2018). The π^*(O) orbitals of (–CO) groups interact with the d_{xz} orbital of Cu^{+} ion on the surface of Cu_2O(bio) NPs (Figure 3.13a), which leads to the

formation of coordination bond between metal-ligands. This in turn helps to stabilize the Cu_2O(bio) NPs via micelle formation (Figure 3.13b). The mass spectra recorded in the presence of Cu-precursor using commercial AA instead of using the bio-extract of *Sechium edule* under identical reaction condition is shown in Figure 3.15. The mass spectrum (Figure 3.15a) shows the unprotonated molecular ion $[M\text{-}H]^-$ at m/z 175 corresponds to AA. At pH 12 (Figure 3.15b), the oxidative product of AA identified was trihydroxybutyric acid (m/z= 135.02), which was present after the synthesis reaction of Cu_2O(bio) NPs (Figure 3.15c). Oxalic acid (m/z= 90.98) was also detected as a degradation product (Szultka et al., 2014).

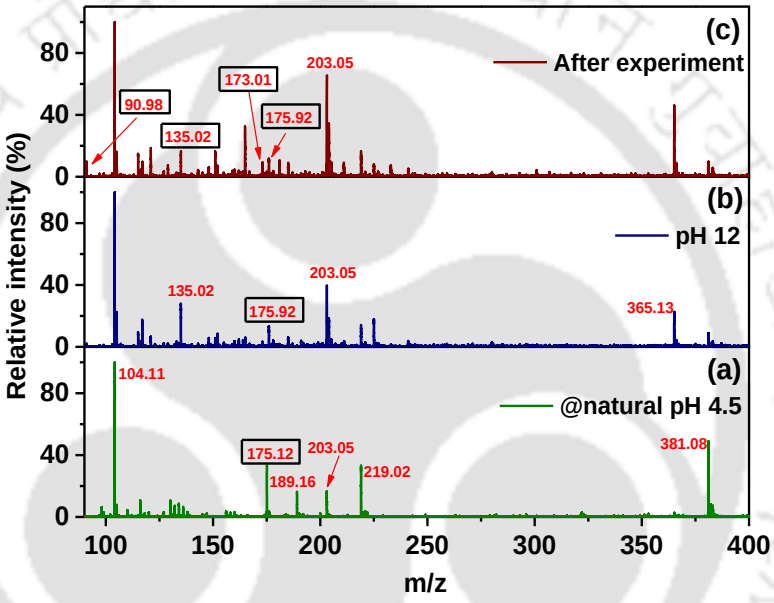

Figure 3.11. Mass spectra of the analytes extracted at (a) natural pH of 4.5, (b) at pH 12 (at which Cu_2O(bio) NPs synthesized using bio-extract), and (c) after 6 h of reaction in the presence of Cu-precursor at the synthesis pH of 12.

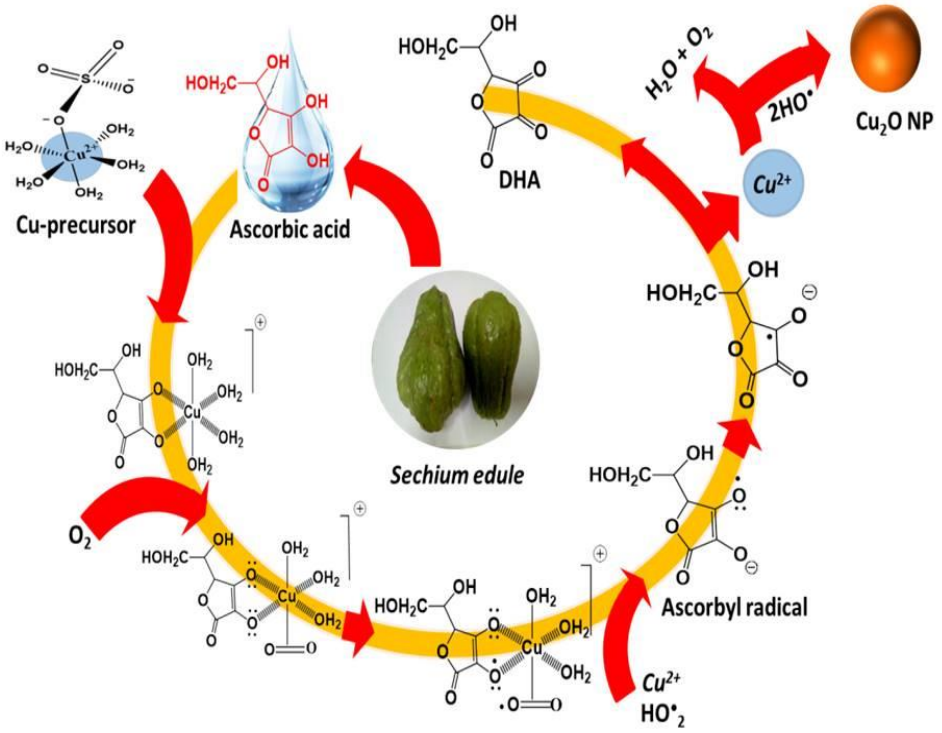

Figure 3.12. Schematic reaction pathway of Cu_2O(bio) NPs synthesis using *Sechium edule* fruit extract.

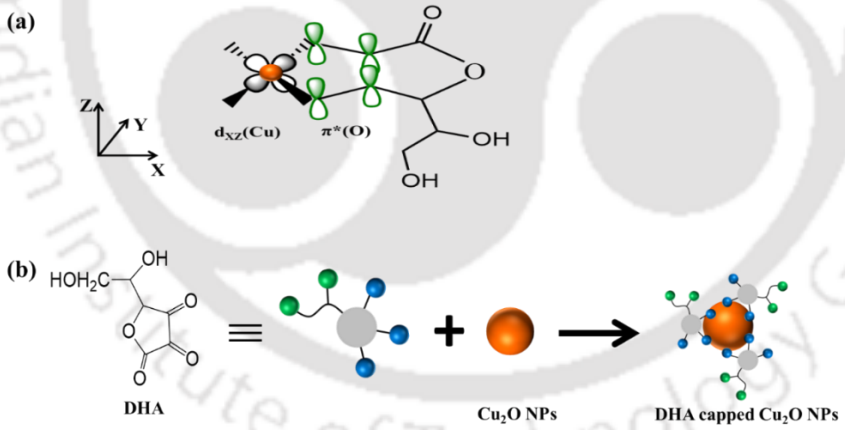

Figure 3.13. (a) π(O) orbital interaction of DHA with the d_{xz} orbital of Cu^+ ion in the surface of Cu_2O(bio) NPs, and (b) Schematic of the formation of DHA capped Cu_2O(bio) NPs.

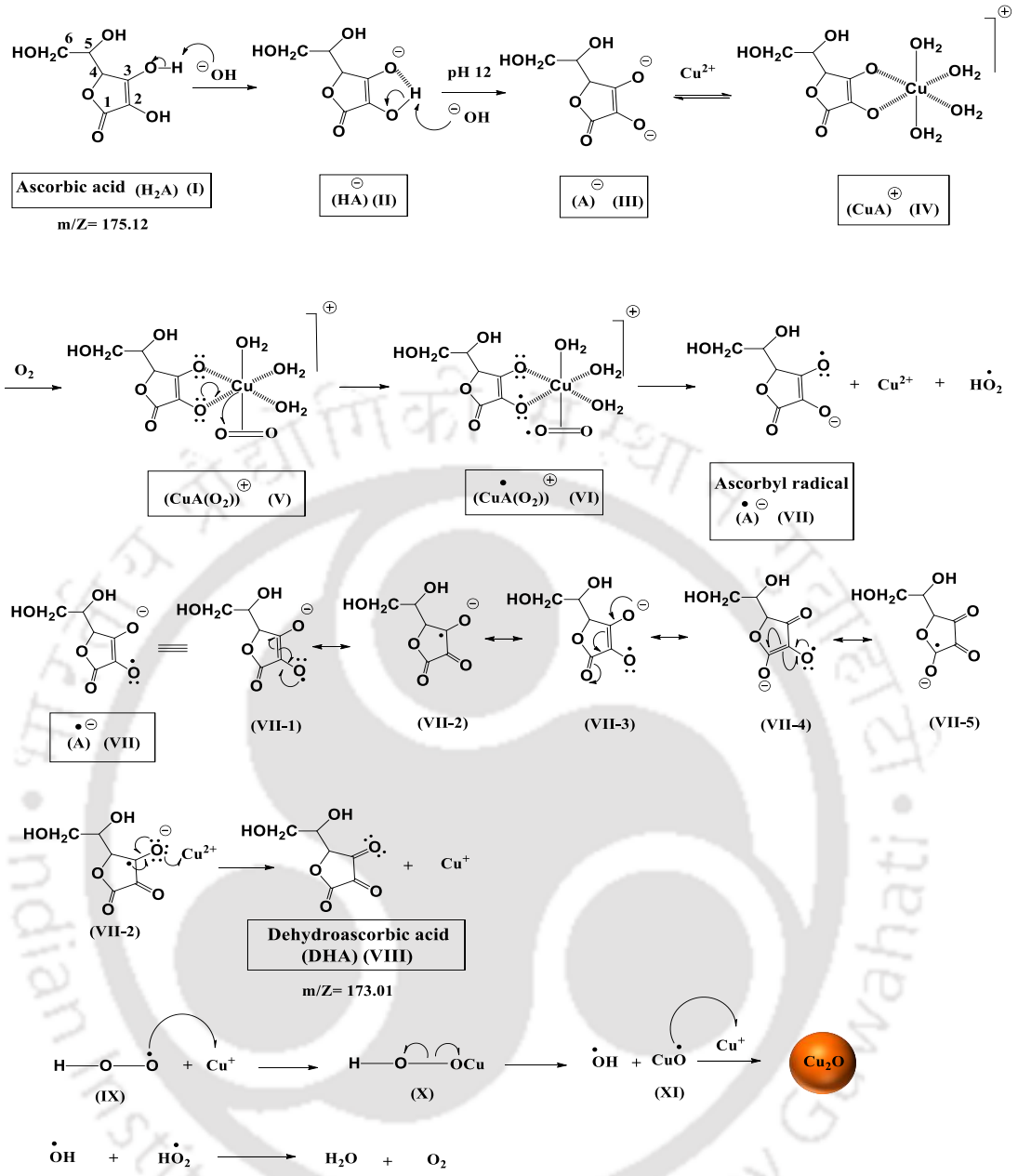

Figure 3.14. Proposed reaction mechanism for the synthesis of Cu_2O(bio) NPs using ascorbic acid as the major compound present in *Sechium edule* extract.

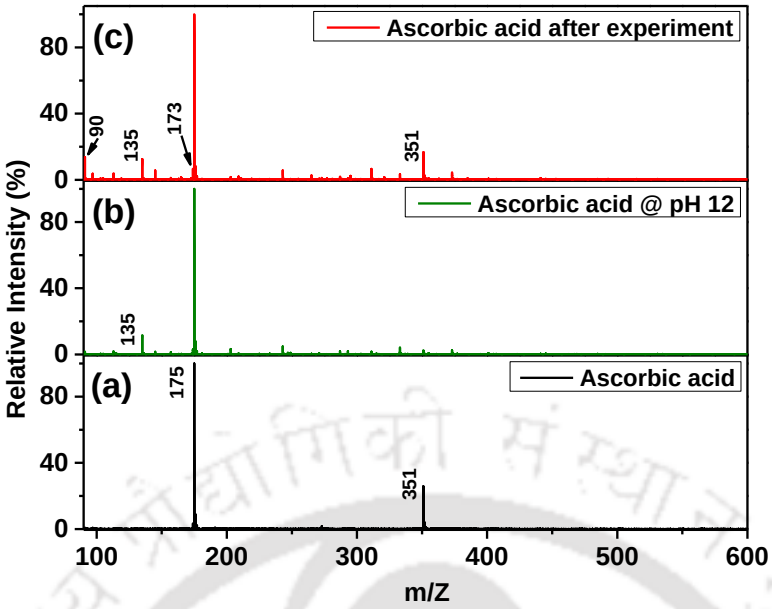

Figure 3.15. Mass spectra of (a) commercial ascorbic acid (pH 3.0), (b) ascorbic acid at pH 12 at which Cu_2O(bio) NPs synthesized, and (c) ascorbic acid after 6 h of reaction in the presence of Cu-precursor at pH 12.

3.4 Electrocatalytic activity of Cu_2O(bio) NPs

3.4.1.1 Cyclic voltammetric (CV) response

In Figure 3.16 depicts the CVs recorded with both bare TCP and Cu_2O(bio) NPs/TCP electrodes in N_2-purged and CO_2-saturated electrolytes. The scan rate was carried out at 50 mV s^{-1} in the range of 0 to −2.0 V vs. Ag/AgCl (3 M KCl) (Albo et al., 2015). The CV shows a modest hysteresis, and the onset reduction potentials were noted −1.40 V and −1.20 V, for both the TCP and Cu_2O(bio)-NPs/TCP electrodes with N_2 and CO_2 (saturation) bubbling, respectively. The increase in current density in the N_2 bubbling condition could be attributed to the water-splitting reaction. However, the current response of Cu_2O(bio)-NPs/TCP electrode was larger than the bare TCP electrode both with N_2-purged and CO_2-saturated electrolytes. A similar trend in CV curves was reported for Cu_2O(bio)-based porous carbon paper electrode by Albo et al. (2015). Furthermore, the Cu_2O(bio)-NPs/TCP electrode exhibited a slightly higher current in CO_2-saturated electrolyte than the bare TCP electrode with N_2 bubbling. The current generated in N_2 bubbling is associated with the hydrogen evolution reaction (HER) on the Cu_2O(bio) NPs/TCP electrode (Figure 3.17a). The current density reported with CO_2 bubbling is mostly of CO_2 reduction for the potential range

varying from −1.2 to −1.7 vs. Ag/AgCl (Figure 3.17b). A possible reason is that the formation of CO-intermediate during ECO_2RR could suppress the HER. A similar result is reported using Cu_2O/CuO/CuS catalyst in Ar and CO_2 saturated $KHCO_3$ solution for the formation of formate (Kahsay et al., 2019).

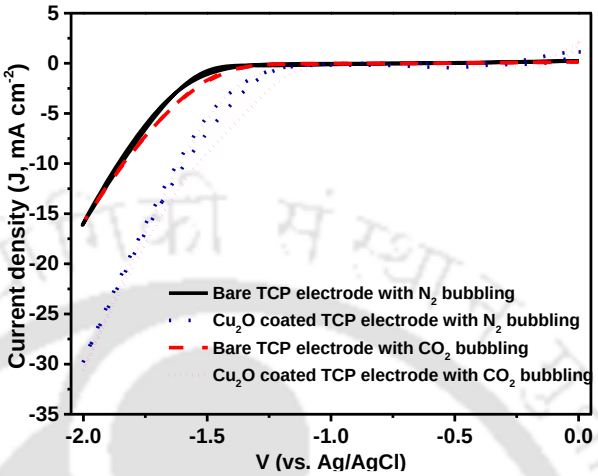

Figure 3.16. Cyclic voltammetry results (scan rate 50 mV s^{-1}) for bare TCP and Cu_2O(bio) NPs/TCP electrodes with N_2 and CO_2 (saturation) bubbling in 0.5 M $KHCO_3$ electrolyte.

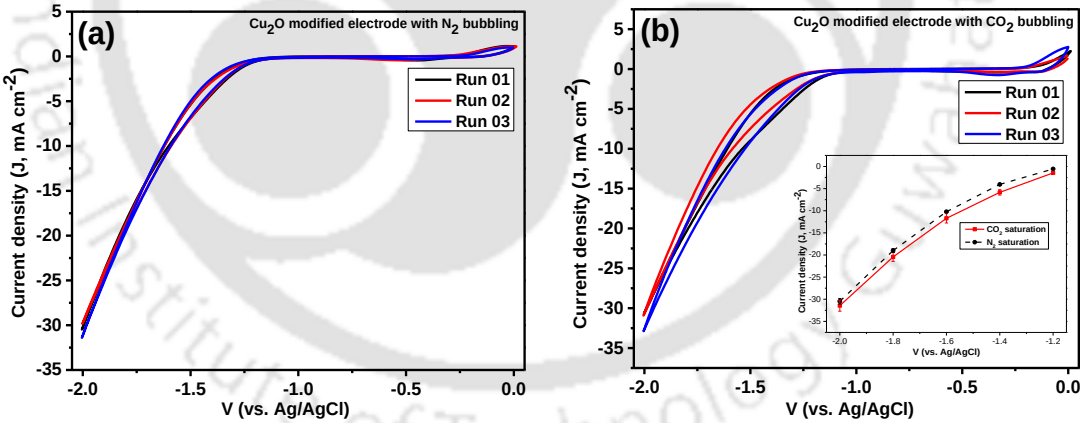

Figure 3.17. Cyclic voltammograms (scan rate 50 mV s^{-1}) for Cu_2O(bio) NPs/TCP electrode with (a) N_2, and (b) CO_2 (saturation) bubbling in 0.5 M $KHCO_3$ electrolyte at three different runs under identical condition [inset (b): Difference in current densities for Cu_2O(bio) NPs/TCP electrode at different potentials in N_2 and CO_2 saturated electrolyte].

To eliminate the effects of binder (nafion + IPA) and the residual bioactive components attached to the surface of Cu_2O(bio) NPs, on the ECO_2RR, two

controlled experiments were conducted, using only binder coated TCP electrode in CO_2 saturated and Cu_2O(bio) NPs coated TCP electrode in N_2-bubbled electrolyte keeping other conditions same. The respective current response graphs and ^1H NMR spectra are shown in Figures 3.18a-3.18b and Figures 3.19a-3.19b. The ^1H NMR spectra of the catholyte recorded at a reaction time of 3600 s didn't show any peak for the formation of $HCOO^-$ or any other reaction products, for both the experiments. It infers that $HCOO^-$ was formed by ECO_2RR catalyzed by Cu_2O(bio) NPs.

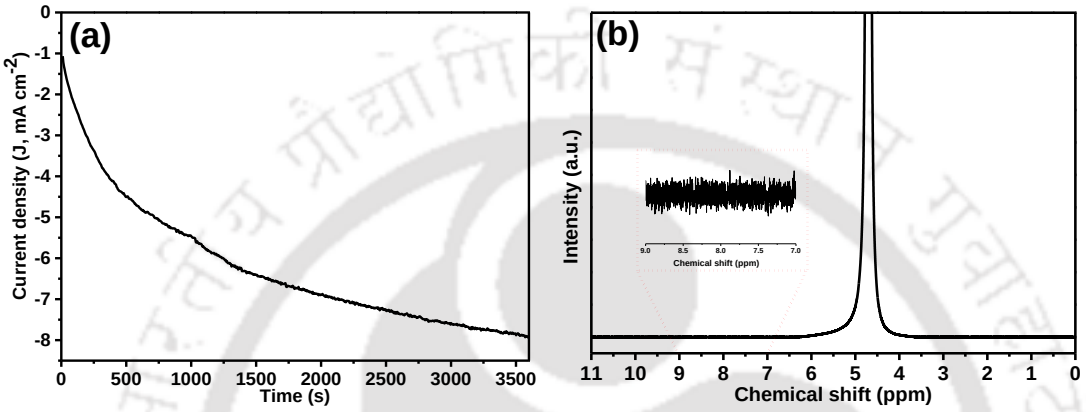

Figure 3.18. (a) Current response recorded using binder (nafion + IPA)/TCP electrode (without Cu_2O(bio) NPs catalyst) at −1.6 V vs. Ag/AgCl in CO_2-saturated 0.5 M $KHCO_3$ electrolyte for 3600 s, (b) NMR spectra of the catholyte collected after 3600 s.

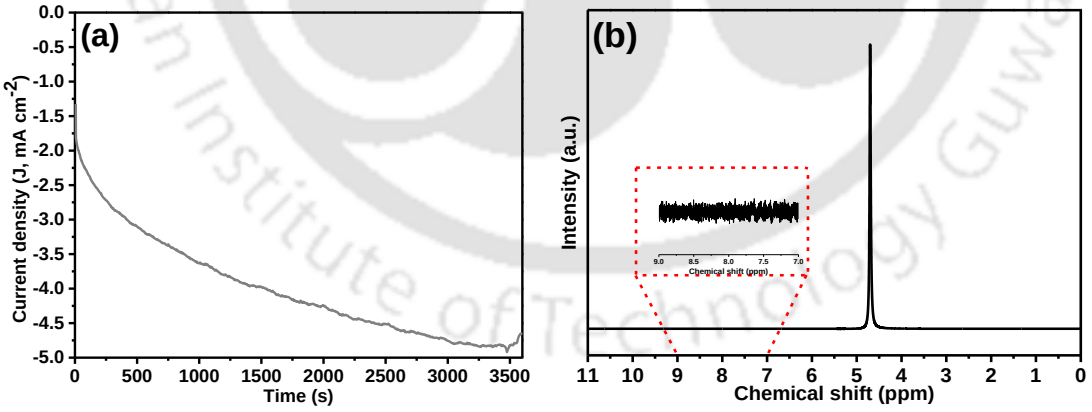

Figure 3.19. (a) Current response for Cu_2O(bio)-NPs/TCP electrode at −1.6 V vs. Ag/AgCl in N_2-bubbled 0.5 M $KHCO_3$ electrolyte for 3600 s and (b) NMR spectra of the catholyte collected after 3600 s of ECO_2RR.

The formation of $HCOO^-$ takes place in a $2e^-$ reduction pathway of CO_2 on the electro(catalytic)-activate surface of Cu_2O(bio) NPs. Adsorption of CO_2 on the

electrode surface is considered as the rate-determining step, and adsorbed CO_2 is then converted to highly reactive $CO_2^{\bullet-}$ radical through a single electron transfer reaction (Equation 3.5) (Bienen et al., 2020). The $CO_2^{\bullet-}$ radical coordinates to the Cu_2O(bio) NPs via its bidentate oxygen atoms. In the presence of HCO_3^-, the unstable $CO_2^{\bullet-}$ radical reacts with a proton and an electron forming $HCOO^-$ (Equation 3.6).

$$CO_2 + e^- \rightarrow CO_2^{\bullet-} \quad (3.5)$$

$$CO_2^{\bullet-} + H^+ + e^- \rightarrow HCOO^- \quad (3.6)$$

Electrode stability study for both bare TCP and Cu_2O(bio)-NPs/TCP electrodes were performed by using the CV analysis for 100 cycles at a scan rate of 50 mV s^{-1} in the potential range of −2 to 0 V vs. Ag/AgCl (Figures 3.20a-3.20b). A considerable increase in the current density (~19%) after 100 cycles for the Cu_2O(bio)-NPs/TCP electrode was observed, which was 65% in the case of bare TCP electrode (insets of Figure 3.20). The increase in current density for both bare TCP and Cu_2O(bio)-NPs/TCP could be due to increase in the surface porosity and/or active catalyst area (Lu et al., 2016). The surface of the Cu_2O(bio)-NPs/TCP electrode became more porous after 1 h of chronoamperometric test of CO_2 reduction and 100 cycles of CV as it is evident from FESEM micrographs (Figures 3.21a-3.21c). It can be seen that Cu_2O(bio) NPs were covered by a thin Nafion film and the inter-particles voids were full at the beginning of electrolysis. After 3600 s of chronoamperometric experiment, this film was mostly delaminated from the top surface of Cu_2O(bio)-NPs/TCP electrode without a major disintegration of Cu_2O(bio) NPs (Figure 3.21b**)**. Higher surface porosity of the electrode helped for an enhanced CO_2 mass transfer which led to an increased current density with the progress of reaction for both bare TCP and Cu_2O(bio)-NPs/TCP electrodes. Further, it can be inferred from the elemental image mappings (Figure 3.22) that the catalyst particles remained densely packed on the electrode surface after 100 cycles of CV.

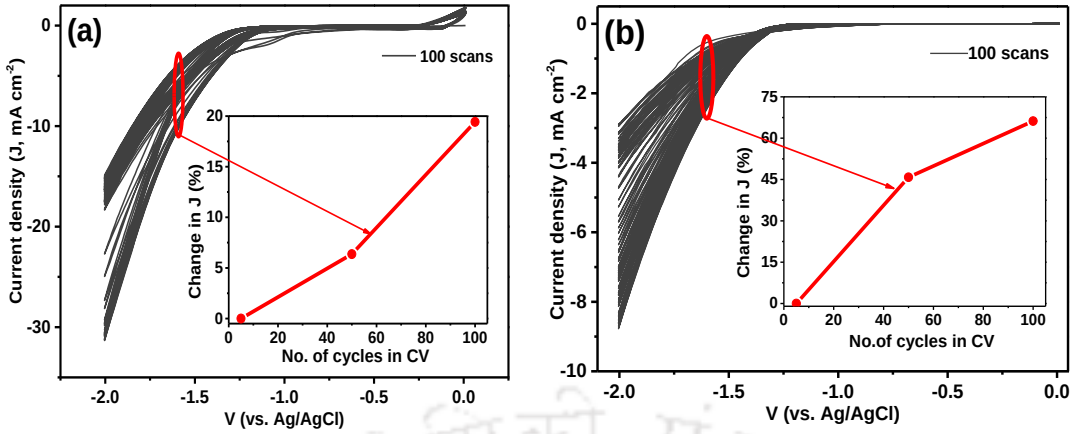

Figure 3.20. Cyclic voltammetry results for the stability analysis of the (a) Cu_2O(bio)-NPs/TCP electrode, and (b) Bare TCP electrode in CO_2-saturated 0.5 M $KHCO_3$ electrolyte for 100 cycles. Insets: the change in percentage current density with the change in the number of CV cycles.

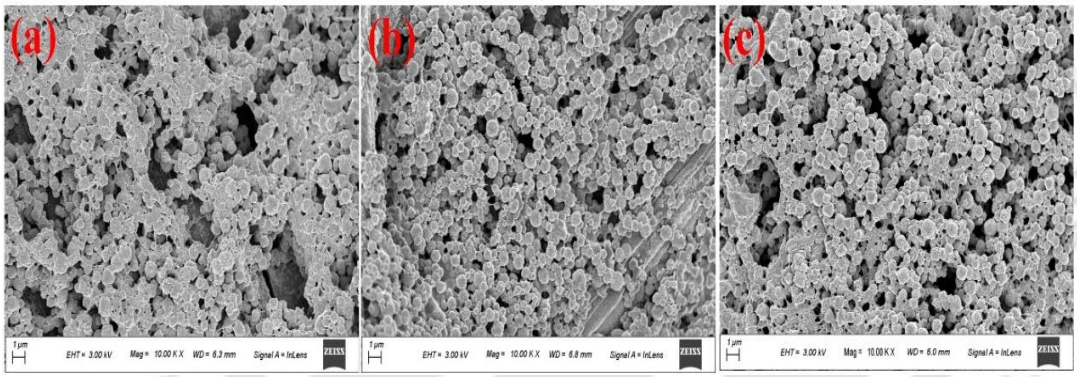

Figure 3.21. FESEM image of Cu_2O(bio) NPs/TCP electrode (a) before experiment, (b) after 1 h of chronoamperometry at −1.60 V vs. Ag/AgCl in CO_2 saturated 0.5 M $KHCO_3$ solution, and (c) after 100 scans of CV in CO_2 saturated 0.5 M $KHCO_3$ solution.

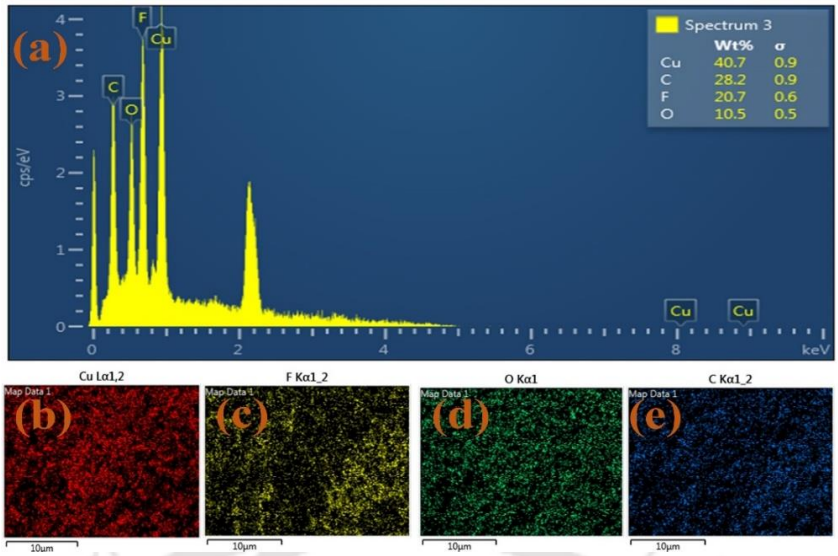

Figure 3.22. (a) Elemental analysis, and (b) – (e) mapping of Cu_2O(bio) NPs/TCP electrode after 100 scans of CV analysis.

3.4.1.2 Electrochemical Impedance spectroscopy (EIS) analysis

EIS was performed to study the electrical conductivity and charge transfer behaviour of Cu_2O(bio) NPs/TCP electrode in comparison to the support TCP both with N_2-purged and CO_2-saturated electrolyte solutions. The Nyquist plot in Figure 3.23 depicts a smaller radius for the Cu_2O(bio) NPs/TCP electrode than bare TCP electrode in CO_2-saturated electrolyte. An amplified diagram of the higher frequency region is illustrated in Figure 3.23(inset). The semicircle at a lower frequency region, obtained from the Nyquist plot corresponds to the charge transfer process and the diameter obtained, is the measure of charge transfer resistance (An et al., 2014). The equivalent electrical circuits were acquired by fitting the experimentally obtained Nyquist plots in the NOVA 1.11 software, as mentioned earlier. The corresponding circuits are shown in the insets of Figure 3.24. The fitted results are summarized in Table 3.3, with their corresponding Chi-square (χ^2) values. The equivalent electrical circuits for the bare TCP electrode both with N_2-purged and CO_2-saturated systems well fitted using the [R(RQ)] type with one Voigt element in series with the solution resistance (R_s), and that for the Cu_2O(bio)-NPs/TCP electrode in both N_2 and CO_2 systems was the [R(RQ)(RQ)] type with two Voigt elements in series with R_s (Sacco, 2017). The charge transfer resistance (R_1) and the constant phase element (CPE, Q_1) are associated with the transport properties within the catalyst. Whereas, the other

resistance (R_2) and the CPE (Q_2) are associated with the reduction reactions on the catalyst surface. The R_s values obtained were <10 Ω, which is in accordance with the reported values of 3.4–33 Ω (Ahn et al., 2017). The lower value of solution resistance is due to the higher concentration of electrolyte used in the CO_2RR (Bard and Faulkner, 2000). All the CPEs, N>0.5 was employed so that the CPEs behave more like a capacitor, where N is the phase shift (value in the range of 0 to 1, the CPE behaves like a pure resistor and pure capacitor at the value of 0 and 1, respectively) (Bard and Faulkner, 2000). The significantly smaller resistance of the Cu_2O(bio)-NPs/TCP electrode in CO_2-saturated electrolyte further indicates an appreciable charge transfer (R_1= 296.6 Ω) from the catalyst surface to the electrolyte solution. The bare TCP electrode showed lower impedance in both the environments (N_2-purged and CO_2-saturated) than the Cu_2O(bio)-NPs/TCP electrodes. Additionally, both the bare TCP and Cu_2O(bio)-NPs/TCP electrodes lowered down impedances in N_2 environment than that in the CO_2 environment.

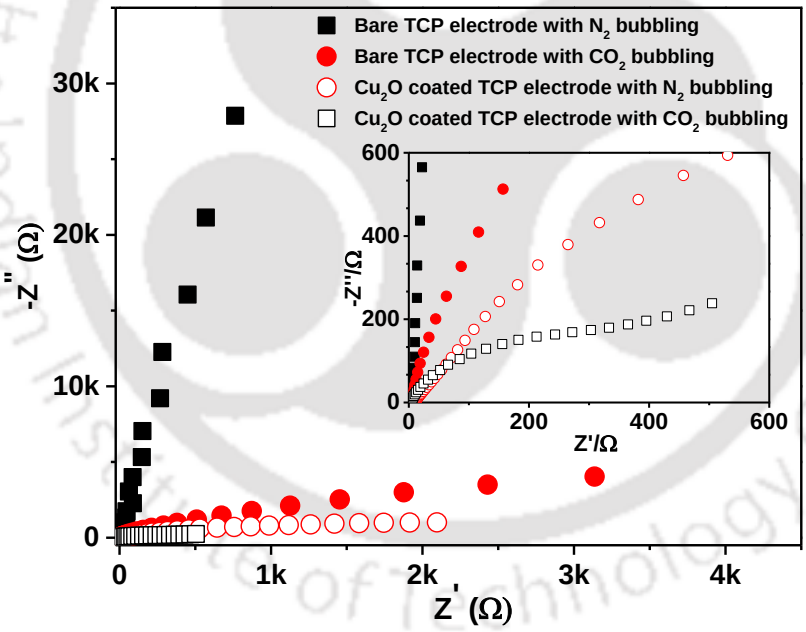

Figure 3.23. Nyquist plot for bare TCP and Cu_2O(bio) NPs/TCP electrode in N_2-purged and CO_2-saturated 0.5 M $KHCO_3$ electrolyte.

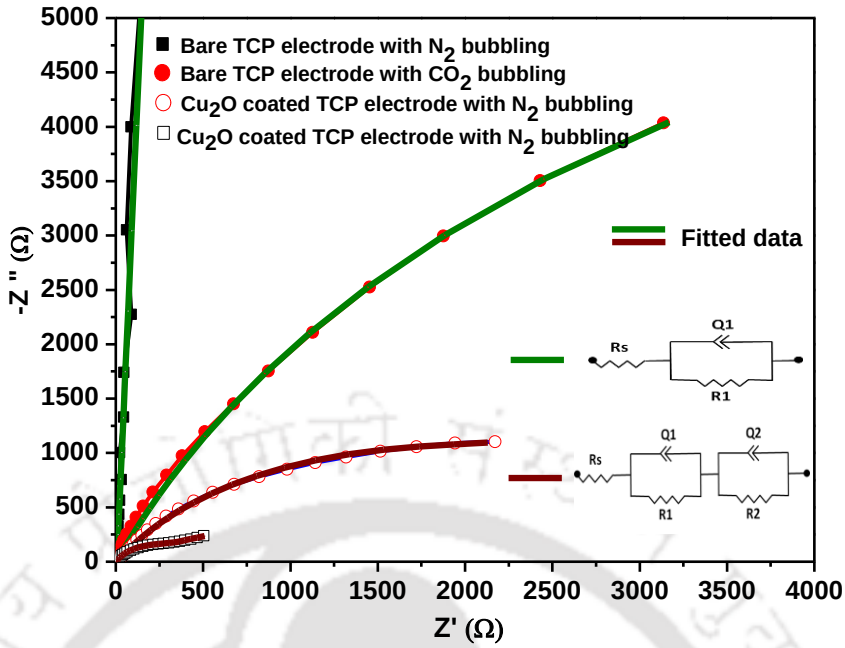

Figure 3.24. Fitted graphs of Nyquist plots for bare TCP and Cu_2O(bio) NPs/TCP electrode in N_2-purged and CO_2-saturated 0.5 M $KHCO_3$ electrolyte.

Table 3.3. Values of the elements in equivalent electric circuit fitted in Nyquist plots of Figure 3.24.

Electrical circuit elements		*TCP electrode in N_2	TCP electrode in CO_2	Cu_2O(bio) coated TCP electrode in N_2	Cu_2O(bio) coated TCP electrode in CO_2
Rs (Ω)		6.00	6.08	7.46	3.18
R1 (Ω)		1.1×10^{12}	14923.00	1560.20	296.60
R2 (Ω)		—	—	1686.40	889.64
Q1	Y0 (Mho)	4.3×10^{-05}	0.000234	0.0012	0.00053
	N	0.98	0.78	0.91	0.77
Q2	Y0 (Mho)	—	—	0.00023	0.00352
	N	—	—	0.73	0.67
χ^2		0.000961	0.030	0.0072	0.008

*TCP: Toray carbon paper

3.4.1.3 Electrochemical CO_2 reduction reaction (ECO_2RR)

The characteristic redox peak of ECO_2RR could not be identified in the cyclic voltammetric analysis. From the voltammogram, the variation in current density in the case of Cu_2O(bio) NPs/TCP electrode both in N_2 and CO_2 saturated electrolyte also

could not be concluded during ECO_2RR. Therefore, the chronoamperometric test was carried out at different potentials of −1.55, −1.60, −1.70, and −1.80 V vs. Ag/AgCl in CO_2-saturated 0.5 M $KHCO_3$ electrolyte for an electrolysis time of 3600 s. Figure 3.25 compares the Faradaic efficiencies (FE). At different potentials, FE of the liquid product was calculated using the following relation (Equation 3.7).

$$FE\ (\%) = \frac{znF}{Q} \times 100 \tag{3.7}$$

Where, z is the number of electrons required for the product evolution, n is the number of moles of the desired products, F is Faradaic constant (96485 C mol^{-1}), and Q is the total charge transfer ($=\int_0^t Idt$, I is the total current response in time, t). FE of H_2 was calculated using the Equation 3.8 (Wang et al., 2018).

$$FE = \frac{F \times 2 \times mol\ H_2}{total\ Q\ (= I \times t)} \times 100 \tag{3.8}$$

At −1.55 V vs. Ag/AgCl, FE of formate production was found to be 12.8% against the total FE of ~58%, and below this potential, no formate production was found.

CO_2 to product formation takes place in multi electron transfer process (from 2 to 12 or more than that). Therefore, the selectivity of product formation depends on the reaction pathway and the stability of the intermediates formed. The reduction of CO_2 on the Cu_2O catalyst surface leads to two competitive reactions involving two electron transfer process i.e., formation of CO and formate ($HCOO^-$). The CO formation occurs via *COOH intermediate pathway and the $HCOO^-$ formation occurs via *OCHO pathway. CO_2 to $HCOO^-$ formation upon adsorption of CO_2 on the electrode surface occurs via the following the five steps (Rabiee et al., 2021).

$$CO_2(g) \rightarrow {CO_2}^*_{(ads)} \tag{3.9}$$

$${CO_2}^*_{(ads)} + 6e^- \rightarrow {CO_2}^{*-}_{(ads)} \tag{3.10}$$

$${CO_2}^{*-}_{(ads)} + H^+ \rightarrow {}^*OCHO_{(ads)} \tag{3.11}$$

$${}^*OCHO_{(ads)} + e^- \rightarrow HCOO^{*-}_{(ads)} \tag{3.12}$$

$$HCOO^{*-}_{(ads)} + e^- \rightarrow HCOO^-_{(aq)} \tag{3.13}$$

Where, the rate-determining step is the protonation of ${CO_2}^{*-}_{(ads)}$ in the step 3. The density function theory calculation of Gibbs free energy (ΔG) for *OCHO and *COOH, on Cu_2O (111) facet is reported to be 0.47 and 0.51 eV, respectively (Ma et al., 2023). This suggested that the $HCOO^-$ formation pathway is more energetically favorable on Cu_2O (111) NPs.

In electrochemical CO_2 reduction, several literatures report on the shortfall of total FE due to H_2 leakage from the electrolysis cell (Natsui et al., 2018), electrolyte resistance at low current density (Yodwong et al., 2020), and unwanted electrode reactions or ion-transport occur through proton exchange membrane (Muroyama et al., 2020). Natsui et al. (2018) reported total FE of 76.6% due to H_2 leakage, using diamond electrode for ECO_2RR. Yamamoto et al. (2000) used activated carbon fibers/Cu and non-activated carbon fibers/Fe electrodes for CO_2 reduction, and reported total FE of 52.9 and 69.6%, respectively (Yamamoto et al., 2000). Li et al. (2018) found total FE of 60% using microporous carbon containing heterogenous N_2 as a working electrode for CO_2 reduction.

The highest FE was found to be 65.3% at −1.60 V vs. Ag/AgCl (Specimen calculation can be found in Table A1.1 in Appendix-I). FE was then fell sharply. The overpotential required to drive the formate production could be not sufficient below −1.60 V (vs. Ag/AgCl) (Gupta et al., 2016), and the sharp fall of FE could be due to the competitive CO_2 reduction reaction with the water splitting reaction at a lower potential due to the faster migration rate of H^+ than CO_2 leading to the reduction to H_2 at a faster rate than ECO_2RR (Li et al., 2016; Wu et al., 2018) . A similar trend in FE for the formate production was also reported for ECO_2RR using Bi/C NPs (Ávila-Bolívar et al., 2019). FE for H_2 production was 24.7% at the −1.60 V, and it increased to 88.5% at −1.80 V. At −1.60 V vs. Ag/AgCl, the Cu_2O-AA/TCP electrode exhibited FE of 66.6% for formate production (^{1}H NMR, Figure A1.1a in Appendix-I). Figure A1.1b in Appendix-I shows the gas chromatogram of the collected gas sample, which indicates the presence of only H_2 gas as a gaseous product from water splitting. The chronoamperograms at −1.60 V are shown in Figure A1.2 in Appendix-I. The current response was increased with the electrolysis time (Figure A1.2 in Appendix-I), and a similar explanation provided earlier (Figure 3.20) is also applicable here. The controlled experiment using bare TCP electrode which was conducted at −1.60 V vs. Ag/AgCl also exhibited a similar trend (Figure A1.2 in Appendix-I). Only H_2 was formed with 75% FE and no product was detected in the ^{1}H NMR spectra (Figure A1.3 in Appendix-I). The chronoamperogram in the case of Cu_2O-AA/TCP electrode is shown in Figure A1.2 in Appendix-I. An initial decrease in the current density could be attributed to the capacitive charge transfer at the electrode surface-electrolyte interface (Firat and Peksoz, 2017). In fact, formate formation was carried out

continuously for 2 h at the fixed applied potential of −1.60 V vs. Ag/AgCl (Figure A1.4 in Appendix-I). The liquid samples were analyzed in 1H NMR at different time intervals (15-120 min) (Figure A1.5 in Appendix-I). FEs for the formate formation at different time intervals are shown in Figure A1.6 in Appendix-I. The maximum FE was found to be 65.3% at 60 min, after that it decreased to 64% at 2 h. Figure A1.7 in Appendix-I shows the total current density (J) and partial current density for the formate formation (j_{HCOO^-}). The J value (formate and H_2) increases with the increase in cathodic potential, whereas the j_{HCOO^-} values are in accordance with the FE of formate, and reached the maximum of 7.6 mA cm^{-2} at −1.60 V (vs. Ag/AgCl).

Single carbon oxygenated product ($HCOO^-$/HCOOH), or a mixture of carbon oxygenates and HCs products ($HCOO^-$/HCOOH, CO, CH_4, C_2H_4, C_2H_6, EtOH) could be formed using Cu_2O(bio) nanomaterials in the ECO_2RR process (Table 3.4). The FEs (%) of $HCOO^-$/HCOOH are found to be 4–67.6% at an overpotential in the range of 0.53 to 1.08 V (vs. Ag/AgCl). In this study, the FE 65.3% of $HCOO^-$ formation was achieved at −1.60 V (vs. Ag/AgCl), which either is comparable or better than most of the earlier studies (Table 3.4).

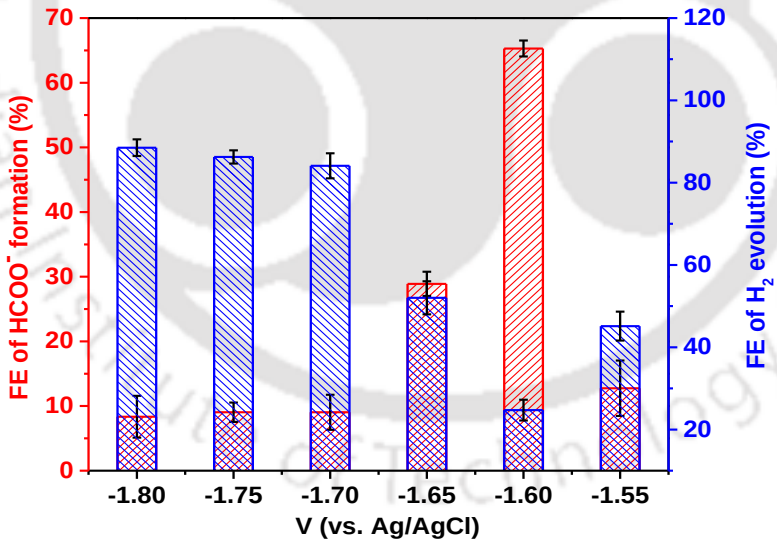

Figure 3.25. Faradaic efficiency (%) of formate and H_2 formation at different applied potentials (V vs. Ag/AgCl). The left Y-axis represents the FE for formate formation and the right Y-axis represents the FE of H_2 formation, and their summation gives the total FE.

Figure 3.26 shows the yield and selectivity of formate formation at different applied potentials (V vs. Ag/AgCl). The yield of formate formation increases from –

1.55 to –1.60 V (vs. Ag/AgCl) and then it falls down thereafter. The maximum yield was found to be 56.8 μmol g^{-1} h^{-1} at –1.60 V (vs. Ag/AgCl). The selectivity of formate formation follows the similar trend. The highest selectivity was found to be 72.5% at the same applied potential.

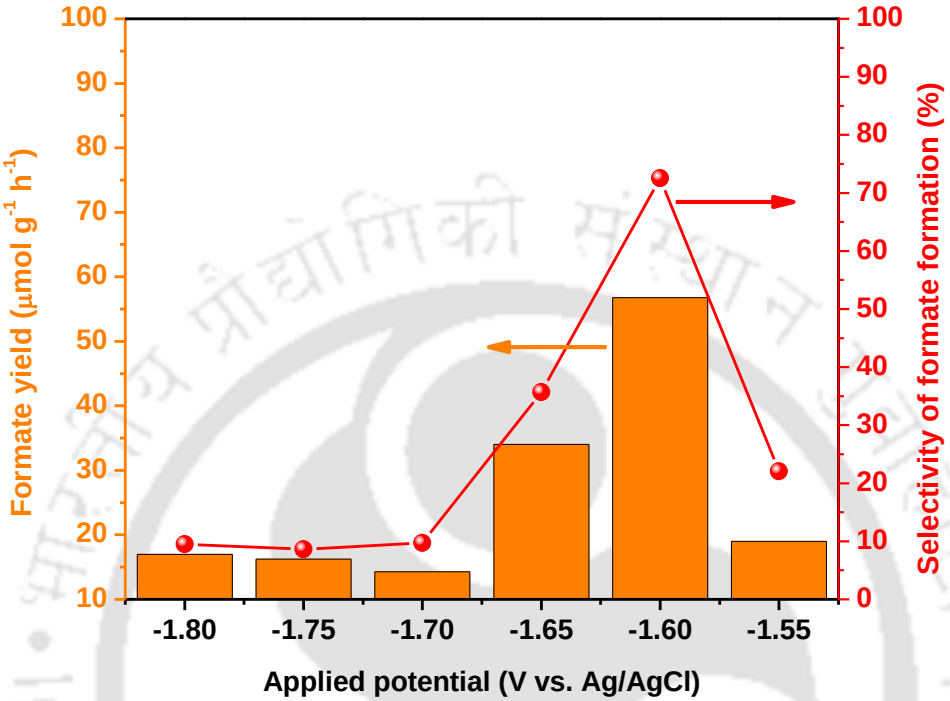

Figure 3.26. Yield and selectivity of formate formation on Cu_2O(bio) NPs/TCP electrode at different applied potentials (vs. Ag/AgCl).

Figure 3.27 shows Cu-based electrocatalysts of varying sizes and shapes used for ECO_2RR forming different useful products.

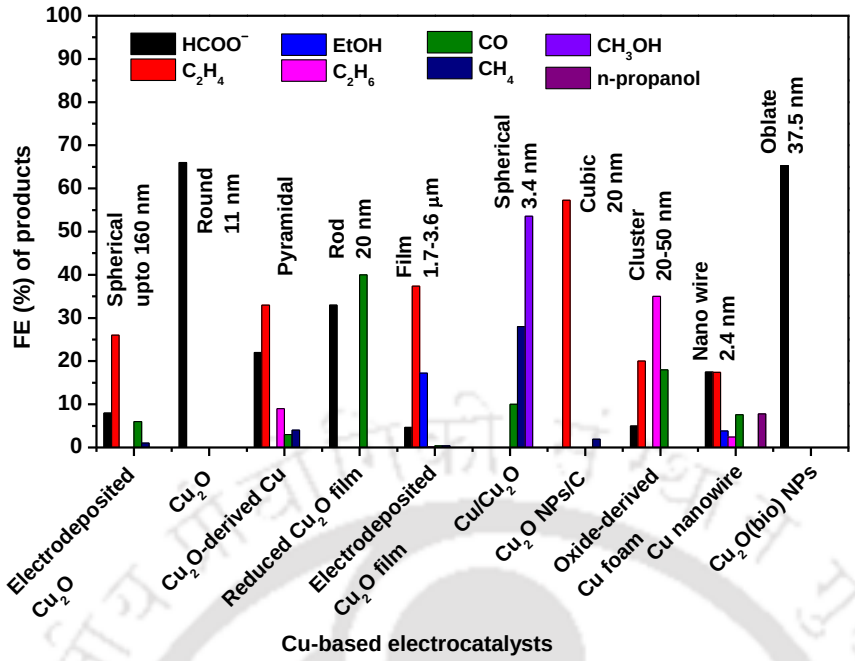

Figure 3.27. Cu-based electrocatalysts of varying sizes and shapes used for ECO_2RR forming different useful products.

Table 3.4. An overview of Faradaic efficiencies of products obtained from ECO_2RR using Cu_2O(bio) NPs/TCP electrode.

Catalyst	Electrolyte	Test condition	FE (%)						Source
			$HCOO^-$ /HCO_2H	C_2H_4	EtOH	C_2H_6	CO	CH_4	
Cu_2O(bio) using *S. edule* fruit extract	0.5 M $KHCO_3$	−1.6 V vs. Ag/AgCl	65.3/—	—	—	—	—	—	**Present work**
Cu_2O/CuS composite	0.1 M $KHCO_3$	−0.9 V vs. RHE	67.6/—	—	N.A.*	—	—	—	Wang et al. (2021)
Cu_2O using Continuous Hydrothermal Flow synthesis method	0.5 M $KHCO_3$	−0.8 V vs. RHE	66/—	—	—	—	—	—	Zhu et al. (2018)
Electrodeposited Cu_2O	0.5 M $KHCO_3$	−1.82 V vs. Ag/AgCl	—/8	26	—	—	6	1	Kim et al. (2015)
Electrodeposited Cu_2O	0.1 M $KHCO_3$	−1.1 V vs. RHE	—/22	12-33	—	0-9	1-3	0-4	Kas et al. (2014)
Reduced Cu_2O film	0.5 M $NaHCO_3$	−0.55 V vs. RHE	—/ 33	—	—	—	40	—	Li and Kanan (2012)
Electrodeposited Cu_2O film	0.1 M $KHCO_3$	−0.99 V vs. RHE	4.66/—	37.48	17.22	0.10	0.37	0.36	Ren et al. (2015)
Cu_2O	0.1 M $KHCO_3$	−0.5 V vs. RHE	—/ 35	—	—	—	—	—	Li and Kanan (2012)

* NA: not available

3.5 Major findings

Synthesis of oblate shaped mesoporous Cu_2O(bio) NPs (average diameter 37.5-42 nm and surface area 16.1 m^2 g^{-1}) has been successfully carried out in an environmentally benign process using S*echium edule* fruit extract rich in ascorbic acid (AA) for electrocatalytic reduction of CO_2. The morphology and crystallinity of Cu_2O(bio) NPs synthesized using bio-analytes was strongly comparable with its counterpart synthesized using pure AA, and dehydroascorbic acid (DHA) was originated which could act as a capping agent through the formation of DHA-Cu ligand via ascorbyl radical intermediate. Nevertheless, XPS analysis showed the presence of amorphous CuO on the surface of Cu_2O(bio) NPs which was left undetectable in X-ray diffraction.

Cu_2O(bio) NPs modified Toray carbon paper electrode was effective in a reduced charge transfer resistance (by 98%) and improved product specificity. CO_2 was chemisorbed at the electrode surface along with C-O(H) and $HCOO^-$ as evident from the overlapping peak at 530.9 eV identified in the XPS spectra. The synthesized Cu_2O(bio) NPs could result in selective ECO_2RR for the formation of formate due to the presence of predominant (111) crystal plane as evidenced from XRD and HRTEM analyses.

Both bio- and AA- mediated Cu_2O NPs catalyzed CO_2 reduction to formate as the sole liquid product. However, a declining activity of Cu_2O(bio) NPs in catalyzing CO_2 reduction could be observed with prolong electrolysis owing to its oxidation to CuO. The maximum current efficiency of formate formation in 60 min of the reaction was around 65.3-66.6% against 24% H_2 evolution from the chronoamperometric test using both the nanocatalysts.

References

Ahn, S.T., Abu-Baker, I., Palmore, G.T.R., 2017. Electroreduction of CO_2 on polycrystalline copper: Effect of temperature on product selectivity. Catal. Today 288, 24–29. https://doi.org/10.1016/j.cattod.2016.09.028

Albo, J., Sáez, A., Solla-Gullón, J., Montiel, V., Irabien, A., 2015. Production of methanol from CO_2 electroreduction at Cu_2O and Cu_2O/ZnO-based electrodes in aqueous solution. Appl. Catal. B Environ. 176–177, 709–717. https://doi.org/10.1016/j.apcatb.2015.04.055

An, X., Li, K., Tang, J., 2014. Cu_2O/reduced graphene oxide composites for the photocatalytic conversion of CO_2. ChemSusChem 7, 1086–1093. https://doi.org/10.1002/cssc.201301194

Avendaño, C., Menéndez, J.C., 2015. Cancer Chemoprevention, in: Medicinal Chemistry of Anticancer Drugs. Elsevier, pp. 701–723. https://doi.org/10.1016/B978-0-444-62649-3.00015-6

Ávila-Bolívar, B., García-Cruz, L., Montiel, V., Solla-Gullón, J., 2019. Electrochemical reduction of CO_2 to formate on easily prepared carbon-supported bi nanoparticles. Molecules 24, 2032. https://doi.org/10.3390/molecules24112032

Bard, A.J., Faulkner, L.R., 2000. Electrochemical methods: Fundamentals and applications, Second. ed, John Wiley & Sons, INC. John Wiley & Sons, INC., New York.

Bhaumik, A., Shearin, A.M., Patel, R., Ghosh, K., 2014. Significant enhancement of optical absorption through nano-structuring of copper based oxide semiconductors: possible future materials for solar energy applications. Phys. Chem. Chem. Phys. 16, 11054–11066. https://doi.org/10.1039/C4CP00827H

Bhosale, M.A., Bhanage, B.M., 2016. A simple approach for sonochemical synthesis of Cu_2O nanoparticles with high catalytic properties. Adv. Powder Technol. 27, 238–244. https://doi.org/10.1016/j.apt.2015.12.008

Bienen, F., Kopljar, D., Geiger, S., Wagner, N., Friedrich, K.A., 2020. Investigation of CO_2 electrolysis on tin foil by electrochemical impedance spectroscopy. ACS Sustain. Chem. Eng. 8, 5192–5199. https://doi.org/10.1021/acssuschemeng.9b07625

Brookshier, M.A., Chusuei, C.C., Goodman, D.W., 1999. Control of CuO particle size

on SiO_2 by spin coating. Langmuir 15, 2043–2046. https://doi.org/10.1021/la981325k

Chelli, V.R., Golder, A.K., 2018. One pot green synthesis of Pt, Co and Pt@Co core-shell nanoparticles using Sechium edule. J. Chem. Technol. Biotechnol. 94, 911–918. https://doi.org/10.1002/jctb.5838

Das, R.K., Golder, A.K., 2017. Co_3O_4 spinel nanoparticles decorated graphite electrode: Bio-mediated synthesis and electrochemical H_2O_2 sensing. Electrochim. Acta 251, 415–426. https://doi.org/10.1016/j.electacta.2017.08.122

Eslami, S., Ebrahimzadeh, M.A., Biparva, P., 2018. Green synthesis of safe zero valent iron nanoparticles by myrtus communis leaf extract as an effective agent for reducing excessive iron in iron-overloaded mice, a thalassemia model. RSC Adv. 8, 26144–26155. https://doi.org/10.1039/C8RA04451A

Favaro, M., Xiao, H., Cheng, T., Goddard, W.A., Yano, J., Crumlin, E.J., 2017. Subsurface oxide plays a critical role in CO_2 activation by Cu(111) surfaces to form chemisorbed CO_2 , the first step in reduction of CO_2. Proc. Natl. Acad. Sci. 114, 6706–6711. https://doi.org/10.1073/pnas.1701405114

Firat, Y.E., Peksoz, A., 2017. Efficiently two-stage synthesis and characterization of CuSe/polypyrrole composite thin films. J. Alloys Compd. 727, 177–184. https://doi.org/10.1016/j.jallcom.2017.08.095

Firmansyah, D.A., Kim, T., Kim, S., Sullivan, K., Zachariah, M.R., Lee, D., 2009. Crystalline phase reduction of cuprous oxide (Cu_2O) nanoparticles accompanied by a morphology change during ethanol-assisted spray pyrolysis. Langmuir 25, 7063–7071. https://doi.org/10.1021/la9001175

Gupta, K., Bersani, M., Darr, J.A., 2016. Highly efficient electro-reduction of CO_2 to formic acid by nano-copper. J. Mater. Chem. A 4, 13786–13794. https://doi.org/10.1039/C6TA04874A

Han, Z., Kortlever, R., Chen, H.-Y., Peters, J.C., Agapie, T., 2017. CO_2 Reduction Selective for C ≥2 Products on Polycrystalline Copper with N-Substituted Pyridinium Additives. ACS Cent. Sci. 3, 853–859. https://doi.org/10.1021/acscentsci.7b00180

Holade, Y., Hickey, D.P., Minteer, S.D., 2016. Halide-regulated growth of electrocatalytic metal nanoparticles directly onto a carbon paper electrode. J. Mater. Chem. A 4, 17154–17162. https://doi.org/10.1039/C6TA08288B

Kahsay, A.W., Ibrahim, K.B., Tsai, M.-C., Birhanu, M.K., Chala, S.A., Su, W.-N., Hwang, B.-J., 2019. Selective and low overpotential electrochemical CO_2 reduction to formate on CuS decorated CuO heterostructure. Catal. Letters 149, 860–869. https://doi.org/10.1007/s10562-019-02657-2

Kas, R., Kortlever, R., Milbrat, A., Koper, M.T.M., Mul, G., Baltrusaitis, J., 2014. Electrochemical CO_2 reduction on Cu_2O-derived copper nanoparticles: Controlling the catalytic selectivity of hydrocarbons. Phys. Chem. Chem. Phys. 16, 12194–12201. https://doi.org/10.1039/c4cp01520g

Khan, M.M.T., Martell, A.E., 1967. Metal ion and metal chelate catalyzed oxidation of ascorbic acid by molecular oxygen. I. cupric and ferric chelate catalyzed oxidation. J. Am. Chem. Soc. 89, 7104–7111. https://doi.org/10.1021/ja01002a046

Kim, D., Lee, S., Ocon, J.D., Jeong, B., Lee, J.K., Lee, J., 2015. Insights into an autonomously formed oxygen-evacuated Cu_2O electrode for the selective production of C_2H_4 from CO_2. Phys. Chem. Chem. Phys. 17, 824–830. https://doi.org/10.1039/c4cp03172e

Lemishko, S.S., Lemishko, A.S., 2017. Cu^{2+}/Cu^{+} redox battery utilizing low-potential external heat for recharge. J. Phys. Chem. C 121, 3234–3240. https://doi.org/10.1021/acs.jpcc.6b12317

Li, C.W., Kanan, M.W., 2012. CO_2 reduction at low overpotential on Cu electrodes resulting from the reduction of thick Cu_2O films. J. Am. Chem. Soc. 134, 7231–7234. https://doi.org/10.1021/ja3010978

Li, Q., Zhu, W., Fu, J., Zhang, H., Wu, G., Sun, S., 2016. Controlled assembly of Cu nanoparticles on pyridinic-N rich graphene for electrochemical reduction of CO_2 to ethylene. Nano Energy 24, 1–9. https://doi.org/10.1016/j.nanoen.2016.03.024

Li, W., Fechler, N., Bandosz, T.J., 2018. Chemically heterogeneous nitrogen sites of various reactivity in porous carbons provide high stability of CO_2 electroreduction catalysts. Appl. Catal. B Environ. 234, 1–9. https://doi.org/10.1016/j.apcatb.2018.04.021

Liu, D., Hu, Y., Shoko, E., Yu, H., Isimjan, T.T., Yang, X., 2021. High selectivity of CO_2 conversion to formate by porous copper hollow fiber: microstructure and pressure effects. Electrochim. Acta 365, 137343. https://doi.org/10.1016/j.electacta.2020.137343

Lu, J., Xiong, T., Zhou, W., Yang, L., Tang, Z., Chen, S., 2016. Metal nickel foam as an efficient and stable electrode for hydrogen evolution reaction in acidic electrolyte under reasonable overpotentials. ACS Appl. Mater. Interfaces 8, 5065–5069. https://doi.org/10.1021/acsami.6b00233

Ma, X., Zhang, Y., Fan, T., Wei, D., Huang, Z., Zhang, Zhihao, Zhang, Zheng, Dong, Y., Hong, Q., Chen, Z., Yi, X., 2023. Facet dopant regulation of Cu_2O boosts electrocatalytic CO_2 reduction to formate. Adv. Funct. Mater. 2213145, 1–13. https://doi.org/10.1002/adfm.202213145

Muroyama, A.P., Pătru, A., Gubler, L., 2020. Review—CO_2 separation and transport via electrochemical methods. J. Electrochem. Soc. 167, 133504. https://doi.org/10.1149/1945-7111/abbbb9

Natsui, K., Iwakawa, H., Ikemiya, N., Nakata, K., Einaga, Y., 2018. Stable and highly efficient electrochemical production of formic acid from carbon dioxide using diamond electrodes. Angew. Chemie 130, 2669–2673. https://doi.org/10.1002/ange.201712271

Nguyen, D.C.T., Cho, K.Y., Oh, W.-C., 2017. Synthesis of mesoporous SiO_2 /Cu_2O–graphene nanocomposites and their highly efficient photocatalytic performance for dye pollutants. RSC Adv. 7, 29284–29294. https://doi.org/10.1039/C7RA03526H

Nikam, A. V., Arulkashmir, A., Krishnamoorthy, K., Kulkarni, A.A., Prasad, B.L. V., 2014. pH-dependent single-step rapid synthesis of CuO and Cu_2O nanoparticles from the same precursor. Cryst. Growth Des. 14, 4329–4334. https://doi.org/10.1021/cg500394p

Nitopi, S., Bertheussen, E., Scott, S.B., Liu, X., Engstfeld, A.K., Horch, S., Seger, B., Stephens, I.E.L., Chan, K., Hahn, C., Nørskov, J.K., Jaramillo, T.F., Chorkendorff, I., 2019. Progress and perspectives of electrochemical CO_2 reduction on copper in aqueous electrolyte. Chem. Rev. 119, 7610–7672. https://doi.org/10.1021/acs.chemrev.8b00705

Odling, G., Ivaturi, A., Chatzisymeon, E., Robertson, N., 2018. Improving carbon-coated TiO_2 films with a $TiCl_4$ treatment for photocatalytic water purification. ChemCatChem 10, 234–243. https://doi.org/10.1002/cctc.201700867

Rabiee, H., Ge, L., Zhang, X., Hu, S., Li, M., Smart, S., Zhu, Z., Wang, H., Yuan, Z., 2021. Stand-alone asymmetric hollow fiber gas-diffusion electrodes with

distinguished bronze phases for high-efficiency CO_2 electrochemical reduction. Appl. Catal. B Environ. 298, 120538. https://doi.org/10.1016/j.apcatb.2021.120538

Ren, D., Deng, Y., Handoko, A.D., Chen, C.S., Malkhandi, S., Yeo, B.S., 2015. Selective electrochemical reduction of carbon dioxide to ethylene and ethanol on copper(I) oxide catalysts. ACS Catal. 5, 2814–2821. https://doi.org/10.1021/cs502128q

Ren, X., Zhang, X., Cao, X., Wang, Q., 2020. Efficient electrochemical reduction of carbon dioxide into ethylene boosted by copper vacancies on stepped cuprous oxide. J. CO2 Util. 38, 125–131. https://doi.org/10.1016/j.jcou.2020.01.018

Sacco, A., 2017. Electrochemical impedance spectroscopy: fundamentals and application in dye-sensitized solar cells. Renew. Sustain. Energy Rev. 79, 814–829. https://doi.org/10.1016/j.rser.2017.05.159

Sahai, A., Goswami, N., Kaushik, S.D., Tripathi, S., 2016. $Cu/Cu_2O/CuO$ nanoparticles: novel synthesis by exploding wire technique and extensive characterization. Appl. Surf. Sci. 390, 974–983. https://doi.org/10.1016/j.apsusc.2016.09.005

Schulze, M., Lorenz, M., Wagner, N., Gülzow, E., 1999. XPS analysis of the degradation of nafion. Fresenius' J. Anal. Chem. 365, 106–113.

Shaughnessy, C.I., Sconyers, D.J., Lee, H.-J., Subramaniam, B., Blakemore, J.D., Leonard, K.C., 2020. Insights into pressure tunable reaction rates for electrochemical reduction of CO_2 in organic electrolytes. Green Chem. 22, 2434–2442. https://doi.org/10.1039/D0GC00013B

Snoeckx, R., Bogaerts, A., 2017. Plasma technology – a novel solution for CO_2 conversion? Chem. Soc. Rev. 46, 5805–5863. https://doi.org/10.1039/C6CS00066E

Szultka, M., Buszewska-Forajta, M., Kaliszan, R., Buszewski, B., 2014. Determination of ascorbic acid and its degradation products by high-performance liquid chromatography-triple quadrupole mass spectrometry. Electrophoresis 35, 585–592. https://doi.org/10.1002/elps.201300439

Tao, Z., Wu, Z., Yuan, X., Wu, Y., Wang, H., 2019. Copper–gold interactions enhancing formate production from electrochemical CO_2 reduction. ACS Catal. 9, 10894–10898. https://doi.org/10.1021/acscatal.9b03158

Teo, J.J., Chang, Y., Zeng, H.C., 2006. Fabrications of hollow nanocubes of Cu_2O and Cu via reductive self-assembly of CuO nanocrystals. Langmuir 22, 7369–7377. https://doi.org/10.1021/la060439q

Ünaleroğlu, C., Zümreoğlu-Karan, B., Zencir, Y., Hökelek, T., 1997. pH-independent decomposition reactions of l-ascorbic acid in aqueous metal solutions—I. formation and structures of Co^{II} and Gd^{III} oxalates. Polyhedron 16, 2155–2161. https://doi.org/10.1016/S0277-5387(96)00563-3

Valodkar, M., Pal, A., Thakore, S., 2011. Synthesis and characterization of cuprous oxide dendrites: new simplified green hydrothermal route. J. Alloys Compd. 509, 523–528. https://doi.org/10.1016/j.jallcom.2010.09.089

Wang, S., Kou, T., Varley, J.B., Akhade, S.A., Weitzner, S.E., Baker, S.E., Duoss, E.B., Li, Y., 2021. Cu_2O/CuS nanocomposites show excellent selectivity and stability for formate generation via electrochemical reduction of carbon dioxide. ACS Mater. Lett. 3, 100–109. https://doi.org/10.1021/acsmaterialslett.0c00520

Wang, W.Z., Wang, G.H., Wang, X.S., Zhan, Y.J., Liu, Y.K., Zheng, C.L., 2002. Synthesis and characterization of Cu_2O nanowires by a novel reduction route. Adv. Mater. 14, 67–69. https://doi.org/10.1002/1521-4095(20020104)14:1<67::AID-ADMA67>3.0.CO;2-Z

Wang, Yuhang, Liu, J., Wang, Yifei, Wang, Yonggang, Zheng, G., 2018. Efficient solar-driven electrocatalytic CO_2 reduction in a redox-medium-assisted system. Nat. Commun. 9. https://doi.org/10.1038/s41467-018-07380-x

Wu, H., Song, J., Xie, C., Hu, Y., Han, B., 2018. Highly efficient electrochemical reduction of CO_2 to formic acid over lead dioxide in an ionic liquid catholyte mixture. Green Chem. 20, 1765–1769. https://doi.org/10.1039/C8GC00471D

Xia, C., Zhu, P., Jiang, Q., Pan, Y., Liang, W., Stavitski, E., Alshareef, H.N., Wang, H., 2019. Continuous production of pure liquid fuel solutions via electrocatalytic CO_2 reduction using solid-electrolyte devices. Nat. Energy 4, 776–785. https://doi.org/10.1038/s41560-019-0451-x

Xiao, L., Li, J., Brougham, D.F., Fox, E.K., Feliu, N., Bushmelev, A., Schmidt, A., Mertens, N., Kiessling, F., Valldor, M., Fadeel, B., Mathur, S., 2011. Water-soluble superparamagnetic magnetite nanoparticles with biocompatible coating for enhanced magnetic resonance imaging. ACS Nano 5, 6315–6324. https://doi.org/10.1021/nn201348s

Yamamoto, T., Tryk, D.A., Hashimoto, K., Fujishima, A., Okawa, M., 2000. Electrochemical reduction of CO_2 in the micropores of activated carbon fibers. J. Electrochem. Soc. 147, 3393. https://doi.org/10.1149/1.1393911

Yin, Z., Palmore, G.T.R., Sun, S., 2019. Electrochemical reduction of CO_2 catalyzed by metal nanocatalysts. Trends Chem. 1, 739–750. https://doi.org/10.1016/j.trechm.2019.05.004

Yodwong, B., Guilbert, D., Phattanasak, M., Kaewmanee, W., Hinaje, M., Vitale, G., 2020. Faraday's efficiency modeling of a proton exchange membrane electrolyzer based on experimental data. Energies 13, 4792. https://doi.org/10.3390/en13184792

Zhang, T., Qiu, Y., Yao, P., Li, X., Zhang, H., 2019. Bi-modified Zn catalyst for efficient CO_2 electrochemical reduction to formate. ACS Sustain. Chem. Eng. 7, 15190–15196. https://doi.org/10.1021/acssuschemeng.9b01985

Zhang, Y., Deng, B., Zhang, T., Gao, D., Xu, A.-W., 2010. Shape effects of Cu_2O polyhedral microcrystals on photocatalytic activity. J. Phys. Chem. C 114, 5073–5079. https://doi.org/10.1021/jp9110037

Zhao, G., Huang, X., Wang, Xiangxue, Wang, Xiangke, 2017. Progress in catalyst exploration for heterogeneous CO_2 reduction and utilization: a critical review. J. Mater. Chem. A 5, 21625–21649. https://doi.org/10.1039/C7TA07290B

Zhao, H.Y., Wang, Y.F., Zeng, J.H., 2008. Hydrothermal synthesis of uniform cuprous oxide microcrystals with controlled morphology. Cryst. Growth Des. 8, 3731–3734. https://doi.org/10.1021/cg8003678

Zhao, M., Gu, Y., Chen, P., Xin, Z., Zhu, H., Wang, B., Zhu, K., Yan, S., Zou, Z., 2019. Highly selective electrochemical CO_2 reduction to CO using a redox-active couple on low-crystallinity mesoporous $ZnGa_2O_4$ catalyst. J. Mater. Chem. A 7, 9316–9323. https://doi.org/10.1039/C9TA00562E

Zhou, D.-L., Feng, J.-J., Cai, L.-Y., Fang, Q.-X., Chen, J.-R., Wang, A.-J., 2014. Facile synthesis of monodisperse porous Cu_2O nanospheres on reduced graphene oxide for non-enzymatic amperometric glucose sensing. Electrochim. Acta 115, 103–108. https://doi.org/10.1016/j.electacta.2013.10.151

Zhu, X., Gupta, K., Bersani, M., Darr, J.A., Shearing, P.R., Brett, D.J.L., 2018. Electrochemical reduction of carbon dioxide on copper-based nanocatalysts using the rotating ring-disc electrode. Electrochim. Acta 283, 1037–1044.

https://doi.org/10.1016/j.electacta.2018.07.025

Zu, B.-K., 2006. The coordination chemistry of vitamin C: an overview. Coord. Chem. Rev. 250, 2295–2307. https://doi.org/10.1016/j.ccr.2006.03.002

CHAPTER 4

A Tunable Bioinspired Process of SnO_2 NPs Synthesis for Electrochemical CO_2-into-formate Conversion

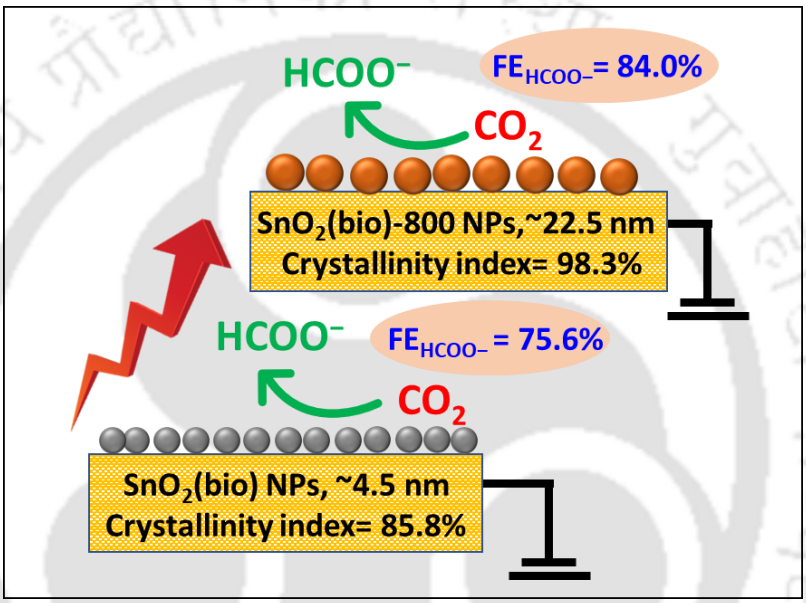

Highlights

- Development of a tunable bioinspired process of SnO_2 NPs synthesis
- Mechanism of formation of SnO_2 NPs mediated by plant-based analyte
- SnO_2 NPs electrocatalyzed CO_2 conversion to $HCOO^-$ with high faradaic efficiency
- Selective $HCOO^-$ formation because of highly crystalline (110) facet in SnO_2 NPs

4.1 Background and executive motivation

In spite of the advancement in the field of carbon-neutral and renewable energy production, the concentration of atmospheric CO_2 has reached above 400 parts per million (ppm), ~14% higher than the safe limit (350 ppm) of CO_2 in the atmosphere, an unsurpassed level in the history of mankind (Kumar et al., 2017). The rapidly increasing concentration of CO_2 in the atmosphere has become a great concern of the environmental threats corollary from the associated greenhouse gas effect (Solomon et al., 2009). Thus, the development of a carbon-neutral economy and the fixation of atmospheric CO_2 becomes an utmost research interest in the field of development of suitable CO_2 conversion technologies (Mikkelsen et al., 2010).

Several technologies, namely, organic carbonates (Pal et al., 2020), carbamates, and ureas (Tomishige et al., 2019), biological conversion (Erşan and Park, 2020), photo- and/or electrochemical reduction (Kumaravel et al., 2020) have been developed with a focus to reduce the CO_2 concentration in the air (Chapter 1). The application of electrochemical process for CO_2 reduction is advantageous over the others because it opens the potentiality of renewable energy storage and conversion of CO_2 to energy storage chemicals; ethylene, syngas, especially liquid chemicals, like formic acid, methanol, and ethanol (Tufa et al., 2020). When electrical energy storage is in consideration, being a low toxic and flammable, formate is supposed to be dominating over the alcohols because of its higher thermodynamic cell voltage in the fuel cell, 1.48 V, in comparison with that of hydrogen (1.23 V), methanol (1.21 V), and ethanol (1.14 V) (Xiang et al., 2020).

However, comparable thermodynamic redox potentials of the products (Jin et al., 2021), elevated kinetic barriers, multiple reaction pathways, and wide range of product formation (Kou et al., 2021) are a few challenges of the electrochemical CO_2 reduction reaction (ECO_2RR) for a selective yield. Various metal catalysts, like Au (Chen et al., 2012; Zheng et al., 2017), In (Gray et al., 2020; Luo et al., 2019), Pd (Jiang et al., 2018; Kortlever et al., 2015), Pt (Ertem et al., 2013; Tomita and Hori, 1998), Pb (Lee and Kanan, 2015), Cu (Duan et al., 2018; Vasileff et al., 2019), Co (Gao et al., 2016), Sn (Chen and Kanan, 2012; Tsujiguchi et al., 2021) etc. have been tested and applied for efficient ECO_2RR to formic acid.

In particular, Sn/Sn-based catalysts have been used for the selective production of HCOOH during ECO_2RR. For instance, SnO_2 nanosphere, urchin-like

SnO_2, SnO_2 microsphere, wavy SnO_2 nanoparticles, SnO_2/graphene synthesized by hydrothermal methods exhibited Faradaic efficiency in the range of 56.0-93.6%, for the selective production of formate (Fu et al., 2016b; Zhang et al., 2014).

Among all energy-dense liquid products obtained during ECO_2RR, formic acid holds its potential for H_2-storage media because of its stability, high volumetric capacity, ease of release of stored H_2 using catalytic decomposition, and direct use in formic acid fuel cell (Liu et al., 2019).

Several conventional methods, like physical methods including spray pyrolysis, ultrasonication, thermal decomposition, electrolysis; and chemical methods including sol-gel, hydrothermal, precipitation, and microemulsion have been reported in the literature for synthesizing SnO_2 and SnO_2-based catalysts (Gebreslassie and Gebretnsae, 2021). However, these methods have some inherent disadvantages like formation of toxic byproducts and the use of extreme operating conditions (high temperature-pressure) (Chapter 1). Besides the conventional techniques, a collateral route by using plant-extract-mediated for synthesizing SnO_2 nanoparticles for application in different fields have been received growing interest to constrain the drawbacks of the conventional techniques (Matussin et al., 2020).

As outlined in Chapter 3, Cu_2O NPs synthesized using fruit extract has been a proven alternative for electrochemical CO_2 reduction to formate ($HCOO^-$) with a faradaic efficiency of 65.3–66.6% within 1 h. With the aim of boosting the efficiency of CO_2 reduction and to surmount the aforementioned formidable concern, the bioinspired protocol developed in the previous study (Chapter 3) is modified and employed for the synthesis of SnO_2-NPs(bio) using *S. edule* fruit extract. The purity and morphological attributes of the as-synthesized SnO_2-NPs(bio) were investigated employing physicochemical characterization techniques, namely, UV-vis spectra, XRD, XPS, etc. The electrocatalytic efficiency of the NPs was studied utilizing cyclic voltammetry (CV) and electrochemical impedance spectroscopy (EIS) analyses. The NPs were then applied for ECO_2RR in a bench-top reactor.

4.2 Results and discussions

4.2.1 Physicochemical characterizations of SnO_2 NPs

4.2.1.1 Thermal analysis of SnO_2 NPs

TGA-DTA graph of as-synthesized SnO_2(bio) NPs is shown in Figure 4.1. The first mass loss of ~8% up to 100°C is associated with the desorption of physisorbed water on the surface of the nanoparticles (Li et al., 2020). The second mass loss of ~10% within the temperature range of 200-400°C could be due to the decomposition of residual oxygen-containing organic matters, which is evident from the exothermic peak at 380°C in the DTA graph (Song et al., 2014). The third mass loss at 445-700°C is also evident from the exothermic peak at 550°C in the DTA graph. After 700°C, no further mass loss was observed suggesting complete transformation to SnO_2. Hence, the calcination temperatures were so chosen as 380, 550, and 800°C.

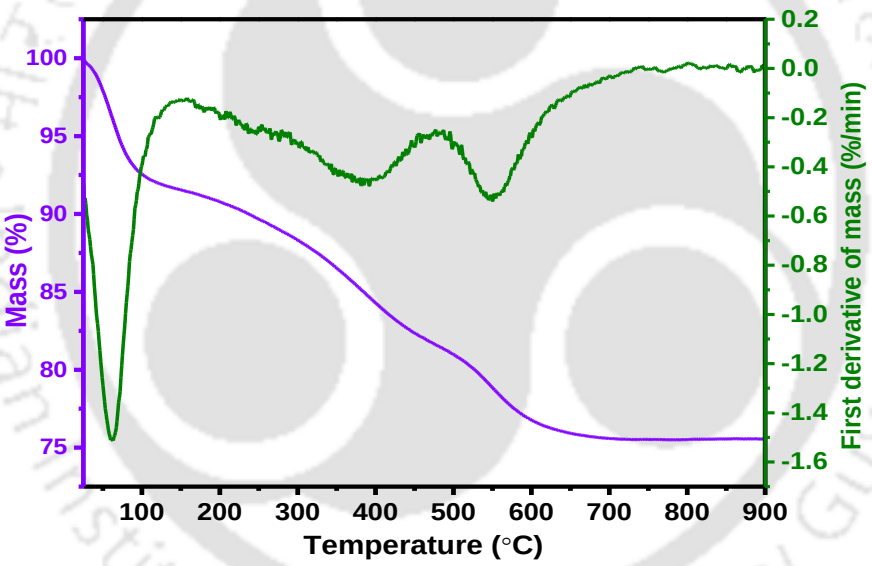

Figure 4.1. TGA and DTG graphs of SnO_2(bio) NPs.

4.2.1.2 XRD analysis

The most thermodynamically stable form of SnO_2 is reported to be rutile, a phase with a tetragonal structure having the space group $P4_2/mnm$ (D_{4h}^{14} symmetry) (Diallo et al., 2016). Its unit cell is tetragonal, consisting of two molecules (two tin atoms and four oxygen atoms). The bulk SnO_2 phase has the lattice constants as, $a_{(bulk)} = b_{(bulk)} = 7.7374$ Å and $c_{(bulk)} = 3.1864$ Å (Diallo et al., 2016).

A typical XRD pattern of as-synthesized SnO_2(bio) NPs as a control and the SnO_2(bio) NPs calcined at different temperatures of 380, 550, and 800°C are shown in Figure 4.2. The calcination temperatures are so chosen from the mass loss vs. temperature curve obtained from the TGA analysis. The diffraction pattern of all the samples can be indexed to the tetragonal rutile phase of SnO_2 (Adán et al., 2007). The crystallinity of the nanoparticles increases with the increase of calcination temperatures. The XRD reflections at 2θ of 26.67°, 33.93°, 38.10°, 51.88°, 54.94°, 58.00°, 62.12°, 64.68°, 66.23°, 71.40°, and 79.08° are associated with the crystal planes of (110), (101), (200), (211), (220), (002), (310), (112), (301), (202), and (321), respectively, of tetragonal rutile phase of bulk SnO_2 (JCPDS file no. 00-001-0657). The SnO_2(control) showed no characteristic pattern. The crystallite size (D) of as-synthesized and calcined SnO_2(bio) NPs were determined using Debye-Scherrer's formula (Equation 4.1) (Diallo et al., 2016).

$$D=\frac{k\lambda}{\beta\cos\theta} \tag{4.1}$$

Where, k= 0.9, λ is X-ray wavelength (1.5406 Å), θ is the Bragg angle of diffraction peaks, β is full width at half maximum (FWHM), respectively. Lattice constants (a and c), crystallite size (D), and d-spacing were calculated using (110) and (101) peaks. The d-spacing was calculated using the (Equation 4.2).

$$d=\frac{n\lambda}{2\sin\theta} \tag{4.2}$$

Lattice parameters (a=b and c), related to the d-spacing and the Miller indices (h, k, l) could be expressed using the (Equation 4.3).

$$\frac{1}{d^2}=\frac{h^2+k^2}{a^2}+\frac{l^2}{c^2} \tag{4.3}$$

The unit cell volume, V was calculated using Equation 4.4.

$$V=a^2c \tag{4.4}$$

With the increase in calcination temperature up to 800°C, the crystallite size also increased from 2.5 to 15.8 nm. At 800°C, the pattern reveals a sharp and narrow FWHM usually resulting from the increasing crystallinity and crystallite size of the particles. Crystallite size (D), d-spacing, lattice parameters (a=b≠c), and cell volumes are summarized in Table 4.1.

The lattice constant values, a= 4.72 Å, and c= 3.17 Å obtained for SnO_2(bio)-800 NPs confirm the dominant valence of Sn is 4+, as the lattice constant for SnO_2 are

a= 3.850 Å and c= 4.901 Å (Diallo et al., 2016). XRD pattern shows preferential exposure of the highly crystalline (110), (101), and (211) planes with other minor peaks in SnO_2(bio)-800 NPs. In contrast, broad peaks are observed for SnO_2(bio) NPs. From this observation, it could be inferred that the higher crystallinity of (110) facet in SnO_2(bio)-800 NPs could facilitate the conversion of CO_2 to $HCOO^-$ (Graetzel, 2004). From the XRD analysis, it is seen that for SnO_2(bio)-380 and SnO_2(bio)-550 NPs, the crystalline nature didn't match well for a typical SnO_2. Therefore, the two samples, labeled as SnO_2(bio) and SnO_2(bio)-800 NPs were utilized for further physicochemical, electrochemical characterizations, and ECO_2RR application. The crystallinity index (CI) of SnO_2(bio) and SnO_2(bio)-800 NPs was calculated by the following Equation 4.5 (Rotaru et al., 2018).

$$CI(\%)=\frac{Sc}{St}\times 100 \quad (4.5)$$

Where, Sc represents the area of the crystalline domain and St is the area of the total domain. CI values of SnO_2(bio) and SnO_2(bio)-800 NPs were found to be 85.8 and 98.3%, respectively. Furthermore, three different batches of SnO_2(bio) and SnO_2(bio)-800 NPs were synthesized under identical experimental conditions. From the XRD diffraction patterns, it can be seen that SnO_2(bio) and SnO_2(bio)-800 NPs exhibited a consistent crystalline structure among the particles of different batches of same type (Figure 4.3). The crystallite size (D) of SnO_2(bio) NPs was calculated to be 2.11, 2.21, 2.13 nm. It was 15.79, 15.86, 15.23 nm for SnO_2(bio)-800 NPs.

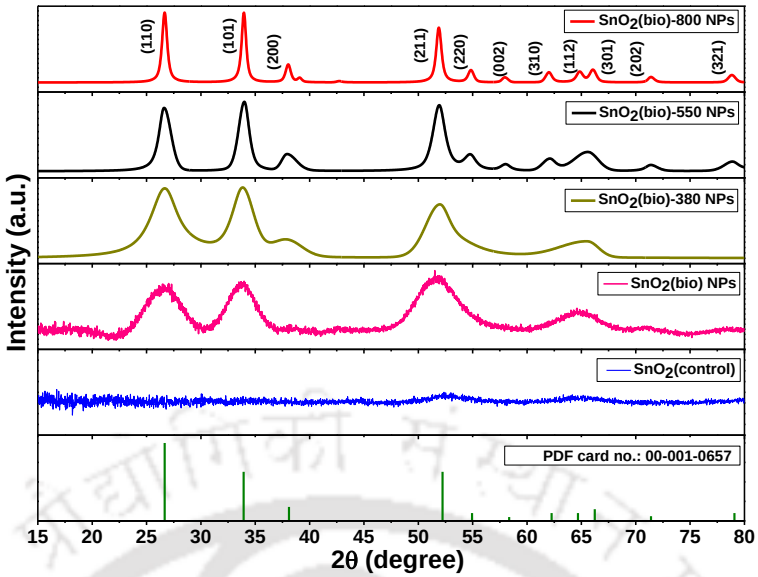

Figure 4.2. XRD patterns of SnO_2(control), SnO_2(bio) NPs and material calcined at 380, 550, and 800°C; XRD traces are labeled as SnO_2(bio)-380, SnO_2(bio)-550, and SnO_2(bio)-800 NPs, respectively.

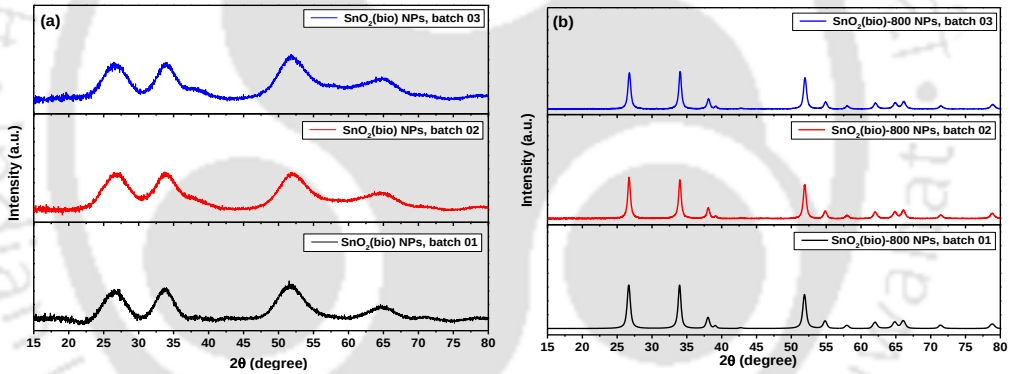

Figure 4.3. XRD pattern of (a) SnO_2(bio) and (b) SnO_2(bio)-800 NPs for three batches of synthesized nanoparticles.

Table 4.1. XRD parameters of SnO_2(bio) and SnO_2(bio) calcined at 380, 550, and 800 °C.

Sample	Crystallite size (D, nm)	d-spacing (nm) (110), (101) planes	lattice constants (Å)	Cell volume V (Å)
SnO_2(bio)	2.1		a=b= 4.72, c=2.73	60.82
SnO_2(bio)-380	2.9		a=b= 4.74, c=2.73	61.34
SnO_2(bio)-550	6.7		a=b= 4.75, c=3.17	71.52
SnO_2(bio)-800	15.8	0.333, 0.263	a=b= 4.72, c=3.17	70.62

4.2.1.3 Optical properties

The UV-vis reflectance spectra of the as-synthesized SnO_2(bio) and SnO_2(bio)-800 NPs are shown in Figure 4.4. The spectra show strong absorption with an absorption edge at 258 and 280 nm for SnO_2(bio) and SnO_2(bio)-800 NPs, respectively. The result is in good aggrement with the value reported in the literature (Graetzel, 2004). This absorption could be due to the s→p direct optical transitions in SnO_2 nanoparticles (Patil et al., 2003).

Kubelka-Munk function was employed to transform the UV-Vis data into an absorbance scale, and the optical bandgap, E_g of SnO_2(bio) and SnO_2(bio)-800 NPs was calculated by using the Tauc plot (Equation 4.6).

$$(\alpha h\nu)^2 = A(h\nu - E_g) \quad (4.6)$$

Where α is the absorption coefficient, h is the Plank's constant, and ν is the frequency. The direct bandgap of as-synthesized SnO_2(bio) and SnO_2(bio)-800 NPs are calculated to be 4.12 and 3.71 eV. The decrease in bandgap could be related to the increased particle size in the calcined SnO_2(bio)-800 NPs. Because of low carrier concentration, absorption of the light by the carriers is decreased, which leads to a lower α value in SnO_2(bio)-800 NPs, which further induces the lower value in bandgap energy. The lowering in the bandgap of SnO_2(bio)-800 NPs could be due to the rising of valence band maxima (VBM) caused by the oxygen vacancies (O_v) present in the sample (Yang et al., 2017). The observed value of the band gap is larger than the value of SnO_2-bulk, possibly due to quantum effects (Yang et al., 2017).

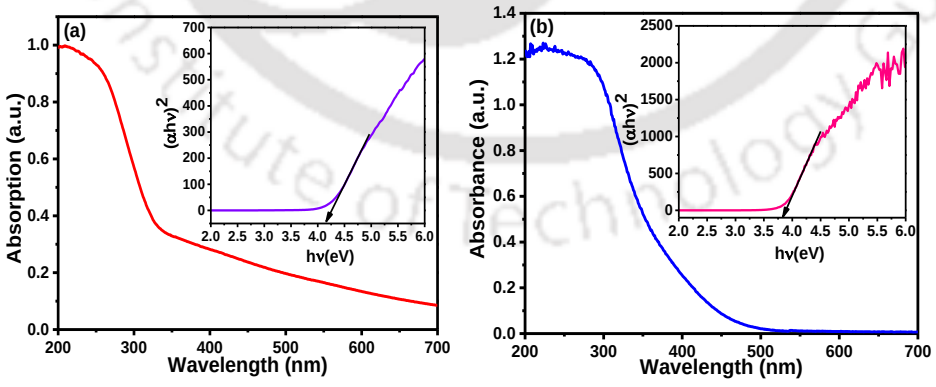

Figure 4.4. UV-Vis diffuse reflectance spectra of (a) SnO_2(bio) and (b) SnO_2(bio)-800 NPs, and their corresponding Tauc plots (insets).

4.2.1.4 BET surface area analysis

The nitrogen adsorption-desorption isotherm of uncalcined SnO_2(bio) and calcined SnO_2(bio)-800, are shown in Figure 4.5. SnO_2(bio) exhibited type-I isotherm, indicating the presence of mostly micropores. The micropore volume was measured to be 0.0633 $cm^3\ g^{-1}$, and the BET surface area was 108.78 $m^2\ g^{-1}$. The calcined sample, SnO_2(bio)-800 showed type-IV adsorption-desorption isotherms with H3 hysteresis loop, indicating the disappearance of micropores and the formation of mesoporous. The steep increase in the adsorption band at p/p_0 ranges of 0.8-0.98 signifies the presence of uniform mesopores. The surface area of SnO_2(bio)-800 NPs was measured to be 18.6 $m^2\ g^{-1}$, the significant reduction of surface area compared to the SnO_2(bio) NPs, is due to the increase in crystallinity with the high calcination temperature of 800°C. The surface area obtained is in accordance with the surface area of SnO_2 nanoparticles calcined at the 700-1000°C temperature range, as reported in the literature (Toledo-Antonio et al., 2003). The transformation of the type of BET surface area found, from the SnO_2(bio) to SnO_2(bio)-800, is a good agreement with the literature (Sergent et al., 2002). The pore size distribution using Barrett-Joyner-Halenda (BJH) method was found to be 3.9 and 18.1 nm for the SnO_2(bio) and SnO_2(bio)-800 NPs, respectively.

Hong et al. (2013) synthesized mesoporous double-shelled SnO_2 yolk-shell structure at 600°C of calcination temperature, with BET surface area of 13.0 $m^2\ g^{-1}$ for the application in Li-ion batteries. Zhang et al. (2021) synthesized mesoporous SnO_2 with a BET surface area of 36.1 $m^2\ g^{-1}$, by using the organic template method. It showed 94.5% FE towards formate formation in ECO_2RR. Kim et al. (Kim et al., 2022) synthesized SnO_x NPs having BET surface area of 10 and 36 $m^2\ g^{-1}$, using the Li-based electrochemical tuning (LiET) method, and it was utilized for ECO_2RR to formate formation with FE of ≥75.0%. Similarly, the mesoporous SnO_2 nanoparticles synthesized in the bioinspired method, namely SnO_2(bio) NPs and its calcined counterpart SnO_2(bio)-800 NPs are expected to show strong electrochemical activity towards ECO_2RR.

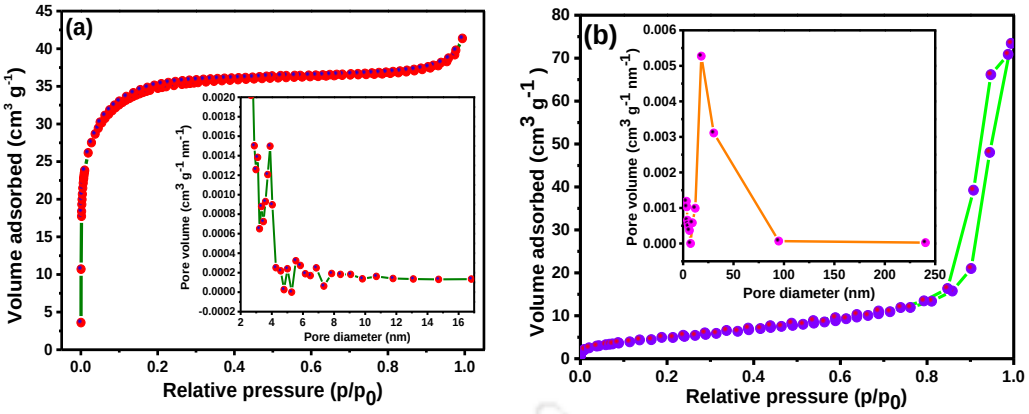

Figure 4.5. BET surface area and BJH pore size distribution (inset) of (a) SnO_2(bio) and (b) SnO_2(bio)-800 NPs.

4.2.1.5 Morphological analysis

Figure 4.6 shows the FESEM images of as-synthesized SnO_2(bio) and SnO_2(bio)-800 NPs. From this figure, it is seen that the particles are spherical and agglomerated as well as forming large clusters in SnO_2(bio) NPs (Figure 4.6a). The average particle size was found to be 4.5 nm. After calcination, the size of the nanoparticles increases with mostly spherical morphology in SnO_2(bio)-800 NPs (Figure 4.6b), and the particle size was found to be 22.5 nm, which is near to the crystallite size (D) determined in XRD analysis. The morphology and particles size of different batches of SnO_2(bio) (4.5 ±0.2 nm) and SnO_2(bio)-800 NPs (22.5 ±0.2 nm) didn't show any noteworthy variation among different batches of the same types of particles (Figures 4.7 and 4.8).

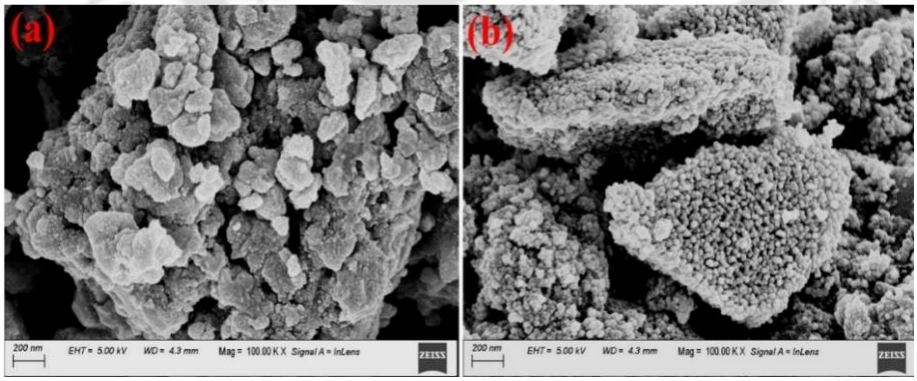

Figure 4.6. FESEM images of (a) as-synthesized SnO_2(bio) NPs, and (b) SnO_2(bio)-800 NPs calcined at 800°C.

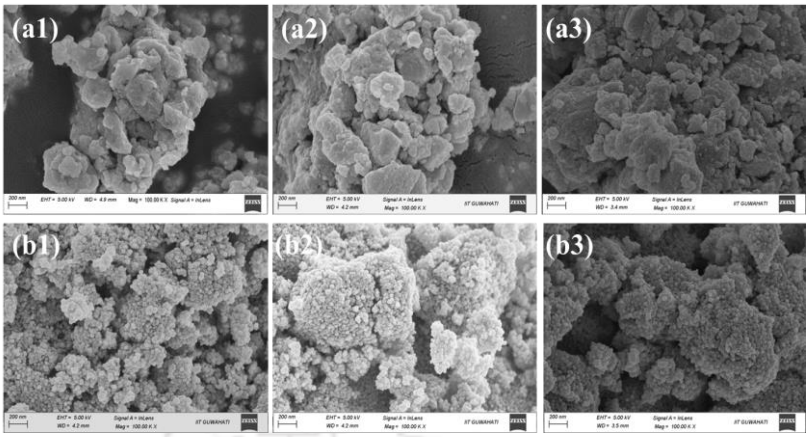

Figure 4.7. FESEM images of (a1-a3) SnO_2(bio) and (b1-b3) SnO_2(bio)-800 NPs for three batches of synthesized nanoparticles, respectively.

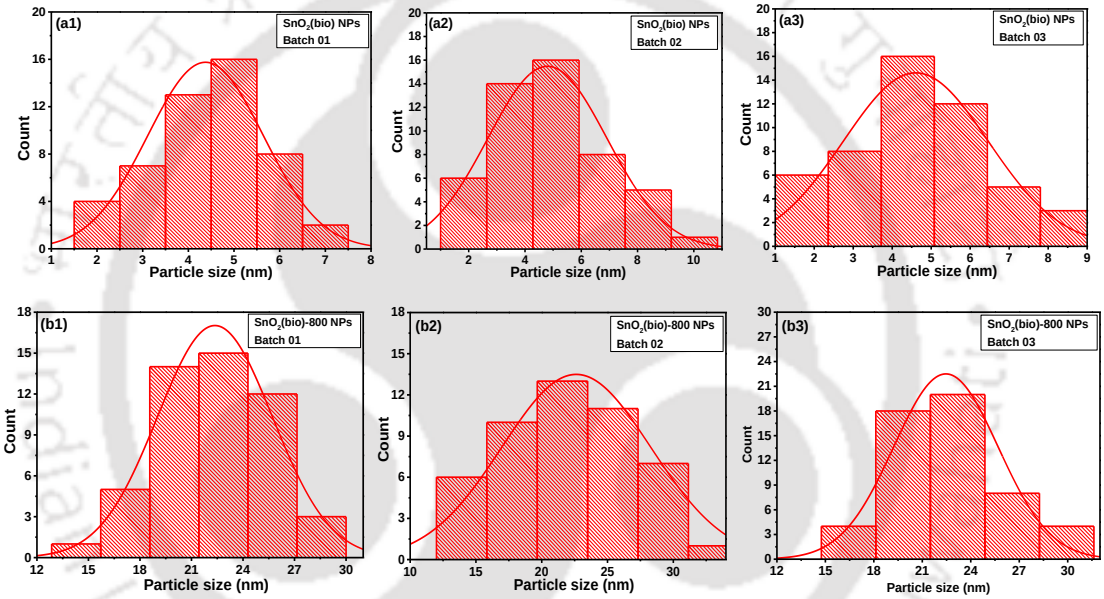

Figure 4.8. Particle size distribution of (a1-a3) SnO_2(bio) and (b1-b3) SnO_2(bio)-800 NPs from FESEM images.

FETEM, HRTEM, and SAED patterns of the as-synthesized SnO_2(bio) and SnO_2(bio)-800 NPs are shown in Figure 4.9. It can be seen that all the particles are nearly spherical (Figures 4.9a1 and 4.9b1). SnO_2(bio) NPs show an average particle size of 3.5 nm (Figure 4.9a2), which is increased to 20 nm in SnO_2(bio)-800 NPs, after calcination (Figure 4.9b2). The results can be correlated with the decrease in bandgap for SnO_2(bio)-800 NPs, in Tauc's plot measurement (Figure 4.4). The spacing of adjacent lattice planes was found to be 0.238 nm corresponding to the (220) plane, in SnO_2(bio) NPs (Figure 4.9a3) (Wang et al., 2020), and 0.334 nm corresponding to the (110) low-energy facet of most thermodynamically stable rutile

SnO_2 (Figure 4.9b3) (Dutta et al., 2015). It is evident that the degree of crystallinity increases in SnO_2(bio)-800 NPs after calcination of SnO_2(bio) NPs, which is also reflected from the SAED patterns. Both the nanoparticles are polycrystalline, as indicated by the diffraction ring observed from the SAED patterns (Figures 4.9a4 and 4.9b4). The continuous ring pattern (Figure 4.9a4) suggests low crystallinity of SnO_2(bio) NPs. The spot ring type of SAED patterns (Figure 4.9b4) in SnO_2(bio)-800 NPs indicates the high crystallinity and orientation of crystals in a number of different directions (Wetchakun et al., 2012). The results are in line with the XRD analysis (Figure 4.2).

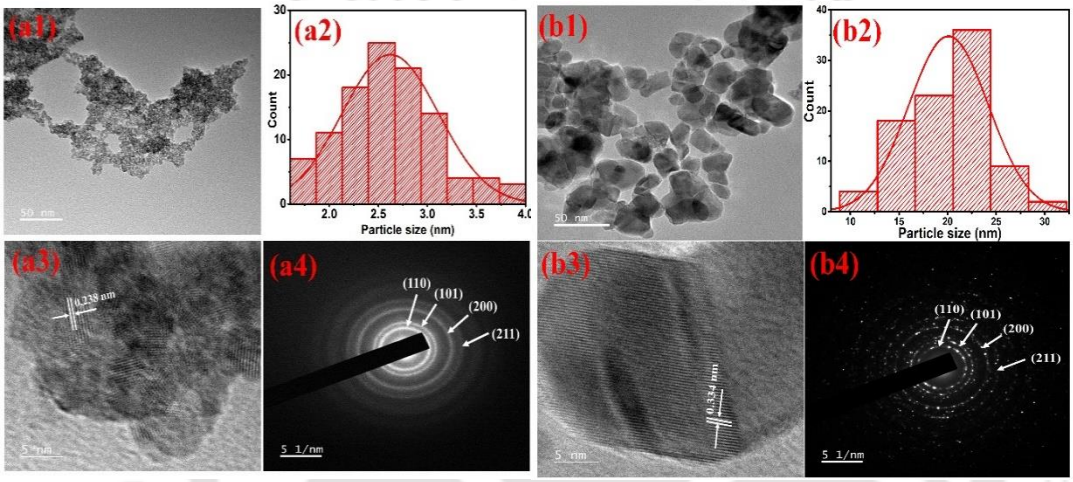

Figure 4.9. FETEM image, particle size distribution, HRTEM image, and SAED pattern of as-synthesized SnO_2(bio) NPs (a1-a4) and SnO_2(bio)-800 NPs calcined at 800°C (b1-b4).

4.2.1.6 EDX spectra

FETEM micrograph, EDX spectrum, elemental mappings of tin, and oxygen of SnO_2(bio) are shown in Figures 4.10a1-4.10a4. The results recorded with SnO_2(bio)-800 NPs are presented in Figures 4.10b1-4.10b4. The spectra show the presence of uniform Sn and O atoms, which confirm both the specimens are composed of Sn and O. The atomic % ratio of Sn and O is found to be comparable with the stoichiometric ratio of 1:2 for SnO_2. The Cu peak was due to the copper coated TEM grid used for sample preparation.

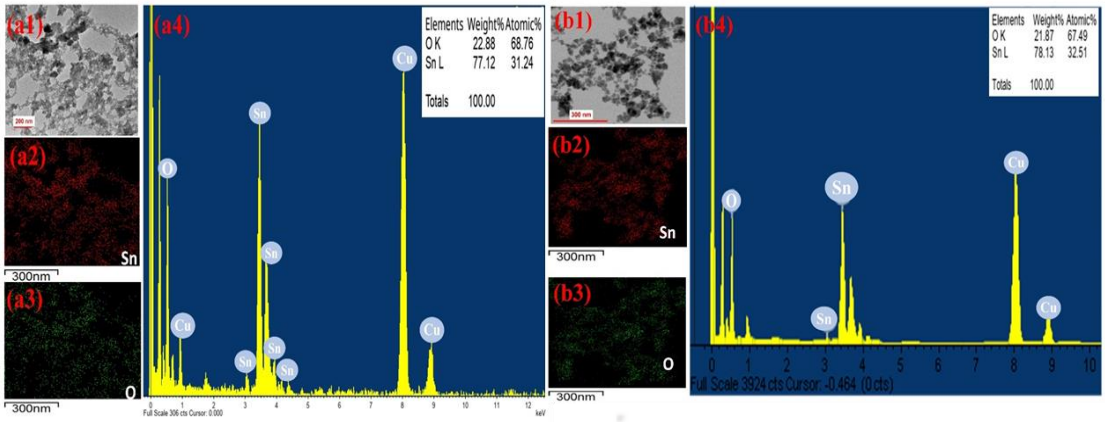

Figure 4.10. FETEM images, EDX spectra, tin and oxygen elemental mappings of SnO_2(bio) (a1-a4), and SnO_2(bio)-800 NPs (b1-b4).

4.2.1.7 XPS analysis

Figure 4.11a shows the XPS survey spectra of SnO_2(bio)-800, SnO_2(bio)-800/TCP electrode after 2 h of ECO_2RR, and SnO_2(bio) NPs (Figure 4.12a). The spectra of SnO_2(bio)-800/TCP showed F (fluorine), besides the coexistence of Sn, O, and C elements. The appearance of C peak could be due to the residue of bio-moiety on the surface of the nanoparticles. Moreover, it also could be due to the adventitious carbon in the environment. The F peak appears from the nafion binder used to prepare the catalyst ink. Figure 4.11b shows the high-resolution XPS of Sn 3d and O 1s of SnO_2(bio)-800 NPs. The Sn 3d spectrum shows that the split $3d_{5/2}$ and $3d_{3/2}$ core states are centered at 486.8 and 495.2 eV, respectively, indicating Sn^{4+} in SnO_2(bio)-800 NPs (Wang et al., 2017). The separation between the Sn $3d_{5/2}$ and $3d_{3/2}$ is calculated to be 8.4 eV, a feature of commercial SnO_2 reported earlier. The high-resolution spectra of SnO_2(bio) NPs (Figure 4.12) showed the Sn^{2+} peaks at 486.3 and 495.1 eV, along with the Sn^{4+} peaks at 487.4 and 495.5 eV (Carvalho et al., 2012).

The O 1s spectrum in Figure 4.11 is asymmetric with split sub-peaks centered at 530.6 and 531.6 eV. The lower binding energy at 530.6 eV is attributed to the oxygen, O^{2-}, and the peak at 531.6 eV could be attributed to the oxygen vacancies (O_v) (Yang et al., 2017). It also well correlates with the Tauc plot results (Figure 4.4). For SnO_2(bio) NPs (Figure 4.12c), the deconvolution of O 1s showed an additional peak at 532.0 eV which could be attributed to the adsorbed water (Chowdhury et al., 2021).

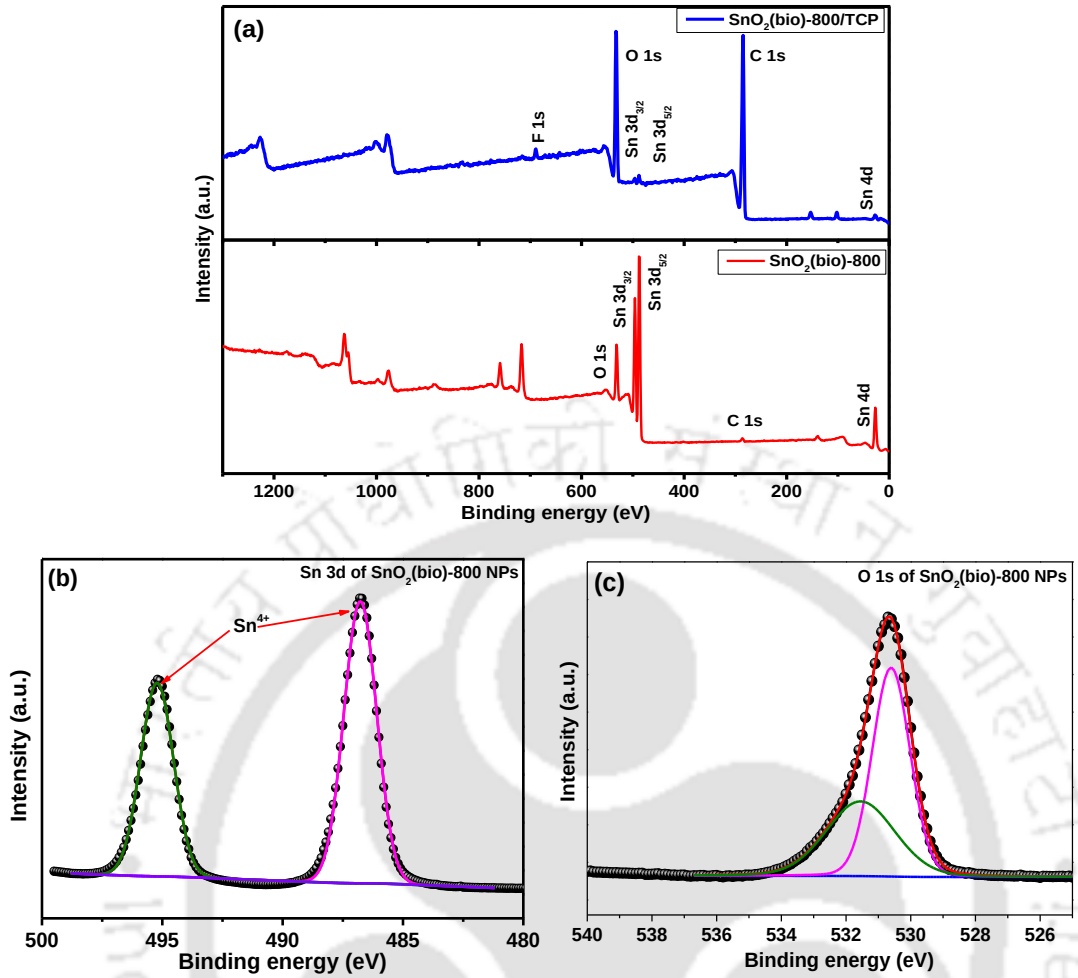

Figure 4.11. (a) XPS survey spectra of SnO_2(bio)-800 NPs and SnO_2(bio)-800/TCP electrode; and high- resolution core level spectra of (b) Sn 3d, and (c) O 1s of SnO_2(bio)-800 NPs.

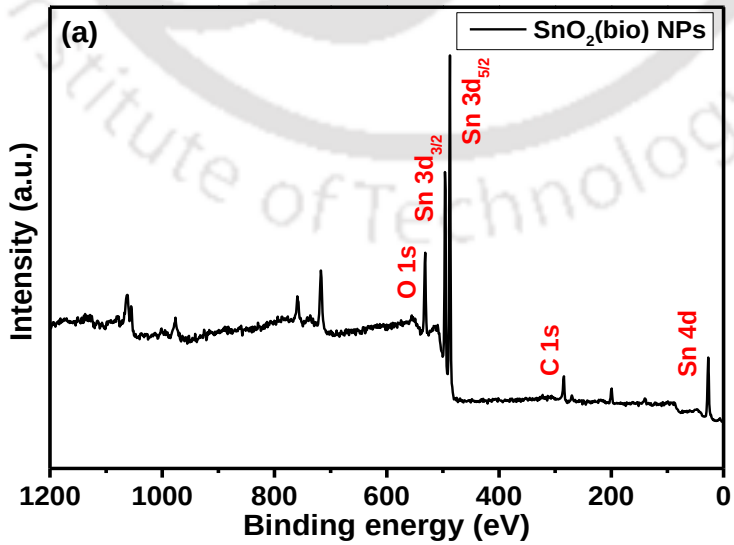

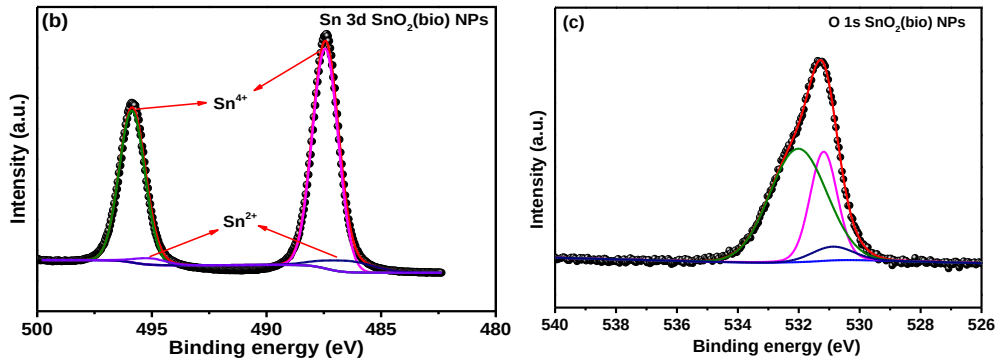

Figure 4.12. (a) XPS survey spectra and high- resolution core level spectra of (b) Sn 3d, and (c) O 1s of SnO_2(bio) NPs.

4.2.2 Formation of SnO_2 NPs

Figure 4.13 shows the schematic of the formation of SnO_2(bio) NPs using *S. edule* fruit extract, enriched with ascorbic acid content. The standard electrode potential (E^0) of the ascorbic acid (H_2A)/ dehydroascorbic acid (DHA) couple is +0.1 V, lower than that of Sn^{4+}/Sn^{2+} (+0.151 V) (Meng et al., 2020). So, it could act as a potential reducing agent for Sn(IV). The two coordinated H_2O molecules from pentahydrate and four Cl atoms form the octahedral crystal structure of $SnCl_4 \cdot 5H_2O$ (structure I) (Taylor and Coddington, 1992). $SnCl_4 \cdot 5H_2O$ added to an aqueous solution dissociates into $[SnCl_4(H_2O)]^0$ (Complex I), hexaaquatin(IV), $[Sn(H_2O)_6]^{4+}$ (Complex II) along with the complex, $[SnCl_x(H_2O)_{6-x}]^{(4-x)+}$ (Taylor and Coddington, 1992). In an acidic medium (pH 4.5), ascorbic acid (H_2A, present in bio-extract or commercially available) dissociates to form the reactive HA^- species. It reacts with Complex I and Complex II forming Complex III (Figure 4.14). This complex decomposes forming dehydroascorbic acid (DHA) (75°C) (Ledendecker et al., 2022) via electron transfer from ascorbic acid to Sn^{4+} ions and Sn^0 is formed in a hot solution. After that, a series of successive thermodynamic reactions could occur, and the highly active Sn^0 reacts with O_2 (in air) forming SnO_2 nanoparticles during drying in a hot air oven (Wang et al., 2010). A similar mechanistic pathway also can be developed involving various electron donor analytes such as gallic acid, caffeic acid and isoquercetin, etc. (Andrés et al., 2017) present in bio-extract leading to the formation of SnO_2 NPs.

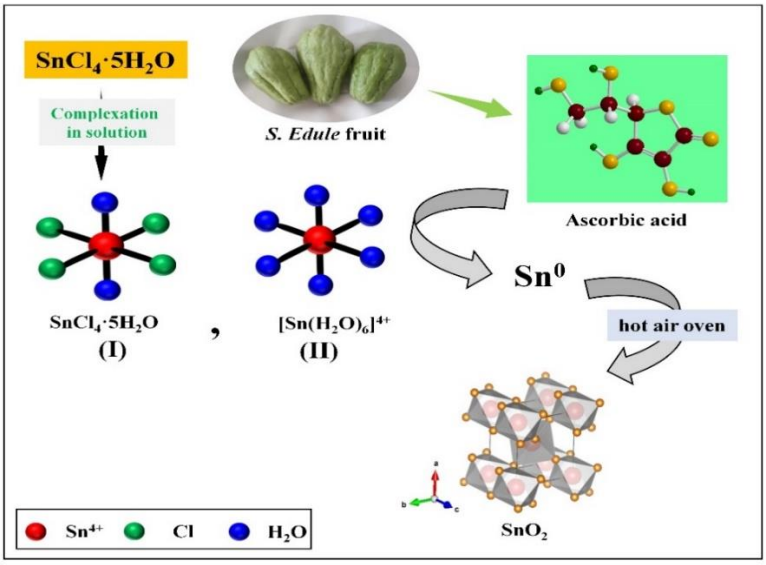

Figure 4.13. Schematic for formation of SnO_2(bio) NPs from the precursor, $SnCl_4 \cdot 5H_2O$ using *S. edule* fruit extract enriched with ascorbic acid.

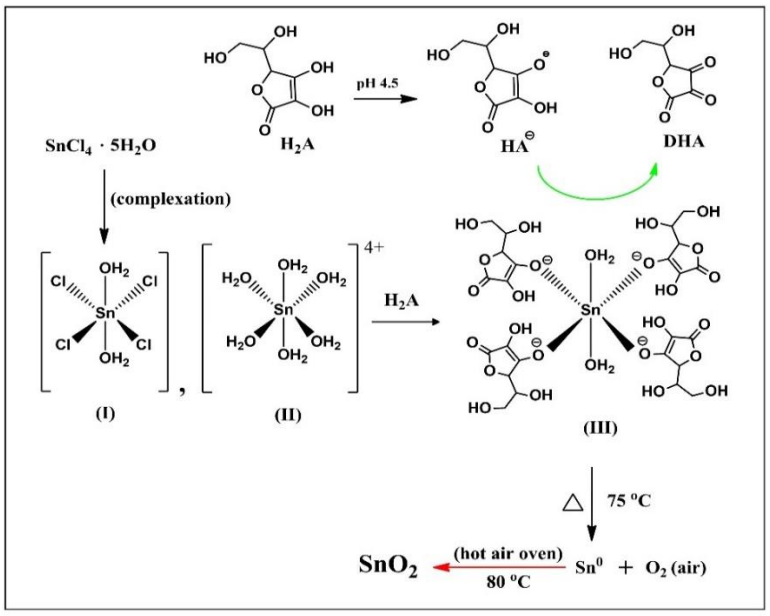

Figure 4.14. Proposed mechanistic pathway of SnO_2(bio) NPs synthesis.

4.2.3 Electrocatalytic functionalities of SnO_2 nanoparticles

4.2.3.1 Cyclic voltammetry (CV) analysis

The performance towards ECO_2RR of SnO_2(bio) and SnO_2(bio)-800 NPs were first studied using CV with a scan rate of 50 mVs^{-1} in 0.5 M $KHCO_3$ electrolyte (Figure 4.15). The anodic and cathodic peaks appeared in the region of no H_2 evolution reaction (HER), and ECO_2RR, at −1.05 to −0.6 V (vs. Ag/AgCl) could be

an indication of the formation and reduction of SnO_x species in this pH condition (Tan et al., 2020). The onset potential of SnO_2(bio)/TCP electrode in CO_2-bubbled electrolyte was −1.45 V (vs. Ag/AgCl), whereas the onset potential of SnO_2(bio)-800/TCP electrode was −1.4 V (vs. Ag/AgCl), a positive shift of 50 mV for SnO_2(bio)-800 NPs. The SnO_2(bio)-800/TCP electrode showed higher current density compared to the SnO_2(bio)/TCP electrode in CO_2-bubbled electrolyte than N_2 one after −1.4 V to −2.5 V (vs. Ag/AgCl), in the region of HER and ECO_2RR, could be an indication of higher selectivity of SnO_2(bio)-800/TCP electrode over SnO_2(bio)/TCP electrode for ECO_2RR. The voltammogram showed an overlapping trend for three different batches of particles in the selected potential range (0 to −2.5 V (vs. Ag/AgCl)). For an example, the current density at the SnO_2(bio)-800 NPs/TCP electrode showed only 3.8% variation at −1.5 V (vs. Ag/Cl) in CO_2 bubbling (Figure 4.16).

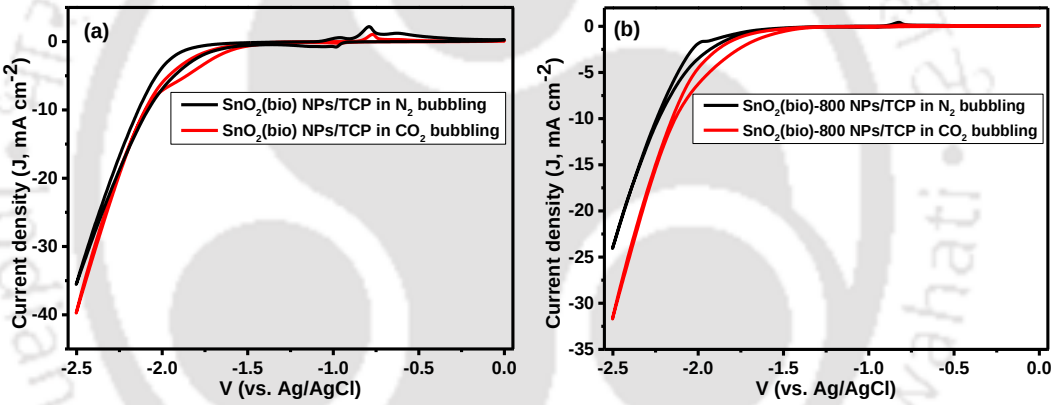

Figure 4.15. Cyclic voltammetry results (scan rate 50 mV s^{-1}) of (a) SnO_2(bio) NPs/TCP and (b) SnO_2(bio)-800 NPs/TCP electrodes with N_2 and CO_2 (saturated) bubbling in 0.5 M $KHCO_3$ electrolyte.

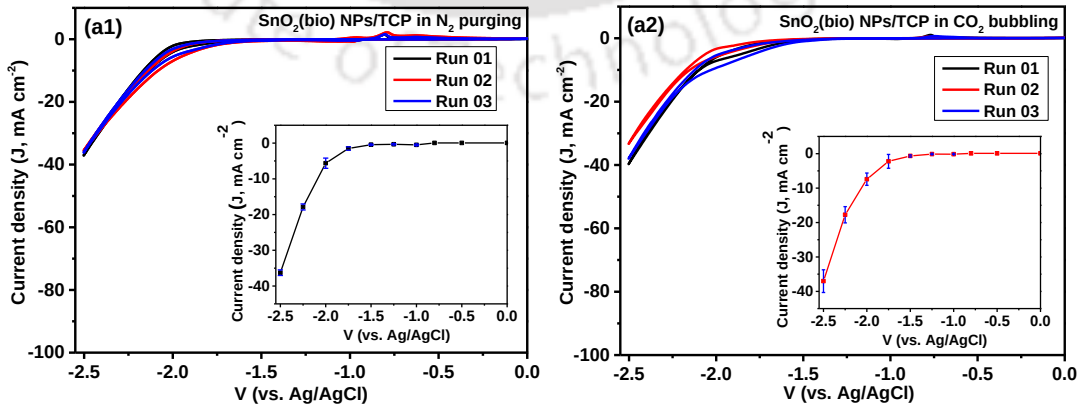

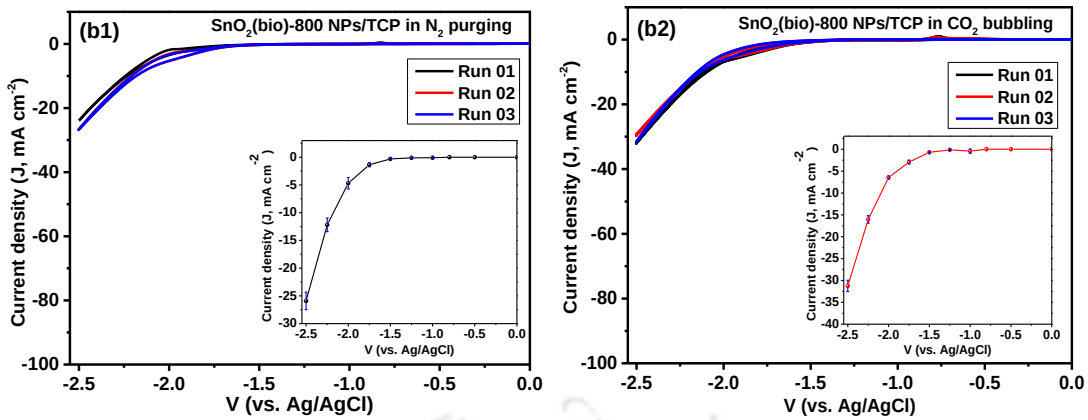

Figure 4.16. Cyclic voltammetry results (scan rate 50 mV s^{-1}) of (a1) in N_2-purging and (a2) CO_2 bubbling for SnO_2(bio) NPs/TCP; and (b1) in N_2-purging and (b2) CO_2 bubbling for SnO_2(bio)-800 NPs/TCP electrodes in 0.5 M $KHCO_3$ electrolyte for three batches of synthesized nanoparticles. Insets are the plots of current density (J) at selected potentials (0 to −2.5 V (vs. Ag/AgCl) with error bars.

4.2.3.2 EIS measurements

In Figures 4.17a and 4.17b, the Nyquist plots of the SnO_2(bio) NPs/TCP and SnO_2(bio)-800 NPs/TCP electrodes in N_2- and CO_2-soaked 0.5 M $KHCO_3$ electrolyte are shown. The EIS data were fitted with an equivalent circuit (Figure 4.18) consisting of series resistances (R_s); the ohmic resistance which is mainly composed of electrolyte resistance and contact resistance between the catalyst and the TCP electrode, the capacitance at the electrode/electrolyte interface (Q_1), the transport resistance in the electrode (R_1), and the charge transfer resistance at the electrode/electrolyte interface in parallel with the capacitance of the charge storage in the electrode (Q_2) (Reñones et al., 2016). R_s values for SnO_2(bio) NPs/TCP electrode are almost similar in N_2- and CO_2-bubbled electrolytes, 2.63 and 2.57 Ω, respectively. On contrary, R_s values of SnO_2(bio)-800/TCP electrode is lower (3.70 Ω) in CO_2-bubbled electrolyte than that in N_2-bubbled electrolyte, which is 24.9 Ω.

The results suggest an improved electrical conductivity of SnO_2(bio)-800/TCP electrode in CO_2 (Chen et al., 2017). A similar trend in EIS is also found for the chainlike mesoporous SnO_2 NPs for the catalytic electrochemical CO_2 reduction to formate (Bejtka et al., 2019). Also, a ~3.5-fold decrease in transport resistance (R_1) for SnO_2(bio)-800/TCP in CO_2-bubbling with respect to N_2-bubbling. On the other

hand, ~1.08-fold decrease was noted in R_1 value for SnO_2(bio) NPs/TCP in the case of CO_2-bubbling with respect to N_2-bubbling (Table 4.2). It could be due to the effective catalytic behavior SnO_2(bio)-800/TCP towards ECO_2RR.

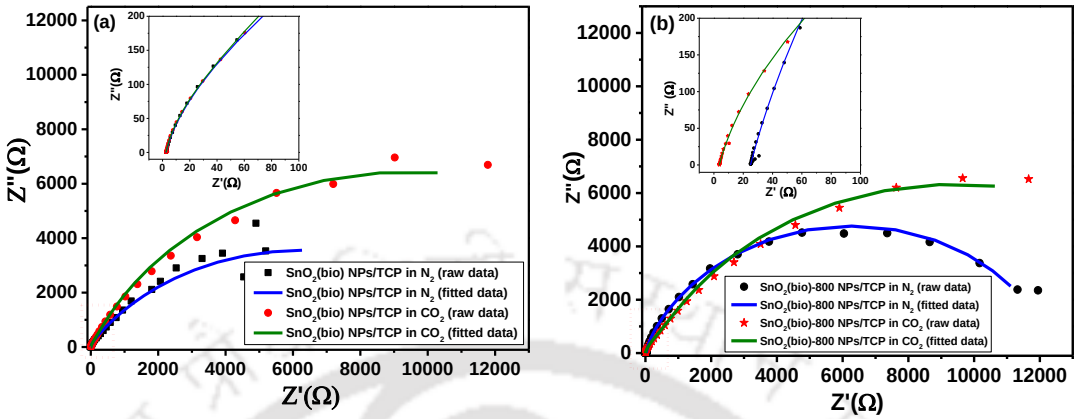

Figure 4.17. Nyquist plots with raw (symbols) and fitted data (lines) of (a) SnO_2(bio)-NPs/TCP and (b) SnO_2(bio)-800 NPs/TCP electrodes with N_2 and CO_2 (saturated) bubbling in 0.5 M $KHCO_3$ electrolyte. Insets are magnified images in the selected region (marked in red).

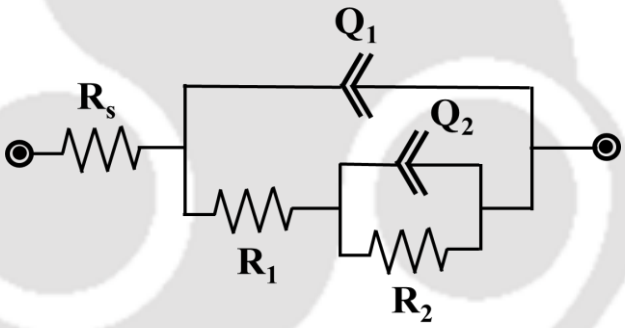

Figure 4.18. Equivalent circuit used for fitting of EIS data.

Table 4.2. Elements in equivalent electric circuit fitted in Nyquist plots of Figure 4.17.

Electrical circuit elements		SnO_2(bio) NPs/TCP electrode in N_2	SnO_2(bio) NPs/TCP electrode in CO_2	SnO_2(bio)-800 NPs/TCP electrode in N_2	SnO_2(bio)-800 NPs/TCP electrode in CO_2
Rs (Ω)		2.63	2.57	24.9	3.70
R1 (Ω)		564	518	4090	1140
R2 (kΩ)		12.4	18.7	8.30	17.7
Q1	Y0 (μMho)	207	177	157	166
	N	0.926	0.937	0.918	0.918

Q2	Y0 (μMho)	388	250	138	262
	N	0.593	0.69	0.737	0.708

4.2.3.3 ECO_2RR performances

The current response curve for SnO_2(bio)/TCP and SnO_2(bio)-800/TCP electrodes for the selected applied potentials, ranges from −1.4 to −2.1 V (vs. Ag/AgCl) in CO_2-bubbled 0.5 M $KHCO_3$ electrolyte for 1 h of ECO_2RR are shown in Figures 4.19a and 4.19b. It is observed that the current density (J) of SnO_2-(bio)-800/TCP electrode is 4.3 to 25.8 $mAcm^{-2}$, higher than that of the SnO_2(bio)/TCP electrode (0.02 to 21.1 mA cm^{-2}). The reason could be the higher electrocatalytic activity of SnO_2-(bio)-800/TCP over SnO_2-(bio)/TCP electrode towards ECO_2RR in the chronometric potential range of −1.4 to −2.1 V (vs. Ag/AgCl).

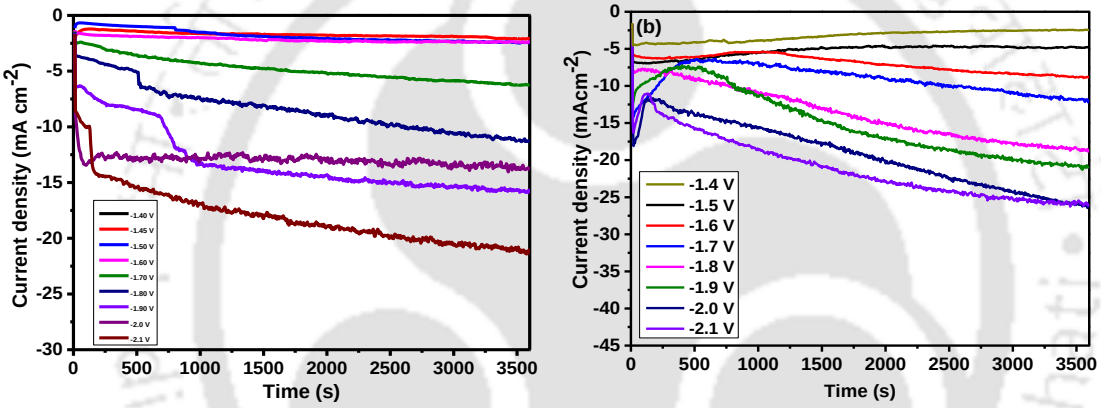

Figure 4.19. Current response curves at various potentials for ECO_2RR on (a) SnO_2(bio)/TCP and (b) SnO_2(bio)-800/TCP electrodes in CO_2-bubbled 0.5 M $KHCO_3$ electrolyte.

The reduction product analysis showed to be formate as a single liquid product together with H_2, in the gas phase. The specimen calculation for the determination of formate concentration is given as a footnote in the Figures A2.1 and A2.2 of Appendix-II.

The corresponding FE in the electrode potential range of −1.4 to −2.1 V (vs. Ag/AgCl) is shown in Figure 4.20. SnO_2(bio)/TCP exhibits maximum FE of 75.6% at −1.5 V (vs. Ag/AgCl) (Figure 4.20a). By contrast, SnO_2(bio)-800/TCP showed a FE of 72.0% at the lower potential of −1.4 V (vs. Ag/AgCl), and the maximum FE was found to be 84.0% at −1.5 V (vs. Ag/AgCl) (Figure 4.20b). The better performance of SnO_2(bio)-800/TCP over SnO_2(bio)/TCP could be related to their morphology and

structural configurations. SnO_2(bio)-800 NPs exhibited a high cumulative volume of BJH pores 0.113 $cm^3\ g^{-1}$, significantly larger than that of the SnO_2(bio) NPs, 0.0633 $cm^3\ g^{-1}$, which could facilitate the better transport of both reactants (H_2O + CO_2) and products ($HCOO^-$ + H_2) during ECO_2RR. SnO_2(bio)-800 NPs exhibited ~3-times more differential pore volume (0.0053 $cm^3\ g^{-1}\ nm^{-1}$) than that of SnO_2(bio)-NPs (BJH pore size distribution in Figure 4.5) (Daiyan et al., 2018).

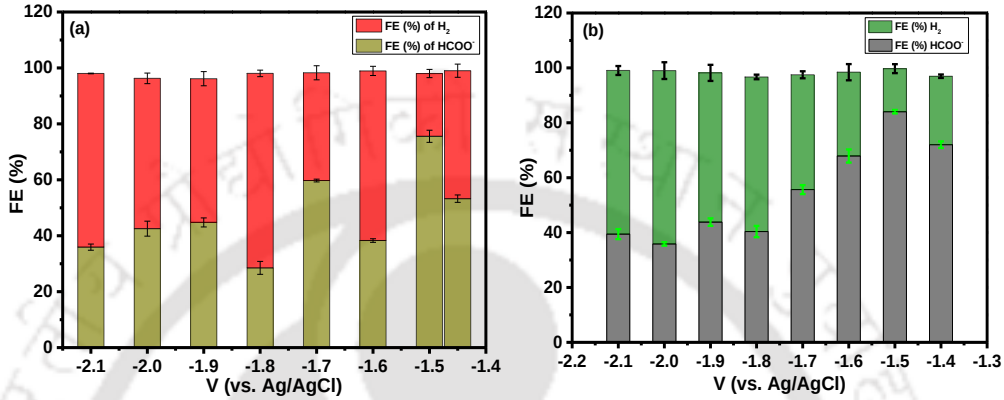

Figure 4.20. FE (%) of H_2 and formate formation from ECO_2RR on (a) SnO_2(bio)/TCP and (b) SnO_2(bio)-800/TCP electrodes in CO_2-bubbled 0.5 M $KHCO_3$ electrolyte at the electrode potential from −1.4 to −2.1 V vs. Ag/AgCl.

The catalytic activity of SnO_2(bio) and SnO_2(bio)-800 coated TCP electrodes for ECO_2RR towards format formation were comparable with most of the Sn-based electrodes reported in the literature (Table 4.3). Further, the variation of current density ($J_{formate}$) for the formation of formate with respect to the applied potential (vs. reversible hydrogen electrode) is presented in Figure 4.21. It is clearly evident that SnO_2(bio)-800 NPs could form formate with a lower overpotential and reasonably high current density.

Table 4.3. SnO_2-based catalysts for ECO_2RR to formate reported in the literature and their comparison with bioinspired SnO_2 NPs.

Catalyst	Synthesis method	Conditions	FE (%) of formate	Reference
SnO_2(bio) NPs SnO_2(bio)-800 NPs	Bio-inspired route using *S. edule* fruit extract	0.5 M $KHCO_3$ −1.5 V (vs. Ag/AgCl)	75.6 84.0	**This work**
SnO_2/MWCNT	Wet impregnation	0.5 M $NaHCO_3$ −1.7 V (vs. SCE)	27.2	(Bashir et al., 2016)

	method			
Wavy SnO_2 NW	Urea assisted hydrothermal	0.5 M $KHCO_3$ −1.0 V (vs. RHE)	87.4	(Chen et al., 2020)
SnO_2 nanosphere	Hydrothermal self-assembly	0.5 M $KHCO_3$ −0.56 V (vs. SHE)	56.0	(Fu et al., 2016b)
Urchin-like SnO_2 nanostructure	Hydrothermal self-assembly	0.5 M $KHCO_3$ −1.0 V (vs. SHE)	62.0	(Liu et al., 2017)
SnO_2 microsphere	Hydrothermal self-assembly	0.5 M $KHCO_3$ −1.70 V (vs. SHE)	62.0	(Fu et al., 2016a)
Mesoporous SnO_2 nanosheet	Hydrothermal method	0.5 M $NaHCO_3$ −1.6 V (vs. Ag/AgCl)	87.0	(Li et al., 2016)
Mesoporous SnO_2 nanosheet	Solvothermal	0.5 M $NaHCO_3$ −0.9 V (vs. RHE)	83.0	(Han et al., 2019)
Porous SnO_2 nanowires	Plasma synthesis	0.1 M $KHCO_3$ −0.8 V (vs. RHE)	80.0	(Kumar et al., 2017)
Sn/SnO_x	Etched method	0.5 M $NaHCO_3$ −0.7 V (vs. RHE)	40.0	(Chen and Kanan, 2012)
Mesoporous SnO_2 NPs	Nanocasting	0.1 M $KHCO_3$ −1.15 V (vs. RHE)	75.2	(Daiyan et al., 2018)
SnO_2 NPs	Flame spray pyrolysis	0.1 M $KHCO_3$ −1.1 V (vs. RHE)	85.0	(Daiyan et al., 2019)
SnO_2/Graphene	Hydrothermal	0.1 M $NaHCO_3$ −1.8 V (vs. SCE)	93.6	(Zhang et al., 2014)
Porous SnO_2 nanosheet	Chemical vapor deposition followed by calcination	0.5 M $NaHCO_3$ −0.7 V (vs. RHE)	92.4	(Liu et al., 2020)
SnO_x NPs	Lithiation-based electrochemical tuning	0.1 M $KHCO_3$ −1.2 V (vs. RHE)	81.0	(Kim et al., 2022)
Ultrathin SnO_2 quantum wires	Modified hydrothermal	0.1 M $KHCO_3$ −1.156 V (vs. RHE)	87.3	(Liu et al., 2019)
SnO_2 /graphene oxide	Hydrothermal method	0.1 M $KHCO_3$ −0.96 V (vs. RHE)	84.4	(Yang et al., 2021)
SnO_2 nanosphere	Combined sol-gel and templating method	0.1 M $KHCO_3$ −1.2 V (vs. RHE)	81.0	(Nguyen-Phan et al., 2022)
Core/Shell Cu/SnO_2 structure	Seed mediated chemical method	0.5 M $KHCO_3$ −0.9 V (RHE) −0.7 V (RHE)	85.0 (C-Cu/SnO_2-1.8) 93.0 (CO Cu/SnO_2-0.8)	(Li et al., 2017)
2 nm SnO_2 NPs	Hydrothermal microwave assisted method	0.1 M $KHCO_3$ ~ 8.0 V (absolute cell potential)	44.9	(Merino-Garcia et al., 2021)

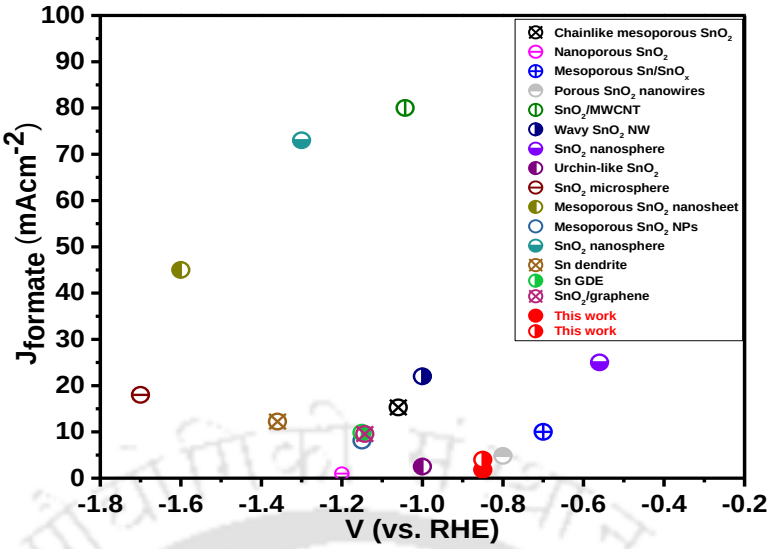

Figure 4.21. Comparison of this work with the literature reported Sn-based electrocatalysts in H-type batch reactor with bicarbonate electrolyte for ECO_2RR: chainlike mesoporous SnO_2 (Bejtka et al., 2019), nanoporous SnO_2 (Liu et al., 2022), mesoporous Sn/SnO_x (Chen and Kanan, 2012), porous SnO_2 nanowires (Kumar et al., 2017), SnO_2/MWCNT (Bashir et al., 2016), wavy SnO_2 NW (Chen et al., 2020), SnO_2 nanosphere (Fu et al., 2016b), urchin-like SnO_2 (Liu et al., 2017), SnO_2 microsphere (Fu et al., 2016a), mesoporous SnO_2 nanosheet (Li et al., 2016), mesoporous SnO_2 NPs (Daiyan et al., 2018), SnO_2 nanosphere (Nguyen-Phan et al., 2022), Sn dendrite (Won et al., 2015), Sn GDE (Wang et al., 2014), SnO_2/graphene (Zhang et al., 2014). The electrode potential is calculated wrt reversible hydrogen electrode for a uniform comparison.

The 2 h of ECO_2RR at −1.5 V (vs. Ag/AgCl) in 0.5 M $KHCO_3$ electrolyte resulted in FE reduced to 61.5%. The corresponding current response graph is shown in Figure 4.22. Although, post-reaction FESEM images (Figure 4.23) indicate the morphology was unchanged after 2 h of ECO_2RR. The XRD pattern of SnO_2(bio)-800/TCP electrode (Figure 4.24) after 2 h of ECO_2RR at −1.5 V (vs. Ag/AgCl) in 0.5 M $KHCO_3$ electrolyte, shows the presence of Sn^0 (Oehl et al., 2015). It is further corroborated by the high-resolution XPS of Sn 3d (Figure 4.25). The result corroborates with the XPS results observed for single crystal SnO_2 NPs reported by Liu et al. (2021) for ECO_2RR to formate formation. Studies reported that the

formation of Sn is due to the reduction of a part SnO_2 on the surface of the catalyst during electrochemical reduction of CO_2 (Dutta et al., 2015).

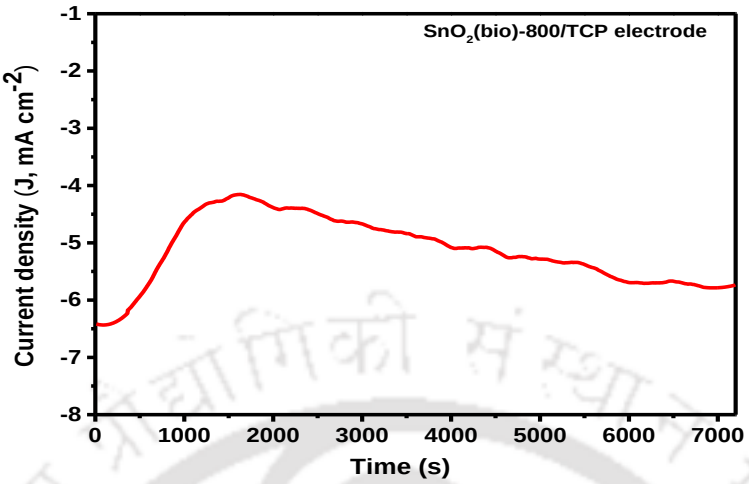

Figure 4.22. Current response of SnO_2(bio)-800/TCP electrode for 2 h of ECO_2RR at −1.5 V (vs. Ag/AgCl) in CO_2 saturated 0.5 M $KHCO_3$ electrolyte.

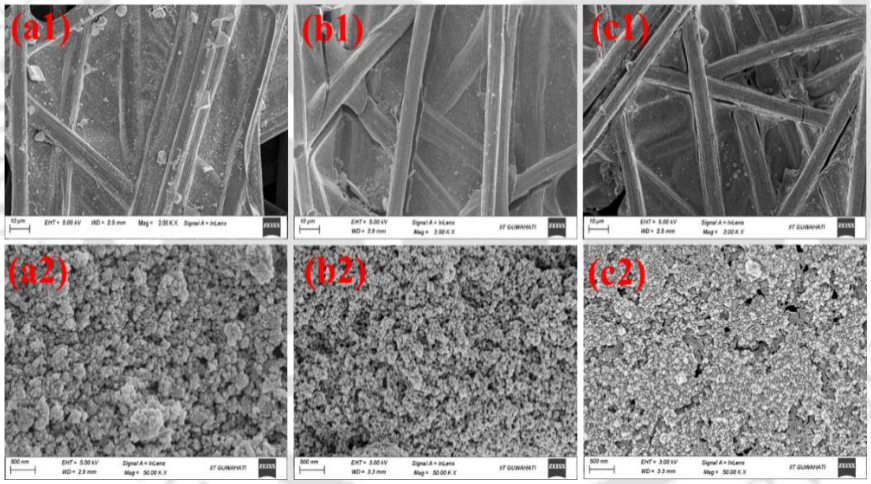

Figure 4.23. FESEM image of SnO_2-SE-800/TCP electrode (a1-a2) before electrochemical analysis, (b1-b2) after 1 h of ECO_2RR at −1.5 V (vs. Ag/AgCl), (c1-c2) after 2 h of ECO_2RR at −1.5 V (vs. Ag/AgCl) in CO_2 saturated 0.5 M $KHCO_3$ electrolyte.

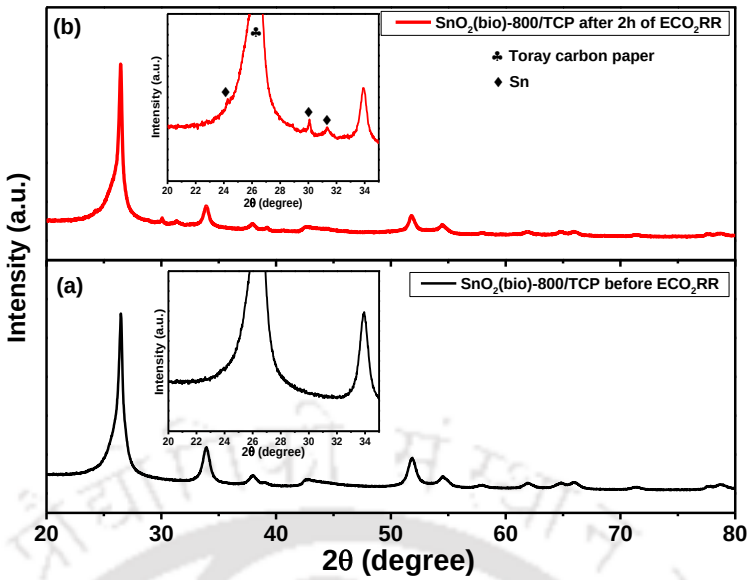

Figure 4.24. XRD pattern of SnO_2(bio)-800/TCP electrode (a) before and (b) after 2 h of ECO_2RR at −1.5 V (vs. Ag/AgCl) in CO_2 saturated 0.5 M $KHCO_3$ electrolyte.

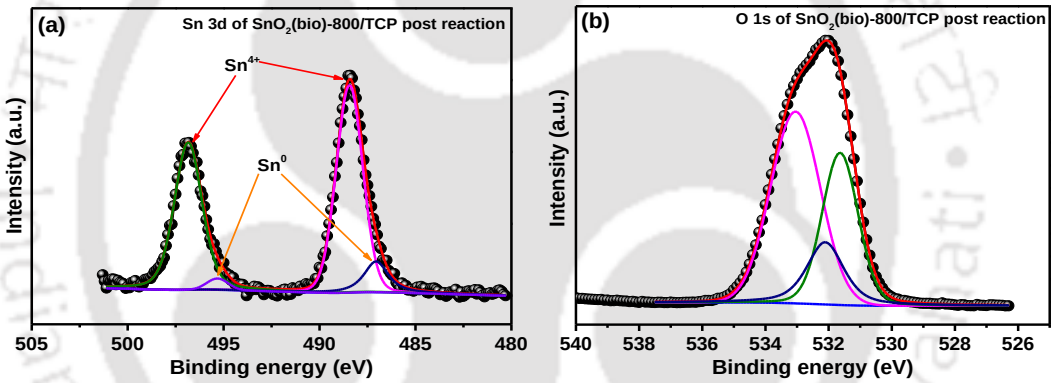

Figure 4.25. High- resolution core level spectra of (a) Sn 3d, (b) O 1s of SnO_2-SE-800/TCP electrode after 2h of electrochemical CO_2 reduction at −1.5 V (vs. Ag/AgCl) in CO_2-bubbled 0.5 M $KHCO_3$ electrolyte.

Figure 4.26 shows Sn-based electrocatalysts of varying sizes and shapes used for ECO_2RR forming formate and CO.

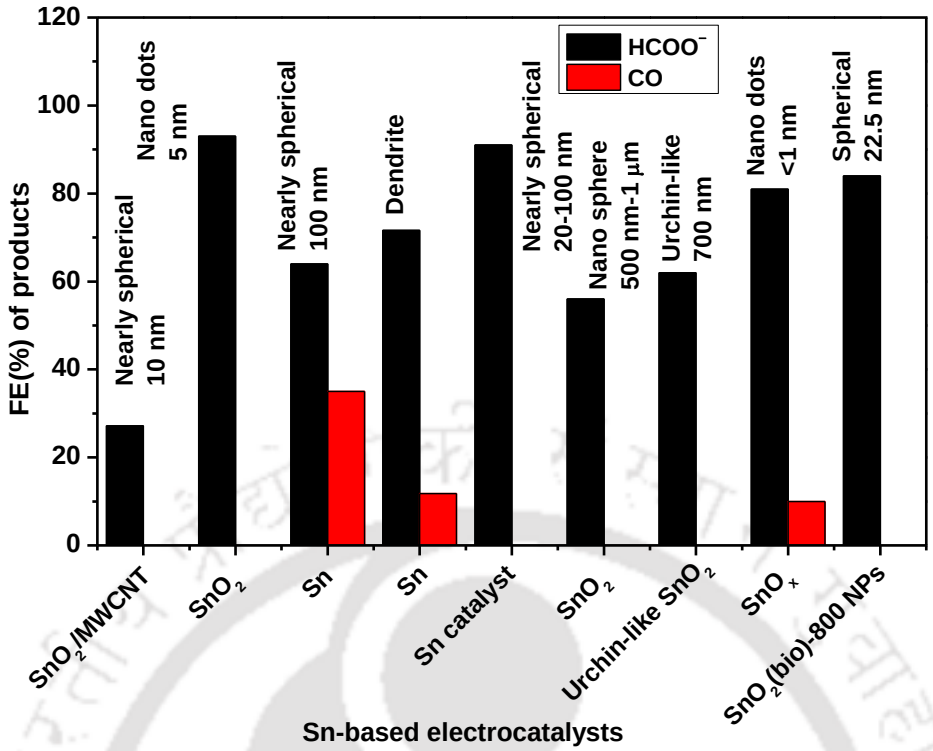

Figure 4.26. Sn-based electrocatalysts of varying sizes and shapes used for ECO_2RR forming formate and CO.

In 2021, the annual worldwide production of formic acid has reached 710 thousand tons with a market size of $1.6 billion and it will grow to $3.85 billion by the year 2030 (Kaya et al., 2023). Currently, 90% of commercial formic acid (FA) production relies on the methyl formate hydrolysis process (Alfath and Lee, 2020). Considering 90% FE of formic acid production at 300 mA cm^{-2} current density, at a cell voltage of 2 V and cathode lifetimes over 210 h, the utility cost of FA was calculated to be 0.17 \$ kg^{-1}, compared to the conventional 0.23-0.46 \$ kg^{-1} (Jouny et al., 2018; Rumayor et al., 2019). Therefore, the ECO_2RR process for formate formation could be an economically viable alternative.

4.3 Major findings

A bioinspired route of synthesizing SnO_2 NPs was developed by using *S. edule* fruit extract laden with ascorbic acid (AA) for the electrochemical CO_2 reduction reaction. After calcination at 800°C, sample labeled as SnO_2(bio)-800 NPs showed an increase in crystallite size from 2.1 to 15.8 nm compared to the as-

synthesized SnO_2(bio) NPs. With increasing crystallinity, the particle size increased from 3.5 to 15.8 nm, and the surface area decreased from 108.8 to 18.6 $m^2 g^{-1}$.

As-synthesized SnO_2(bio) NPs and SnO_2(bio)-800 NPs were utilized to prepare modified SnO_2(bio)/TCP and SnO_2(bio)-800/TCP electrodes for electrochemical reduction of CO_2. Both materials electrocatalyzed CO_2 to formate ($HCOO^-$) as a single liquid product. The maximum faradaic efficiency of formate formation was found to be 84.0% vs. 75.6% using SnO_2(bio)-800 NPs and SnO_2(bio) NPs, respectively for 1 h of the chronoamperometric test. The higher FE (%) for SnO_2(bio)-800 NPs could be due to the increase in crystallinity of (110) facets after calcination at 800°C compared to the SnO_2(bio) NPs.

However, XPS analysis showed the presence of Sn^0, a most familiar issue with the SnO_2-based catalysts to utilize it as the electrochemical reduction of CO_2 corroborating the fall of FE to 61.5% after 2 h of chronoamperometry catalyzed by SnO_2(bio)-800 NPs. The results achieved in the present study warrant the SnO_2(bio)-800 NPs/TCP electrodes based ECO_2RR system for their applications in the continuous processes for the production of value-added chemicals.

References

Adán, C., Bahamonde, A., Fernández-García, M., Martínez-Arias, A., 2007. Structure and activity of nanosized iron-doped anatase TiO_2 catalysts for phenol photocatalytic degradation. Appl. Catal. B Environ. 72, 11–17. https://doi.org/10.1016/j.apcatb.2006.09.018

Alfath, M., Lee, C.W., 2020. Recent advances in the catalyst design and mass transport control for the electrochemical reduction of carbon dioxide to formate. Catalysts 10. https://doi.org/10.3390/catal10080859

Andrés, O., Ángel, D., León-garcía, E., Vela-gutiérrez, G., Cruz, J. De, García-varela, R., García, H.S., 2017. Chayote (Sechium edule (Jacq.) Swartz), in: Fruit and Vegetable Phytochemicals: Chemistry and Human Health. pp. 979–992. https://doi.org/https://doi.org/10.1002/9781119158042.ch47

Bashir, S., Hossain, S.S., Ahmed, S., Al-ahmed, A., Hossain, M.M., 2016. Electrocatalytic reduction of carbon dioxide on SnO_2/MWCNT in aqueous electrolyte solution. J. CO_2 Util. 16, 346–353. https://doi.org/10.1016/j.jcou.2016.09.002

Bejtka, K., Zeng, J., Sacco, A., Castellino, M., Hernández, S., Farkhondehfal, M.A., Savino, U., Ansaloni, S., Pirri, C.F., Chiodoni, A., 2019. Chainlike mesoporous SnO_2 as a well-performing catalyst for electrochemical CO_2 reduction. ACS Appl. Energy Mater. 2, 3081–3091. https://doi.org/10.1021/acsaem.8b02048

Carvalho, D.H.Q., Schiavon, M.A., Raposo, M.T., Paiva, R. De, Alves, J.L.A., Paniago, R.M., Speziali, N.L., Ferlauto, A.S., Ardisson, J.D., 2012. Synthesis and characterization of SnO_2 thin films prepared by dip-coating method. Phys. Procedia 28, 22–27. https://doi.org/10.1016/j.phpro.2012.03.664

Chen, Y., Kanan, M.W., 2012. Tin oxide dependence of the CO_2 reduction efficiency on tin electrodes and enhanced activity for tin/tin oxide thin-film catalysts. J. Am. Chem. Soc. 134, 1986–1989. https://doi.org/10.1021/ja2108799

Chen, Y., Li, C.W., Kanan, M.W., 2012. Aqueous CO_2 reduction at very low overpotential on oxide-derived Au nanoparticles. J. Am. Chem. Soc. 134, 19969–19972.

Chen, Z., Fan, T., Zhang, Y., Xiao, J., Gao, M., Duan, N., Zhang, J., Li, J., Liu, Q., Yi, X., Luo, J., 2020. Wavy SnO_2 catalyzed simultaneous reinforcement of carbon dioxide adsorption and activation towards electrochemical conversion of

CO_2 to HCOOH. Appl. Catal. B Environ. 261, 118243. https://doi.org/10.1016/j.apcatb.2019.118243

Chen, Z., Yao, S., Liu, L., 2017. 3D hierarchical porous structured carbon nanotube aerogel-supported Sn spheroidal particles: An efficient and selective catalyst for electrochemical reduction of CO_2 to formate. J. Mater. Chem. A 5, 24651–24656. https://doi.org/10.1039/c7ta07495f

Chowdhury, A., Peela, N.R., Golder, A.K., 2021. Synthesis of Cu_2O NPs using bioanalytes present in *Sechium edule*: Mechanistic insights and application in electrocatalytic CO_2 reduction to formate. J. CO2 Util. 51, 101622. https://doi.org/10.1016/j.jcou.2021.101622

Daiyan, R., Lovell, E.C., Bedford, N.M., Saputera, W.H., Wu, K., Lim, S., Horlyck, J., Ng, Y.H., Lu, X., Amal, R., 2019. Modulating activity through defect engineering of tin oxides for electrochemical CO_2 reduction. Adv. Sci. 6, 1–9. https://doi.org/10.1002/advs.201900678

Daiyan, R., Lu, X., Saputera, W.H., Ng, Y.H., Amal, R., 2018. Highly selective reduction of CO_2 to formate at low overpotentials achieved by a mesoporous tin oxide electrocatalyst. ACS Sustain. Chem. Eng. 6, 1670–1679. https://doi.org/10.1021/acssuschemeng.7b02913

Diallo, A., Manikandan, E., Rajendran, V., Maaza, M., 2016. Physical & enhanced photocatalytic properties of green synthesized SnO_2 nanoparticles via aspalathus linearis. J. Alloys Compd. 681, 561–570. https://doi.org/10.1016/j.jallcom.2016.04.200

Duan, Y.X., Meng, F.L., Liu, K.H., Yi, S.S., Li, S.J., Yan, J.M., Jiang, Q., 2018. Amorphizing of Cu nanoparticles toward highly efficient and robust electrocatalyst for CO_2 reduction to liquid fuels with high faradaic efficiencies. Adv. Mater. 30, 1–7. https://doi.org/10.1002/adma.201706194

Dutta, A., Kuzume, A., Rahaman, M., Vesztergom, S., Broekmann, P., 2015. Monitoring the chemical state of catalysts for CO_2 electroreduction: An in operando study. ACS Catal. 5, 7498–7502. https://doi.org/10.1021/acscatal.5b02322

Erşan, S., Park, J.O., 2020. Light-independent biological conversion of CO_2. Joule 4, 2047–2051. https://doi.org/10.1016/j.joule.2020.08.007

Ertem, M.Z., Konezny, S.J., Araujo, C.M., Batista, V.S., 2013. Functional role of

pyridinium during aqueous electrochemical reduction of CO_2 on Pt(111). J. Phys. Chem. Lett. 4, 745–748.

Fu, Y., Li, Y., Zhang, X., Liu, Y., Qiao, J., Zhang, J., Wilkinson, D.P., 2016a. Novel hierarchical SnO_2 microsphere catalyst coated on gas diffusion electrode for enhancing energy efficiency of CO_2 reduction to formate fuel. Appl. Energy 175, 536–544. https://doi.org/10.1016/j.apenergy.2016.03.115

Fu, Y., Li, Y., Zhang, X., Liu, Y., Zhou, X., Qiao, J., 2016b. Electrochemical CO_2 reduction to formic acid on crystalline SnO_2 nanosphere catalyst with high selectivity and stability. Chinese J. Catal. 37, 1081–1088. https://doi.org/10.1016/S1872-2067(15)61048-8

Gao, W., Emaminejad, S., Nyein, H.Y.Y., Challa, S., Chen, K., Peck, A., Fahad, H.M., Ota, H., Shiraki, H., Kiriya, D., Lien, D.H., Brooks, G.A., Davis, R.W., Javey, A., 2016. Fully integrated wearable sensor arrays for multiplexed in situ perspiration analysis. Nature 529, 509–514. https://doi.org/10.1038/nature16521

Gebreslassie, Y.T., Gebretnsae, H.G., 2021. Green and Cost-Effective Synthesis of Tin Oxide Nanoparticles: A Review on the Synthesis Methodologies, Mechanism of Formation, and Their Potential Applications. Nanoscale Res. Lett. 16. https://doi.org/10.1186/s11671-021-03555-6

Graetzel, L.V. and M., 2004. Highly ordered SnO_2 nanorod arrays from controlled aqueous Growth. Angew. Chemie - Int. Ed. 43, 3666–3670. https://doi.org/10.1002/anie.200454000

Gray, C.L., Sowa, B., Morais, C., Rayess, P., 2020. Highly efficient formic acid and carbon dioxide electro-reduction to alcohols on indium oxide electrodes. Sustain. Energy Fuels 4, 4030–4038. https://doi.org/10.1039/d0se00623h

Han, N., Wang, Y., Deng, J., Zhou, J., Wu, Y., Yang, H., Ding, P., Li, Y., 2019. Self-templated synthesis of hierarchical mesoporous SnO_2 nanosheets for selective CO_2 reduction. J. Mater. Chem. A 7, 1267–1272. https://doi.org/10.1039/c8ta10959a

Hong, Y.J., Son, M.Y., Kang, Y.C., 2013. One-pot facile synthesis of double-shelled SnO_2 yolk-shell-structured powders by continuous process as anode materials for Li-ion batteries. Adv. Mater. 25, 2279–2283. https://doi.org/10.1002/adma.201204506

Jiang, B., Zhang, X., Jiang, K., Wu, D., Cai, W., 2018. Boosting formate production

in electrocatalytic CO_2 reduction over wide potential window on Pd surfaces. J. Am. Chem. Soc. 140, 2880–2889. https://doi.org/10.1021/jacs.7b12506

Jin, S., Hao, Z., Zhang, K., Yan, Z., Chen, J., 2021. Advances and challenges for the electrochemical reduction of CO_2 to CO: From fundamentals to industrialization. Angew. Chemie Int. Ed. 133, 2–24. https://doi.org/10.1002/ange.202101818

Jouny, M., Luc, W., Jiao, F., 2018. General techno-economic analysis of CO_2 electrolysis systems. Ind. Eng. Chem. Res. 57, 2165–2177. https://doi.org/10.1021/acs.iecr.7b03514

Kaya, K., Ditz, D., Jaworski, A., Chen, J., Monti, S., Barcaro, G., Budnyk, S., Slabon, A., Palkovits, R., 2023. Enhanced solar CO_2 photoreduction to formic acid by platinum immobilization on bipyridine covalent triazine framework with defects. Adv. Sustain. Syst. 2300071, 1–12. https://doi.org/10.1002/adsu.202300071

Kim, M.K., Lee, H., Won, J.H., Sim, W., Kang, S.J., Choi, H., Sharma, M., Oh, H.S., Ringe, S., Kwon, Y., Jeong, H.M., 2022. Design of less than 1 nm scale spaces on SnO_2 nanoparticles for high-performance electrochemical CO_2 reduction. Adv. Funct. Mater. 32, 1–10. https://doi.org/10.1002/adfm.202107349

Kortlever, R., Balemans, C., Kwon, Y., Koper, M.T.M., 2015. Electrochemical CO_2 reduction to formic acid on a Pd-based formic acid oxidation catalyst. Catal. Today 244, 58–62. https://doi.org/10.1016/j.cattod.2014.08.001

Kou, Z., Li, X., Wang, T., Ma, Y., Zang, W., Nie, G., Wang, J., Wang, J., 2021. Fundamentals, on-going advances and challenges of electrochemical carbon dioxide reduction. Electrochem. Energy Rev. 5, 82–111. https://doi.org/10.1007/s41918-021-00096-5

Kumar, B., Atla, V., Brian, J.P., Kumari, S., Nguyen, T.Q., Sunkara, M., Spurgeon, J.M., 2017. Reduced SnO_2 porous nanowires with a high density of grain boundaries as catalysts for efficient electrochemical CO_2-into-HCOOH conversion. Angew. Chemie - Int. Ed. 56, 1–6. https://doi.org/10.1002/anie.201612194

Kumaravel, V., Bartlett, J., Pillai, S.C., 2020. Photoelectrochemical conversion of carbon dioxide (CO_2) into fuels and value-added products. ACS Energy Lett. 5, 486–519. https://doi.org/10.1021/acsenergylett.9b02585

Ledendecker, M., Paciok, P., Osowiecki, W.T., Pander, M., Heggen, M., Göhl, D., Kamat, G.A., Erbe, A., Mayrhofer, K.J.J., Alivisatos, A.P., 2022. Engineering

gold-platinum core-shell nanoparticles by self-limitation in solution. Commun. Chem. 5, 1–7. https://doi.org/10.1038/s42004-022-00680-w

Lee, C.H., Kanan, M.W., 2015. Controlling H^+ vs CO_2 reduction selectivity on Pb electrodes. ACS Catalylsisis 5, 465–469.

Li, F., Chen, L., Knowles, G.P., Macfarlane, D.R., Zhang, J., 2016. Hierarchical mesoporous SnO_2 nanosheets on carbon cloth : A robust and flexible electrocatalyst for CO_2 reduction with high efficiency and selectivity. Angew. Chemie 55, 1–6. https://doi.org/10.1002/anie.201608279

Li, Jian, Chen, C., Li, Jialin, Li, S., Dong, C., 2020. Synthesis of tin-glycerate and it conversion into SnO_2 spheres for highly sensitive low-ppm-level acetone detection. J. Mater. Sci. Mater. Electron. 31, 16539–16547. https://doi.org/10.1007/s10854-020-04208-7

Li, Q., Fu, J., Zhu, W., Chen, Z., Shen, B., Wu, L., Xi, Z., Wang, T., Lu, G., Zhu, J.J., Sun, S., 2017. Tuning Sn-Catalysis for Electrochemical Reduction of CO_2 to CO via the Core/Shell Cu/SnO_2 Structure. J. Am. Chem. Soc. 139, 4290–4293. https://doi.org/10.1021/jacs.7b00261

Liu, G., Li, Z., Shi, J., Sun, K., Ji, Y., Wang, Z., 2020. Black reduced porous SnO_2 nanosheets for CO_2 electroreduction with high formate selectivity and low overpotential. Appl. Catal. B Environ. 260, 118134. https://doi.org/10.1016/j.apcatb.2019.118134

Liu, H., Miao, B., Chuai, H., Chen, X., Zhang, S., Ma, X., 2022. Nanoporous tin oxides for efficient electrochemical CO_2 reduction to formate. Green Chem. Eng. 3, 138–145. https://doi.org/10.1016/j.gce.2021.11.001

Liu, H., Su, Y., Kuang, S., Hensen, E.J.M., Zhang, S., Ma, X., 2021. Highly efficient CO_2 electrolysis within a wide operation window using octahedral tin oxide single crystals. J. Mater. Chem. A 9, 7848–7856. https://doi.org/10.1039/d1ta00285f

Liu, S., Xiao, J., Lu, X.F., Wang, J., Wang, X., Lou, X.W. (David), 2019. Efficient electrochemical reduction of CO_2 to HCOOH over Sub-2 nm SnO_2 quantum wires with exposed grain boundaries. Angew. Chemie - Int. Ed. 58, 8499–8503. https://doi.org/10.1002/anie.201903613

Liu, Y., Fan, M., Zhang, X., Zhang, Q., Guay, D., Qiao, J., 2017. Design and engineering of urchin-like nanostructured SnO_2 catalysts via controlled facial

hydrothermal synthesis for efficient electro-reduction of CO_2. Electrochim. Acta 248, 123–132. https://doi.org/10.1016/j.electacta.2017.07.140

Luo, W., Xie, W., Li, M., Zhang, J., Züttel, A., 2019. 3D hierarchical porous indium catalyst for highly efficient electroreduction of CO_2. J. Mater. Chem. A 7, 4505–4515. https://doi.org/10.1039/c8ta11645h

Matussin, S., Harunsani, M.H., Tan, A.L., Khan, M.M., 2020. Plant-extract-mediated SnO_2 nanoparticles: Synthesis and applications. ACS Sustain. Chem. Eng. 8, 3040–3054. https://doi.org/10.1021/acssuschemeng.9b06398

Meng, X., Wu, T., Liu, X., He, X., Noda, T., Wang, Y., Segawa, H., Han, L., 2020. Highly reproducible and efficient $FASnI_3$ perovskite solar cells fabricated with volatilizable reducing solvent. J. Phys. Chem. Lett. 11, 2965–2971. https://doi.org/10.1021/acs.jpclett.0c00923

Merino-Garcia, I., Tinat, L., Albo, J., Alvarez-Guerra, M., Irabien, A., Durupthy, O., Vivier, V., Sánchez-Sánchez, C.M., 2021. Continuous electroconversion of CO_2 into formate using 2 nm tin oxide nanoparticles. Appl. Catal. B Environ. 297. https://doi.org/10.1016/j.apcatb.2021.120447

Mikkelsen, M., Jørgensen, M., Krebs, F.C., 2010. The teraton challenge. A review of fixation and transformation of carbon dioxide. Energy Environ. Sci. 3, 43–81. https://doi.org/10.1039/b912904a

Nguyen-Phan, T.D., Hu, L., Howard, B.H., Xu, W., Stavitski, E., Leshchev, D., Rothenberger, A., Neyerlin, K.C., Kauffman, D.R., 2022. High current density electroreduction of CO_2 into formate with tin oxide nanospheres. Sci. Rep. 12, 1–10. https://doi.org/10.1038/s41598-022-11890-6

Oehl, N., Hardenberg, L., Knipper, M., Kolny-Olesiak, J., Parisi, J., Plaggenborg, T., 2015. Critical size for the β- to α-transformation in tin nanoparticles after lithium insertion and extraction. CrystEngComm 17, 3695–3700. https://doi.org/10.1039/c5ce00148j

Pal, T.K., De, D., Bharadwaj, P.K., 2020. Metal–organic frameworks for the chemical fixation of CO_2 into cyclic carbonates. Coord. Chem. Rev. 408, 213173. https://doi.org/10.1016/j.ccr.2019.213173

Patil, P.S., Kawar, R.K., Seth, T., Amalnerkar, D.P., Chigare, P.S., 2003. Effect of substrate temperature on structural, electrical and optical properties of sprayed tin oxide (SnO2) thin films. Ceram. Int. 29, 725–734.

https://doi.org/10.1016/S0272-8842(02)00224-9

Reñones, P., Moya, A., Fresno, F., Collado, L., Vilatela, J.J., De, V.A., Shea, P.O., 2016. Hierarchical TiO_2 nano fibres as photocatalyst for CO_2 reduction: Influence of morphology and phase composition on catalytic activity. J. CO_2 Util. 15, 24–31. https://doi.org/10.1016/j.jcou.2016.04.002

Rotaru, R., Savin, M., Tudorachi, N., Peptu, C., Samoila, P., 2018. Ferromagnetic iron oxide–cellulose nanocomposites prepared by ultrasonication. Polym. Chem. 9, 860–868. https://doi.org/10.1039/c7py01587a

Rumayor, M., Dominguez-Ramos, A., Irabien, A., 2019. Environmental and economic assessment of the formic acid electrochemical manufacture using carbon dioxide: Influence of the electrode lifetime. Sustain. Prod. Consum. 18, 72–82. https://doi.org/10.1016/j.spc.2018.12.002

Sergent, N., Gélin, P., Périer-Camby, L., Praliaud, H., Thomas, G., 2002. Preparation and characterisation of high surface area stannic oxides: Structural, textural and semiconducting properties. Sensors Actuators, B Chem. 84, 176–188. https://doi.org/10.1016/S0925-4005(02)00022-9

Solomon, S., Plattner, G.-K., Knutti, R., Friedlingstein, P., 2009. Irreversible climate change due to carbon dioxide emissions. Proc. Natl. Acad. Sci. U. S. A. 106, 1704–9. https://doi.org/10.1073/pnas.0812721106

Song, J., Xu, L., Xing, R., Li, Q., Zhou, C., Liu, D., Song, H., 2014. Synthesis of au/graphene oxide composites for selective and sensitive electrochemical detection of ascorbic acid. Sci. Rep. 4, 1–7. https://doi.org/10.1038/srep07515

Tan, D., Lee, W., Kim, Y.E., Ko, Y.N., Youn, M.H., Jeon, Y.E., Hong, J., Jeong, S.K., Park, K.T., 2020. SnO_2/ZnO composite hollow nanofiber electrocatalyst for efficient CO_2 reduction to formate. ACS Sustain. Chem. Eng. 8, 10639–10645. https://doi.org/10.1021/acssuschemeng.0c03481

Taylor, M.J., Coddington, J.M., 1992. The constitution of aqueous tin(IV) chloride and bromide solutions and solvent extracts studied by ^{119}Sn NMR and vibrational spectroscopy. Polyhedron 11, 1531–1544. https://doi.org/10.1016/S0277-5387(00)83148-4

Toledo-Antonio, J.., Gutiérrez-Baez, R., Sebastian, P.., Vázquez, A., 2003. Thermal stability and structural deformation of rutile SnO_2 nanoparticles. J. Solid State Chem. 174, 241–248. https://doi.org/10.1016/S0022-4596(03)00181-6

Tomishige, K., Tamura, M., Nakagawa, Y., 2019. CO_2 conversion with alcohols and amines into carbonates, ureas, and carbamates over CeO_2 catalyst in the presence and absence of 2-cyanopyridine. Chem. Rec. 19, 1–27. https://doi.org/10.1002/tcr.201800117

Tomita, Y., Hori, Y., 1998. Electrochemical reduction of carbon dioxide at a platinum electrode in acetonitrile-water mixtures. Stud. Surf. Sci. Catal. 114, 581–584. https://doi.org/10.1016/s0167-2991(98)80826-4

Tsujiguchi, T., Kawabe, Y., Jeong, S., Ohto, T., Kukunuri, S., Kuramochi, H., Takahashi, Y., Nishiuchi, T., Masuda, H., Wakisaka, M., Hu, K., Elumalai, G., Fujita, J.I., Ito, Y., 2021. Acceleration of electrochemical CO_2 reduction to formate at the Sn/ reduced graphene oxide interface. ACS Catal. 11, 3310–3318. https://doi.org/10.1021/acscatal.0c04887

Tufa, R.A., Chanda, D., Ma, M., Aili, D., Demissie, T.B., Vaes, J., Li, Q., Liu, S., Pant, D., 2020. Towards highly efficient electrochemical CO_2 reduction: Cell designs, membranes and electrocatalysts. Appl. Energy 277, 115557. https://doi.org/10.1016/j.apenergy.2020.115557

Vasileff, A., Zhi, X., Xu, C., Ge, L., Jiao, Y., Zheng, Y., Qiao, S.Z., 2019. Selectivity control for electrochemical CO_2 reduction by charge redistribution on the surface of copper alloys. ACS Catal. 9, 9411–9417. https://doi.org/10.1021/acscatal.9b02312

Wang, D., Zhang, M., Chen, Z., Li, H., Chen, A., Wang, X., Yang, J., 2017. Enhanced formaldehyde sensing properties of hollow SnO_2 nanofibers by graphene oxide. Sensors Actuators, B Chem. 250, 533–542. https://doi.org/10.1016/j.snb.2017.04.164

Wang, H., Sun, F., Zhang, Y., Li, L., Chen, H., Yu, J.C., 2010. Photochemical growth of nanoporous SnO_2 at the air–water interface and its high photocatalytic activity. J. Mater. Chem. 20, 5641–5645. https://doi.org/10.1039/b926930d

Wang, J., Liu, S., Cao, X., Wang, Z., Guo, Y., Li, X., Liu, C., Jiang, W., Wang, H., Wang, N., Wu, S., Tao, H., Ding, W., 2020. One-pot synthesis and gas sensitivity of SnO_2 nanoparticles prepared using two Sn salts of $SnCl_4 \cdot 5H_2O$ and $SnCl_2 \cdot 2H_2O$. Appl. Phys. A Mater. Sci. Process. 126, 1–7. https://doi.org/10.1007/s00339-019-3230-4

Wang, Q., Dong, H., Yu, H., 2014. Fabrication of a novel tin gas diffusion electrode

for electrochemical reduction of carbon dioxide to formic acid. RSC Adv. 4, 59970–59976. https://doi.org/10.1039/c4ra10775f

Wetchakun, N., Incessungvorn, B., Wetchakun, K., Phanichphant, S., 2012. Influence of calcination temperature on anatase to rutile phase transformation in TiO_2 nanoparticles synthesized by the modified sol-gel method. Mater. Lett. 82, 195–198. https://doi.org/10.1016/j.matlet.2012.05.092

Won, D.H., Choi, C.H., Chung, J., Chung, M.W., Kim, E.H., Woo, S.I., 2015. Rational design of a hierarchical tin dendrite electrode for efficient electrochemical reduction of CO2. ChemSusChem 8, 3092–3098. https://doi.org/10.1002/cssc.201500694

Xiang, H., Miller, A., Bellini, M., Christensen, H., Scott, K., Yu, E.H., 2020. Production of formate by CO_2 electrochemical reduction and its application in energy storage. Sustain. Energy Fuels 4, 277–284. https://doi.org/10.1039/c9se00625g

Yang, Y., Wang, Y., Yin, S., 2017. Applied surface science oxygen vacancies confined in SnO_2 nanoparticles for desirable electronic structure and enhanced visible light photocatalytic activity. Appl. Surf. Sci. 420, 399–406. https://doi.org/10.1016/j.apsusc.2017.05.176

Yang, Z., Yang, C., Han, J., Zhao, W., Shao, S., Li, S., Gao, H., Xie, H., Zhang, X., 2021. Boosting electrochemical CO_2 reduction to formate using SnO_2/graphene oxide with amide linkages. J. Mater. Chem. A 9, 19681–19686. https://doi.org/10.1039/d1ta02780h

Zhang, S., Kang, P., Meyer, T.J., 2014. Nanostructured tin catalysts for selective electrochemical reduction of carbon dioxide to formate. J. Am. Chem. Soc. 136, 1734–1737.

Zhang, Shun, Sun, M., Wang, K.Y., Cheng, L., Zhang, Shu, Wang, C., 2021. Conversion of organically directed selenidostannate into porous SnO_2 exhibiting effective electrochemical reduction of CO_2 to C1 products. ACS Sustain. Chem. Eng. 9, 2358–2366. https://doi.org/10.1021/acssuschemeng.0c08634

Zheng, X., Luna, P. De, Du, X., Yang, P., Sargent, E.H., Zheng, X., Luna, P. De, Garcı, F.P., 2017. Sulfur-modulated tin sites enable highly selective electrochemical reduction of CO_2 to formate. Joule 1, 794–805. https://doi.org/10.1016/j.joule.2017.09.014

This page is intentionally left blank

CHAPTER 5

A Simple Template-free Bioinspired Route of 1D Bi_2S_3 Nanorods Synthesis for Electrochemical CO_2 Reduction to Formate

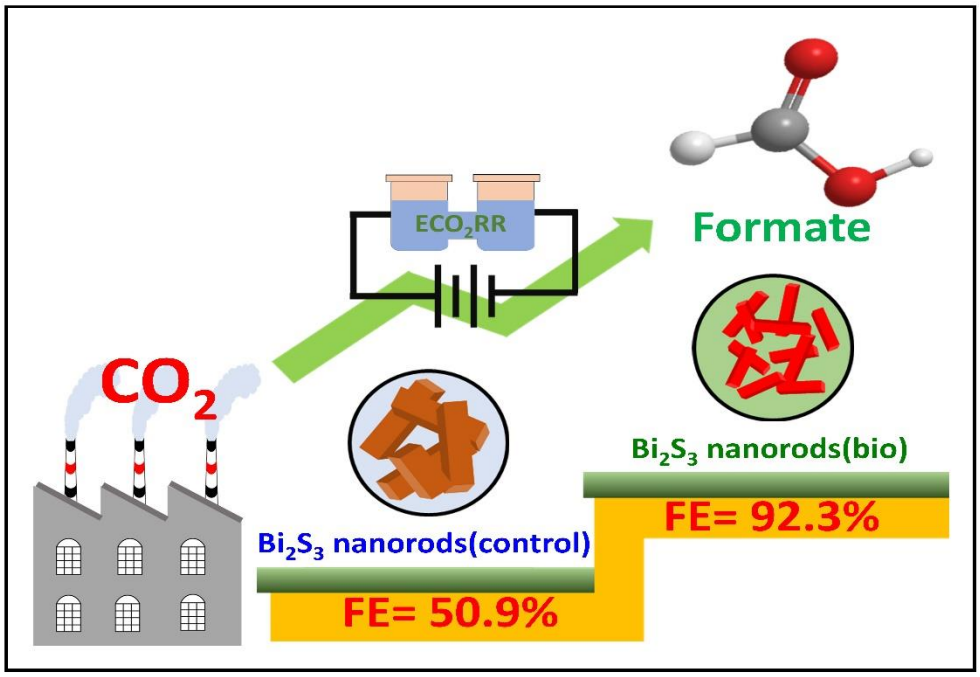

Highlights

- Development of a bioinspired process of template-free synthesis of 1D Bi_2S_3 nanorods
- Mechanistic exploitation of Bi_2S_3 nanorods formation mediated by plant-based analyte
- Bi_2S_3 nanorods electrocatalyzed CO_2 conversion to $HCOO^-$ with high Faradaic efficiency
- Oxidation of Bi_2S_3-NRs(bio) to $Bi_2O_2CO_3$, could serve as active sites during ECO_2RR

5.1 Background and executive motivation

In recent time, the consumption of fossil fuels holds 81% of the global primary energy demand (Welsby et al., 2021) with the rapid industrial growth. It results in a meteoric rise of CO_2 concentration in the atmosphere. According to a recent report, the global emission rate of CO_2 increased by 31.79% within a span of 15 years from 2003 to 2018 (Zhao et al., 2021). It causes the grievous greenhouse effect. Thus, CO_2 mitigation technologies partake a paramount role in the sustainable life of living beings on earth (Mikulčić et al., 2019). The direct conversion of CO_2 to different chemicals and fuels using electrochemical reduction reactions exhibits immense opportunities to combat adverse environmental consequences (Chapter 1) resulting from uncontrolled CO_2 emission (Sun et al., 2017).

Among almost 16 different C_1-C_3 value-added products from the electrochemical CO_2 reduction reaction (ECO_2RR), formic acid is considered the most prospective contestant according to the series $CO \approx HCOOH > CH_3OH >> C_2H_4 > CH_4$ (Sun et al., 2017). Traditionally, as a building block chemical, formic acid is used in animal feed and silage (27%), the leather industry (22%), rubber industries (7%), food technology and medicine (14%), textile industry (9%), and drilling fluids (~4%) with ~17% in miscellaneous applications (Han et al., 2020). Over recent years, formic acid has been utilized as a potential candidate as a fuel cell feedstock in a formic acid fuel cell and hydrogen storage (volumetric H_2 storage capacity of 53.4 g L^{-1} at STP) (Zell and Langer, 2018). Besides the traditional routes, formic acid (HCOOH)/formate ($HCOO^-$) serves as syngas ($CO + H_2$) equivalent in the 'formate bio-economy process (Morrison et al., 2019).

Several metals, like Pd and Hg (d- block transition metals), Cd (d- block metal), and In, Sn, Sb, Tl, Pb, Bi (post-transition p- block metals), and their metal-based materials were utilized to electrocatalyze CO_2 reduction for the selective production of HCOOH/ $HCOO^-$ with the faradaic efficiency (FE) in the range of 62.0-99.5% (Chatterjee et al., 2021). Among these catalysts, except Sn and Bi, others suffer either from high cost and/or toxicity. As the cost-effective and practically non-toxic (LD_{50} 5000-15000 mg kg^{-1}) (Egorova and Ananikov, 2017) metals, Sn (e.g., median lethal dose of SnO_2, LD_{50} (oral, mice and rats) value of 20000 mg kg^{-1}) (Johnson et al., 2014) and Bi (e.g., median lethal dose of Bi_2S_3, LD_{50} (oral, rat) value of 5000 mg kg^{-1}) (Rohr, 2002) are popularly used for ECO_2RR. Nevertheless, due to low utilization efficiency,

Sn-based catalysts fall behind as a competent electrocatalyst for ECO_2RR (An et al., 2021).

Focusing more on the application perspectives, bismuth sulfide (Bi_2S_3) is potentially used and in photoconductive materials, solar cells, electrochemical storage of hydrogen, lithium-ion batteries, and tomography imaging (Ai et al., 2011; Malca et al., 2017). Different methods used for synthesizing Bi_2S_3 nanomaterials for large-scale production, excellent quality crystals, and controllable particle size include chemical (hydrothermal, solvothermal, and ionothermal), pyrolysis, sol-gel, sonochemical (Wang et al., 2002), and molten salt methods (Wu et al., 2022). However, the development of Bi-based nanomaterials has been tethered by the disadvantages such as high temperature, high pressure (using autoclave), prolonged heating period, and a substantial amount of organic solvents to carry out the synthesis reaction. The uses of complexing agents like ethylenediaminetetraacetic acid (EDTA), triethanolamine (TEA), and sodium tartrate are also common in synthesizing Bi_2S_3 nanorods (Bi_2S_3-NRs, 20-30 nm), including ultrasound-assisted method (Wang et al., 2002). Luo et al. (2013) reported a template-free wet chemical route for synthesizing Bi_2S_3 nanorods (40 nm) at 240°C and 1 MPa. Large Bi_2S_3 nanorods (a few hundred nm) are formed in a hydrothermal method by autoclaving at 120°C, using thiourea as a sulphur source (Mukkabla et al., 2015). The molten salt method could form rod-like Bi_2S_3 single crystals (330 nm) at 250-350°C (Wu et al., 2022).

Bi-based catalysts are accepted as efficient electrocatalysts owing to their high selectivity and FE towards formic acid production (Wei et al., 2022; X. Zhang et al., 2018), and moderately positive standard redox potential (Bi^{3+}/Bi 0.308 V vs. SHE), due to their positive free energy of hydrogen adsorption (Jiang et al., 2021). Y. Zhang et al. (2018) reported the synthesis of micro-urchin structure of sulphide-derived Bi nanorods having self-assembled micro-rod, with FE of 84% at a current density of −6 mA cm^{-2} for the production of $HCOO^-$. Yang et al. (2020) synthesized 2D Bi nanosheet, which exhibited 99% FE towards $HCOO^-$ at a current density of −16 mA cm^{-2} (Yang et al., 2020). A Bi electrocatalyst of hexagonal sheet structure exhibited 100% FE at −3.5 mA cm^{-2} of current density (Jiang et al., 2021).

Herein, we propose a simple surfactant/morphological template-free bioinspired route for the low-temperature synthesis of pure 1D Bi_2S_3-NRs(bio) using *Sechium edule* (commonly known as squash or chayote) fruit extract, and employed for ECO_2RR for

the selective formation of $HCOO^-$ to outperform FE achieved in Chapter 3 and Chapter 4. This work reports an in-depth characterization of various physicochemical, morphological, and dimensional attributes of Bi_2S_3-NRs(bio). The chemical states of Bi_2S_3 nanorods were also thoroughly investigated by using X-ray photoelectron spectroscopy. The role of bio-active compounds forming Bi_2S_3-NRs(bio) with controlled morphology and size and their functionality for the capping of nanorods are also investigated. Afterwards, the Bi_2S_3-NRs(bio) modified carbon electrode was fabricated by simple drop-casting, and it's the performance was tested for efficient and selective ECO_2RR in a semi-batch reactor.

5.2 Results and Discussion

5.2.1 XRD analysis

Figure 5.1a shows the XRD pattern of the as-synthesized Bi_2S_3-NRs(bio). The characteristic peaks observed at 2θ= 15.7, 17.6, 22.4, 23.7, 24.9, 25.2, 27.4, 28.7, 31.8, 33.0, 33.9, 35.6, 36.6, 39.1, 40.0, 42.7, 45.6, 46.5, 52.7, and 59.2° correspond to (020), (120), (220), (101), (130), (310), (021), (211), (221), (301), (330), (240), (231), (041), (141), (421), (002), (431), (351), and (242) planes with a good agreement to the previous report (Chen et al., 2013). The lattice constants were calculated as, a= 11.24, b= 11.27, and c= 3.39 Å. A significant increase in the intensity of (211) plane compared to the (130) plane is because of predominant crystalline growth in (211) plane (Onwudiwe and Nkwe, 2020). Figure 5.1b shows the primitive XRD peaks of the sample Bi_2S_3NRs(bio0). Figure 5.1c shows the incipient peaks of the sample Bi_2S_3NRs(bio1). Furthermore, the only broad peak at 27.9° for the sample Bi_2S_3NRs(bio2) could be the presence of Bi_2O_3 (JCPDS Card No. 71-2274) (Jabeen Fatima et al., 2015) (Figure 5.1d). The Bi_2S_3-NRs(control) synthesized without using the bio-extract/ reducing agent also shows a similar XRD pattern (Figure 5.1e) as in Bi_2S_3-NRs(bio) (Figure 5.1a) and the diffraction peaks of orthorhombic Bi_2S_3 with the Pbnm (62) space group (JCPDS Card No. 01-089-8963) is shown in (Figure 5.1f) (Wang et al., 2020). Therefore, only two samples, namely Bi_2S_3-NRs(bio) and Bi_2S_3-NRs(control) were considered for further investigations.

No trace of an impure phase was detected. The diffraction patterns of Bi_2S_3-NRs(bio) for all three batches of Bi_2S_3-NRs(bio) exhibited the same crystal characteristic of Bi_2S_3 (Figure 5.2).

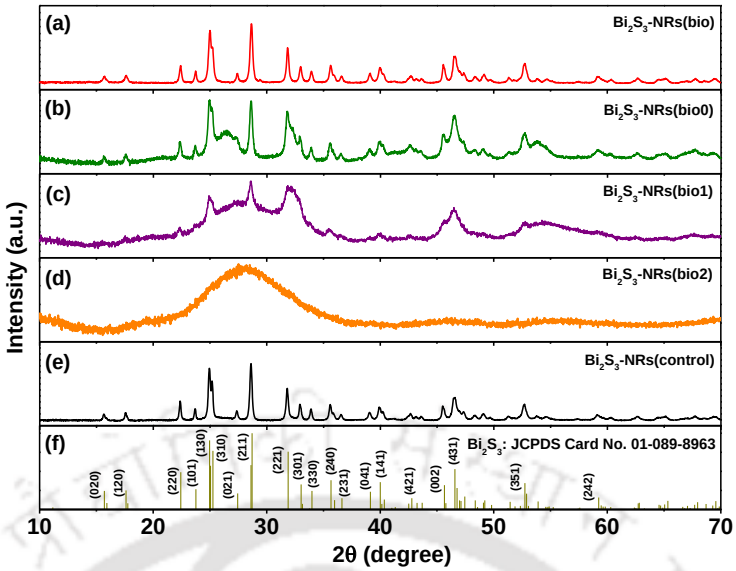

Figure 5.1. XRD patterns of (a) Bi_2S_3-NRs(bio), (b) Bi_2S_3NRs(bio0), and (c) Bi_2S_3NRs(bio1). (d) Bi_2S_3NRs(bio2), (e) Bi_2S_3-NRs(control), and (f) JCPDS reference diffractogram of Bi_2S_3.

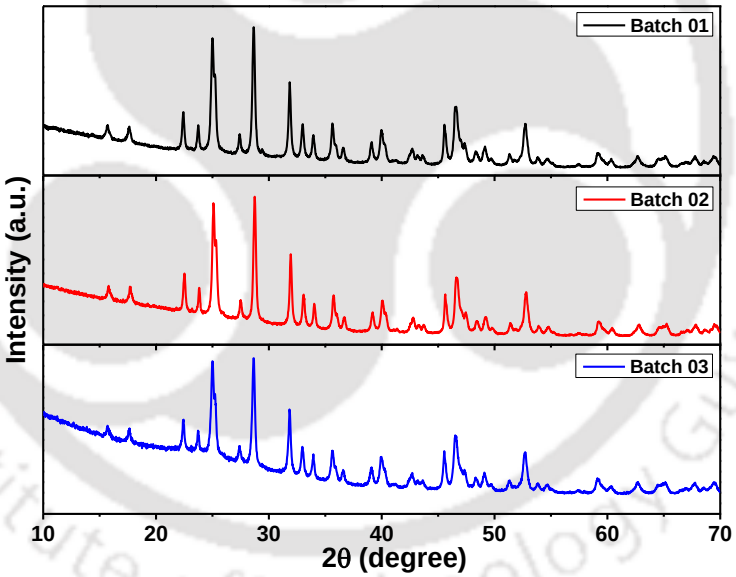

Figure 5.2. XRD patterns of Bi_2S_3-NRs(bio) of three batches of synthesized nanorods under identical synthesis condition.

5.2.2 Optical properties

The synthesized Bi_2S_3-NRs(bio) exhibited strong optical absorption in the UV-vis range with a broad peak at 400-650 nm (Figure 5.3a). This could be attributed to the $^3P_1 \rightarrow {}^1S_0$ transition that occurs in the visible range, when a strong absorption of UV radiation results in the transition of $6s^2$ (ground state)→6s6p (excited state) band in Bi^{3+}

(Yadav and Rai, 2017). The diffuse reflectance (R_∞) data was transformed to an equivalent absorption coefficient (α), employing the Kubelka-Munk (K-M) function, according to Equation 5.1 (Karmaoui et al., 2018).

$$\alpha \approx \frac{k}{S} = \frac{(1-R_\infty)^2}{2R_\infty} \equiv F(R_\infty) \quad (5.1)$$

Where, k and S are the K-M absorption, and scattering coefficients, respectively. The band gap energy (E_g) of Bi_2S_3-NRs(bio) and Bi_2S_3-NRs(control) were estimated by the Tauc plot method. α with direct allowed transition can be expressed as Equation 5.2. Here, h, ν, and A are the Plank's constant, frequency of light, and a constant, respectively.

$$(\alpha h\nu)^2 = A(h\nu - E_g) \quad (5.2)$$

The calculated band gap energy, E_g of Bi_2S_3-NRs(bio) is 1.51 eV (inset of Figure 5.3a), which is larger than the bulk material (E_g 1.3 eV). This blue shift could be either due to the electronic transitions from the energetically lowest-lying states (1P→1P), with reference to the expected allowed transitions (1S→1S) in the case of bulk Bi_2S_3 or the confined three-dimensional nanostructure formed in the synthesis method (Martha et al., 2021).

Figure 5.3b shows the UV-vis absorption spectra and the Tauc plot (inset of Figure 5.3b) of Bi_2S_3-NRs(control). Apart from the broad peak at 400-650 nm observed in Bi_2S_3-NRs(bio), a wide absorption band noted in the wavelength region of 400 nm arises due to the electron transition from the valence band of (O_{2p} + Bi_{6s}) hybrid orbital to the conduction band of empty Bi_{6p} orbital in Bi_2O_3 (Huang et al., 2019). The bandgap energy, E_g, was calculated to be 1.21 eV, which is less than that of Bi_2S_3-NRs(bio) and could be due to the synergistic effects of Bi_2S_3 and Bi_2O_3 present in Bi_2S_3-NRs(control).

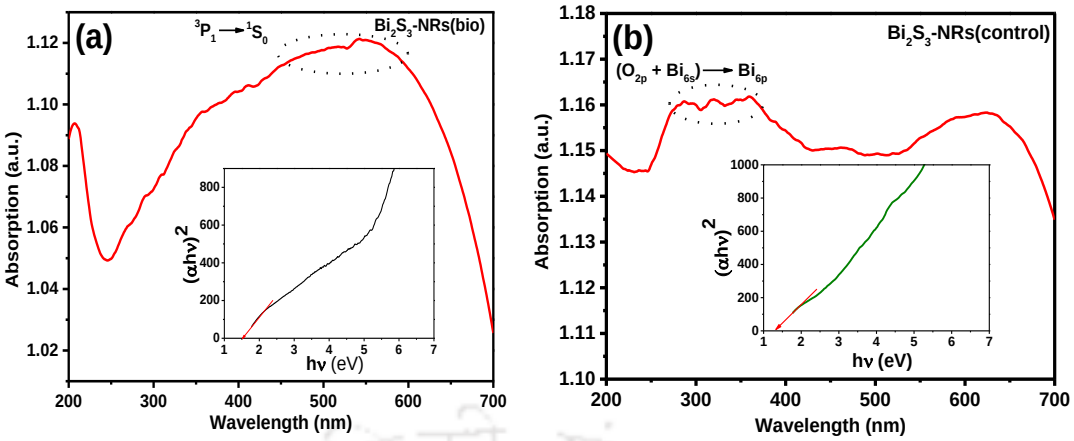

Figure 5.3. UV-vis absorption spectra and Tauc plot (insets) of (a) Bi_2S_3-NRs(bio) and (b) Bi_2S_3-NRs(control).

5.2.3 Thermal analysis of Bi_2S_3-NRs(bio)

The thermogravimetric (TGA/DTG) analyses were performed to understand the thermal stability of Bi_2S_3 nanorods and the nature of bio-moieties attached to its surface (Figure 5.4a). The corresponding mass change rate curves were obtained by differentiating the TG curves. For Bi_2S_3-NRs(bio), the first mass loss of ~5% at 130-200°C could be attributed to the removal of solvent residue and adsorbed water on the surface (Caputo et al., 2017). Similarly, the first mass loss in Bi_2S_3-NRs(control) was observed to be ~2%. The higher mass loss in Bi_2S_3-NRs(bio) is due to the removal of hydrophilic polyphenolic compounds capped onto the surface of the nanorods (Rao and Paria, 2014). The second mass loss of 4.4% at 200-325°C is attributed to the decomposition of biomolecules like ascorbic acid, starch, and stable lignin molecules attached to the surface of Bi_2S_3-NRs(bio) (Chelli and Golder, 2019). This mass loss was absent in the TGA of Bi_2S_3-NRs(control) (Figure 5.4b). The third mass loss of 3.5% at 325-650°C could be due to the degradation of oxygen-containing functional groups present in nanorods. The major mass loss after 650°C is resulted as the net effect from the loss of sulfur as SO_2 and formation of Bi_2O_3 (Chufa et al., 2021).

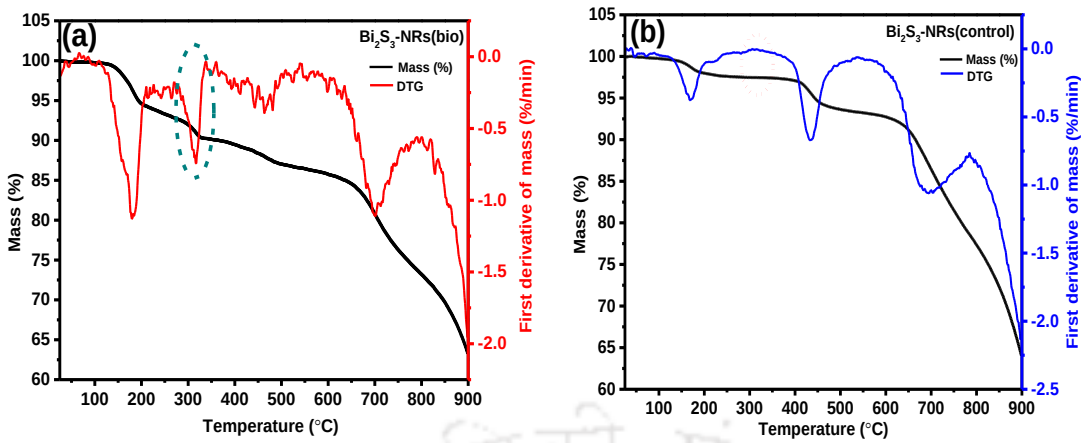

Figure 5.4. Mass vs. temperature profile for TGA of (a) Bi_2S_3-NRs(bio) and (b) Bi_2S_3-NRs(control).

5.2.4 BET surface area analysis

The surface area influences the electrocatalytic activity of a nanocatalyst (Farooq et al., 2019). Therefore, the measurement of the surface area of a functional material is important before its electrocatalytic applications. In general, the high specific surface area could shorten the ion diffusion path and enhance electro-active material utilization (Liang et al., 2017). The higher surface area provides more active sites for a catalyst, which facilitates the adsorption and reaction site for the electrocatalytic activity. The N_2 adsorption-desorption isotherm of Bi_2S_3-NRs(bio) and Bi_2S_3-NRs(control) using the BET method are shown in Figures 5.5a-5.5b. Both the isotherms show type-IV with H3 type hysteresis loop. It implies that Bi_2S_3 nanorods are mesoporous in nature (Jiang et al., 2016). The hysteresis loop starts at p/p_0= 0.85 with high adsorption at p/p_0= 1.0. The compact type of hysteresis loop indicates uniform pore size distribution (Feng et al., 2014). The surface area was measured to be 13.4 m^2 g^{-1}, which is comparable with the surface area and BET-type reported earlier (Ayodhya and Veerabhadram, 2017). The BJH pore-size distribution curve of Bi_2S_3-NRs(bio) is shown in inset of Figure 5.5a, having an average pore size of 25 nm. The BET surface area of Bi_2S_3-NRs(control) (Figure 5.5b) was found to be almost half (7.03 m^2 g^{-1}) compared to Bi_2S_3-NRs(bio).

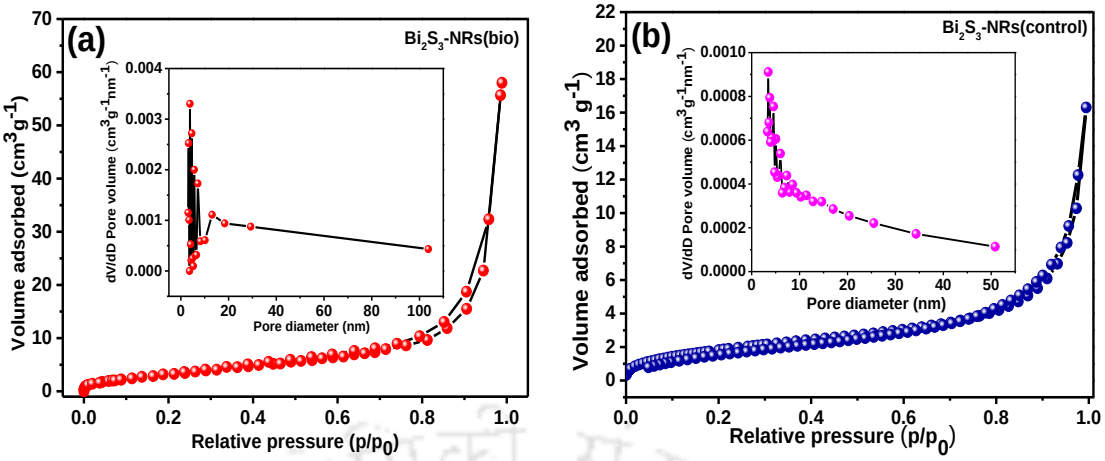

Figure 5.5. (a) N_2 adsorbtion-desorption isotherm of BET analysis and (b) BJH pore size distribution of Bi_2S_3-NRs(bio).

5.2.5 Morphological analysis

The FESEM images (Figures 5.6a1-5.6a2) show distinct rod-shaped Bi_2S_3-NRs(bio). The length and diameter of the nanorods were in the range of 209-668 nm and 25-100 nm, respectively. The morphology and particle size (Figures 5.7a-5.7c and 5.8a1-5.8a3) did not show any noteworthy variations for all three batches of nanorods, with an average particle diameter of 49 ± 1.3 nm. The rod structure formed in Bi_2S_3-NRs(control) had a larger length of 700-1670 nm. The surface was also non-uniform (Figures 5.6b1-5.6b2). The average Bi_2S_3-NRs(control) diameter was found to be 259.5 nm with a wide particles size distribution ranging from 103.5 to 441.5 nm (Figure 5.8b).

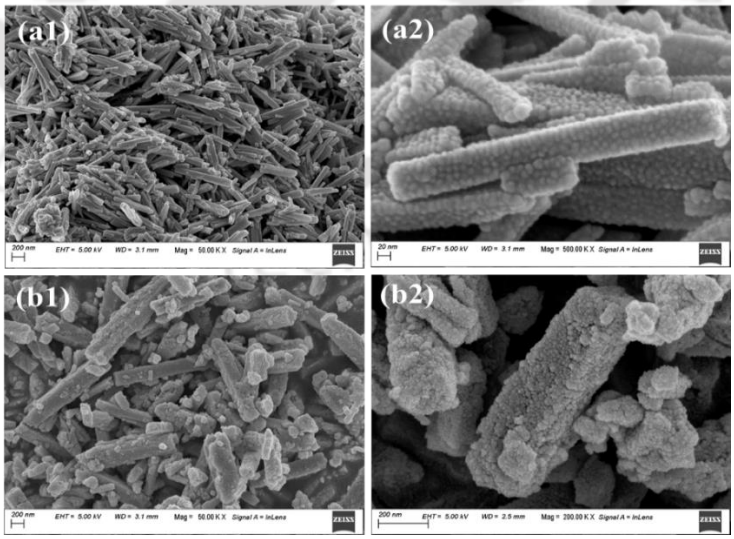

Figure 5.6. FESEM images of Bi_2S_3-NRs(bio) at (a1) low and (a2) high resolutions, and Bi_2S_3-NRs(control) at (b1) low and (b2) high resolutions.

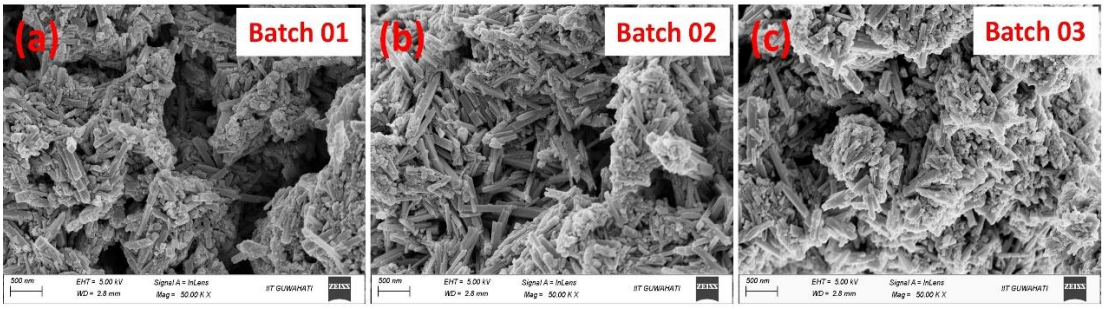

Figure 5.7. (a)-(c) FESEM images of Bi_2S_3-NRs(bio) of three batches of synthesized nanorods under identical synthesis condition.

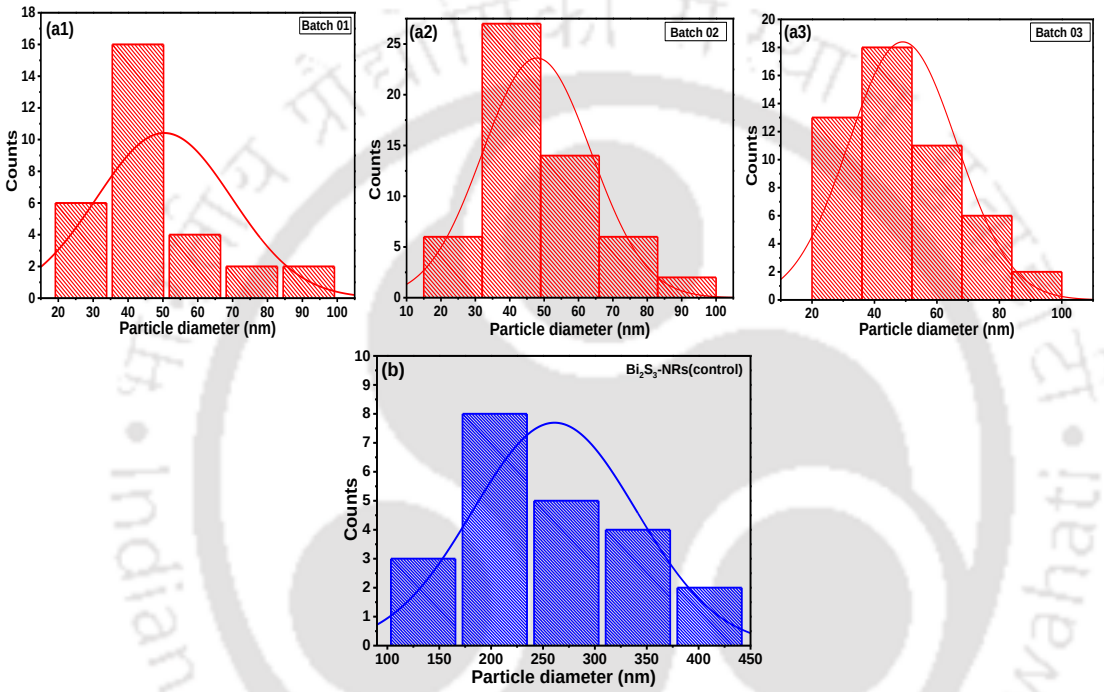

Figure 5.8. Particle size distributions of (a1)-(a3) Bi_2S_3-NRs(bio) of three batches of synthesized nanorods under identical synthesis condition, and (b) Bi_2S_3-NRs(control) determined using FESEM images.

Figure 5.9 shows the FETEM, HRTEM, and SAED pattern of Bi_2S_3-NRs(bio). The low-magnification FETEM image (Figure 5.9a) reveals well-defined rod morphology. The average length and diameter of the nanorods range from 134.2 to 728.7 nm and 12.4 to 81.8 nm, respectively. The diameter of Bi_2S_3-NRs(bio) synthesized using bio-analytes is comparable with the literature reported Bi_2S_3-NRs, synthesized in a conventional method (Wu et al., 2011). The formation of the crystals of Bi_2S_3-NRs(bio) was further confirmed by High-resolution transmission electron microscopy (HRTEM). Bi_2S_3-NRs(bio) exhibit lattice fringe distances of 0.197 and

0.552 nm (Figure 5.9c) corresponding to (002) and (200) planes, respectively, and the crystal growth of nanorod along the direction of (001), could be due to the highest surface energy of (001) plane with the fastest growth velocity that helps Bi_2S_3 nanoparticles to grow in the preferred direction during the ripening process (Wang et al., 2009). The selected area electron diffraction (SAED) pattern in Figure 5.9c (inset) shows single crystallinity. FETEM images of Bi_2S_3-NRs(control) show the formation of agglomerated nanorods with irregular shape (Figure 5.10).

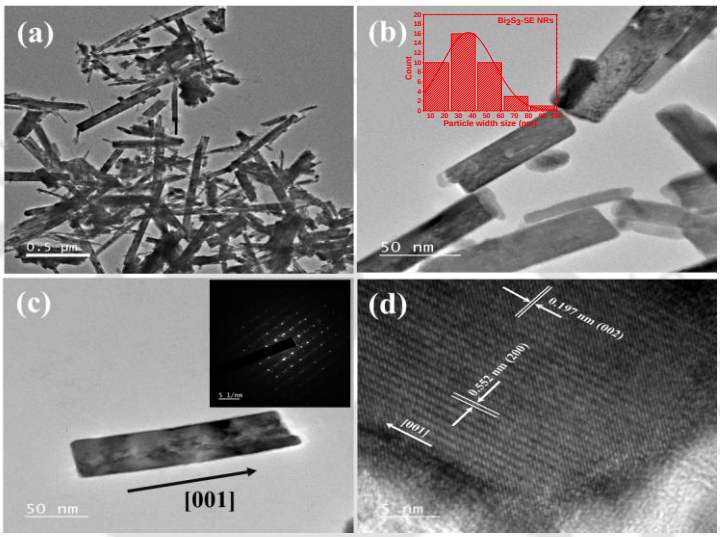

Figure 5.9. (a)-(c) FETEM micrographs, (d) HRTEM image of Bi_2S_3-NRs(bio). The inset of (c) is the SAED pattern of a single nanorod.

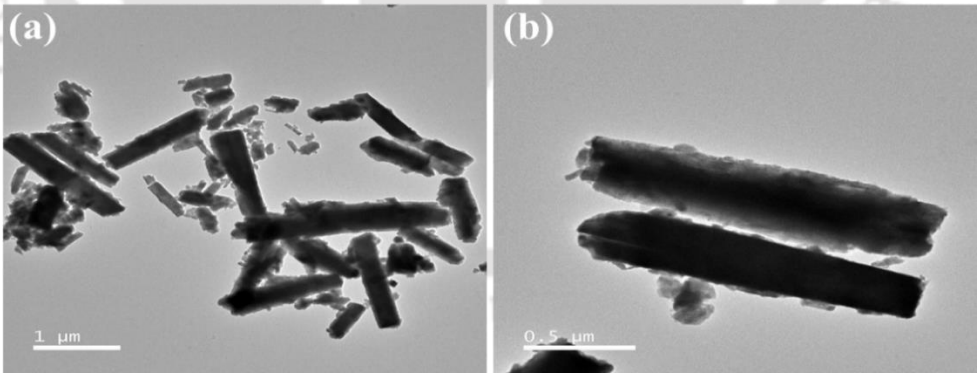

Figure 5.10. (a) Low and (b) high resolution FETEM images of Bi_2S_3-NRs(control).

The FETEM image of Bi_2S_3-NRs(bio) (Figure 5.11a) employed for the EDX analyses is shown in Figure 5.11b. It reveals that nanorods contain 41.65% Bi and 58.35% S which agree with the stoichiometric ratio of Bi:S (2:3) for Bi_2S_3. The EDX

elemental mapping of these nanorods (Figure 5.11a) exhibits a homogeneous distribution of Bi and S over the entire nanorods (Figures 5.11c and 5.11d).

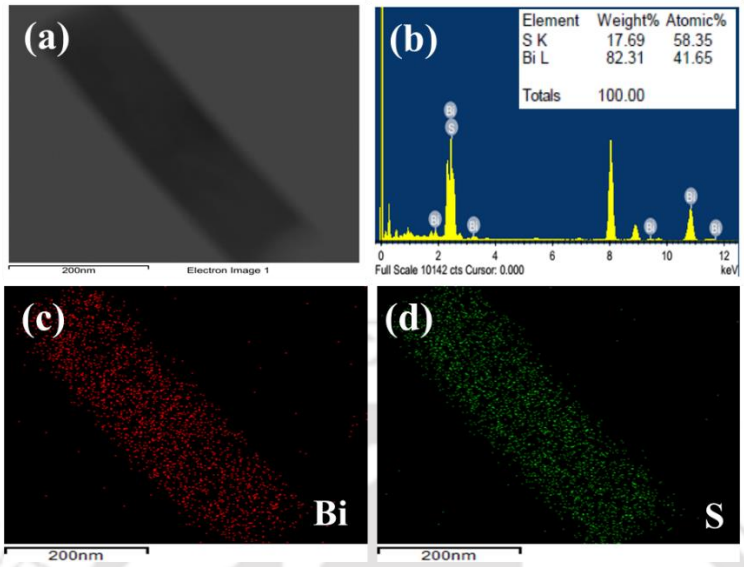

Figure 5.11. (a) FETEM micrograph, (b) EDX spectrum, and (c) and (d) TEM mapping images of Bi_2S_3-NRs(bio).

5.2.6 XPS analysis

The survey spectrum of Bi_2S_3-NRs(bio) is shown in Figure 5.12. The spectrum reveals the presence of Bi, S, C, and O elements. The presence of C 1s and O 1s is from the adsorption of molecules of atmospheric gases such as O_2, CO_2, and H_2O on the surface of the powder samples. F in the survey spectrum at 689 eV refers to F (fluorine) from the Nafion binder used in the fabrication of Bi_2S_3-NRs(bio)/TCP electrode.

Figures 5.13a1 and 5.13a2 show the high-resolution XPS of Bi 4f and S 2p region for Bi_2S_3-NRs(bio) and Bi_2S_3-NRs(control). The Bi 4f spectra of Bi_2S_3-NRs(bio) (Figure 5.13a1) exhibit two predominant peaks at 158.3 and 163.7 eV which are attributed to the spin-orbital splitting of Bi $4f_{7/2}$ and $4f_{5/2}$, respectively, a feature of Bi^{3+} of Bi_2S_3 (Zhu et al., 2017). The peaks at 161.08 and 161.9 eV correspond to the doublet of the S 2p region, ascribing to the spin state of S $2p_{3/2}$ and S $2p_{1/2}$, respectively. This spin-orbital doublet of S 2p confirms the valence state of sulfur, S^{2-} in Bi_2S_3-NRs(bio) (Miniach and Gryglewicz, 2018). For Bi 4f spectra of Bi_2S_3-NRs(control) (Figure 5.13a2), similar peaks appeared at 158.6 and 163.7 eV. In addition, the peaks at 159.4 and 164.3 eV are the features of Bi_2O_3 (Zhu et al., 2017). The Bi-S:Bi-O area ratio is calculated to be 1:1.1 for Bi_2S_3-NRs(control). The absence of oxides in Bi_2S_3-NRs(bio)

is resulted from the antioxidant property of AA, capped on the surface of nanorods, which prevents further oxidation of S^{2-} during the synthesis process (Shahbazi et al., 2020). A very weak signal of S 2p at 161.2 eV is found for Bi_2S_3-NRs(control). The presence of a surface Bi-SO_x bond could cause the decrease in the unoccupied density of states of the 6p orbital of Bi, and it is shifted to the 2s orbital of S due to the electron-withdrawing effect of O atoms in (SO_x) (Thomson et al., 2010). It is also notable in S 2s spectra (Figure 5.13b1). The peaks shifted more than 0.5 eV of binding energy implying that Bi is bonded to the higher electronegative element, O, besides the Bi-S bond in Bi_2S_3-NRs(control). Moreover, the typical Bi 4f spin-orbital doublet splitting of 5.3 eV indicates the presence of Bi^{3+} in both specimens.

Figures 5.13b1 and 5.13b2 show the high-resolution XPS of the S 2s region of Bi_2S_3-NRs(bio) and Bi_2S_3-NRs(control). The deconvolution of the S 2s region reveals two peaks at 225.2 and 227.8 eV, attributed to S^{2-} of Bi_2S_3 and neutral sulfur (S^0) in Bi_2S_3-NRs(bio), respectively. The presence of S^0 could be attributed to it's formation during Bi_2S_3-NRs(bio) synthesis, as interstitial sulfur crystal (Zhu et al., 2017). The characteristic peak for Bi-S in Bi_2S_3-NRs(control) appeared at 224.8 eV, and the peak at 231.5 eV is attributed to the oxidized sulfur species, SO_x (Zhu et al., 2017).

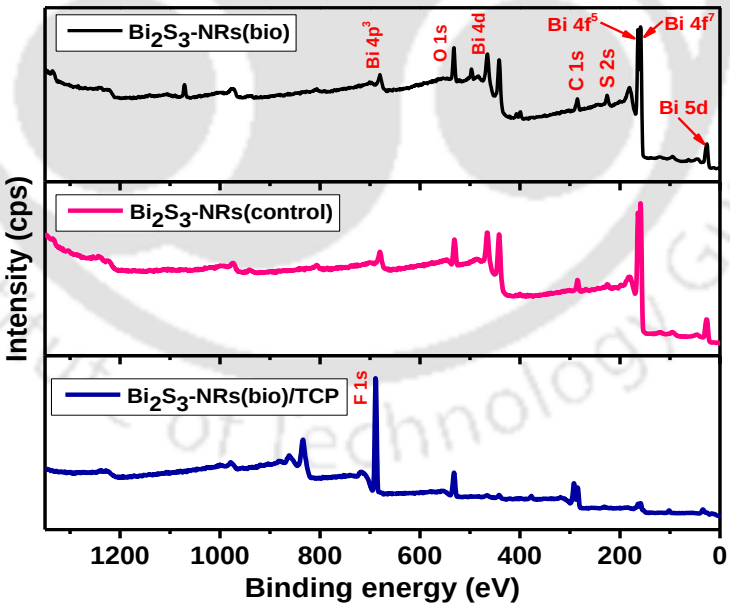

Figure 5.12. XPS survey spectra of Bi_2S_3-NRs(bio), Bi_2S_3-NRs(control), and Bi_2S_3-NRs(bio)/TCP.

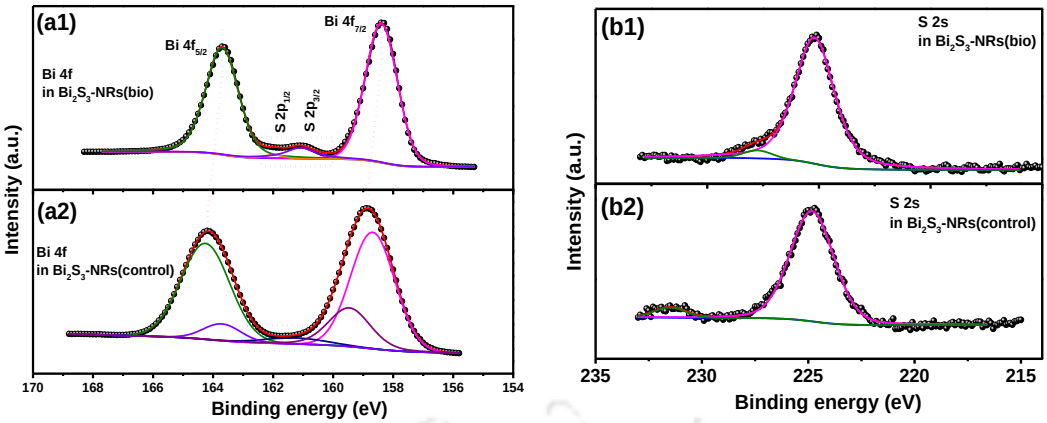

Figure 5.13. High resolution XPS for (a1, a2) Bi 4f of Bi_2S_3-NRs(bio), and Bi_2S_3-NRs(control) and (b1, b2) S 2s of Bi_2S_3-NRs(bio), and Bi_2S_3-NRs(control).

5.2.7 Formation of Bi_2S_3 nanorods and its stabilization

The mechanistic approach for the formation of Bi_2S_3 nanorods in the absence and presence of bio-extract is proposed with the help of the following reaction pathways. In the absence of bio-extract (Equations 5.3-5.12), in an acidic medium, hydrolysis of $Bi(NO_3)_3$ to insoluble $BiONO_3$ (Equations 5.3-5.4) is replaced by the soluble $[Bi(NO_3)(H_2O)_6]^{2+}$ complex formation (Equation 5.5) (Wei et al., 2022). Thiourea $[CS(NH_2)_2]$ reacts with H_2O to form NH_3, H_2S, and CO_2 (Equations 5.6-5.8) (Hu et al., 2001). The overall reaction is shown in Equation 5.9.

$$Bi(NO_3)_3 \cdot 5H_2O \xrightarrow{H^+} Bi^{3+} + 3NO_3^- + 5H_2O \tag{5.3}$$

$$Bi^{3+} + NO_3^- + H_2O \leftrightarrow BiONO_3\downarrow + 2H^+ \tag{5.4}$$

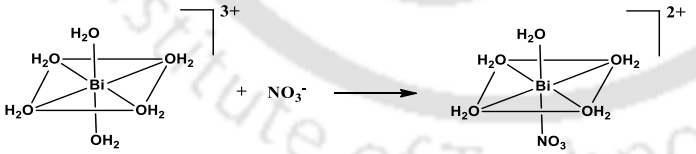

(5.5)

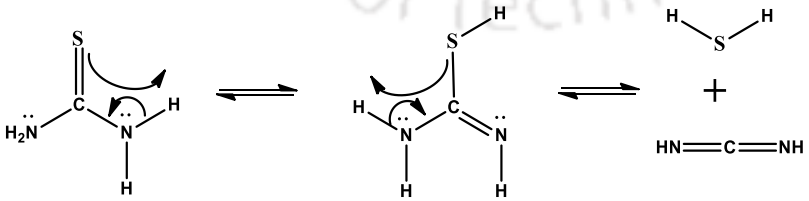

(5.6)

$$NH_2CSNH_2 \leftrightarrow CH_2N_2 + H_2S \tag{5.7}$$

$$CH_2N_2 + H_2O \leftrightarrow NH_3 + CO_2 \tag{5.8}$$

$$NH_2CSNH_2\ (Tu) + 2H_2O \rightarrow 2NH_3 + H_2S + CO_2 \tag{5.9}$$

In an acidic media, H_2S readily dissociates into H^+ and SH^- ions, which further react with $Bi[(NO_3)(H_2O)_6]^{2+}$ complex to form $Bi[(SH)(H_2O)_6]^{2+}$ and Bi_2S_3 nanoseeds (Equations 5.10-5.12).

$$H_2S \rightarrow H^+ + SH^- \quad (5.10)$$

$$Bi[(NO_3)(H_2O)_6]^{2+} + H^+ + SH^- \rightarrow Bi[(SH)(H_2O)_6]^{2+} + HNO_3 \quad (5.11)$$

$$2Bi[(SH)(H_2O)_6]^{2+} + H^+ + SH^- \rightarrow Bi_2S_3 + 2H_2O \quad (5.12)$$

Bi^{3+} reacts with thiourea (Tu) to form yellow coloured $[Bi(Tu)_6]^{3+}$ complex (Equation 5.13) (Luigi et al., 1977), which further is decomposed at 75°C (reaction temperature) to form dark brown Bi_2S_3 (Equation 5.14). High stability of $[Bi(Tu)_6]^{3+}$ complex could be due to the π-dative interaction of $S \rightarrow Bi^{3+}$ (L→M, back donation) (Golovnev et al., 2010). Here, in $[Bi(Tu)_6]^{3+}$ complex, Tu acts both as a complexing agent with Bi^{3+} and also as a sulfur source (Atri et al., 2020). In fact, the reactions (Equations 5.3-5.12 and 5.14) could take place simultaneously.

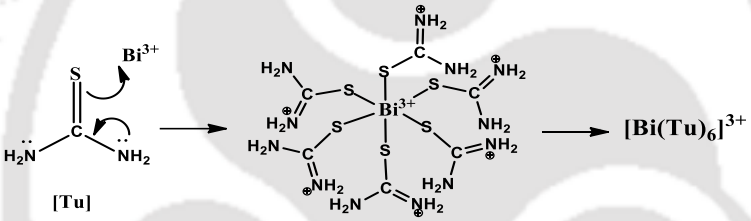

(5.13)

$$[Bi(Tu)_6]^{3+} \rightarrow Bi_2S_3 + NH_3 + CO_2 \quad (5.14)$$

In the presence of bio-extract, the formation of yellow-coloured $[Bi(Tu)_x]^{3+}$ complex prevents the excessive free Bi^{3+} concentration for the uncontrolled formation of Bi_2S_3. The hydrogen of −OH groups of AA from *S. edule* fruit extract binds with the unsaturated sulfur of Bi_2S_3-NRs(bio). On the other hand, the oxygen atoms oriented themselves towards the nearest Bi atom. The (001) planes, due to their highest surface energy, promote the growth velocity in the [001] direction. As a consequence, during the ripening process, the small particles are consumed to form large Bi_2S_3 particles, which prefer to grow in the [001] direction (Figure 5.14). Moreover, Bi-S bonds along the c-axis are the shortest, and the bond energy is maximum. Therefore, after the bond formation between Bi^{3+} and S^{2-} ions along the [001] direction, the energy required for the bond cleavage is also very high. Consequently, Bi_2S_3 nanorods grow along the c-axis became thermodynamically and kinetically more stable (Wang et al., 2009). The surface capping of AA also could reduce the size of Bi_2S_3-NRs(bio).

For the sample Bi_2S_3-NRs(bio2), also shown from the XRD analysis (Figure 3d), the formation of Bi_2O_3 at an alkaline pH (~9), could follow as in Equation 15 (Sudrajat and Sujaridworakun, 2017).

$$2BiONO_3 + 2HO^- \leftrightarrow Bi_2O_3 + 2NO_3^- + H_2O \quad (5.15)$$

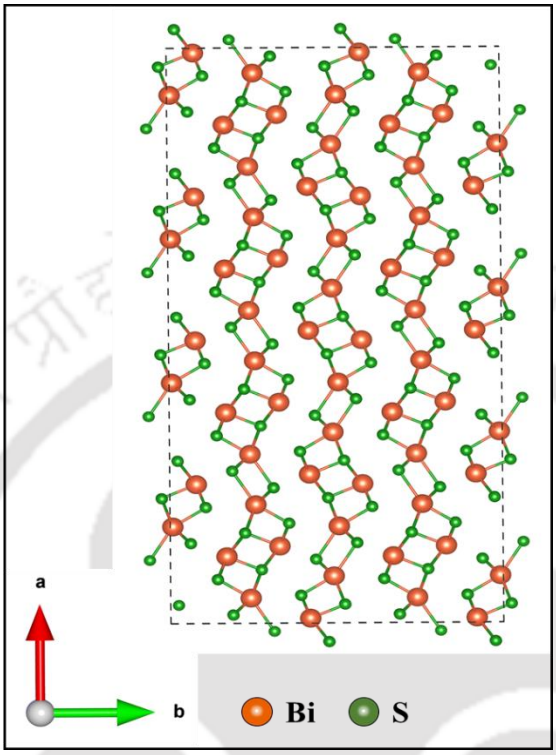

Figure 5.14. Representation of Bi_2S_3 crystal structure with Pbnm (62) space group (Momma and Izumi, 2011).

5.3 Electrocatalytic activity of Bi_2S_3-NRs(bio)

5.3.1 Cyclic voltammetric (CV) response

The cyclic voltammetry study was conducted using Bi_2S_3-NRs(bio)/TCP electrode in N_2- and CO_2(saturated)-bubbled 0.5 M $KHCO_3$ solution (Figure 5.15) to understand the electrochemical behaviour of Bi_2S_3-NRs(bio) towards ECO_2RR. The anodic peaks appeared at −0.24 and −0.64 V vs. AgCl, ascribing the oxidation of metallic Bi to Bi (III) during the cathodic sweep. The cathodic peaks noted in the potential range of −0.4 to −0.85 V are for the reduction of Bi(III) to metallic Bi (Valyulene et al., 2007). A significant difference in current density was observed starting from the onset potential, −1.4 V (vs. Ag/AgCl) with Bi_2S_3-NRs(bio)/TCP electrode in CO_2-saturated 0.5 M $KHCO_3$ solution. The higher response current infers

to strong electrocatalytic activity of Bi_2S_3-NRs(bio) towards ECO_2RR in an aqueous solution (Y. Zhang et al. 2018). The cyclic voltammograms recorded with Bi_2S_3-NRs(bio)/TCP electrodes for three batches of nanorods exhibited an overlapping nature both in N_2- and CO_2(saturated)-bubbled electrolyte (Figure 5.16).

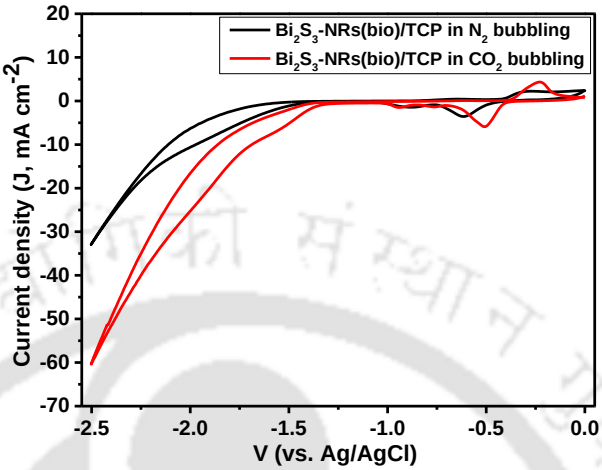

Figure 5.15. Cyclic voltammograms recorded with Bi_2S_3-NRs(bio)/TCP electrode in N_2- and CO_2(saturated)-bubbled 0.5 M $KHCO_3$ solution.

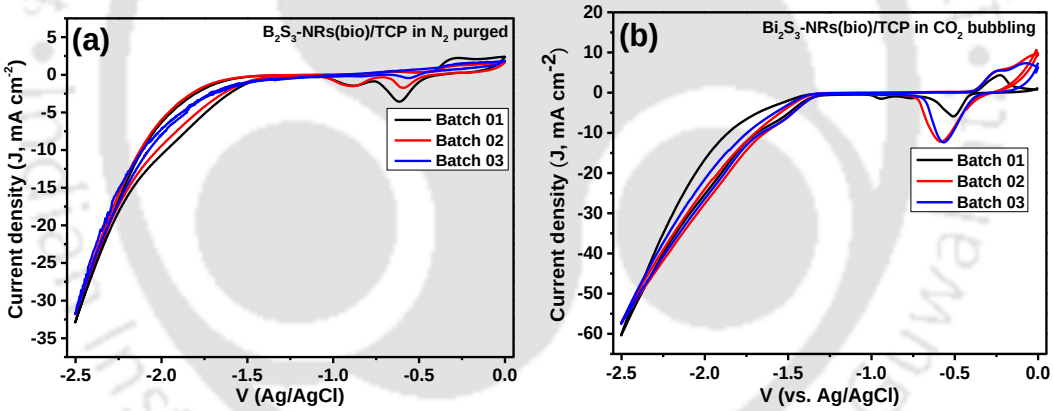

Figure 5.16. Cyclic voltammograms recorded using Bi_2S_3-NRs(bio)/TCP electrode in (a) N_2- and (b) CO_2(saturated)- bubbled 0.5 M $KHCO_3$ solution for three batches of synthesized nanorods under identical synthesis condition.

5.3.2 EIS measurements

EIS measurements were carried out to investigate the electrical conductivity and the charge transfer kinetics of the modified electrodes. Figure 5.17 shows the Nyquist plot captured with Bi_2S_3-NRs(bio)/TCP electrode in N_2- and CO_2(saturated)-bubbled solution. The smaller radius of Bi_2S_3-NRs(bio)/TCP electrode in CO_2 saturated 0.5 M $KHCO_3$ solution than that in N_2-purged solution is clearly visible. The equivalent circuit

is shown in Figure 5.17(inset). It is composed of a resistance (R_s) in series (associated with the solution resistance), a parallel between the resistance (R_1) and a constant phase element (Q_1, CPE), and another parallel resistance (R_2) and constant phase element (Q_2). Altogether, it is a [R(RQ)(RQ)] type of circuit. The fitted electrical elements are summarized in Table 5.1. R_s stands for the bulk electrolyte solution resistance between the reference (Ag/AgCl) and Bi_2S_3-NRs(bio)/TCP electrodes. The value was found to be 1.60 Ω in both the cases with N_2- and CO_2(saturated)-bubbling. The higher electrolyte concentration is accountable for a low R_s value (Ahn et al., 2017). R_1 is for the charge transfer (CT) resistance at the Bi_2S_3-NRs(bio)/TCP electrode-electrolyte interface. A relatively smaller value of R_1 (249 Ω) in the CO_2-saturated 0.5 M $KHCO_3$ solution, compared to its value (369 Ω) in the N_2-purged solution, offers an appreciable charge transfer of Bi_2S_3-NRs(bio)/TCP electrode with CO_2 saturation. All CPE values with N>0.5 imply the pseudocapacitance behaviour of the Bi_2S_3-NRs(bio)/TCP electrode. The values of N= 0 and N=1 signify the resistance and an ideal capacitor behaviour, respectively.

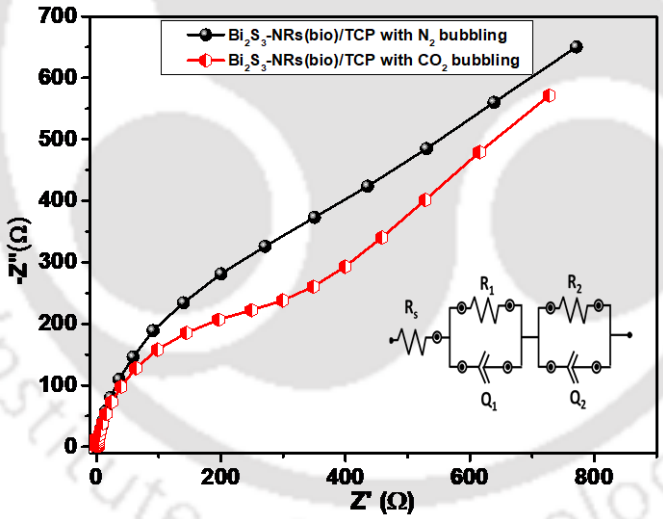

Figure 5.17. Nyquist plot recorded with Bi_2S_3-NRs(bio)/TCP electrode in N_2- and CO_2(saturated)-bubbled 0.5 M $KHCO_3$ aqueous solution.

Table 5.1. Fitted values of the elements in equivalent electric circuit diagram corresponding to the Nyquist plots shown in Figure 5.17.

Modified electrodes	Electrical circuit elements						
	R_s (Ω)	R_1 (Ω)	R_2 (Ω)	Y_0 (μMho)	N	Y_0 (mMho)	N
Bi_2S_3-SE/TCP electrode in N_2	1.60	369	2980	403	0.965	1.42	0.794
Bi_2S_3-SE/TCP electrode in CO_2	1.60	249	1990	227	0.998	1.50	0.755

5.3.3 Electrochemical CO_2 reduction reaction (ECO_2RR)

Chronoamperometric tests were done for further conclusive evidence towards the ECO_2RR with Bi_2S_3-NRs(bio)/TCP electrode. Figure 5.18a shows the corresponding current response graphs at different applied potentials in the range of −1.4 to −2.1 V (vs. Ag/AgCl) in CO_2-saturated electrolyte for 3600 s of ECO_2RR. The increase in current densities in the higher potentials with electrolysis time could be due to increased H_2 production rates. Figure 5.18b compares the FE of the products formed. The FE of formate formation was calculated using the following expression (Equation 5.16).

$$FE(\%)=\frac{ZnF}{Q}\times 100 \qquad (5.16)$$

Where Z represents the number of electrons required for one mole of formate production, n is the moles of the formate, F is the Faraday constant (96485 C mol^{-1}), and Q represents the total quantity of electricity passed for the ECO_2RR.

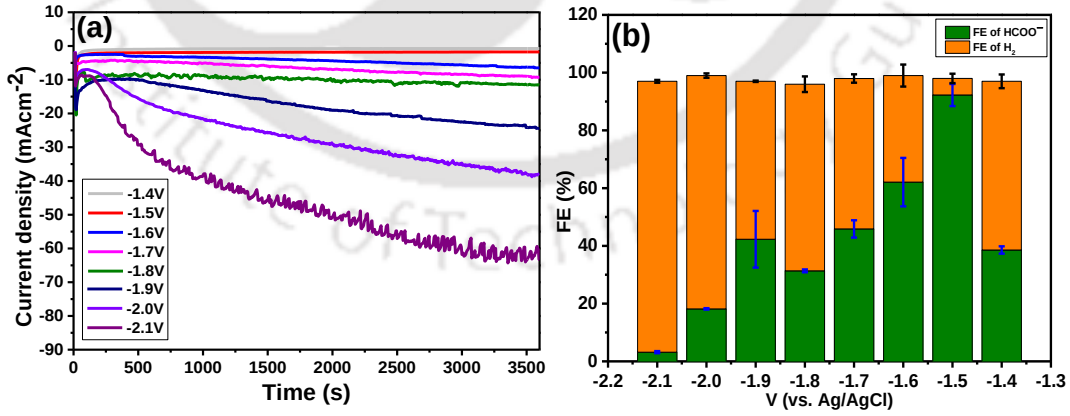

Figure 5.18. (a) Current response and (b) Faradaic efficiency (%) of formate and H_2 formation with Bi_2S_3-NRs(bio)/TCP electrode at different applied potential (vs. Ag/AgCl) in CO_2-saturated 0.5 M $KHCO_3$ solution for 3600 s of ECO_2RR.

The FE% of H_2 production was calculated using the following relation (Equation 5.17). Here, n is the mole of H_2 production.

$$FE(\%)=\frac{F\times 2\times n_{H_2}}{\text{Total Q}}\times 100 \quad (5.17)$$

The FE of $HCOO^-$ formation was found to be 38.6% at −1.4 V (vs. Ag/AgCl), and below this potential, no product was found. The highest FE of formate formation of 92.3% was found at −1.5 V (vs. Ag/AgCl). The NMR spectra is shown in Figure 5.19. After that, the FE fell gradually due to more H_2 production with the increase in potential from −1.4 to −2.1 V (vs. Ag/AgCl). The FE of formate formation was retained at 90.1% after 2 h of electrolysis (Figure 5.20). Whereas, the Bi_2S_3-NRs(control)/TCP electrode exhibited 50.9% of FE towards formate formation at −1.5 V (vs. Ag/AgCl) (Figure 5.21). Table 5.2 compares the FE of formate formation using Bi-based nanocatalysts of different morphologies reported in the literature. FE was found to be 84-100% at the applied potential range of −0.70 to −0.6 V (vs. RHE).

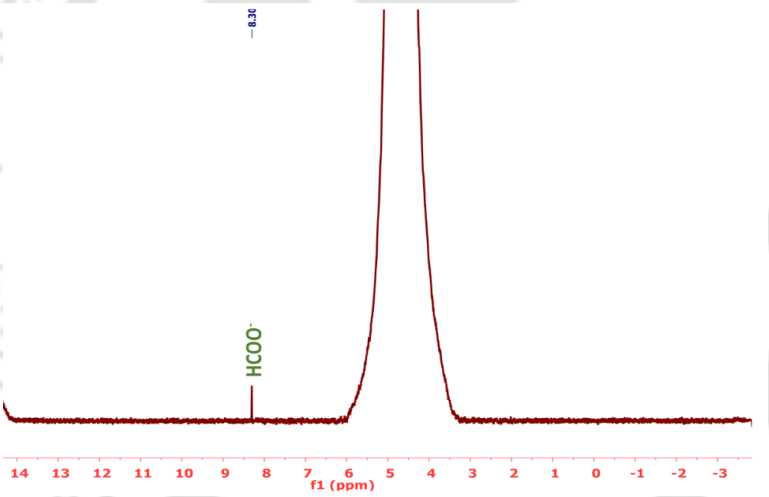

Figure 5.19. NMR spectra of catholyte after 3600 s of CO_2 reduction at −1.5 V (vs. Ag/AgCl).

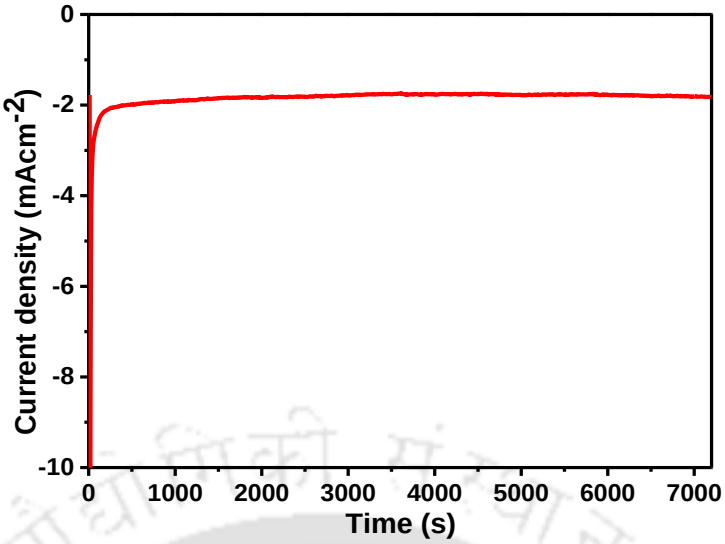

Figure 5.20. Variation and stability of current density with Bi_2S_3-NRs(bio)/TCP electrode for 2 h of ECO_2RR at −1.50 V vs. Ag/AgCl.

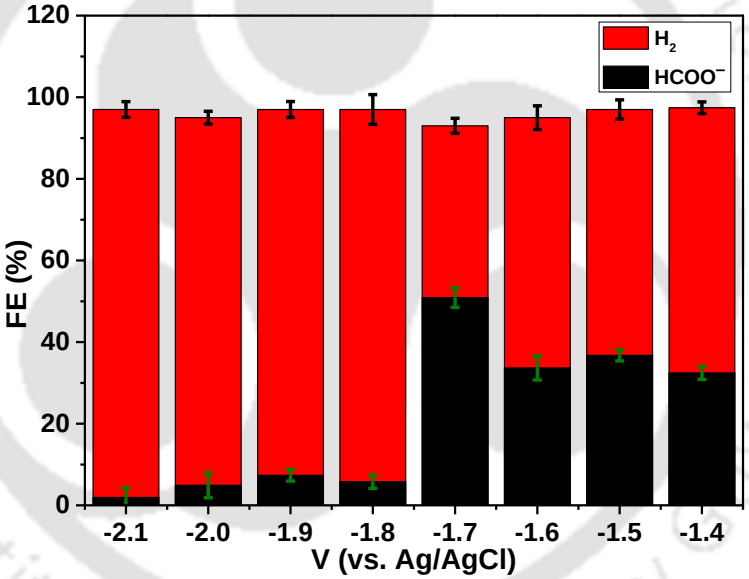

Figure 5.21. Faradaic efficiency (%) of format and H_2 formation using Bi_2S_3-NRs(control)/TCP electrode at different applied potentials (vs. Ag/AgCl).

Table 5.2. Comparison of $HCOO^-$ formation using various Bi and Bi-based catalysts for electrochemical CO_2 reduction.

Catalyst	Method of synthesis	Electrolyte	Applied potential	FE (%) of $HCOO^-$	Source
Bi_2S_3-NRs(bio)	Bioinspired route, using *S. edule* fruit	0.5 M $KHCO_3$	−1.5 V (vs. Ag/AgCl) / −0.85 V (RHE)*	92.3	**This work**
Bi NPs	Modified aqueous reduction, PEG 10,000 as stabilizer	0.5 M $KHCO_3$	−0.83 V (vs. RHE)	94.7	X. Zhang et al. (2018)
Bi nanosheets	Exfoliation process, using ultrasonication	0.1 M $KHCO_3$	−1.1 V (vs. RHE)	86.0	W. Zhang et al. (2018)
Bi_2S_3-derived Bi	Electrochemical reduction method	0.5 M $NaHCO_3$	−0.75 V (vs. RHE)	84.0	Y. Zhang et al. (2018)
Bi nanosheets	Hydrothermal method	0.5 M $NaHCO_3$	−0.90 V (vs. RHE)	95.0	Han et al. (2018)
Bi nanotubes	Chemical method	0.5 M $KHCO_3$	−1.0 V (vs. RHE)	97.0	Fan et al. (2020)
Bi catalyst	Electrodeposition method	0.5 M $KHCO_3$	−0.70 V (vs. RHE)	91.8	Li et al. (2021)
Bi NPs	Electrodeposition method	0.5 M $KHCO_3$	−0.78 V (vs. RHE)	97.4	Wei et al. (2022)
Ultrathin Bi nanosheets	Electrochemical reduction method	0.5 M $NaHCO_3$	−1.0 V (vs. RHE)	90.0	Su et al. (2018)
Bi nanoflakes	Electrodeposition method	0.1 M $NaHCO_3$	−0.6 V (vs. RHE)	100.0	Kim et al. (2017)
Size tunable nano-Bi	Hydrothermal method	0.5 M $KHCO_3$	−1.60 V (vs. SCE)	98.4	Qiu et al. (2017)

* E (vs. RHE) = E (vs. Ag/AgCl) + 0.236 V + 0.0591 × pH

The FESEM images (Figure 5.22) and EDX elemental mapping (Figure 5.23) of Bi_2S_3-NRs(bio)/TCP electrode before and after 1 h and 2 h of electrolysis showed a well-distribution of Bi_2S_3 particles on the TCP support even after ECO_2RR. Figure 5.24a shows the high-resolution XPS of Bi 4f region of Bi_2S_3-NRs(bio)/TCP electrode after 2 h of ECO_2RR. The peaks appear at 158.5, and 163.8 eV correspond to the spin-orbital splitting of Bi $4f_{7/2}$ and $4f_{5/2}$, respectively. The peaks at 159.5 and 164.9 eV could be an indication of Bi-O. The area ratio of Bi-S:Bi-O is calculated to be 1:0.15. Figure 5.24b shows the S 2s of Bi_2S_3-NRs(bio)/TCP electrode. The two peaks appear at 226.1, and 231.7 eV correspond to the Bi-S bond and presence of SO_x, respectively. O 1s XPS shows peak at 530.4 eV attributed to the binding energy of CO_3^{2-} group (Figure 5.25) (Zhao et al., 2019). To support this observation further, XRD analysis of Bi_2S_3-NRs(bio)/TCP electrode after 2 h of electrolysis at −1.5 V (vs. Ag/AgCl) was carried out (Figure 5.26). The results show the presence of $Bi_2O_2CO_3$ peaks (JCPDS card no. 41-1488) (Qin et al., 2021). It could be formed during the ECO_2RR. The consumption of H^+ with simultaneous ECO_2RR and hydrogen evolution reaction could reduce the local concentration of H^+, and it increases the local OH^- concentration near the vicinity

of the Bi_2S_3-NRs(bio)/TCP electrode increasing the local pH (>3) with respect to the bulk electrolyte. The alkaline medium promotes the oxidation of Bi_2S_3 to $Bi_2O_2CO_3$, which may serve as the active sites for ECO_2RR (Fan et al., 2021).

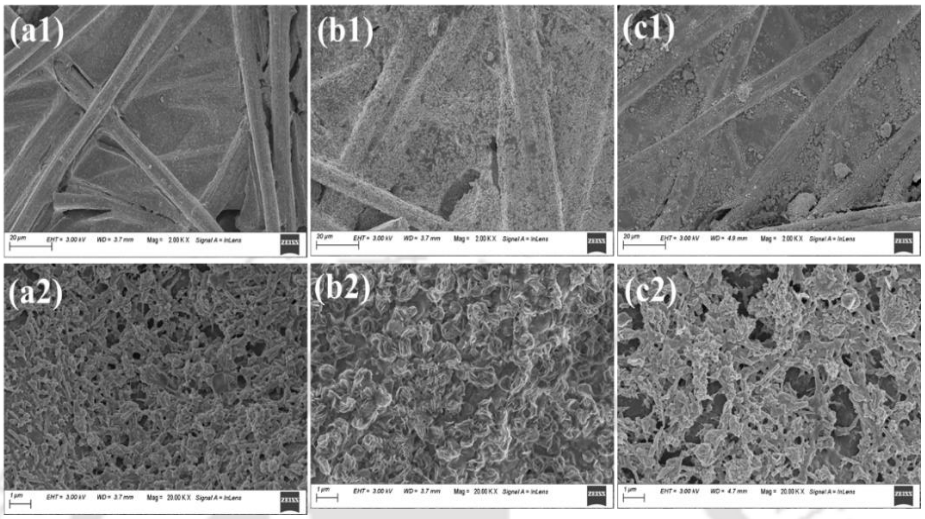

Figure 5.22. FESEM images of Bi_2S_3-NRs(bio)/TCP electrodes: (a1), (a2) before; (b1), (b2) after 1 h ECO_2RR; and (c1), (c2) after 2 h ECO_2RR at −1.50 V vs. Ag/AgCl.

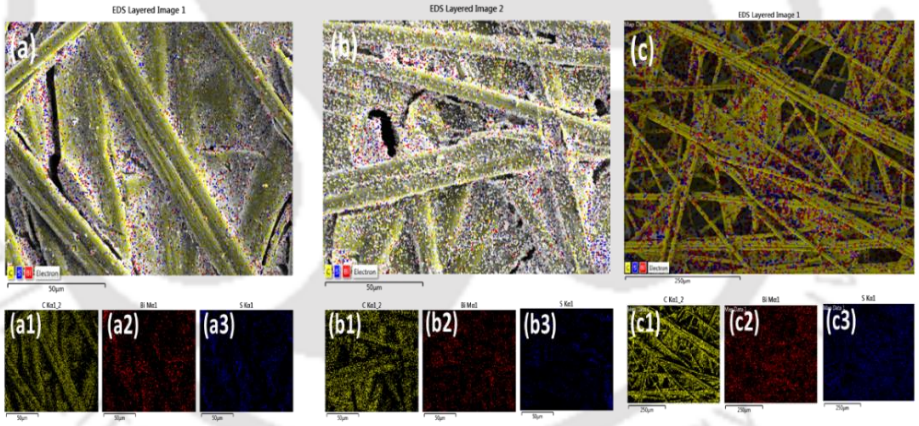

Figure 5.23. EDX images of Bi_2S_3-NRs(bio)/TCP electrodes: (a) before; (b) after 1 h of ECO_2RR; and (c) after 2 h of ECO_2RR at −1.50 V vs. Ag/AgCl.

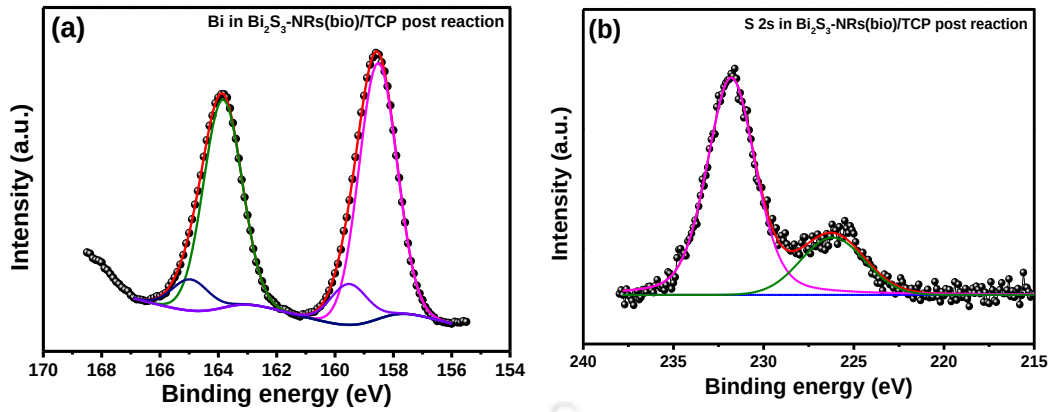

Figure 5.24. High-resolution XPS of a) Bi 4f, and b) S 2s of Bi_2S_3-NRs(bio)/TCP after 2 h of ECO_2RR in 0.5 M $KHCO_3$ solution at −1.5 V (vs. Ag/AgCl).

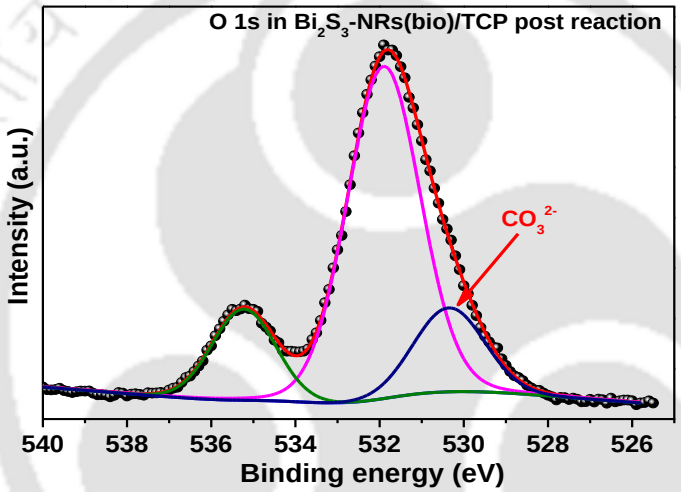

Figure 5. 25. High resolution XPS of O 1s of Bi_2S_3-NRs(bio)/TCP after 2 h of ECO_2RR in 0.5 M $KHCO_3$ solution at −1.5 V (vs. Ag/AgCl).

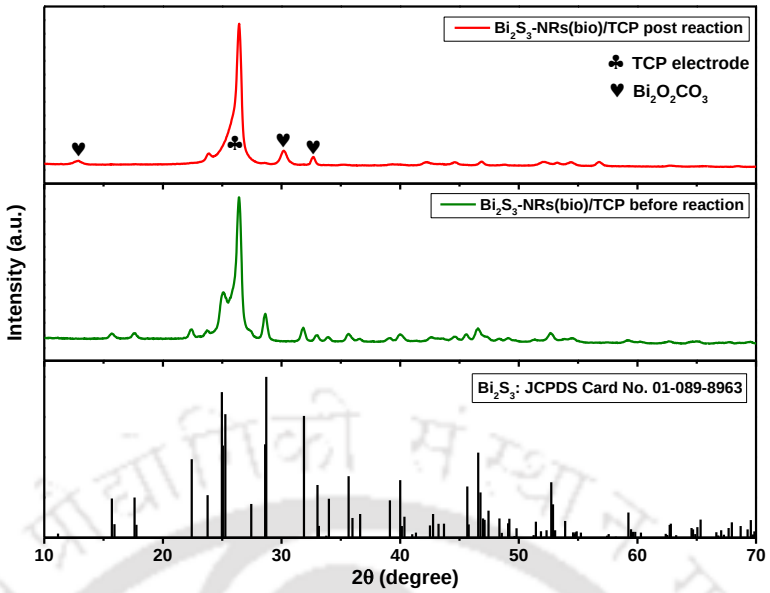

Figure 5.26. XRD patterns of Bi_2S_3-NRs(bio)/TCP electrode before and after 2 h of ECO_2RR at −1.5 V (vs. Ag/AgCl) in CO_2-saturated 0.5 M $KHCO_3$ solution.

Figure 5.27 shows Bi-based electrocatalysts of varying sizes and shapes used for ECO_2RR forming formate.

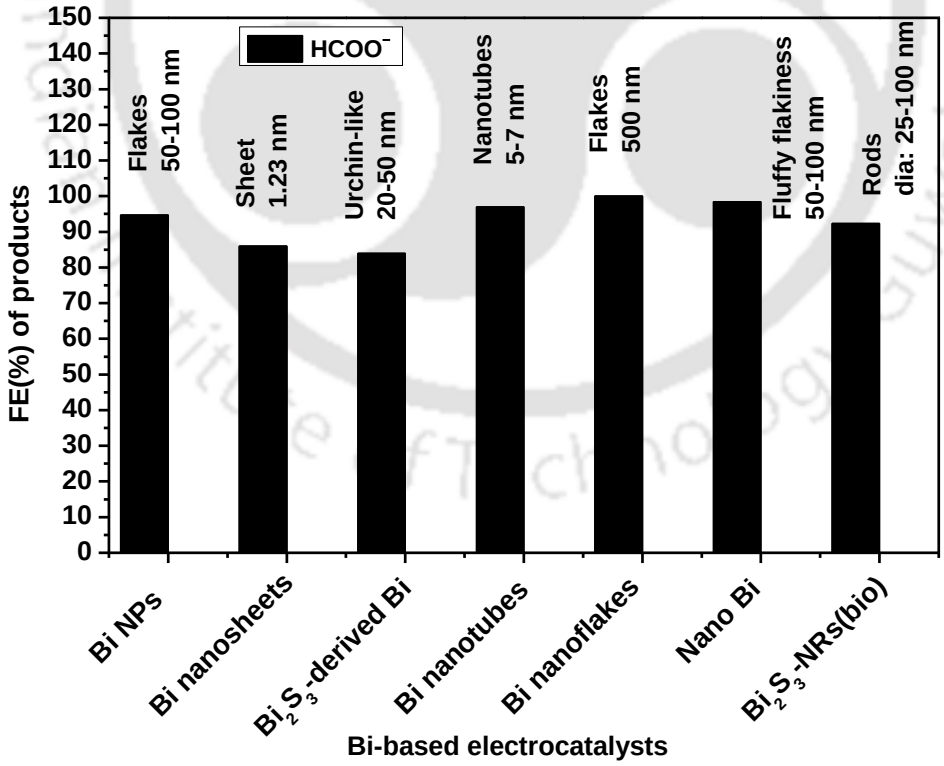

Figure 5.27. Bi-based electrocatalysts of varying sizes and shapes used for ECO_2RR forming formate.

5.4 Major findings

A template-free bioinspired process of synthesizing 1D Bi_2S_3-NRs, namely, Bi_2S_3-NRs(bio), is successfully developed. Bi_2S_3-NRs(control) synthesized without using the bio-extract/reducing agent showed that AA present in *S. edule* fruit also could act as a capping agent. The absence of oxides in Bi_2S_3-NRs(bio) in comparison with Bi_2S_3-NRs(control) is resulted from the antioxidant property of AA, capped on the surface of nanorods, which prevents further oxidation of S^{2-} during the synthesis process. A 4.4% mass loss at 200-325 °C temperature supported strong adherence of bio-moieties on the surface of Bi_2S_3-NRs(bio), and it in turn assisted the morphological and dimensional control of nanorods compared to Bi_2S_3-NRs(control) with about 2- and 4-folds decrease in the length and diameter of Bi_2S_3-NRs(bio). The BET surface area of Bi_2S_3-NRs(bio) was found to be 13.4 $m^2 g^{-1}$ which is 2 folds more than that of Bi_2S_3-NRs(control).

Both Bi_2S_3-NRs(bio) and Bi_2S_3-NRs(control) modified TCP electrodes could catalyze CO_2 reduction towards $HCOO^-$ formation. Bi_2S_3-NRs(bio) exhibited the maximum FE of 92.3 vs. 50.9%, using Bi_2S_3-NRs(control), in 1 h of electrolysis. Bi_2S_3-NRs(bio) could be oxidized to $Bi_2O_2CO_3$ during ECO_2RR as evidenced from the XPS and XRD analyses, and the later could also serve as active sites for the ECO_2RR.

References

Ahn, S.T., Abu-Baker, I., Palmore, G.T.R., 2017. Electroreduction of CO_2 on polycrystalline copper: Effect of temperature on product selectivity. Catal. Today 288, 24–29. https://doi.org/10.1016/j.cattod.2016.09.028

Ai, K., Liu, Y., Liu, J., Yuan, Q., He, Y., Lu, L., 2011. Large-scale synthesis of Bi_2S_3 nanodots as a contrast agent for in vivo X-ray computed tomography imaging. Adv. Mater. 23, 4886–4891. https://doi.org/10.1002/adma.201103289

An, X., Li, S., Hao, Xiaoqiong, Xie, Z., Du, X., Wang, Z., Hao, Xiaogang, Abudula, A., Guan, G., 2021. Common strategies for improving the performances of tin and bismuth-based catalysts in the electrocatalytic reduction of CO_2 to formic acid/formate. Renew. Sustain. Energy Rev. 143, 110952. https://doi.org/10.1016/j.rser.2021.110952

Atri, S., Gusain, M., Kumar, P., Uma, S., Nagarajan, R., 2020. Role of the solvent medium in the wet-chemical synthesis of $CuSbS_2$, Cu_3SbS_3, and bismuth substituted Cu_3SbS_3. J. Chem. Sci. 132, 1–8. https://doi.org/10.1007/s12039-020-01831-z

Ayodhya, D., Veerabhadram, G., 2017. Investigation of structural, optical, catalytic, fluorescence studies of eco-friendly synthesized Bi_2S_3 nanostructures. Superlattices Microstruct. 102, 103–118. https://doi.org/10.1016/j.spmi.2016.12.027

Caputo, F., Mameli, M., Sienkiewicz, A., Licoccia, S., Stellacci, F., Ghibelli, L., Traversa, E., 2017. A novel synthetic approach of cerium oxide nanoparticles with improved biomedical activity. Sci. Rep. 7, 4636. https://doi.org/10.1038/s41598-017-04098-6

Chatterjee, S., Dutta, I., Lum, Y., Lai, Z., Huang, K.W., 2021. Enabling storage and utilization of low-carbon electricity: Power to formic acid. Energy Environ. Sci. 14, 1194–1246. https://doi.org/10.1039/d0ee03011b

Chelli, V.R., Golder, A.K., 2019. One pot green synthesis of Pt, Co and Pt@Co core-shell nanoparticles using Sechium edule. J. Chem. Technol. Biotechnol. 94, 911–918. https://doi.org/10.1002/jctb.5838

Chen, J., Qin, S., Song, G., Xiang, T., Xin, F., Yin, X., 2013. Shape-controlled solvothermal synthesis of Bi_2S_3 for photocatalytic reduction of CO_2 to methyl formate in methanol. Dalt. Trans. 42, 15133–15138. https://doi.org/10.1039/c3dt51887f

Chufa, B.M., Gonfa, B.A., Anshebo, T.Y., 2021. Enhanced photocatalytic activity of reduced graphene oxide/bismuth sulfide nanostructure composites for the degradation of methylene blue. J. Nanomater. 2021, 1–12. https://doi.org/10.1155/2021/1309961

Egorova, K.S., Ananikov, V.P., 2017. Toxicity of metal compounds: Knowledge and myths. Organometallics 36, 4071–4090. https://doi.org/10.1021/acs.organomet.7b00605

Fan, K., Jia, Y., Ji, Y., Kuang, P., Zhu, B., Liu, X., Yu, J., 2020. Curved surface boosts

electrochemical CO_2 reduction to formate via bismuth nanotubes in a wide potential window. ACS Catal. 10, 358–364. https://doi.org/10.1021/acscatal.9b04516

Fan, T., Ma, W., Xie, M., Liu, H., Zhang, J., Yang, S., Huang, P., Dong, Y., Chen, Z., Yi, X., 2021. Achieving high current density for electrocatalytic reduction of CO_2 to formate on bismuth-based catalysts. Cell Reports Phys. Sci. 2, 100353. https://doi.org/10.1016/j.xcrp.2021.100353

Farooq, U., Phul, R., Alshehri, S.M., Ahmed, J., Ahmad, T., 2019. Electrocatalytic and enhanced photocatalytic applications of sodium niobate nanoparticles developed by citrate precursor route. Sci. Rep. 9, 4488. https://doi.org/10.1038/s41598-019-40745-w

Feng, J., Li, J., Lv, W., Xu, H., Yang, H., Yan, W., 2014. Synthesis of polypyrrole nano-fibers with hierarchical structure and its adsorption property of Acid Red G from aqueous solution. Synth. Met. 191, 66–73. https://doi.org/10.1016/j.synthmet.2014.02.013

Golovnev, N.N., Leshok, A.A., Novikova, G. V., Petrov, A.I., 2010. Stability of bismuth(III), indium(III), lead(II), and cadmium(II) monocomplexes with selenourea and thiourea. Russ. J. Inorg. Chem. 55, 130–132. https://doi.org/10.1134/S0036023610010225

Han, N., Ding, P., He, L., Li, Youyong, Li, Yanguang, 2020. Promises of main group metal–based nanostructured materials for electrochemical CO_2 reduction to formate. Adv. Energy Mater. 10, 1–19. https://doi.org/10.1002/aenm.201902338

Han, N., Wang, Y., Yang, H., Deng, J., Wu, J., Li, Yafei, Li, Yanguang, 2018. Ultrathin bismuth nanosheets from in situ topotactic transformation for selective electrocatalytic CO_2 reduction to formate. Nat. Commun. 9, 1320. https://doi.org/10.1038/s41467-018-03712-z

Hu, J.Q., Deng, B., Zhang, W.X., Tang, K.B., Qian, Y.T., 2001. A convenient hydrothermal route to mineral Ag_3CuS_2 nanorods. Int. J. Inorg. Mater. 3, 639–642. https://doi.org/10.1016/S1466-6049(01)00163-5

Huang, Y., Qin, J., Hu, C., Liu, X., Wei, D., Seo, H.J., 2019. Cs-doped α-Bi_2O_3 microplates: Hydrothermal synthesis and improved photochemical activities. Appl. Surf. Sci. 473, 401–408. https://doi.org/10.1016/j.apsusc.2018.12.165

Jabeen Fatima, M.J., Niveditha, C. V., Sindhu, S., 2015. α-Bi_2O_3 photoanode in DSSC and study of the electrode-electrolyte interface. RSC Adv. 5, 78299–78305. https://doi.org/10.1039/c5ra12760b

Jiang, H., Wang, L., Li, Y., Gao, B., Guo, Y., Yan, C., Zhuo, M., Wang, H., Zhao, S., 2021. High-selectivity electrochemical CO_2 reduction to formate at low overpotential over Bi catalyst with hexagonal sheet structure. Appl. Surf. Sci. 541, 148577. https://doi.org/10.1016/j.apsusc.2020.148577

Jiang, Y., Hu, J., Li, J., 2016. Synthesis and visible light responsed photocatalytic activity of

Sn doped Bi_2S_3 microspheres assembled by nanosheets. RSC Adv. 6, 39810–39817. https://doi.org/10.1039/c6ra02621d

Johnson, W., Bergfeld, W.F., Belsito, D. V., Hill, R.A., Klaassen, C.D., Liebler, D.C., Marks, J.G., Shank, R.C., Slaga, T.J., Snyder, P.W., Andersen, F.A., 2014. Safety assessment of tin(IV) oxide as used in cosmetics. Int. J. Toxicol. 33, 40S-46S. https://doi.org/10.1177/1091581814559309

Karmaoui, M., Jorge, A.B., McMillan, P.F., Aliev, A.E., Pullar, R.C., Labrincha, J.A., Tobaldi, D.M., 2018. One-Step Synthesis, Structure, and Band Gap Properties of SnO 2 Nanoparticles Made by a Low Temperature Nonaqueous Sol–Gel Technique. ACS Omega 3, 13227–13238. https://doi.org/10.1021/acsomega.8b02122

Kim, S., Dong, W.J., Gim, S., Sohn, W., Park, J.Y., Yoo, C.J., Jang, H.W., Lee, J.L., 2017. Shape-controlled bismuth nanoflakes as highly selective catalysts for electrochemical carbon dioxide reduction to formate. Nano Energy 39, 44–52. https://doi.org/10.1016/j.nanoen.2017.05.065

Li, Jiayu, Li, Jinxia, Liu, X., Chen, J., Tian, P., Dai, S., Zhu, M., Han, Y.F., 2021. Probing the role of surface hydroxyls for Bi, Sn and In catalysts during CO_2 reduction. Appl. Catal. B Environ. 298, 120581. https://doi.org/10.1016/j.apcatb.2021.120581

Liang, K., Wang, C., Xu, X., Leng, J., Ma, H., 2017. Capacitive and photocatalytic performance of Bi2S2 nanostructures synthesized by solvothermal method. Phys. Lett. A 381, 652–657. https://doi.org/10.1016/j.physleta.2016.12.005

Luigi, B., Battaglia, P., Corradi, A.B., Pelizzi, G., Vidoni, M.E., Generate, C., Azeglio, V.M.D., 1977. Cationic and anionic bismuth(III) in chloro-thiourea complexes: crystal structure of $[Bi(tu)_6][Bi\{(tu)_{1.5}Cl_{1.5}\}Cl_3]_2$(tu = thiourea). J. Chem. Soc. Dalt. Trans. 1975–1978.

Luo, Y., Chen, H., Li, X., Gong, Z., Wang, X., Peng, X., He, M., Sheng, Z., 2013. Wet chemical synthesis of Bi_2S_3 nanorods for efficient photocatalysis. Mater. Lett. 105, 12–15. https://doi.org/10.1016/j.matlet.2013.04.006

Malca, M.Y., Bao, H., Bastaille, T., Saadé, N.K., Kinsella, J.M., Friščić, T., Moores, A., 2017. Mechanically activated solvent-free assembly of ultrasmall Bi_2S_3 nanoparticles: A novel, simple, and sustainable means to access chalcogenide nanoparticles. Chem. Mater. 29, 7766–7773. https://doi.org/10.1021/acs.chemmater.7b02134

Martha, P.R., Wu, J.J., Asiri, A.M., Anandan, S., 2021. Rice grain like Bi_2S_3 nanorods and its photocatalytic performance. Mater. Sci. Eng. B 268, 115144.

Mikulčić, H., Skov, I.R., Dominković, D.F., Wan Alwi, S.R., Manan, Z.A., Tan, R., Duić, N., Hidayah Mohamad, S.N., Wang, X., 2019. Flexible carbon capture and utilization technologies in future energy systems and the utilization pathways of captured CO_2. Renew. Sustain. Energy Rev. 114, 109338. https://doi.org/10.1016/j.rser.2019.109338

Miniach, E., Gryglewicz, G., 2018. Solvent-controlled morphology of bismuth sulfide for supercapacitor applications. J. Mater. Sci. 53, 16511–16523. https://doi.org/10.1007/s10853-018-2785-3

Momma, K., Izumi, F., 2011. VESTA 3 for three-dimensional visualization of crystal, volumetric and morphology data. J. Appl. Crystallogr. 44, 1272–1276. https://doi.org/10.1107/S0021889811038970

Morrison, A.R.T., van Beusekom, V., Ramdin, M., van den Broeke, L.J.P., Vlugt, T.J.H., de Jong, W., 2019. Modeling the electrochemical conversion of carbon dioxide to formic acid or formate at elevated pressures. J. Electrochem. Soc. 166, E77–E86. https://doi.org/10.1149/2.0121904jes

Mukkabla, R., Deepa, M., Srivastava, A.K., 2015. Enhanced lithium-ion storage capability of a bismuth sulfide/graphene oxide/poly(3,4-ethylenedioxythiophene) composite. ChemPhysChem 16, 3242–3253. https://doi.org/10.1002/cphc.201500515

Onwudiwe, D.C., Nkwe, V.M., 2020. Morphological variations in Bi_2S_2 nanoparticles synthesized by using a single source precursor. Heliyon 6, e04505. https://doi.org/10.1016/j.heliyon.2020.e04505

Qin, H., Yang, Y., Shi, W., She, Y., 2021. Few-layer $Bi_2O_2CO_3$ nanosheets derived from electrochemically exfoliated bismuthene for the enhanced photocatalytic degradation of ciprofloxacin antibiotic. RSC Adv. 11, 13731–13738. https://doi.org/10.1039/d1ra00528f

Qiu, Y., Du, J., Dong, W., Dai, C., Tao, C., 2017. Selective conversion of CO_2 to formate on a size tunable nano-Bi electrocatalyst. J. CO_2 Util. 20, 328–335. https://doi.org/10.1016/j.jcou.2017.05.024

Rao, K.J., Paria, S., 2014. Green synthesis of gold nanoparticles using aqueous *Aegle marmelos* leaf extract and their application for thiamine detection. RSC Adv. 4, 28645–28652. https://doi.org/10.1039/c4ra03883e

Rohr, O., 2002. Bismuth – the new ecologically green metal for modern lubricating engineering. Ind. Lubr. Tribol. 54, 153–164. https://doi.org/10.1108/00368790210431709

Shahbazi, M.A., Faghfouri, L., Ferreira, M.P.A., Figueiredo, P., Maleki, H., Sefat, F., Hirvonen, J., Santos, H.A., 2020. The versatile biomedical applications of bismuth-based nanoparticles and composites: Therapeutic, diagnostic, biosensing, and regenerative properties. Chem. Soc. Rev. 49, 1253–1321. https://doi.org/10.1039/c9cs00283a

Su, P., Xu, W., Qiu, Y., Zhang, T., Li, X., Zhang, H., 2018. Ultrathin Bismuth Nanosheets as a Highly Efficient CO2 Reduction Electrocatalyst. ChemSusChem 11, 848–853. https://doi.org/10.1002/cssc.201702229

Sudrajat, H., Sujaridworakun, P., 2017. Low-temperature synthesis of δ-Bi_2O_3 hierarchical nanostructures composed of ultrathin nanosheets for efficient photocatalysis. Mater. Des.

130, 501–511. https://doi.org/10.1016/j.matdes.2017.05.087

Sun, Z., Ma, T., Tao, H., Fan, Q., Han, B., 2017. Fundamentals and challenges of electrochemical CO_2 reduction using two-dimensional materials. Chem 3, 560–587. https://doi.org/10.1016/j.chempr.2017.09.009

Thomson, J.W., Cademartiri, L., MacDonald, M., Petrov, S., Calestani, G., Zhang, P., Ozin, G.A., 2010. Ultrathin Bi_2S_3 nanowires: Surface and core structure at the cluster-nanocrystal transition. J. Am. Chem. Soc. 132, 9058–9068. https://doi.org/10.1021/ja101908k

Valyulene, G., Zhelene, A., Jasulaitene, V., Shimkunaite, B., 2007. Electrochemical behavior and composition of bismuth sulfide coatings. Russ. J. Appl. Chem. 80, 1322–1326. https://doi.org/10.1134/S1070427207080113

Wang, H., Zhu, J.J., Zhu, J.M., Chen, H.Y., 2002. Sonochemical method for the preparation of bismuth sulfide nanorods. J. Phys. Chem. B 106, 3848–3854. https://doi.org/10.1021/jp0135003

Wang, Y., Chen, J., Wang, P., Chen, L., Chen, Y., Wu, L., 2009. Syntheses, growth mechanism, and optical properties of [001] growing Bi2S3 nanorods. J. Phys. Chem. C 113, 16009–16014.

Wang, Y., Cheng, L., Liu, J., Xiao, C., Zhang, B., Xiong, Q., Zhang, T., Jiang, Z., Jiang, H., Zhu, Y., Li, Y., Li, C., 2020. Rich bismuth-oxygen bonds in bismuth derivatives from Bi_2S_3 pre-catalysts promote the electrochemical reduction of CO_2. ChemElectroChem 7, 2864–2868. https://doi.org/10.1002/celc.202000656

Wei, X., Zhang, W., Liu, Depei, Liu, Duanduan, Yan, Y., Zhang, J., Yang, Y., Yan, S., Zou, Z., 2022. Bi particles with exposed (012) facet on 3D substrate as highly active and durable electrode for CO_2 reduction to formate. J. CO2 Util. 55, 101797. https://doi.org/10.1016/j.jcou.2021.101797

Welsby, D., Price, J., Pye, S., Ekins, P., 2021. Unextractable fossil fuels in a 1.5 °C world. Nature 597, 230–234. https://doi.org/10.1038/s41586-021-03821-8

Wu, J., Qin, F., Cheng, G., Li, H., Zhang, J., Xie, Y., Yang, H.J., Lu, Z., Yu, X., Chen, R., 2011. Large-scale synthesis of bismuth sulfide nanorods by microwave irradiation. J. Alloys Compd. 509, 2116–2126. https://doi.org/10.1016/j.jallcom.2010.10.160

Wu, J., Yang, L., Jia, T., Liu, D., 2022. Salt-assisted synthesis of rod-Like Bi_2S_3 single crystals for gas-phase elemental mercury removal. Energy and Fuels 36, 2591–2599. https://doi.org/10.1021/acs.energyfuels.1c04286

Yadav, R.S., Rai, S.B., 2017. Surface analysis and enhanced photoluminescence via Bi^{3+} doping in a Tb^{3+} doped Y_2O_3 nano-phosphor under UV excitation. J. Alloys Compd. 700, 228–237. https://doi.org/10.1016/j.jallcom.2017.01.074

Yang, F., Elnabawy, A.O., Schimmenti, R., Song, P., Wang, J., Peng, Z., Yao, S., Deng, R., Song, S., Lin, Y., Mavrikakis, M., Xu, W., 2020. Bismuthene for highly efficient carbon dioxide electroreduction reaction. Nat. Commun. 11. https://doi.org/10.1038/s41467-020-14914-9

Zell, T., Langer, R., 2018. CO_2-based hydrogen storage-formic acid dehydrogenation, Physical Sciences Reviews. https://doi.org/10.1515/psr-2017-0012

Zhang, W., Hu, Y., Ma, L., Zhu, G., Zhao, P., Xue, X., Chen, R., Yang, S., Ma, J., Liu, J., Jin, Z., 2018. Liquid-phase exfoliated ultrathin Bi nanosheets: Uncovering the origins of enhanced electrocatalytic CO2 reduction on two-dimensional metal nanostructure. Nano Energy 53, 808–816. https://doi.org/10.1016/j.nanoen.2018.09.053

Zhang, X., Hou, X., Zhang, Q., Cai, Y., Liu, Y., Qiao, J., 2018. Polyethylene glycol induced reconstructing Bi nanoparticle size for stabilized CO_2 electroreduction to formate. J. Catal. 365, 63–70. https://doi.org/10.1016/j.jcat.2018.06.019

Zhang, Y., Li, F., Zhang, X., Williams, T., Easton, C.D., Bond, A.M., Zhang, J., 2018. Electrochemical reduction of CO_2 on defect-rich Bi derived from Bi_2S_3 with enhanced formate selectivity. J. Mater. Chem. A 6, 4714–4720. https://doi.org/10.1039/C8TA00023A

Zhao, H., Li, G., Tian, F., Jia, Q., Liu, Y., Chen, R., 2019. g-C_3N_4 surface-decorated $Bi_2O_2CO_3$ for improved photocatalytic performance: Theoretical calculation and photodegradation of antibiotics in actual water matrix. Chem. Eng. J. 366, 468–479. https://doi.org/10.1016/j.cej.2019.02.088

Zhao, J., Shahbaz, M., Dong, X., Dong, K., 2021. How does financial risk affect global CO_2 emissions? The role of technological innovation. Technol. Forecast. Soc. Change 168, 120751. https://doi.org/10.1016/j.techfore.2021.120751

Zhu, Z., Iyemperumal, S.K., Kushnir, K., Carl, A.D., Zhou, L., Brodeur, D.R., Grimm, R.L., Titova, L. V., Deskins, N.A., Rao, P.M., 2017. Enhancing the solar energy conversion efficiency of solution-deposited Bi_2S_3 thin films by annealing in sulfur vapor at elevated temperature. Sustain. Energy Fuels 1, 2134–2144. https://doi.org/10.1039/c7se00398f

CHAPTER 6

Synthesis of Spinel Type 2D Co_3O_4 Nanodiscs using Gallic Acid for Electrochemical NH_3 Formation by N_2 Reduction

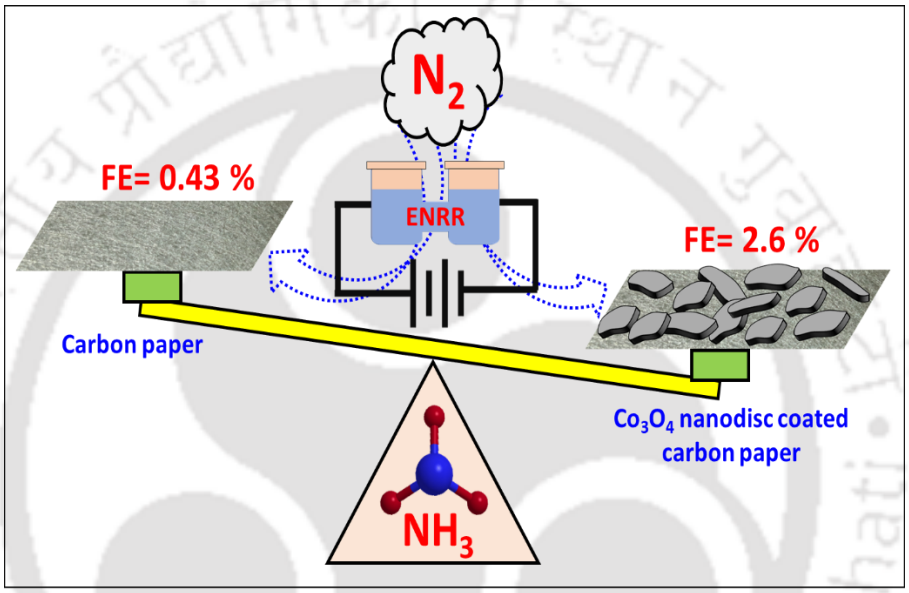

Highlights

- Development of 2D spinel Co_3O_4 nanodiscs (NDs) in a bioinspired route
- Mechanistic exploitation of 2D Co_3O_4 NDs formation by gallic acid
- Co_3O_4 NDs electrocatalyzed N_2 reduction to NH_3
- Co_3O_4 NDs facilitated electron transfer for N_2 reduction reaction
- 6-fold higher Faradaic efficiency of NH_3 formation over bare carbon paper

6.1 Background and executive motivation

In the preceding chapters (Chapter 3, Chapter 4, and Chapter 5), the impact and performance of bioinspired metal catalysts towards the electrochemical reduction of CO_2 (ECO_2RR) has been successfully demonstrated and built up. Along with catalytic CO_2 reduction to value-added chemicals, catalytic N_2 reduction for the production of NH_3 also has gained tremendous attention due to its high hydrogen capacity (17.8% w/w) and energy density (4.32 $kWhL^{-1}$) (Chu et al., 2019a). In fact, NH_3 is considered as the second highest chemical commodity. It is extensively used in fertilizer (~60%) (Aziz et al., 2017), dye, and explosive production. NH_3 is an effective energy carrier and liquid fuel for developing fuel-cells (Liu et al., 2021a).

NH_3 is considered as the second highest chemical commodity. It is extensively used in fertilizer (~60%) dye and explosive production (Aziz et al., 2017). NH_3 is an effective energy carrier and liquid fuel for developing fuel-cells (Chu et al., 2019b; Liu et al., 2021b) due to its high hydrogen capacity (17.8% w/w) (Aziz et al., 2017) and energy density (4.32 kWh L^{-1}) (Ghavam et al., 2021).

Currently, large-scale NH_3 production is carried out following the Haber-Bosch process, a *de facto* process (1,000 to 1,500 tons day^{-1}) (Ghavam et al., 2021). In this process, the reaction is carried out at high temperature (400-600°C) and pressure (about 30 MPa). It also is a contributor to greenhouse gas emissions (2.16 tons CO_2/ tons NH_3) (Ghavam et al., 2021). Almost 96% of H_2 used in this process is derived from fossil fuels (>90%). The limitations of this process have spurred to development of green processes for the synthesis of NH_3.

As an alternative technique, electrochemical N_2 reduction reaction (ENRR) has great industrial importance for the production of NH_3 under ambient conditions. The process is also energy efficient and eco-friendly as it emits less or no carbon (Chu et al., 2019c).

To date, novel metals, like Ag (Li et al., 2021a), Au (Shi et al., 2017), Rh (H. M. Liu et al., 2018), and Ru (Kordali et al., 2000) have been successfully used for ENRR for NH_3 formation (Yang et al., 2021). Despite their potential practical applications, they are currently forbidden due to their scarcity and extremely high cost. On the other hand, earth-abundant transition metals (Ti, Fe, Mo, Mn) and their sulphides, nitrides, and oxides are found to be promising for efficient ENRR (Gao et

al., 2019). Among these, metal oxides are considered to be front runners owing to cost-effective synthesis, tunable activity, and environmental benignity (Xu et al., 2021). MoS_2 exhibited Faradaic efficiency (FE) of 1.17% towards NH_3 formation with 8.08×10^{-11} mol s^{-1} cm^{-2} yield rate (L. Zhang et al., 2018b). An array of TiO_2 nanosheets on Ti plate exhibited 2.50% FE of NH_3 formation and yield rate of 9.16×10^{-11} mol s^{-1} cm^{-2} at–0.7 V RHE (R. Zhang et al., 2018). Annealed Cr_2O_3 nanofibers showed FE and yield of NH_3 production 8.56% and 28.13 µg h^{-1} $g_{cat.}^{-1}$, respectively (Du et al., 2018). Wu et al. (2018) reported the yield of 11.6 µg h^{-1} $g_{cat.}^{-1}$ and FE of 3.0% at –0.8 V vs. RHE using hydrothermally synthesized Mn_3O_4 nanocubes. Mn-doped TiO_2 offered 12% FE with NH_3 yield of 20.05 µg h^{-1} $mg_{cat.}^{-1}$ at −0.5 V (vs. RHE) (Chen et al., 2021) resulted from induced oxygen vacancy due to Mn-doping. Metal-free $BiVO_4$ exhibited 10% FE with NH_3 yield of 8.60 µg h^{-1} $mg_{cat.}^{-1}$ at −0.5 V (vs. RHE) (Yao et al., 2019).

Cobalt-based oxides, more specifically spinel type Co_3O_4, where Co^{3+} and Co^{2+} ions are occupied in the octahedral (O_h) and tetrahedral (T_d) lattice sites, have been extensively used in various fields of electrochemical applications like water splitting, fuel cells, Li-ion battery, CO_2 reduction reactions (Iravani and Varma, 2020). Moreover, it is well-reported that the different morphologies of Co_3O_4 nanostructures possess different facets, which could directly influence its catalytic activities (Xiao et al., 2013; Xu et al., 2011). Different nanostructures, like Co_3O_4 2D leaf-like nanosheets, 3D oval-shaped microparticles, and 1D needle-like nanorods were used in supercapacitor applications with capacitance values up to 111 F g^{-1} (Zhu et al., 2010). Hexagonal platelet Co_3O_4 nanoparticles showed the optical bandgaps of 1.88 and 2.58 eV Deori et al. (2013). It could reach the specific capacitance of 476 F g^{-1} at 0.5 A g^{-1} and an energy density of 42.3 Wh kg^{-1} and power density of 1.56 kW kg^{-1} (Deori et al., 2013). Ortho-hexagon spinel Co_3O_4 nanoparticles exhibited a power density of 1500 mW m^{-2} in microbial fuel cell (Ge et al., 2015).

MOF-derived Zn-doped Co_3O_4 nanopolyhedron could yield 22.71 µg h^{-1} $mg_{cat.}^{-1}$ NH_3 (L. Wen et al., 2021). Urchin-like Al-doped Co_3O_4 nanospheres formed in the hydrothermal method showed a yield rate of 6.48×10^{-11} mol s^{-1} cm^{-2} and FE of 6.25% (Lv et al., 2020). NH_3 yield of 235.0 µg h^{-1} $mg_{cat.}^{-1}$ and FE of 16.3% are reported at –0.30 V vs. RHE catalyzed by fluidized Co_3O_4 nanoparticles synthesized using laser ablation (Li et al., 2021b).

This study reports a facile template-free bioinspired route of synthesizing Co_3O_4 nanodisc (NDs) using gallic acid, via hydrothermal treatment to investigate its catalytic activity towards ENRR. The crystalline and optical properties, surface area and morphology, and elemental and structural attributes of Co_3O_4 NDs were thoroughly investigated. This work further deepens in ENRR to NH_3 using Co_3O_4 NDs modified Toray carbon paper (TCP) electrode (Co_3O_4 NDs/TCP) in an H-type reactor under ambient conditions, to probe its catalytic performance for ENRR.

6.2 Results and discussions

6.2.1 Investigating physiochemical attributes of Co_3O_4 NDs

6.2.1.1 Optical properties

The UV-vis diffuse reflectance spectra of Co_3O_4 NDs is shown in Figure6.1. The two spectral broadband of Co_3O_4 NDs are observed in the wavelength range of 420-450 and 730-760 nm. The absorption peaks at 435 and 735 nm are due to the bandgap transitions in spinel-type Co_3O_4 from $p(O^{2-})$ to $t_2(Co^{2+})$ and $p(O^{2-})$ to $e_g(Co^{3+})$, respectively (Victoria et al., 2015). The kubelka-Munk function was used to obtain the Tauc plot (inset, Figure 6.1), and the bandgap energy (E_g) was calculated using Equation 6.1.

$$(\alpha h\nu)^2 = A(h\nu - E_g) \quad (6.1)$$

Where, α is the absorption coefficient, h is the Plank's constant, and ν reflects the frequency. The direct bandgap energy of Co_3O_4 NDs indicates two distinct values at 1.78 (E_{g1}) and 2.07 eV (E_{g2}), which is in good agreement with the value reported earlier (Bhargava et al., 2018) and implies the formation of pure and p-type Co_3O_4 NDs (UmaSudharshini et al., 2020). The formation of such narrow bandgap could be correlated to the presence of oxygen vacancy (Tomon et al., 2021).

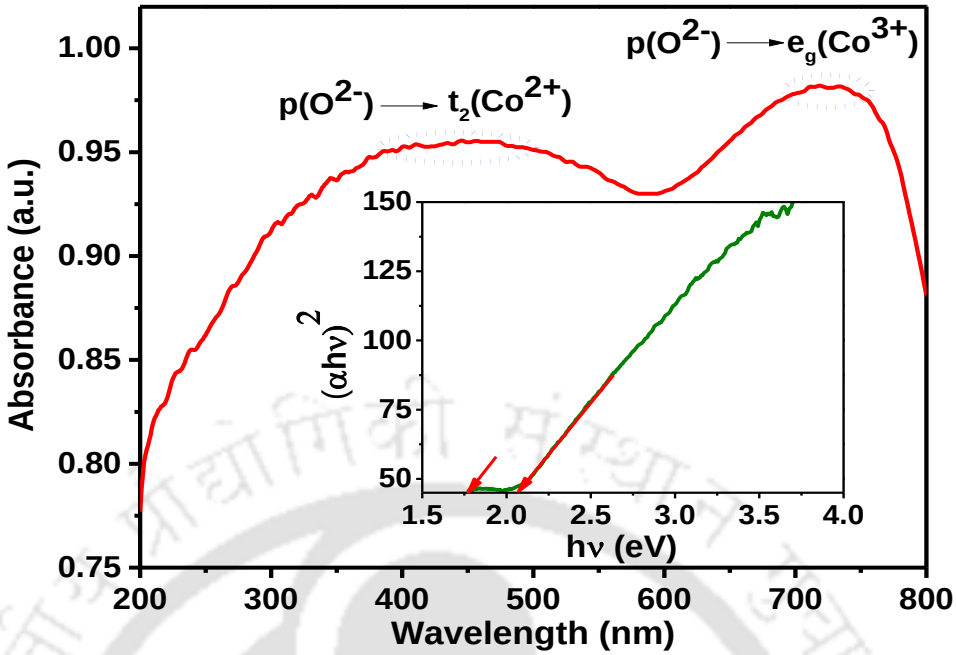

Figure 6.1. UV-vis diffuse reflectance spectra of Co_3O_4 NDs.

6.2.1.2 XRD analysis

The XRD pattern of Co_3O_4 NDs is shown in Figure 6.2. The sharp peaks are located at 2θ values of 18.99°, 31.25°, 36.84°, 38.56°, 44.81°, 55.64°, 59.35°, 65.22°, 74.08°, 77.33°, and 78.37° which correspond to (111), (220), (311), (222), (400), (422), (511), (440), (620), (533), and (622) planes, respectively. The diffraction pattern well matched with the JCPDS file no. 00-009-0418 for the spinel type cubic Co_3O_4, with the space group Fd-3m (Lambert et al., 2015). The dominant peak at 36.84°, corresponding to (311) indicates the preferential particle growth in (311) direction. The absence of other peaks, such as CoO or metallic Co indicates the formation of high purity Co_3O_4 NDs. The average crystallite size (D) was calculated from the FWHM (β) of the (311) diffraction plane by using Debye–Scherrer formula (Equation 6.2) (Jha and Rode, 2013). The calculated average crystallite size was 40 nm.

$$D=\frac{0.9\lambda}{\beta\cos\theta} \qquad (6.2)$$

Where, β, λ, and θ are the full width at half maximum, X-ray wavelength, and Bragg diffraction angle, respectively.

The lattice parameter (a) of the cubic crystallite structure of Co_3O_4 NDs was calculated by using the relation in Equation 6.3 (Al-Tuwirqi et al., 2011).

$$a=d_{hkl}\sqrt{h^2+k^2+l^2} \quad (6.3)$$

Where, h, k, and l are miller indices, and d_{hkl} is the interplanar distances calculated using Bragg's law. The value of d_{hkl} and a calculated based on the (311) plane were found to be 0.2436 nm and 8.079 Å, respectively.

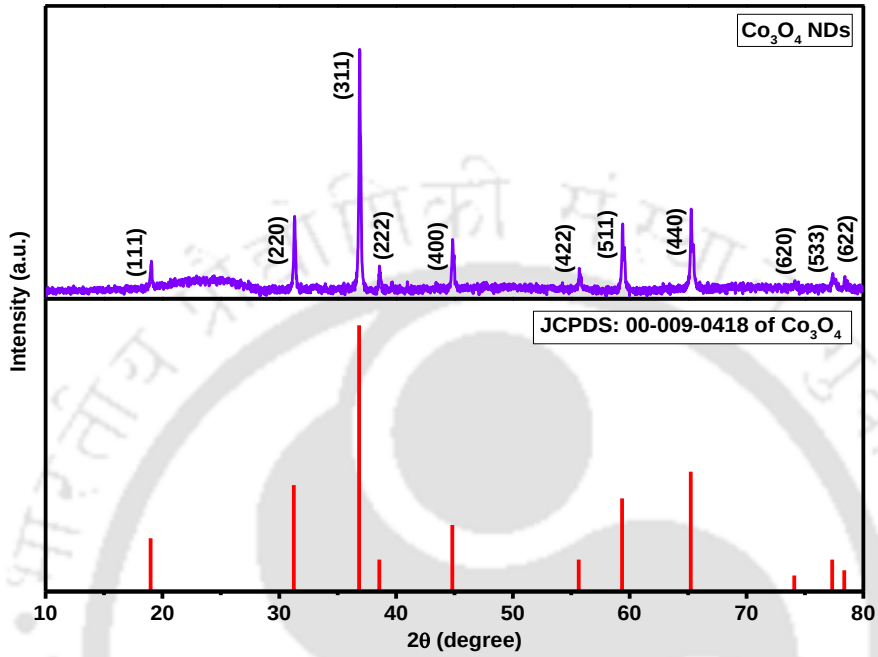

Figure 6.2. XRD pattern of Co_3O_4 NDs and JCPDS diffraction reference.

6.2.1.3 BET analysis

Figure 5 shows the N_2 adsorption-desorption isotherm of Co_3O_4 NDs. It exhibits type-IV isotherm with type H3 hysteresis loop, which is a characteristic feature of typical mesoporous materials (Yan et al., 2012). The specific surface area was found to be 5.6 $m^2\ g^{-1}$ which is close to the Co_3O_4 dendritic structure calcined at 750°C with a specific surface area of 9.3 $m^2\ g^{-1}$. A relatively narrow Brunauer-Emmett-Teller (BJH) pore size distribution was noted (inset, Figure 5) with a sharp peak at 4.2 nm. The higher calcination temperature causes aggregation of nanocrystals and induces the reduction in pores between the Co_3O_4 nanoparticles, resulting a smaller BET surface area.

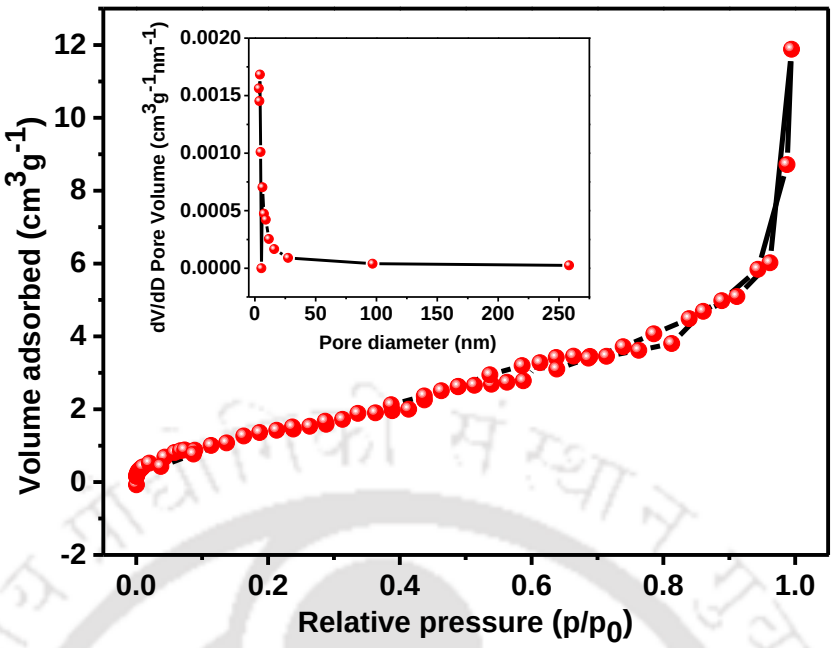

Figure 6.3. N_2 adsorption-desorption isotherm and BJH pore size distribution (inset) of Co_3O_4 NDs.

6.2.1.4 Morphological attributes of Co_3O_4 NDs

The FESEM images show the surface morphology of Co_3O_4 NDs (Figures 6a and 6b). The particles are 2D disc types with irregular shapes. The equivalent diameter (Figure 6.5) and average thickness were found to be 240 and 35.5 nm, respectively.

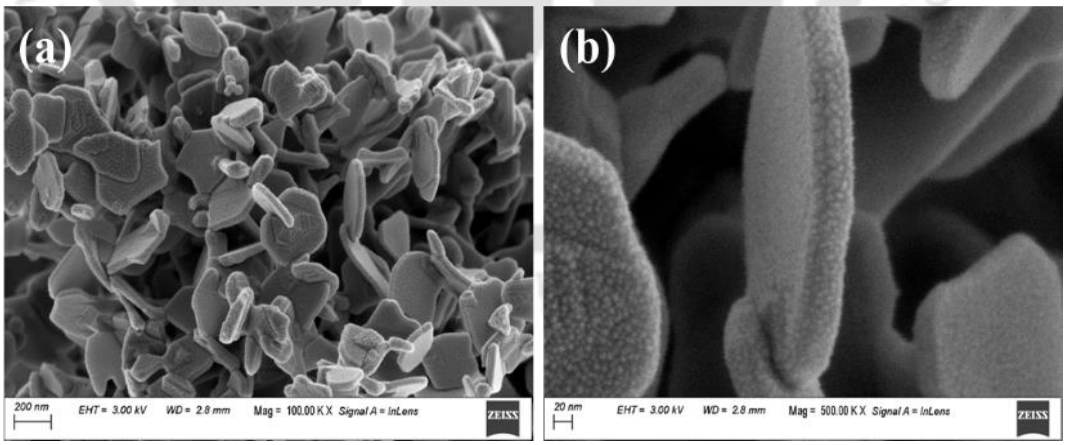

Figure 6.4. (a) Low resolution and (b) high-resolution FESEM images of Co_3O_4 NDs.

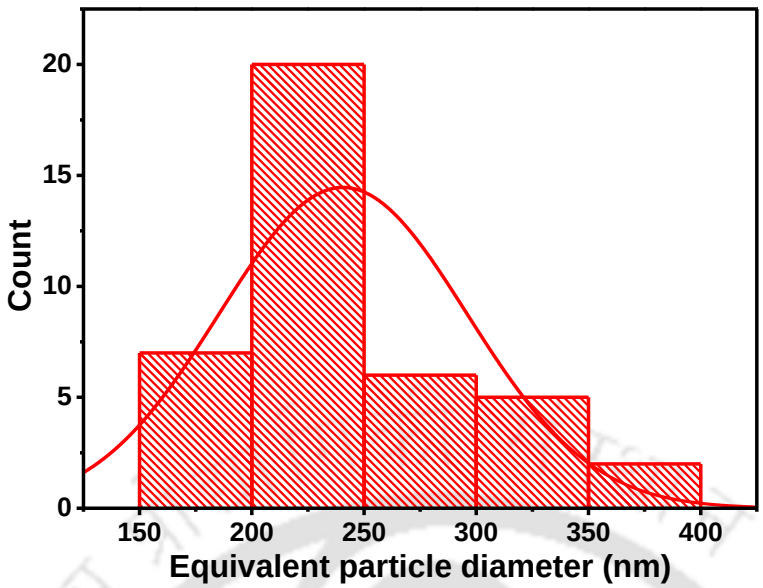

Figure 6.5. Particles size distribution of Co_3O_4 NDs determined from FESEM image.

Figure 6.6 shows the FETEM images of the Co_3O_4 NDs. The particles are interconnected with each other in an agglomerated form (Al-Qirby et al., 2017). The HRTEM image (Figure 6.6c) reveals highly crystalline structure of Co_3O_4 NDs. The d-spacing value is calculated to be 0.24 nm which is corresponding to the lattice fringes of the (311) plane of cubic Co_3O_4 crystal. This corroborates the result found in the XRD analysis. The selected-area electron diffraction (SAED) pattern shows single crystalline nature (Figure 6.6d). The crystal growth along the (311) plane of Co_3O_4 nanostructures exhibits improved charge transfer properties for better electrocatalytic functionalities (Hong et al., 2015; Su et al., 2014).

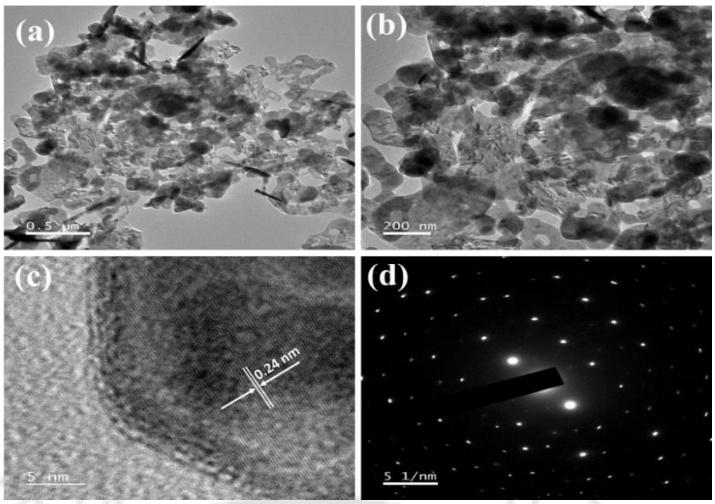

Figure 6.6. (a) Low magnification and (b) high magnification FETEM images, (c) HRTEM image, and (d) SAED pattern of Co_3O_4 NDs.

The TEM-EDX mapping shows the homogeneous distributions of Co and O in the specimen of Co_3O_4 NDs (Figures 6.7a to 6.7c), and Co and O were found to present at their stoichiometric ratio (Figure 6.7d). The atomic ratio of Co:O was estimated to be 3:4 (inset table, Figure 6.7d).

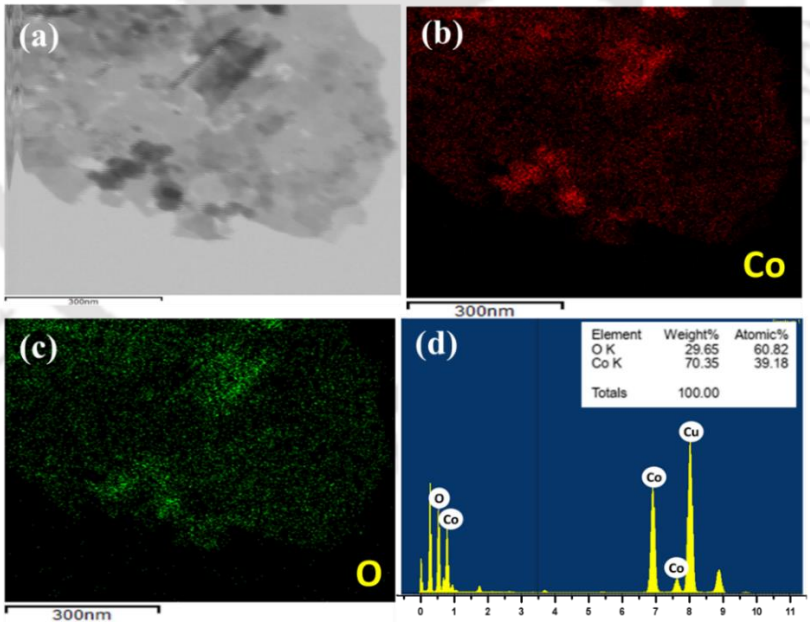

Figure 6.7. (a) FESEM image of the portion selected for TEM-EDX analysis, (b)-(c) TEM-EDX maps of Co and O spectrum of Co_3O_4 NDs, and (d) EDX spectrum of Co_3O_4 NDs.

6.2.1.5 XPS analysis

The survey spectra of Co_3O_4 NDs is shown in Figure 6.8a, and the same of Co_3O_4 NDs/TCP electrode after 2 h of electrolysis is shown in Figure 6.8b. It is seen that only Co, O, and C elements were present in the specimen. F peak in Co_3O_4 NDs/TCP was due to the nafion binder used for the catalyst ink preparation. High-resolution XPS spectrum of Co 2p exhibits two major peaks at a binding energy of 780.3 and 795.4 eV which corresponds to Co $2p_{3/2}$ and Co $2p_{1/2}$, respectively, with a spin-orbital coupling of 15.1 eV (Figure 6.9a) (Paul et al., 2021). Additionally, two pairs of fitted peaks are assigned to Co^{3+} (779.8 and 794.9 eV) of an octahedral site (O_h) and Co^{2+} (781.1 and 796.4 eV) of a tetrahedral site (T_d) of Co_3O_4 (Zhao et al., 2019). Two shake-up satellite peaks at 789.6 and 804.9 eV are the characteristics of the Co^{2+} oxidation state, confirming the presence of CoO structure in Co_3O_4 (Xu et al., 2018). Figure 6.9b shows O 1s spectrum, which was split into three peaks of O_I, O_{II}, and O_{III} at 529.8, 531.0, and 532.9 eV attributed to Co-O, O_2^{2-} or O^- belonging to defective oxides, and C-OH/C-O-C, respectively (Zhao et al., 2019). The ratio of peak areas O_{II}/O_I was calculated to estimate the relative amount of oxygen vacancies that existed in Co_3O_4 NDs, to be 0.68. Moreover, in the calcination step, the release of NO_x from the decomposition of precursor could result in the formation of oxygen vacancy (Yu et al., 2022).

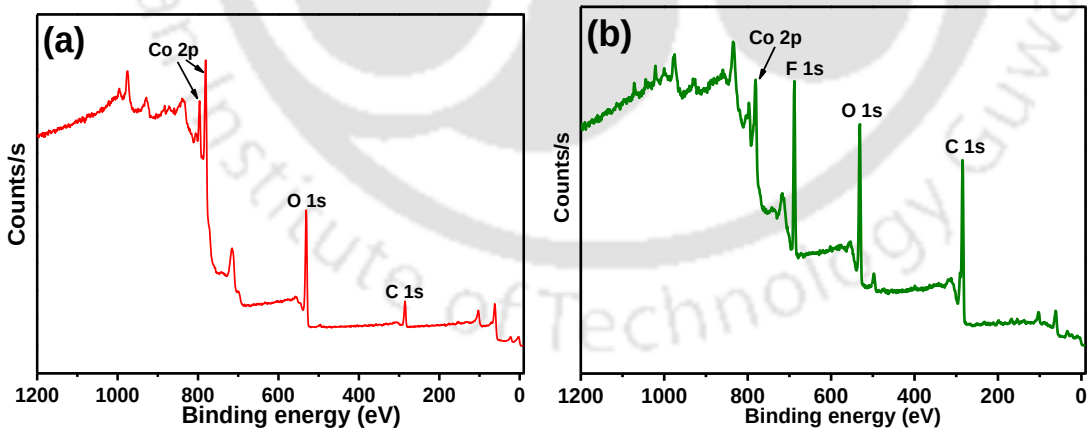

Figure 6.8. Survey spectra of (a) Co_3O_4 NDs, and (b) Co_3O_4 NDs/TCP after 2 h of electrolysis at −1.25 V (vs. Ag/AgCl) in N_2 environment in 0.1 M Na_2SO_4 solution.

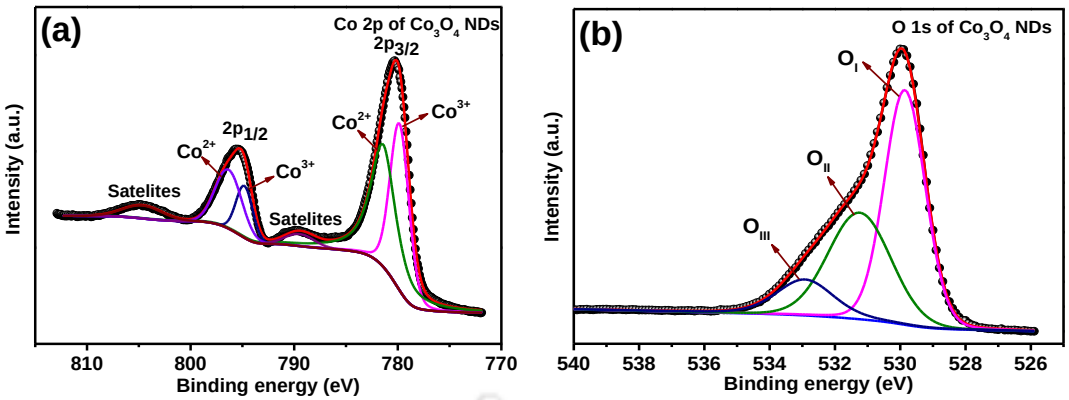

Figure 6.9. High-resolution XPS spectra of (b) Co 2p and (c) O 1s of Co_3O_4 NDs.

6.2.1.6 Mechanistic aspects of Co_3O_4 NDs formation

In an aqueous solution, $Co(NO_3)_2.6H_2O$ dissociates following the reaction shown in Equation 6.4. At an alkaline pH (~11), the adjacent (2,3) phenolic groups of gallic acid, via its chelating effects reacts with Co^{2+} ion and forms a stable cobalt-phenolate complex with a square planar structure. The complex transforms to Co_3O_4 NDs with the calcination at 700°C (Figure 6.10a). Figure 6.10b represents the spinel structure of Co_3O_4 with two types of Co atoms, namely, Co^{2+} and Co^{3+} occupying one-eight and half of the tetrahedral and octahedral interstices, respectively.

$$Co(NO_3)_2 \rightarrow Co^{2+} + 2NO_3^- + 6H_2O \qquad (6.4)$$

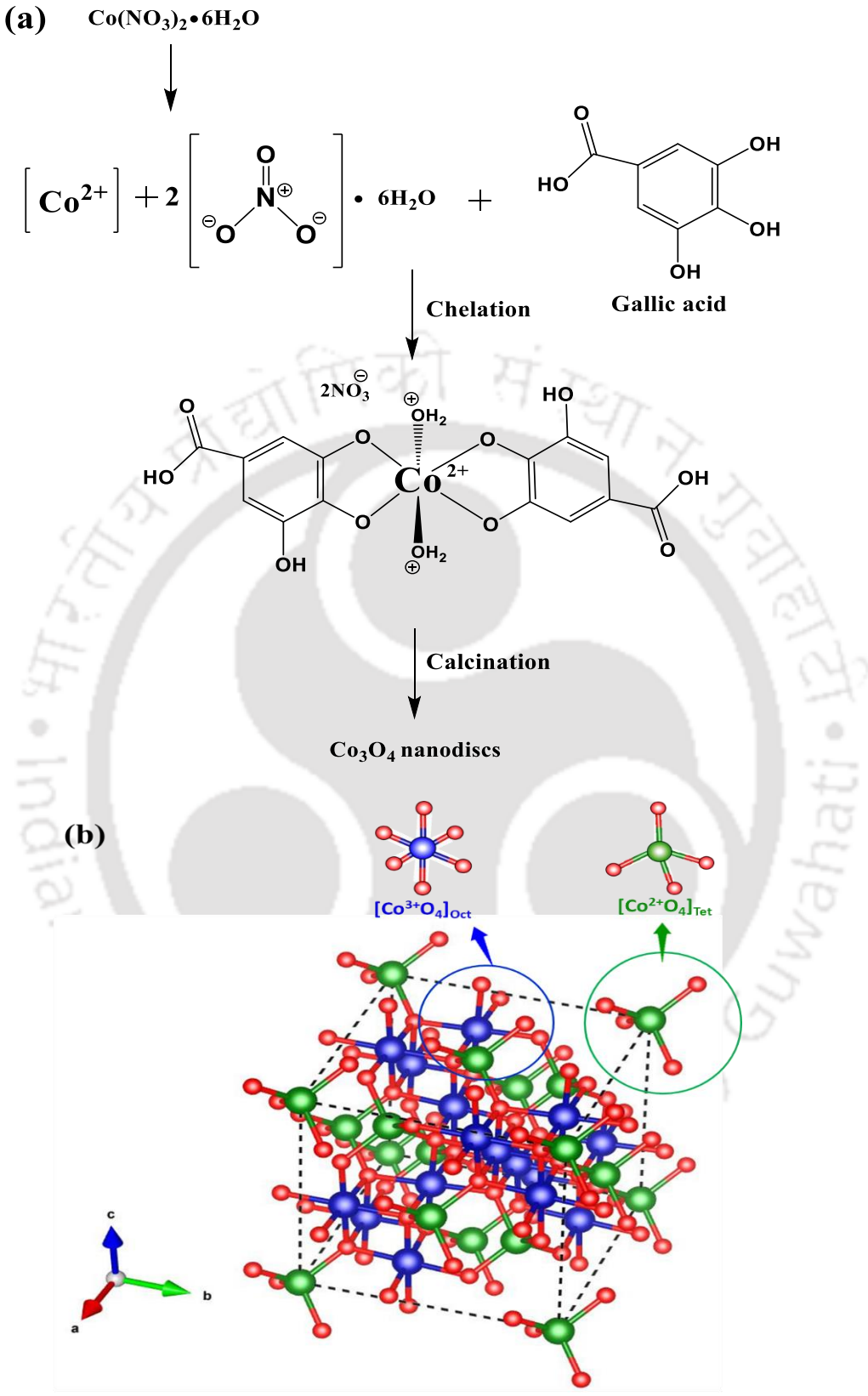

Figure 6.10. (a) Proposed mechanistic pathway of Co_3O_4 formation and (b) Illustration of Co_3O_4 spinel structure with tetrahedral Co^{2+} and octahedral Co^{3+} ions.

Ostwald ripening could be responsible for this kind of anisotropic growth of the nanoparticles (Jin et al., 2012; Yesuraj et al., 2022). The Co_3O_4 nuclei is first formed, and then the gallic acid molecules get adsorbed onto the surface of the nuclei due to its higher surface energy. Due to the hydrogen bonding and electrostatic interactions, the capped nuclei are assembled quickly into large-disc like structures (Figure 6.11) (Xu et al., 2006).

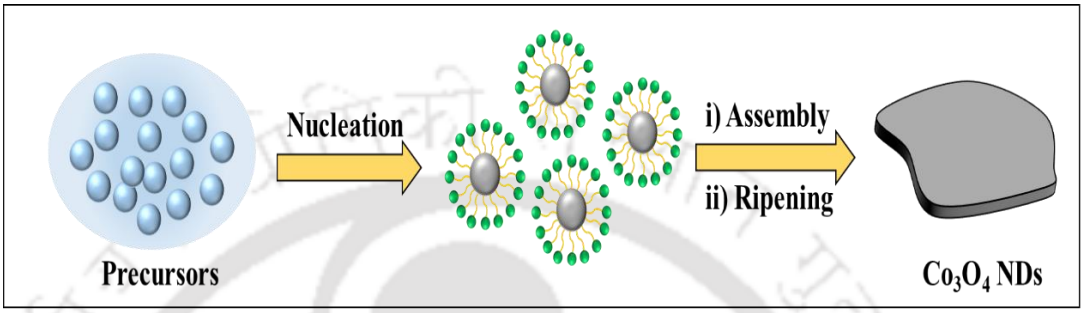

Figure 6.11. Schematic illustration of formation and growth of Co_3O_4 NDs using gallic acid.

6.2.2 Electrochemical performance of Co_3O_4 ND/TCP

6.2.2.1 Linear sweep voltammetry (LSV) analysis

The linear sweep voltammetry (LSV) was first performed under Ar and N_2 environment (with bubbling) in 0.1 M Na_2SO_4 electrolyte to understand the catalytic activity of Co_3O_4 ND/TCP for ENRR (Figure 6.12). The onset potential starts at −1.15 V (vs. Ag/AgCl). A distinct enhancement of current density was observed for the Co_3O_4 ND/TCP/N_2 system with that for the Co_3O_4 ND/TCP/Ar systems in the potential window of −1.2 ~ −2.0 V (vs. Ag/AgCl) because of the noteworthy response of Co_3O_4 ND/TCP towards ENRR (Zhao et al., 2021).

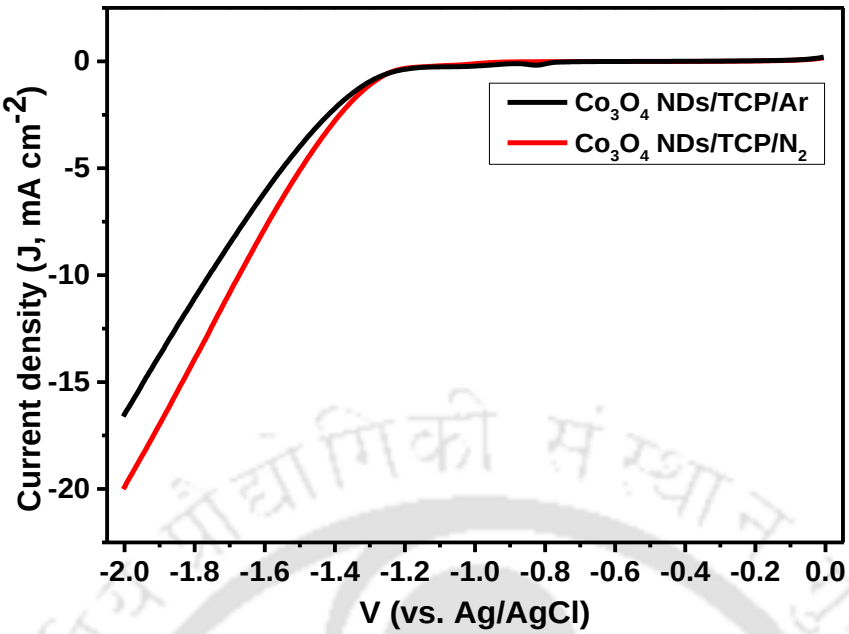

Figure 6.12. Linear sweep voltammetric profiles recorded in Co_3O_4 NDs/TCP/N_2 and Co_3O_4 NDs/TCP/Ar systems in 0.1 M Na_2SO_4 electrolyte at 20 mV s^{-1} of scan rate.

6.2.2.2 Electrochemical impedance spectroscopy of Co_3O_4 ND/TCP

The electrochemical impedance spectroscopic (EIS) study was carried out both in the bare TCP/N_2, Co_3O_4 NDs/TCP/N_2 and Co_3O_4 NDs/TCP/Ar systems in 0.1 M Na_2SO_4 electrolyte. The Nyquist plots are presented in Figure 6.13. The inset shows the Randle's equivalent circuits for bare TCP/N_2 ($R_s[R_{ct}CPE]$), and Co_3O_4 NDs/TCP/N_2 and Co_3O_4 NDs/TCP/Ar systems ($R_s(C_{dl}[R_{ct}Z_W])$) modelled from the EIS analysis. The parameters R_s, R_{ct}, CPE, C_{dl}, and Z_W correspond to the solution resistance, charge transfer resistance, constant phase element, double layer capacitance, and Warburg impedance, respectively. The fitted values of the circuit elements are summarized in Table 6.1. The almost similar R_s values (~0.46 Ω difference) of bare TCP/N_2, Co_3O_4 NDs/TCP were found both in Co_3O_4 NDs/TCP/N_2 and Co_3O_4 NDs/TCP/Ar systems. It could be due to the same electrolyte solution. Bare TCP/N_2 exhibited the highest charge transfer resistance of 9.19×10^6 μΩ among all 03 systems. Co_3O_4 NDs/TCP/N_2 exhibited a smaller diameter circle with a ~3.5 fold lower R_{ct} value in comparison to Co_3O_4 NDs/TCP/Ar. It implies a faster electron transfer for an enhanced faradaic reaction for ENRR (Xu et al., 2019). The higher C_{dl} value, 66.0 μF of the Co_3O_4 NDs/TCP/N_2 system than that of 49.5 μF for the Co_3O_4 NDs/TCP/Ar system because of the higher

capacitive behavior of the latter. Z_W is indicative of mass transfer by diffusion, which is 1.6 fold higher in Co_3O_4 NDs/TCP/N_2 than Co_3O_4 NDs/TCP/Ar in 0.1 M Na_2SO_4 electrolyte. A slower mass transfer in the Co_3O_4 NDs/TCP/N_2 system could improve the selectivity and efficiency of the reaction by allowing better control of the reaction intermediates during the reduction of N_2 (Nolen and Fedkiw, 1990).

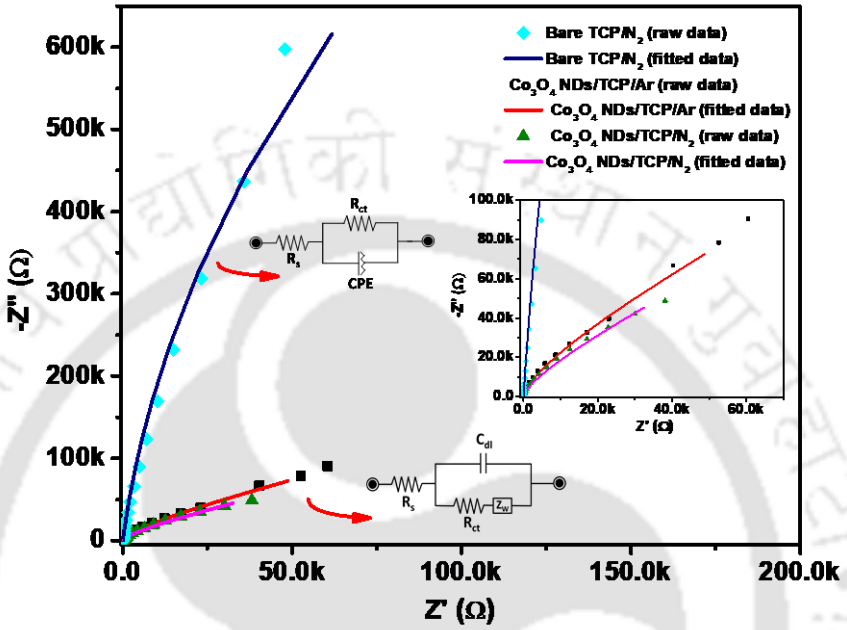

Figure 6.13. Nyquist plots for bare TCP, Co_3O_4 NDs/TCP/N_2 and Co_3O_4 NDs/TCP/Ar systems in 0.1 M Na_2SO_4 electrolyte.

Table 6.1. Values of the elements in equivalent electric circuit determined by the fitting of Nyquist plots.

Electrical circuit elements	**Bare TCP/N_2 system**	**Co_3O_4 NDs/TCP/Ar system**	**Co_3O_4 NDs/TCP/N_2 system**
R_s (Ω)	6.13	6.59	6.20
R_{ct} (μΩ)	9.19×10^6	72.8	20.3
C_{dl} (μF)	---	49.5	66.0
Q, Y_o (μMho)	24.2	---	---
W, Y_o (μMho)	---	36.1	58.7
N	0.979	---	---

6.2.2.3 Co_3O_4 ND/TCP for ENRR forming NH_3

ENRR for the formation of NH_3 at the Co_3O_4 NDs/TCP electrode was monitored by chronoamperometry tests. Figure 6.14a shows the current response vs. time graph for 1 h of electrolysis at the potential range from −1.22 to −1.55 V (vs. Ag/AgCl). It is noticeable that the current density increases with the applied potential, which is also observed in the LSV analysis (Figure 6.12).

Figure 6.14b shows the FE and yield of NH_3. FE of NH_3 production was found to be 1.1% at the onset potential of −1.20 V (vs. Ag/AgCl), whereas, the highest FE of 2.6% was achieved at −1.25 V (vs. Ag/AgCl). After that the FE was gradually decreased down to 0.18% at −1.55 V (vs. Ag/AgCl); while the maximum yield of NH_3 production was achieved to be 8.8 μg h^{-1} $mg_{cat.}^{-1}$. The control experiments were conducted using bare TCP/N_2 and Co_3O_4 NDs/TCP/Ar electrodes at −1.25 V (vs. Ag/AgCl). The corresponding UV-vis spectra are shown in Figure 6.15. Co_3O_4 NDs/TCP/Ar electrode exhibited a petty FE of 0.08% with the yield of NH_3 formation of 0.53 μg h^{-1} $mg_{cat.}^{-1}$. Whereas, the TCP/N_2 system showed the FE of 0.43% with the yield of 0.88 μg h^{-1} $mg_{cat.}^{-1}$. NH_3 detected in the Co_3O_4 NDs/TCP/Ar system could be due to the reduction of N_2 that was potentially contaminated in Ar gas (L. Zhang et al., 2018a). There was no evidence of N_2H_4 formation based on the analytical method by Watt and Chrisp after 1 h of electrolysis at −1.25 V (vs. Ag/AgCl). It confirms selective production of NH_3 on Co_3O_4 ND/TCP electrode (Figure 6.16).

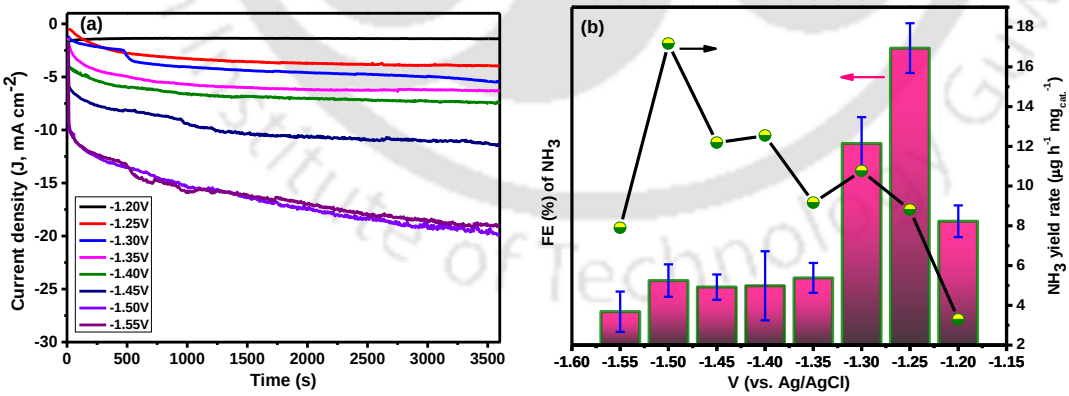

Figure 6.14. (a) Current response graph and (b) FE and yield of NH_3 production with Co_3O_4 NDs/TCP/N_2 system in 0.1 M Na_2SO_4 electrolyte at different applied potentials (vs. Ag/AgCl) for 1 h of chronoamperometry test.

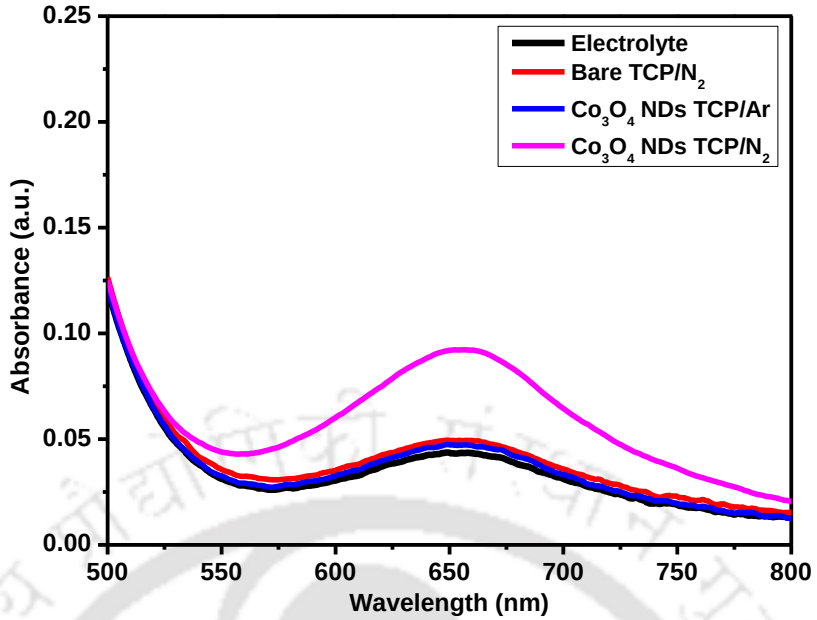

Figure 6.15. UV-vis spectra of 0.1 M Na_2SO_4 electrolyte solution at beginning and after 1 h of electrolysis using bare TCP/N_2, Co_3O_4 NDs TCP/Ar, and Co_3O_4 NDs TCP/N_2 electrodes at −1.25 V (vs. Ag/AgCl) in 0.1 M Na_2SO_4 electrolyte.

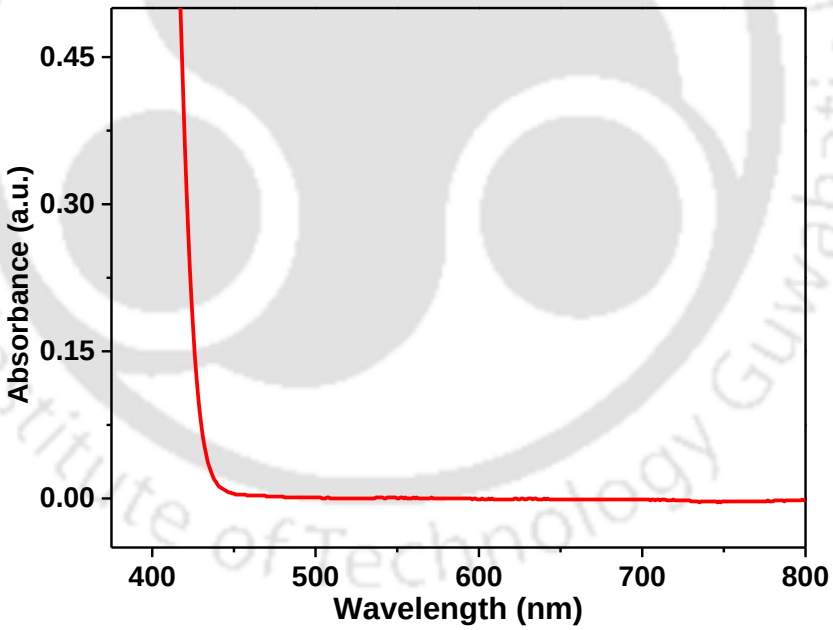

Figure 6.16. UV-Vis spectrum of the electrolyte after electrolysis in N_2 environment in 0.1 M Na_2SO_4 at −1.25 V (vs. Ag/AgCl) for detection of N_2H_4 using Watt and Chrisp method.

The performance of Co_3O_4 NDs/TCP electrode for ENRR for the formation of NH_3 was compared with different catalysts including both Co-based materials under

variants experimental conditions (Table 6.2). Co_3O_4 NDs outperformed most of the ENRR catalysts under ambient conditions. For example, FE of 0.15, 0.6, 0.217, 2.17, 1.50, 2.5, 1.90, and 2.17 are reported for Fe_2O_3-CNT, amorphous $Pd_{0.2}Cu_{0.8}$/rGO, Rh nanosheets, cubic sub-micron SnO_2, Co_3O_4@CNT, TiO_2 nanosheet, γ-Fe_2O_3, SnO_2/C catalysts, respectively.

Table 6.2. Performance of Co_3O_4 NDs/TCP electrode in the present work in comparison to earlier studies for ENRR forming NH_3 using various catalysts at atmospheric pressure and room temperature.

Catalyst	**Preparation method**	**Conditions**	**Faradaic efficiency (%) and yield (μg h^{-1} $mg_{cat.}^{-2}$)**	**Reference**
Co_3O_4 NDs	Bioinspired route using gallic acid, Hydrothermal method	0.1 M Na_2SO_4 −1.25 V (vs. Ag/AgCl), (−0.24 V vs. RHE)*	2.6%, 8.8	**This work**
Amorphous $Pd_{0.2}Cu_{0.8}$/rGO composite	Chemical reduction method	0.1 M KOH −0.2 V (vs. RHE)	0.6%, 2.8	Shi et al. (2018)
Poly(N-ethyl-benzene-1,2,4,5-tetracarboxylic diimide)/C	Chemical reflux method	0.5 M Li2SO4 −0.5 V (vs. RHE)	2.58%, 1.23	G. F. Chen et al. (2017)
FeS@MoS_2/CFC	Hydrothermal method	0.5 M Li_2SO_4 −0.5 V (vs. RHE)	2.96%, 6.34	Guo et al. (2019)
Rh nanosheets	Chemical method	0.1 M KOH −0.2 V (vs. RHE)	0.217 %, 23.88	H. M. Liu et al. (2018)
Cubic sub-micron SnO_2	Hydrothermal method	0.1 M Na_2SO_4 −0.7 V (vs. RHE)	2.17%, 3.99	L. Zhang et al. (2018c)
Co_3O_4@CNT	Chemical method	0.1 M Na_2SO_4 −0.49 V (vs. RHE)	1.50%, 27.16	Wen et al. (2021)
$BiVO_4$	Hydrothermal method	0.2 M Na_2SO_4 −0.5 V (vs. RHE)	10.04%, 8.60	Yao et al. (2019)

Mn_3O_4 Nanocube	Hydrothermal method	0.1 M Na_2SO_4 −0.8 V (vs. RHE)	3.0%, 11.6	Wu et al. (2018)
Ti_3C_2OH QDs	Chemical method	0.1 M HCl −0.5 V (vs. RHE)	13.30%, 62.94	Jin et al. (2020)
Mn-TiO_2	Chemical method	0.1 M Na_2SO_4 −0.5 V (vs. RHE)	11.93%, 20.05	Chen et al. (2021)
TiO_2 nanosheet	Hydrothermal method	0.1 M Na_2SO_4 −0.7 V (vs. RHE)	2.5%, 5.6	R. Zhang et al. (2018)
TiO_2-rGO	Hydrothermal method	0.1 M Na_2SO_4 −0.9 V (vs. RHE)	3.3%, 15.13	X. Zhang et al. (2018)
Mn-CeO_2/CP	Chemical method	0.1 M HCl −0.3 V (vs. RHE)	9.1%, 27.79	Ji et al. (2022)
γ-Fe_2O_3 (<50 nm)	Commercial	0.1 M KOH 0.0 V (vs. RHE)	1.9%, 0.212	Kong et al. (2017)
Fe_3O_4/Ti	Hydrothermal method	0.1 M Na_2SO_4 −0.4 V (vs. RHE)	2.6%, 4.91	Q. Liu et al. (2018)
MoO_3 nanosheets	Hydrothermal method	0.1 M HCl −0.3 V (vs. RHE)	1.9%, 29.43	Han et al. (2018)
Fe_2O_3-CNT	Chemical method	Dilute $KHCO_3$ −0.2 V (vs. RHE	0.15%, 0.044	S. Chen et al. (2017)

* E(*RHE*)= E(*Ag*/*AgCl*) + 0.198 V + 0.059 × pH

Further, the chronoamperometry test was extended up to 2 h. It was noted that FE fell to 1.80% after the electrolysis at −1.25 V (vs. Ag/AgCl) for 2 h of against 2.6% in 1 h. Figure 6.17 shows the current density graph for 2 h of the chronoamperometry test. The FESEM images of fresh and used Co_3O_4 NDs/TCP electrodes after 1 and 2 h of electrolysis didn't show significant morphological changes (Figure 6.18). The chemical alteration of the surface of the Co_3O_4 NDs/TCP electrode during electrolysis of 2 h of was examined further by XRD and XPS analysis. Figure 6.19 shows the XRD pattern of Co_3O_4 NDs/TCP after 2 h of electrolysis. No additional peaks and phase change were noted except the decrease in peak intensity (Cai et al., 2018).

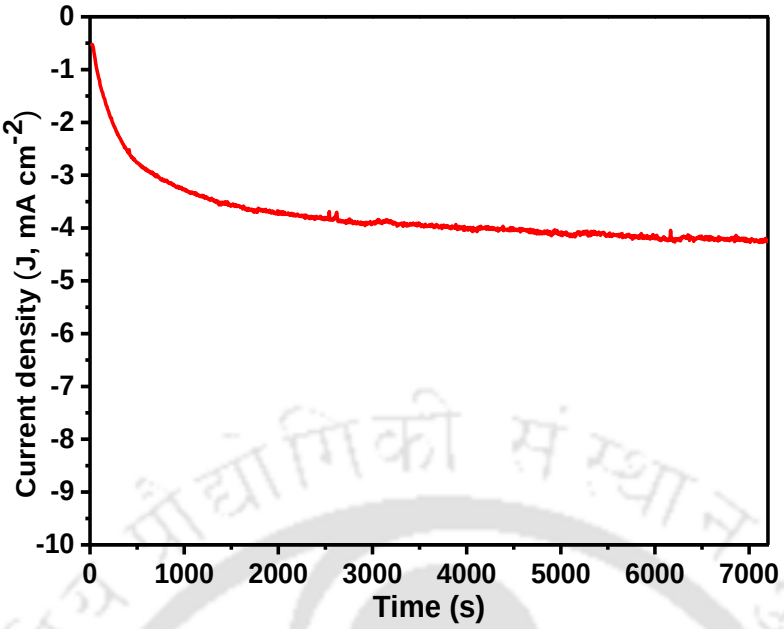

Figure 6.17. Current response recorded with Co_3O_4 NDs/TCP electrode in N_2 environment in 0.1 M Na_2SO_4 at −1.25 V (vs. Ag/AgCl) for 2 h of chronoamperometry test.

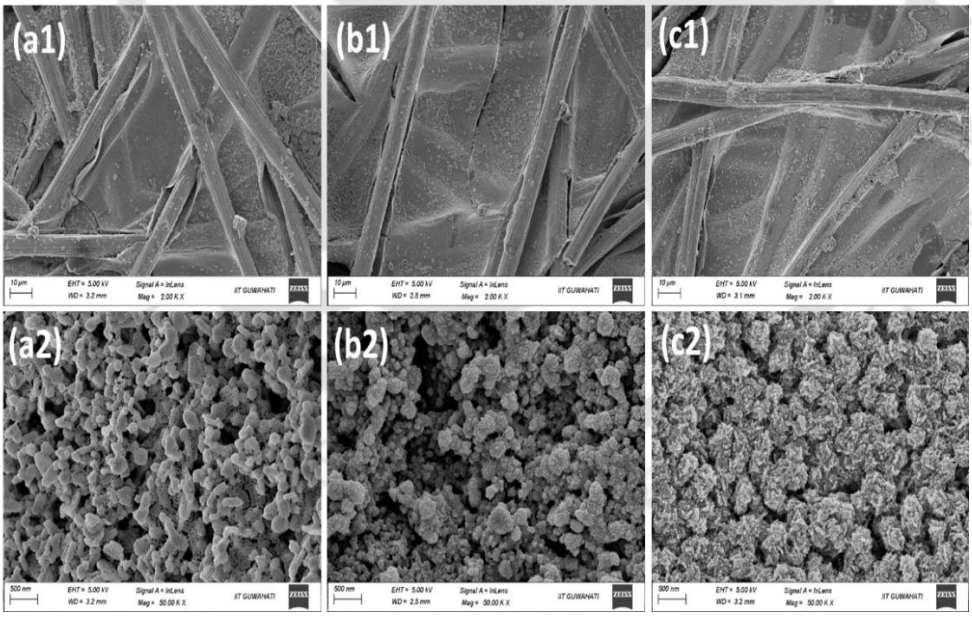

Figure 6.18. FESEM images of Co_3O_4 NDs/TCP electrodes: (a1) and (a2) for unused electrodes, (b1) and (b2) after 1 h of ENRR, and (c1) and (c2) after 2 h of ENRR at −1.25 V vs. Ag/AgCl in N_2- environment in 0.1 M Na_2SO_4 electrolyte.

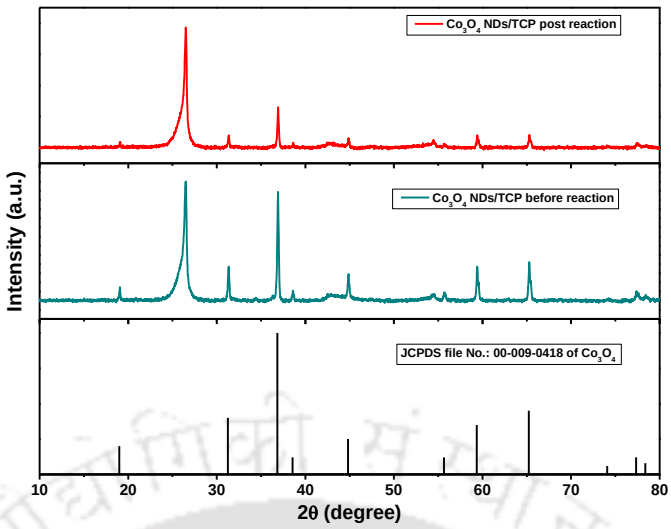

Figure 6.19. XRD patterns of Co_3O_4 NDs/TCP before and after of 2 h of ENRR for NH_3 formation in 0.1 M Na_2SO_4 electrolyte at −1.25 V (vs. Ag/AgCl).

Figure 6.20 shows the Co 2p and O 1s spectra of Co_3O_4 NDs/TCP, after 2 h of electrolysis. It can be observed that both spectra were shifted towards the higher binding energy (blue shift). The binding energy gap of Co $2p_{3/2}$ and Co $2p_{1/2}$ was increased from 15.1 (unused catalyst, Figure 6.9a) to 16.1 eV after ENRR Figure 6.20a. The two pairs of fitted peaks corresponding to Co^{3+} are at the binding energy of 780.3 and 795.5 eV, and it is 781.3 and 802.8 eV for Co^{2+}. The ratio of Co^{3+}/Co^{2+} decreased to 0.45 compared to 0.73 for the as-synthesized Co_3O_4 NDs. It could be due to induction of oxygen vacancies during ENRR. Furthermore, an increase in the area under the satellite peaks at the binding energy of 781.3 and 802.8 eV were observed. This features could be an indication of the formation of $Co(OH)_2$ on the catalyst surface during the electrolysis (Yamada et al., 2010). The formation of $Co(OH)_2$ was also confirmed from the O 1s spectra (Figure 6.20b). The O 1s peak at 529.8 eV, appeared in the unused catalyst, was also decreased after ENRR, whereas an increase in the peak at 531.2 eV was noted. The characteristic peak along with O_I and O_{II} at a higher binding energy of 533.3 eV could be assigned to the surface adsorbed water molecules and/or carbon-oxygen bond of organic carbon because of contamination (O_w) (Xiao et al., 2020). The ratio of peak areas O_{II}/O_I was calculated to be 37.8 because of increased surface defects due to enhanced oxygen vacancies during cathodic reaction (Duan et al., 2019). It is

proposed here that, Co^{2+} (Td) could easily bond with the N≡N, and Co^{3+} (O_h) facilitates the electron transfer for N_2 reduction reaction (Chen et al., 2022).

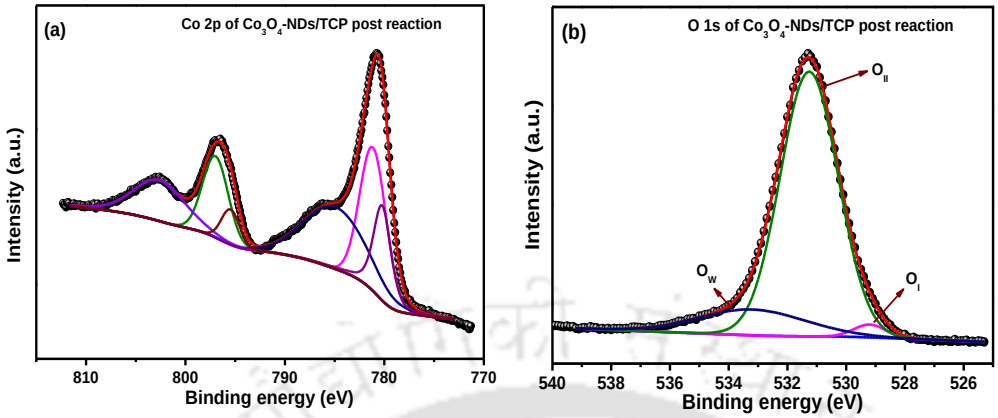

Figure 6.20. High resolution XPS spectra of (a) Co 2p and (b) O 1s of Co_3O_4 NDs/TCP after 2 h of ENRR for NH_3 formation in 0.1 M Na_2SO_4 electrolyte at −1.25 V (vs. Ag/AgCl).

To be economically feasible, electrochemical N_2 reduction for NH_3 production process needs to achieve energy efficiency of >60% and faradaic efficiency of >90% with a current density above 300 mA cm^{-2} (Fernandez and Hatzell, 2020). Considering the electricity cost (0.03 \$ kWh^{-1}) in the next decades, for 2000 ton NH_3 day^{-1} production scale, the estimated production cost of a single-stage and two-staged ENRR process is ~750 and ~420 \$ ton^{-1}, respectively, which is higher than that of the Haber-Bosch process, 159 \$ ton^{-1}. To compete with the Haber-Bosch process, with a lower production scale of 0.03 ton NH_3 day^{-1}, the production cost of a single and two-staged ENRR process is estimated to be ~930 and ~510 \$ ton^{-1}, respectively. At this production scale, the cost of NH_3 production in the Haber-Bosch process is ~4000 \$ ton^{-1}. Therefore, the Haber-Bosch parity can be met by a single and two-staged ENRR process at scales below 4 and 30 ton NH_3 day^{-1}, respectively (Fernandez and Hatzell, 2020).

6.3 Major findings

This work demonstrates successful one-pot synthesis of pristine Co_3O_4 NDs in an environmentally benign method using gallic acid as a reducing agent. The narrow bandgaps of 1.78 and 2.07 eV were corresponding to the O^{2-} to Co^{2+}/Co^{3+} charge

transfer couples in correlation with the presence of oxygen vacancy, and it facilitate electron and charge transport for enhanced N_2 reduction reaction. Co_3O_4 NDs were formed with diameter and thickness of 240 and 35.5 nm, respectively, with a preferential anisotropic growth of the particles along the (311) direction owing to the Ostwald ripening. A 1.6-fold high Warburg resistance (Z_W) for Co_3O_4 NDs/TCP/N_2 over Co_3O_4 NDs/TCP/Ar in 0.1 M Na_2SO_4 electrolyte resulted a slower mass transfer in the Co_3O_4 NDs/TCP/N_2 system which improved the selectivity and efficiency of ENRR forming NH_3. It offered 2.6% FE of NH_3 production with a yield rate of 8.8 μg h^{-1} $mg_{cat.}^{-1}$ at −1.25 V (vs. Ag/AgCl) which is six times higher than that of the bare TCP electrode. Electrolysis up to 2 h caused a marginal fall in FE to 1.80% due to the formation of $Co(OH)_2$. Co^{2+} in tetrahedral sites easily bond with the N≡N, and the Co^{3+} in octahedral sites facilitate the electron transfer for N_2 reduction reaction.

References

Al-Qirby, L.M., Radiman, S., Siong, C.W., Ali, A.M., 2017. Sonochemical synthesis and characterization of Co_3O_4 nanocrystals in the presence of the ionic liquid [EMIM][BF_4]. Ultrason. Sonochem. 38, 640–651. https://doi.org/10.1016/j.ultsonch.2016.08.016

Al-Tuwirqi, R.M., Al-Ghamdi, A. A., Al-Hazmi, F., Alnowaiser, F., Al-Ghamdi, Attieh A., Aal, N.A., El-Tantawy, F., 2011. Synthesis and physical properties of mixed Co_3O_4/CoO nanorods by microwave hydrothermal technique. Superlattices Microstruct. 50, 437–448. https://doi.org/10.1016/j.spmi.2011.06.007

Aziz, M., Putranto, A., Biddinika, M.K., Wijayanta, A.T., 2017. Energy-saving combination of N_2 production, NH_3 synthesis, and power generation. Int. J. Hydrogen Energy 42, 27174–27183. https://doi.org/10.1016/j.ijhydene.2017.09.079

Bhargava, R., Khan, S., Ahmad, N., Ansari, M.M.N., 2018. Investigation of structural, optical and electrical properties of Co_3O_4 nanoparticles. AIP Conf. Proc. 1953, 1–5. https://doi.org/10.1063/1.5032369

Cai, Z., Bi, Y., Hu, E., Liu, W., Dwarica, N., Tian, Y., Li, X., Kuang, Y., Li, Y., Yang, X.Q., Wang, H., Sun, X., 2018. Single-crystalline ultrathin Co_3O_4 nanosheets with massive vacancy defects for enhanced electrocatalysis. Adv. Energy Mater. 8, 1–8. https://doi.org/10.1002/aenm.201701694

Chen, G.F., Cao, X., Wu, S., Zeng, X., Ding, L.X., Zhu, M., Wang, H., 2017. Ammonia Electrosynthesis with High Selectivity under Ambient Conditions via a Li+ Incorporation Strategy. J. Am. Chem. Soc. 139, 9771–9774. https://doi.org/10.1021/jacs.7b04393

Chen, H., Wu, T., Li, X., Lu, S., Zhang, F., Wang, Y., Zhao, H., Liu, Q., Luo, Y., Asiri, A.M., Feng, Z.S., Zhang, Y., Sun, X., 2021. Modulating oxygen vacancies of TiO2 nanospheres by Mn-doping to boost electrocatalytic N_2 reduction. ACS Sustain. Chem. Eng. 9, 1512–1517. https://doi.org/10.1021/acssuschemeng.0c09009

Chen, S., Perathoner, S., Ampelli, C., Mebrahtu, C., Su, D., Centi, G., 2017. Electrocatalytic synthesis of ammonia at room temperature and atmospheric pressure from water and nitrogen on a carbon-nanotube-based electrocatalyst. Angew. Chemie - Int. Ed. 56, 2699–2703. https://doi.org/10.1002/anie.201609533

Chen, Y., He, J., Pang, H., Jiang, P., Qu, F., Yu, D., Zhang, J., 2022. New insight into electrochemical denitrification using a self-organized nanoporous VO-Co3O4/Co cathode: Plasma-assistant oxygen vacancies catalyzed efficient nitrate reduction. Sci. Total Environ. 850, 157845. https://doi.org/10.1016/j.scitotenv.2022.157845

Chu, K., Liu, Y., Li, Y., Zhang, H., Tian, Y., 2019a. Efficient electrocatalytic N 2 reduction on CoO quantum dots. J. Mater. Chem. A 7, 4389–4394. https://doi.org/10.1039/C9TA00016J

Chu, K., Liu, Y.P., Li, Y.B., Zhang, H., Tian, Y., 2019b. Efficient electrocatalytic N_2 reduction on CoO quantum dots. J. Mater. Chem. A 7, 4389–4394. https://doi.org/10.1039/c9ta00016j

Chu, K., Liu, Y.P., Wang, J., Zhang, H., 2019c. NiO nanodots on graphene for efficient electrochemical N_2 reduction to NH_3. ACS Appl. Energy Mater. 2, 2288–2295. https://doi.org/10.1021/acsaem.9b00102

Deori, K., Ujjain, S.K., Sharma, R.K., Deka, S., 2013. Morphology controlled synthesis of nanoporous Co_3O_4 nanostructures and their charge storage characteristics in supercapacitors. ACS Appl. Mater. Interfaces 5, 10665–10672. https://doi.org/10.1021/am4027482

Du, H., Guo, X., Kong, R.M., Qu, F., 2018. Cr_2O_3 nanofiber: a high-performance electrocatalyst toward artificial N_2 fixation to NH_3 under ambient conditions. Chem. Commun. 54, 12848–12851. https://doi.org/10.1039/c8cc07186a

Duan, S.F., Ji, Y.F., Wang, W., Han, D.F., Wang, H.Y., Wei, Q.Y., Li, C.F., Jia, F., Han, D.X., Niu, L., Qin, D.D., Tao, C.L., 2019. Unraveling the impact of electrochemically created oxygen vacancies on the performance of ZnO nanowire photoanodes. ACS Sustain. Chem. Eng. 7, 18165–18173. https://doi.org/10.1021/acssuschemeng.9b05442

Fernandez, C.A., Hatzell, M.C., 2020. Editors' Choice—Economic considerations for low-temperature electrochemical ammonia production: Achieving Haber-Bosch parity. J. Electrochem. Soc. 167, 143504. https://doi.org/10.1149/1945-7111/abc35b

Gao, L., Wang, F., Yu, M.A., Wei, F., Qi, J., Lin, S., Xie, D., 2019. A novel phosphotungstic acid-supported single metal atom catalyst with high activity and selectivity for the synthesis of NH_3 from electrochemical N_2 reduction: A DFT

prediction. J. Mater. Chem. A 7, 19838–19845. https://doi.org/10.1039/c9ta06470b

Ge, B., Li, K., Fu, Z., Pu, L., Zhang, X., 2015. The addition of ortho-hexagon nano spinel Co_3O_4 to improve the performance of activated carbon air cathode microbial fuel cell. Bioresour. Technol. 195, 180–187. https://doi.org/10.1016/j.biortech.2015.06.054

Ghavam, S., Vahdati, M., Wilson, I.A.G., Styring, P., 2021. Sustainable ammonia production processes. Front. Energy Res. 9, 1–19. https://doi.org/10.3389/fenrg.2021.580808

Guo, Y., Yao, Z., Timmer, B.J.J., Sheng, X., Fan, L., Li, Y., Zhang, F., Sun, L., 2019. Boosting nitrogen reduction reaction by bio-inspired FeMoS containing hybrid electrocatalyst over a wide pH range. Nano Energy 62, 282–288. https://doi.org/10.1016/j.nanoen.2019.05.051

Han, J., Ji, X., Ren, X., Cui, G., Li, L., Xie, F., Wang, H., Li, B., Sun, X., 2018. MoO_3 nanosheets for efficient electrocatalytic N_2 fixation to NH_3. J. Mater. Chem. A 6, 12974–12977. https://doi.org/10.1039/c8ta03974g

Hong, W., Wang, J., Li, Z., Yang, S., 2015. Hierarchical Co_3O_4@Au-decorated PPy core/shell nanowire arrays: An efficient integration of active materials for energy storage. J. Mater. Chem. A 3, 2535–2540. https://doi.org/10.1039/c4ta04707a

Iravani, S., Varma, R.S., 2020. Sustainable synthesis of cobalt and cobalt oxide nanoparticles and their catalytic and biomedical applications. Green Chem. 22, 2643–2661. https://doi.org/10.1039/d0gc00885k

Jha, A., Rode, C. V., 2013. Highly selective liquid-phase aerobic oxidation of vanillyl alcohol to vanillin on cobalt oxide (Co_3O_4) nanoparticles. New J. Chem. 37, 2669–2674. https://doi.org/10.1039/c3nj00508a

Ji, Y., Cheng, W., Li, C., Liu, X., 2022. Oxygen vacancies of CeO_2 nanospheres by Mn-doping: An efficient electrocatalyst for N_2 reduction under ambient conditions. Inorg. Chem. 61, 28–31. https://doi.org/10.1021/acs.inorgchem.1c02989

Jin, R., Chen, G., Pei, J., Xu, H., Lv, Z.S., 2012. Solvothermal synthesis and growth mechanism of ultrathin Sb_2Te_3 hexagonal nanoplates with thermoelectric transport properties. RSC Adv. 2, 1450–1456. https://doi.org/10.1039/c1ra00642h

Jin, Z., Liu, C., Liu, Z., Han, J., Fang, Y., Han, Y., Niu, Y., Wu, Y., Sun, C., Xu, Y., 2020. Rational Design of Hydroxyl-Rich $Ti_3C_2T_x$ MXene Quantum Dots for High-Performance Electrochemical N_2 Reduction. Adv. Energy Mater. 10, 1–8. https://doi.org/10.1002/aenm.202000797

Kong, J., Lim, A., Yoon, C., Jang, J.H., Ham, H.C., Han, J., Nam, S., Kim, D., Sung, Y.E., Choi, J., Park, H.S., 2017. Electrochemical synthesis of NH_3 at low temperature and atmospheric pressure using a γ-Fe_2O_3 catalyst. ACS Sustain. Chem. Eng. 5, 10986–10995. https://doi.org/10.1021/acssuschemeng.7b02890

Kordali, V., Kyriacou, G., Lambrou, C., 2000. Electrochemical synthesis of ammonia at atmospheric pressure and low temperature in a solid polymer electrolyte cell. Chem. Commun. 1673–1674. https://doi.org/10.1039/b004885m

Lambert, T.N., Vigil, J.A., White, S.E., Davis, D.J., Limmer, S.J., Burton, P.D., Coker, E.N., Beechem, T.E., Brumbach, M.T., 2015. Electrodeposited $Ni_xCo_{3-x}O_4$ nanostructured films as bifunctional oxygen electrocatalysts. Chem. Commun. 51, 9511–9514. https://doi.org/10.1039/c5cc02262b

Li, W., Li, K., Ye, Y., Zhang, S., Liu, Y., Wang, G., Liang, C., Zhang, H., Zhao, H., 2021a. Efficient electrocatalytic nitrogen reduction to ammonia with aqueous silver nanodots. Commun. Chem. 4, 1–11. https://doi.org/10.1038/s42004-021-00449-7

Li, W., Ye, Y., Zhang, S., Liang, C., Zhang, H., 2021b. A fluidized electrocatalysis approach for ammonia synthesis using oxygen vacancy-rich Co_3O_4 nanoparticles. Inorg. Chem. Front. 8, 4026–4034. https://doi.org/10.1039/d1qi00721a

Liu, H.M., Han, S.H., Zhao, Y., Zhu, Y.Y., Tian, X.L., Zeng, J.H., Jiang, J.X., Xia, B.Y., Chen, Y., 2018. Surfactant-free atomically ultrathin rhodium nanosheet nanoassemblies for efficient nitrogen electroreduction. J. Mater. Chem. A 6, 3211–3217. https://doi.org/10.1039/c7ta10866d

Liu, Q., Xu, T., Luo, Y., Kong, Q., Li, T., Lu, S., Alshehri, A.A., Alzahrani, K.A., Sun, X., 2021a. Recent advances in strategies for highly selective electrocatalytic N2 reduction toward ambient NH3 synthesis. Curr. Opin. Electrochem. 29, 100766. https://doi.org/10.1016/j.coelec.2021.100766

Liu, Q., Xu, T., Luo, Y., Kong, Q., Li, T., Lu, S., Alshehri, A.A., Alzahrani, K.A., Sun, X., 2021b. Recent advances in strategies for highly selective electrocatalytic N_2

reduction toward ambient NH_3 synthesis. Curr. Opin. Electrochem. 29, 100766. https://doi.org/10.1016/j.coelec.2021.100766

Liu, Q., Zhang, X., Zhang, B., Luo, Y., Cui, G., Xie, F., Sun, X., 2018. Ambient N_2 fixation to NH_3 electrocatalyzed by a spinel Fe_3O_4 nanorod. Nanoscale 10, 14386–14389. https://doi.org/10.1039/c8nr04524k

Lv, X.W., Liu, Y., Hao, R., Tian, W., Yuan, Z.Y., 2020. Urchin-like Al-Doped Co_3O_4 nanospheres rich in surface oxygen vacancies enable efficient ammonia electrosynthesis. ACS Appl. Mater. Interfaces 12, 17502–17508. https://doi.org/10.1021/acsami.0c00647

Nolen, T.R., Fedkiw, P.S., 1990. Reaction selectivity enhancement under periodic-current control. The reduction of nitrobenzene on the rotating disk electrode. Proc. - Electrochem. Soc. 90, 141–163. https://doi.org/10.1149/1.2087049

Paul, B., Bhanja, P., Sharma, S., Yamauchi, Y., Alothman, Z.A., Wang, Z.L., Bal, R., Bhaumik, A., 2021. Morphologically controlled cobalt oxide nanoparticles for efficient oxygen evolution reaction. J. Colloid Interface Sci. 582, 322–332. https://doi.org/10.1016/j.jcis.2020.08.029

Shi, M.M., Bao, D., Li, S.J., Wulan, B.R., Yan, J.M., Jiang, Q., 2018. Anchoring PdCu Amorphous Nanocluster on Graphene for Electrochemical Reduction of N_2 to NH_3 under Ambient Conditions in Aqueous Solution. Adv. Energy Mater. 8, 1–6. https://doi.org/10.1002/aenm.201800124

Shi, M.M., Bao, D., Wulan, B.R., Li, Y.H., Zhang, Y.F., Yan, J.M., Jiang, Q., 2017. Au sub-nanoclusters on TiO_2 toward highly efficient and selective electrocatalyst for N_2 conversion to NH_2 at ambient conditions. Adv. Mater. 29, 2–7. https://doi.org/10.1002/adma.201606550

Su, D., Xie, X., Munroe, P., Dou, S., Wang, G., 2014. Mesoporous hexagonal Co_3O_4 for high performance lithium ion batteries. Sci. Rep. 4, 6519. https://doi.org/10.1038/srep06519

Tomon, C., Krittayavathananon, A., Sarawutanukul, S., Duangdangchote, S., Phattharasupakun, N., Homlamai, K., Sawangphruk, M., 2021. Enhancing bifunctional electrocatalysts of hollow Co3O</sub>4</sub> nanorods with oxygen vacancies towards ORR and OER for Li–O_2 batteries. Electrochim. Acta 367, 137490. https://doi.org/10.1016/j.electacta.2020.137490

UmaSudharshini, A., Bououdina, M., Venkateshwarlu, M., Manoharan, C., Dhamodharan, P., 2020. Low temperature solvothermal synthesis of pristine Co_3O_4 nanoparticles as potential supercapacitor. Surfaces and Interfaces 19, 100535. https://doi.org/10.1016/j.surfin.2020.100535

Victoria, S.G., Ezhil Raj, A.M., Ravidhas, C., 2015. An insight in the structural, morphological, electrical and optical properties of spray pyrolysed Co_3O_4 thin films. Mater. Chem. Phys. 162, 852–859. https://doi.org/10.1016/j.matchemphys.2015.07.015

Wen, J., Chang, H., Huang, T., Hossain, M., Liu, Z., Sun, H., Zhu, Y., Chen, Y., Huang, Q., Wu, Y., 2021. A simple synthesis of Co_3O_4@CNT to boost electrochemical nitrogen fixation. Electrochim. Acta 367, 137421. https://doi.org/10.1016/j.electacta.2020.137421

Wen, L., Li, X., Zhang, R., Liang, H., Zhang, Q., Su, C., Zeng, Y.J., 2021. Oxygen vacancy engineering of MOF-derived Zn-doped Co_3O_4 nanopolyhedrons for enhanced electrochemical nitrogen fixation. ACS Appl. Mater. Interfaces 13, 14181–14188. https://doi.org/10.1021/acsami.0c22767

Wu, X., Xia, L., Wang, Y., Lu, W., Liu, Q., Shi, X., Sun, X., 2018. Mn_3O_4 nanocube: An efficient electrocatalyst toward artificial N_2 fixation to NH_3. Small 14, 6–11. https://doi.org/10.1002/smll.201803111

Xiao, J., Kuang, Q., Yang, S., Xiao, F., Wang, S., Guo, L., 2013. Surface structure dependent electrocatalytic activity of Co_3O_4 anchored on graphene sheets toward oxygen reduction reaction. Sci. Rep. 3, 1–8. https://doi.org/10.1038/srep02300

Xiao, Z., Huang, Y.C., Dong, C.L., Xie, C., Liu, Z., Du, S., Chen, W., Yan, D., Tao, L., Shu, Z., Zhang, G., Duan, H., Wang, Y., Zou, Y., Chen, R., Wang, S., 2020. Operando identification of the dynamic behavior of oxygen vacancy-rich Co_3O_4 for oxygen evolution reaction. J. Am. Chem. Soc. 142, 12087–12095. https://doi.org/10.1021/jacs.0c00257

Xu, A.W., Antonietti, M., Cölfen, H., Fang, Y.P., 2006. Uniform hexagonal plates of vaterite $CaCO_3$ mesocrystals formed by biomimetic mineralization. Adv. Funct. Mater. 16, 903–908. https://doi.org/10.1002/adfm.200500716

Xu, M., Wang, F., Zhao, M., Yang, S., Song, X., 2011. Molten hydroxides synthesis of hierarchical cobalt oxide nanostructure and its application as anode material for

lithium ion batteries. Electrochim. Acta 56, 4876–4881. https://doi.org/10.1016/j.electacta.2011.03.027

Xu, M., Xia, Q., Yue, J., Zhu, X., Guo, Q., Zhu, J., Xia, H., 2019. Rambutan-like hybrid hollow spheres of carbon confined Co_3O_4 nanoparticles as advanced anode materials for sodium-ion batteries. Adv. Funct. Mater. 29, 1807377. https://doi.org/10.1002/adfm.201807377

Xu, T., Liang, J., Li, S., Xu, Z., Yue, L., Li, T., Luo, Y., Liu, Q., Shi, X., Asiri, A.M., Yang, C., Sun, X., 2021. Recent advances in nonprecious metal oxide electrocatalysts and photocatalysts for N_2 reduction reaction under ambient condition. Small Sci. 1, 2000069. https://doi.org/10.1002/smsc.202000069

Xu, W., Lyu, F., Bai, Y., Gao, A., Feng, J., Cai, Z., Yin, Y., 2018. Porous cobalt oxide nanoplates enriched with oxygen vacancies for oxygen evolution reaction. Nano Energy 43, 110–116. https://doi.org/10.1016/j.nanoen.2017.11.022

Yamada, Y., Yano, K., Fukuzumi, S., 2010. Cu/Co_3O_4 nanoparticles as catalysts for hydrogen evolution from ammonia borane by hydrolysis. J. Phys. Chem. C 114, 16456–16462. https://doi.org/10.1039/C1EE02639A

Yan, N., Hu, L., Li, Y., Wang, Y., Zhong, H., Hu, X., Kong, X., Chen, Q., 2012. Co_3O_4 nanocages for high-performance anode material in lithium-ion batteries. J. Phys. Chem. C 116, 7227–7235. https://doi.org/10.1021/jp2126009

Yang, M., Jin, Z., Wang, C., Cao, X., Wang, X., Ma, H., Pang, H., Tan, L., Yang, G., 2021. Fe foam-supported FeS_2-MoS_2 electrocatalyst for N_2 reduction under ambient conditions. ACS Appl. Mater. Interfaces 13, 55040–55050. https://doi.org/10.1021/acsami.1c16284

Yao, J.X., Bao, D., Zhang, Q., Shi, M.M., Wang, Y., Gao, R., Yan, J.M., Jiang, Q., 2019. Tailoring oxygen vacancies of $BiVO_4$ toward highly efficient noble-metal-free electrocatalyst for artificial N_2 fixation under ambient conditions. Small Methods 3, 2–7. https://doi.org/10.1002/smtd.201800333

Yesuraj, J., Lee, H.O., Pandiyan, M. kumar, Jayavelu, J., Bhagavathiachari, M., Kim, K., 2022. Bio-engineered hexagon-shaped Co_3O_4 nanoplates on deoxyribonucleic acid (DNA) scaffold: An efficient electrode material for an asymmetric supercapacitor and electrocatalysis application. J. Mol. Struct. 1256, 132499. https://doi.org/10.1016/j.molstruc.2022.132499

Yu, H., Guo, C., Zhang, X., Cheng, X., Xu, Y., Gao, S., Huo, L., 2022. Tailoring oxygen vacancy of Co_3O_4 microcubes by annealing $Co_3[Co(CN)_6]_2$ template in air for ultrasensitive humidity mapping. Small Struct. 3, 2100166. https://doi.org/10.1002/sstr.202100166

Zhang, L., Ji, X., Ren, X., Luo, Y., Shi, X., Asiri, A.M., Zheng, B., Sun, X., 2018a. Efficient electrochemical N_2 reduction to NH_3 on MoN nanosheets array under ambient conditions. ACS Sustain. Chem. Eng. 6, 9550–9554. https://doi.org/10.1021/acssuschemeng.8b01438

Zhang, L., Ji, X., Ren, X., Ma, Y., Shi, X., Tian, Z., Asiri, A.M., Chen, L., Tang, B., Sun, X., 2018b. Electrochemical ammonia synthesis via nitrogen reduction reaction on a MoS_2 catalyst: Theoretical and experimental studies. Adv. Mater. 30, 1–6. https://doi.org/10.1002/adma.201800191

Zhang, L., Ren, X., Luo, Y., Shi, X., Asiri, A.M., Li, T., Sun, X., 2018c. Ambient NH_3 synthesis via electrochemical reduction of N_2 over cubic sub-micron SnO_2 particles. Chem. Commun. 54, 12966–12969. https://doi.org/10.1039/c8cc06524a

Zhang, R., Ren, X., Shi, X., Xie, F., Zheng, B., Guo, X., Sun, X., 2018. Enabling effective electrocatalytic N_2 conversion to NH_3 by the TiO_2 nanosheets array under ambient conditions. ACS Appl. Mater. Interfaces 10, 28251–28255. https://doi.org/10.1021/acsami.8b06647

Zhang, X., Liu, Q., Shi, X., Asiri, A.M., Luo, Y., Sun, X., Li, T., 2018. TiO_2 nanoparticles-reduced graphene oxide hybrid: An efficient and durable electrocatalyst toward artificial N_2 fixation to NH_3 under ambient conditions. J. Mater. Chem. A 6, 17303–17306. https://doi.org/10.1039/c8ta05627g

Zhao, X., Hu, G., Chen, G.F., Zhang, H., Zhang, S., Wang, H., 2021. Comprehensive understanding of the thriving ambient electrochemical nitrogen reduction reaction. Adv. Mater. 33, 1–46. https://doi.org/10.1002/adma.202007650

Zhao, Y., Liu, Y., Du, J., Zhang, X., Zhou, J., Li, X., Wu, C., Zhu, Z., Xie, E., Pan, X., 2019. Facile synthesis of interconnected carbon network decorated with Co_3O_4 nanoparticles for potential supercapacitor applications. Appl. Surf. Sci. 487, 442–451. https://doi.org/10.1016/j.apsusc.2019.05.142

Zhu, T., Chen, J.S., Lou, X.W., 2010. Shape-controlled synthesis of porous Co_3O_4 nanostructures for application in supercapacitors. J. Mater. Chem. 20, 7015–7020.

https://doi.org/10.1039/c0jm00867b

CHAPTER 7

Conclusions and Scopes for Future Studies

The key findings of the entire doctoral work are concluded in this chapter. On the foundation of the results of the current study, remarks and recommendations for the direction of future work are also included.

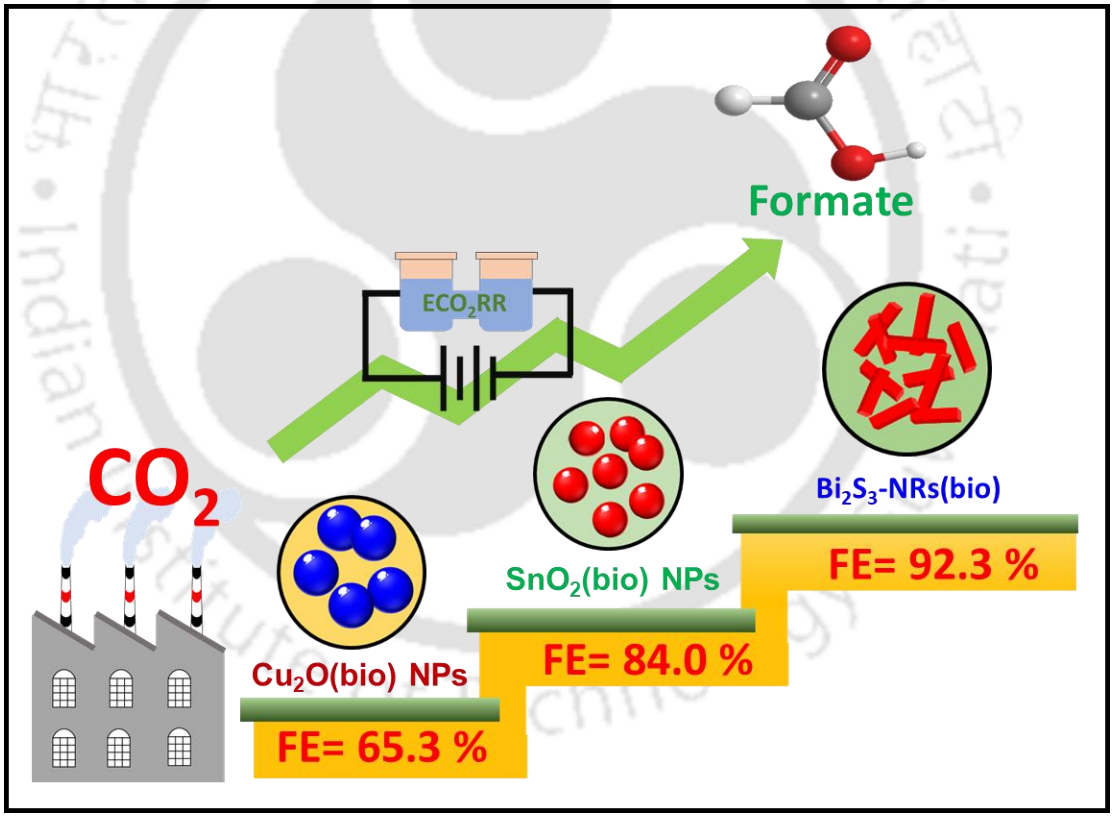

7.1 Overall conclusions

The bulk of the investigations is on the bioinspired synthesis of spherical and tailor-made metal oxides and metal sulphide nano-structures using reducing and/or capping agents present in the vegetal extract of *Sechium edule* (chayote). Further, Co_3O_4 nanodiscs are synthesized using commercially available gallic acid, a major bioactive compound identified in many plant and plant organs. The bioinspired nanoparticles are decorated onto the carbon paper (Toray carbon paper) electrodes by the drop-casting method for electrochemical CO_2 reduction (ECO_2RR) and N_2 reduction reactions (ENRR).

Ascorbic acid (AA) was identified as the major bioactive component in the bio-extract, which acted as both reducing and capping agents for synthesizing metal oxides and metal sulphide nanoparticles. Based on the mass spectroscopic study, plausible mechanisms for the formation of nanoparticles and their interactions with the capping agents are reported.

From the work reported in Chapter 3, Chapter 4, and Chapter 5, the overall conclusions are summarized as follows.

- A bioinspired route has been successfully developed for the synthesis of Cu_2O NPs, SnO_2 NPs, and Bi_2S_3 NRs using *Sechium edule* fruit extract.
- Mechanistic routes of nanoparticles synthesis using AA, a reducing and capping agent, have been investigated—
  i) The formation of Cu(II)O in the absence of bio-extract could be irrefutable evidence of the role of bio-extract in synthesizing and stabilizing Cu_2O NPs in the presence of AA and dehydroascorbic acid (DHA).
  ii) In an acidic medium (pH 4.5), AA dissociates to reactive HA^- species and forms a stable complex with Sn^{4+}. After a series of thermodynamic reactions, Sn^{4+} reduces to Sn^0 and finally, SnO_2 nanoparticles are formed.
  iii) Bi_2S_3-NRs(control) synthesized without using the bio-extract/reducing agent helped to understand that AA present in *Sechium edule* fruit also could act as a capping agent. The absence of oxides in Bi_2S_3-NRs(bio) in comparison with Bi_2S_3-NRs(control) has resulted from the antioxidant property of AA, capped on the surface of nanorods, which prevents further oxidation of S^{2-} during the synthesis process.

- The thermal stability analysis of nanoparticles reveals—
  i) Biomolecules present on Cu_2O(bio) NPs is not more than 8%.
  ii) No further mass loss was observed >700 °C suggesting complete transformation to SnO_2.
  iii) Mass loss of 4.4% at 200-325°C is attributed to the decomposition of biomolecules like ascorbic acid, starch, and stable lignin molecules attached to the surface of Bi_2S_3-NRs(bio). This mass loss was absent in the TGA of Bi_2S_3-NRs(control) synthesized without using bio-extract.
- The structural analysis confirms—
  i) The predominant (111) crystalline plane in Cu_2O(bio) NPs plays a key role in the selective formation of formate.
  ii) The predominant crystalline (110) facet and the increased crystallinity index (CI) in SnO_2(bio)- 800 NPs from 85.8 to 98.3% compared to SnO_2(bio) NPs.
  iii) A significant increase in the intensity of the (211) plane compared to the (130) plane suggested the predominant growth of crystal of Bi_2S_3-NRs in the (211) plane.
- The surface area analysis suggests—
  i) Type-II isotherm with mesoporous nature of Cu_2O(bio) NPs.
  ii) High-temperature calcination caused a reduction in micropores of as-synthesized SnO_2(bio) NPs forming mesoporous SnO_2(bio)- 800 NPs at 800°C.
  iii) Type-IV isotherm and H3 type hysteresis loop suggest a uniform pore size distribution of Bi_2S_3-NRs(bio).
- The morphological attributes can be concluded as—
  i) The lattice fringe with an interplanar distance of 0.245 nm was a good agreement with the XRD analysis of Cu_2O(bio) NPs.
  ii) The interplanar distance of 0.334 nm corresponds to the (110) low-energy facet of the most thermodynamically stable SnO_2 rutile phase.
  iii) Bi_2S_3-NRs(bio) exhibits lattice fringe distances of 0.197 and 0.552 nm corresponding to (002) and (200) planes, respectively, and the growth of nanorods along the direction of the (001) plane.
- The investigations on oxidation states of the components in the synthesized nanoparticles confirm that—

i) XPS analysis suggested the presence of 49.7% amorphous CuO, on the surface of Cu_2O(bio) NPs.

ii) Only Sn^{4+} was present in SnO_2(bio)- 800 NPs, calcined at 800°C, compared to the mixture of Sn^{2+} and Sn^{4+}, present in as-synthesized SnO_2(bio) NPs.

iii) Capping of AA on Bi_2S_3-NRs(bio) prevented the formation of Bi_2O_3.

Table 7.1 summarizes some of the typical physicochemical characterizations of Cu_2O(bio) NPs, SnO_2(bio)-800 NPs, and Bi_2S_3 NRs(bio) catalysts.

Table 7.1. Physicochemical characteristic attributes of Cu_2O(bio) NPs, SnO_2(bio)-800 NPs, and Bi_2S_3 NRs(bio) catalysts synthesized using *Sechium edule* fruit extract.

Catalysts	Physicochemical characterizations		
	Band gap (eV)	Surface area ($m^2\ g^{-1}$)	Particles size (nm)
Cu_2O(bio) NPs	1.98	16.1	37.5
SnO_2(bio)-800 NPs	3.71	18.6	22.5
Bi_2S_3 NRs(bio)	1.51	13.4	49.0

- Cu_2O(bio) NPs, SnO_2(bio)-800 NPs, and Bi_2S_3 NRs(bio) coated Toray carbon paper (TCP) electrode exhibited formation of formate ($HCOO^-$) as the sole liquid product
- Bi_2S_3 NRs(bio) showed a clear superiority with 92.3% Faradaic efficiency (FE) compared to the other two catalysts, Cu_2O(bio) NPs, SnO_2(bio)-800 NPs (Table 7.2)—
  i) The presence of a predominant (111) crystal plane in Cu_2O(bio) NPs was mostly responsible for the formation of $HCOO^-$ with 65.3% FE.
  ii) Higher FE for SnO_2(bio)- 800 NPs resulted from the increase in crystallinity of (110) facets after calcination at 800°C compared to the SnO_2(bio) NPs.
  iii) Formation of $Bi_2O_2CO_3$ during ECO_2RR served as the active sites for enhanced $HCOO^-$ formation.

Table 7.2. Cu_2O(bio) NPs, SnO_2(bio)-800 NPs, Bi_2S_3 NRs(bio) catalysts towards ECO_2RR in ambient conditions.

Catalysts	Electrocatalytic activity		
	Applied potential (V vs. Ag/AgCl)	FE of formate (%)	Current density (J, mA cm^{-2})
Cu_2O(bio) NPs	-1.6	65.3	5.8
SnO_2(bio)-800 NPs	-1.5	84.0	4.8
Bi_2S_3 NRs(bio)	-1.5	92.3	2.0

Chapter 6 is founded on the synthesis of Co_3O_4 nanodiscs (Co_3O_4 NDs) in a bioinspired process for electrochemical N_2 reduction for NH_3 production. This work demonstrates a successful one-pot synthesis of pristine Co_3O_4 NDs using gallic acid as a reducing agent. The narrower bandgaps of 1.78 and 2.07 eV, corresponding to the O^{2-} to Co^{2+}/Co^{3+} charge transfer couples in correlation with the presence of oxygen vacancy facilitate the electron and charge transport for enhanced N_2 reduction reaction. Preferential anisotropic growth of the particles along the (311) direction with diameter and thickness of 240 and 35.5 nm, respectively, were formed owing to the Ostwald ripening. The 1.6-fold higher Warburg resistance (Z_W) observed for Co_3O_4 NDs/TCP/N_2 compared to Co_3O_4 NDs/TCP/Ar resulted in slower mass transfer in the former system, which improved the selectivity and efficiency of ENRR, leading to higher yields of NH_3 formation. Six times higher faradaic efficiency, 2.6% was reflected by the Co_3O_4 NDs/TCP electrode compared to the bare TCP. Moreover, Co_3O_4 NDs/TCP offered NH_3 production with a yield rate of 8.8 µg h^{-1} $mg_{cat.}^{-1}$ at −1.25 V (vs. Ag/AgCl) in 0.1 M Na_2SO_4 electrolyte.

Although, a marginal fall in FE to 1.80%, compromised due to the formation of $Co(OH)_2$, was also observed. In the spinel structure of Co_3O_4 NDs, Co^{2+} in tetrahedral sites easily forms bonds with the N≡N, and the Co^{3+} in octahedral sites, which facilitate the electron transfer for N_2 reduction reaction.

7.2 Scope for future studies

- This study (Chapters 3-5) reports on the formation of formate. Bioinspired metal oxides and sulphides electrocatalysts of various morphologies and physiochemical

attributes may be investigated for the production of C_1 (CO, CH_4, CH_3OH), C_2 (C_2H_4, C_2H_6, CH_3CH_2OH, CH_3COOH, etc.) hydrocarbons.

- The catalytic performances of synthesized electrocatalysts were evaluated for a maximum of 2 h. Prolong (>1000 h) electrocatalytic study for the formation of formate and NH_3 along with C_1 and higher hydrocarbons may be performed targeting industrial applications.
- Separation of liquid product from the electrolyte solution was not within the scope of the present work. Product separation would be an imperative objective of future investigations.
- In this study, the tests were performed in a semi-batch reactor. The studies in a continuous reactor may be considered in future.
- More studies are recommended on the design of electrode and catalysts immobilization on the support electrode to eliminate the reduction in its functionality including the loss of catalyst from the electrode surface during the reaction.
- This work was on an individual process of electrochemical CO_2 and N_2 reduction to value-added products. Simultaneous electrochemical reduction of CO_2 and N_2 to urea also would be promising for further investigations.

Appendix-I

Table A1.1. Specimen calculation of Faradaic efficiency (FE).

Relative peak area ratio (formate) $= \frac{\text{Singlet peak area at 8.29 ppm (formate)}}{\text{Triplet peak area at 7.16 ppm (phenol)}}$

Catholate volume= 100 mL

Formate production from CO_2 reduction= 2 electrons

$N_{formate} = C_{formate} \times V \times N_A$

$= (2.27 \times 10^{-3}\ mol.L^{-1}) \times 100\ mL \times 10^{-3}\ L \times 6.023 \times 10^{23}\ mol^{-1} \times 2\ e$

$= 2.74 \times 10^{20}\ e$

$Q_o = \int_0^{3600} I.dt = 67\ C$

$N_{total} = Q_o/e = (67\ C)/(1.602 \times 10^{-19}\ (C/e))$

$= 4.19 \times 10^{20}\ e$

$FE = (N_{formate}/N_{total}) \times 100$

$= 65.3\%$

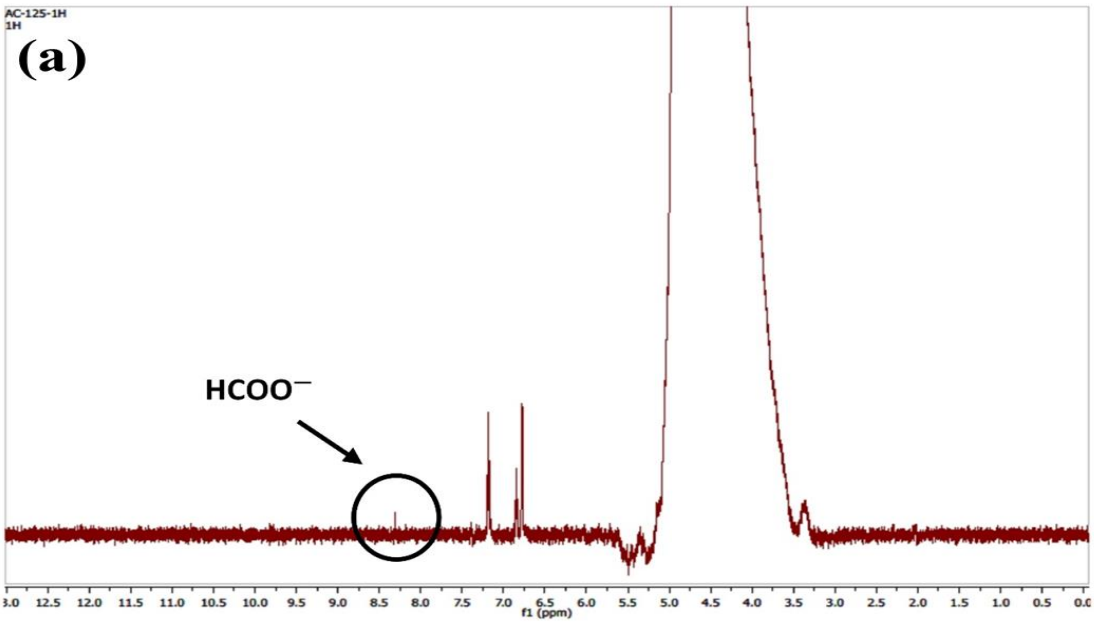

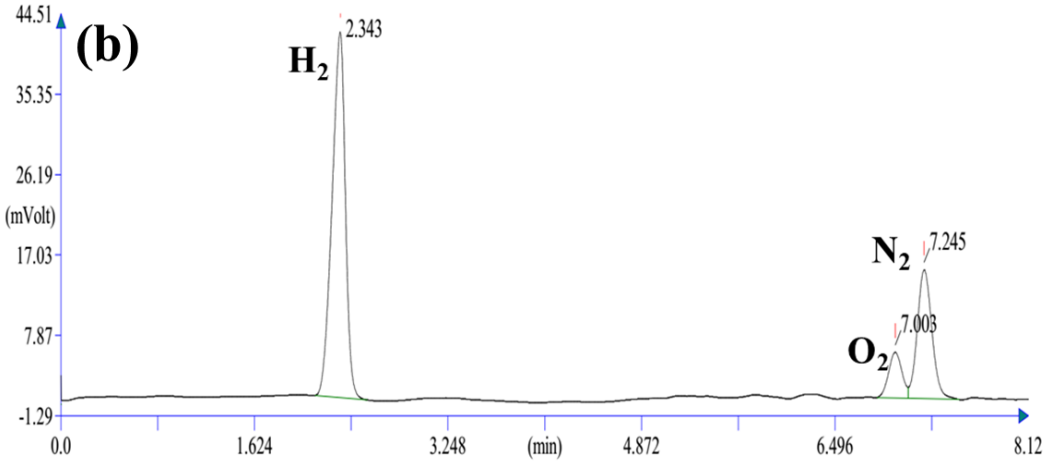

Figure A1.1. (a) NMR spectra of the catholyte and (b) gas chromatogram of the gaseous sample collected after 3600 s of ECO_2RR at −1.6 V vs. Ag/AgCl applied potential, using Cu_2O(bio) NPs/TCP electrode.

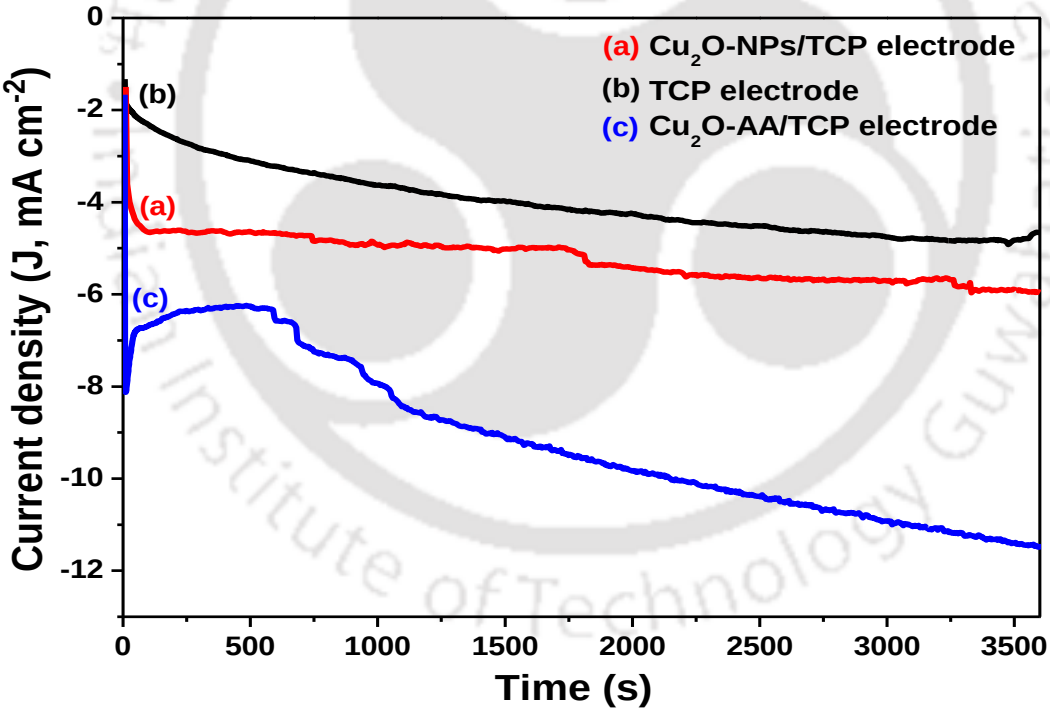

Figure A1.2. Current response for (a) TCP, electrode, (b) Cu_2O(bio) NPs/TCP electrode, and (c) Cu_2O-AA/TCP electrode at −1.6 V in CO_2-saturated 0.5 M $KHCO_3$ electrolyte for 3600 s.

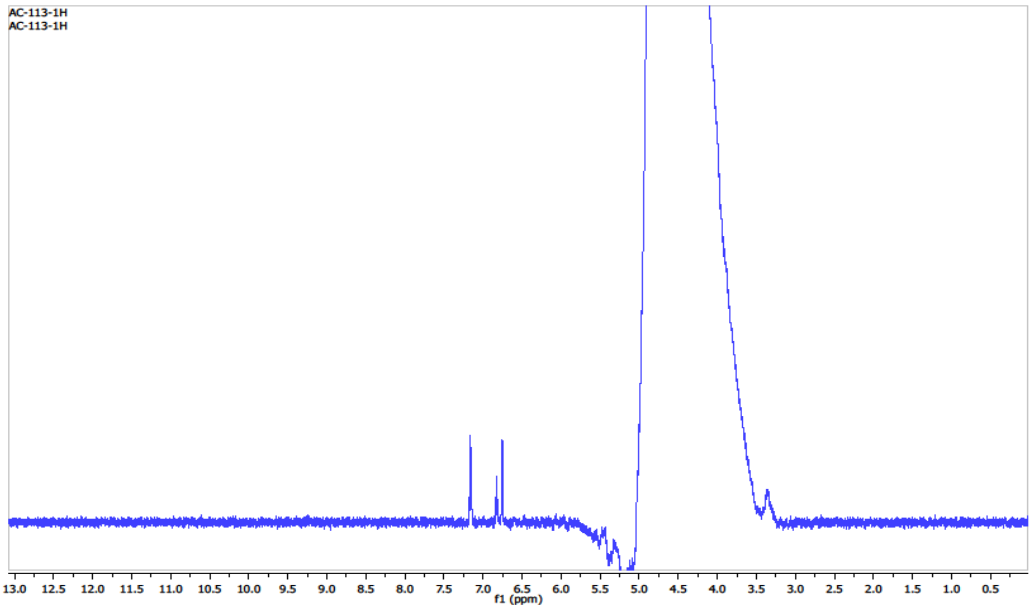

Figure A1.3. NMR spectra of the catholyte collected after 3600 s of ECO_2 RR at −1.6 V vs. Ag/AgCl applied potential using bare TCP electrode.

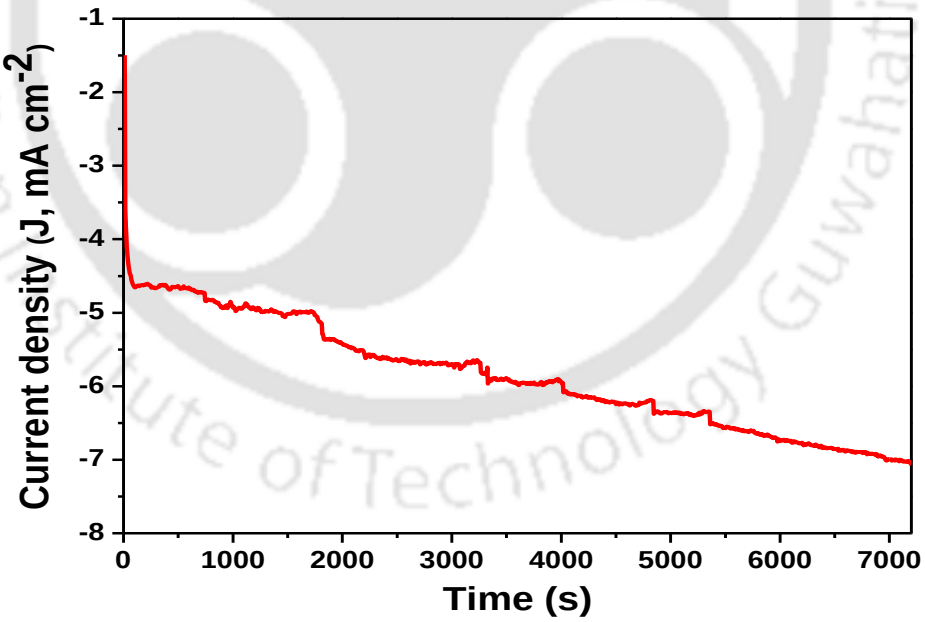

Figure A1.4. Current response recorded during ECO_2RR using Cu_2O(bio) NPs/TCP electrode at −1.60 V vs. Ag/AgCl in CO_2-saturated 0.5 M $KHCO_3$ electrolyte for a span of 7200 s.

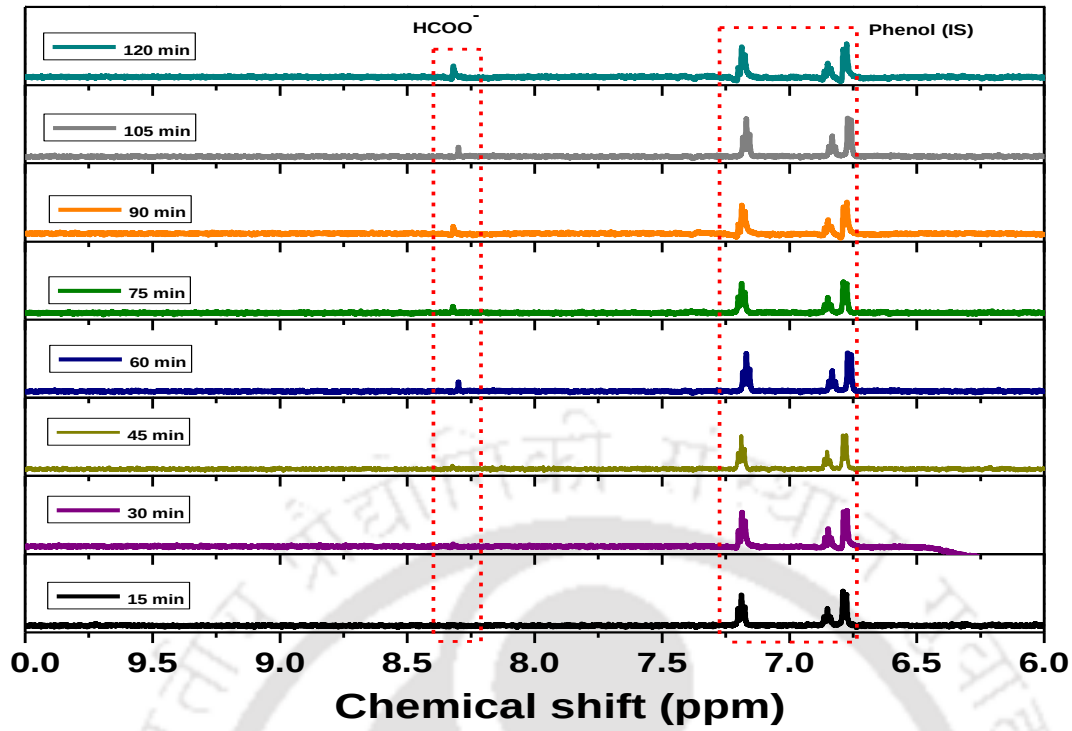

Figure A1.5. NMR spectra of formate formation at different time intervals for the experiment as in Figure A1.4.

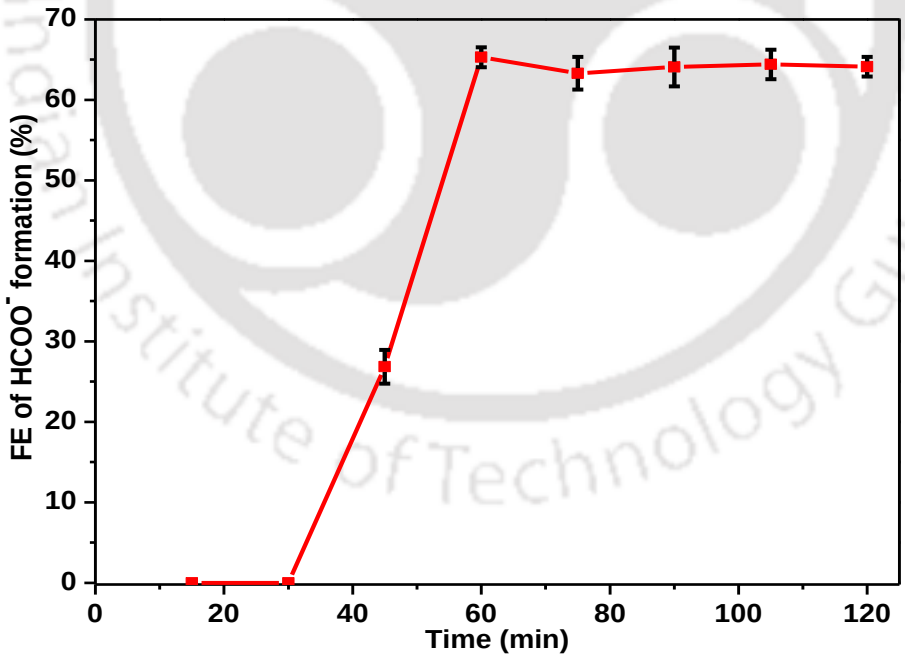

Figure A1.6. Faradaic efficiency of formate formation at different time intervals for the experiment as in Figures A1.4 and A1.5.

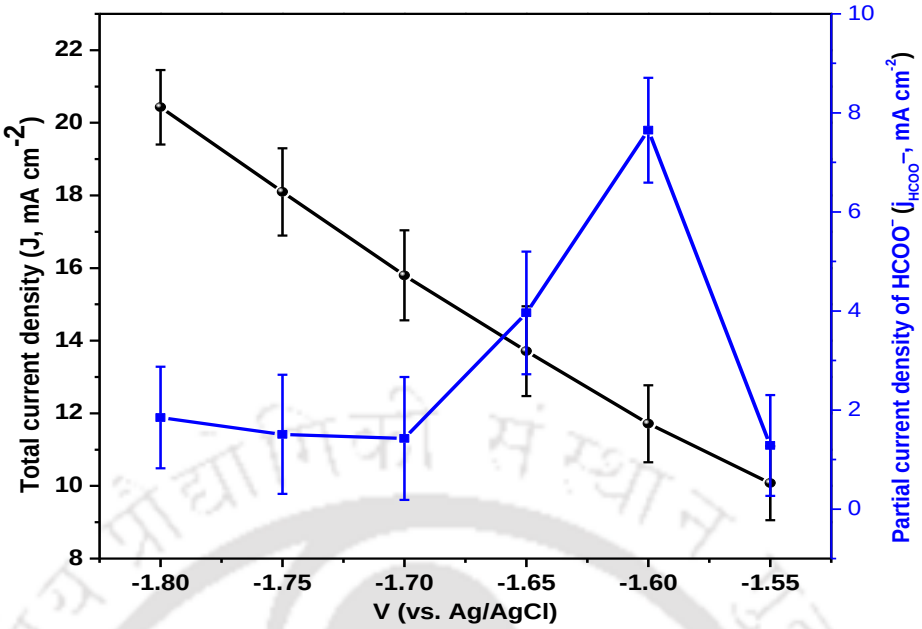

Figure A1.7. Total current density (J) and partial current density of $HCOO^-$ (j_{HCOO^-}) formation at different applied potentials (vs. Ag/AgCl).

This page is intentionally left blank

Appendix-II

Calibration curve for formate and calculation of formate concentration in the catholyte

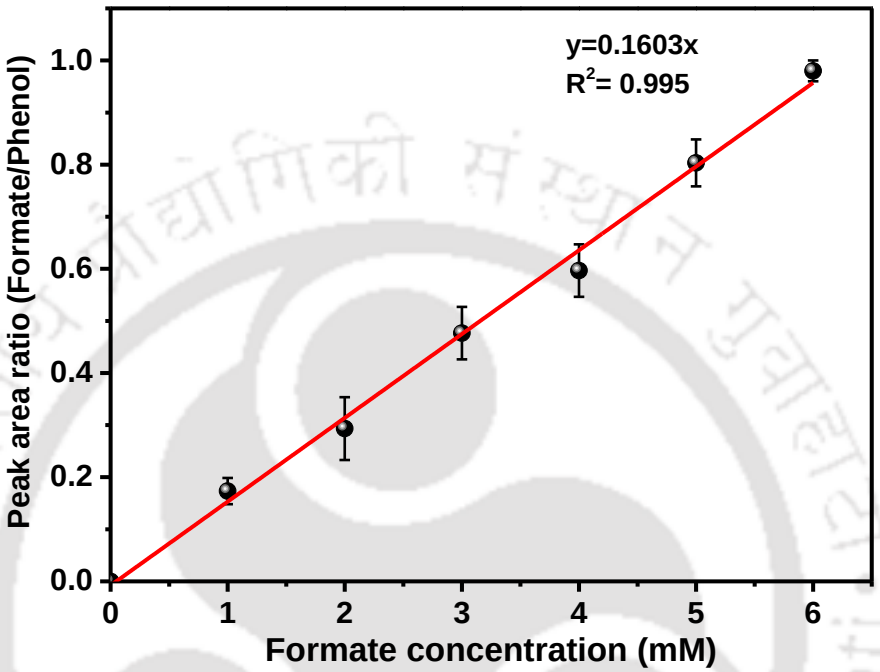

Figure A2.1. Calibration curve for formate (phenol as an internal standard (IS)) for quantification of liquid product analyzed by 1 H NMR spectroscopy recorded at 600 MHz on a Bruker Avance III HD NMR spectrometer (Bruker, Germany).

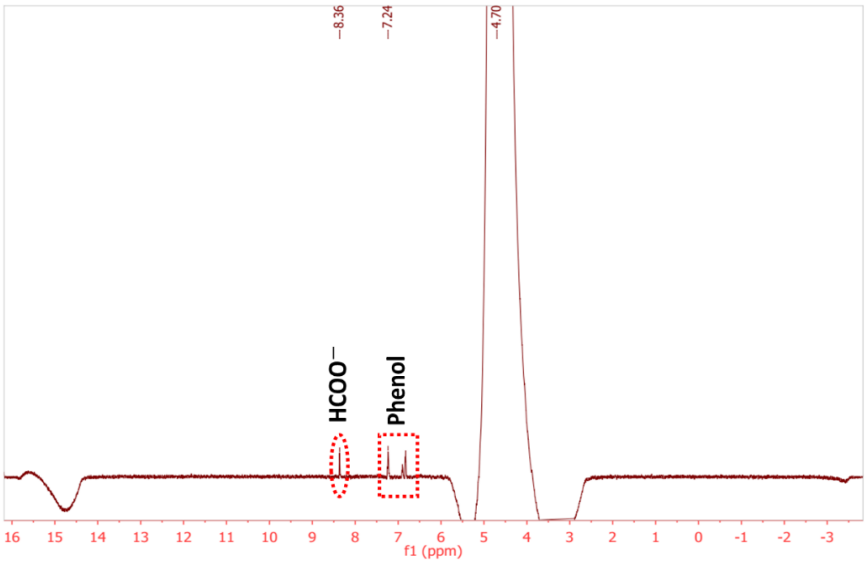

Figure A2.2. NMR spectra of catholyte after 3600 s of CO_2 reduction at −1.5 V (vs. Ag/AgCl).

[SnO_2(bio)-800/TCP showed a FE of 72.0% at −1.4 V (vs. Ag/AgCl), and the maximum FE was found to be 84.0% at −1.5 V (vs. Ag/AgCl) (Figure 4.22). Concentration of formate was determined at different potentials using calibration curve (Figure A2.1) derived from the NMR analysis using the method reported in the literature (Ren et al., 2015). A specimen calculation is shown herewith. The NMR spectra of formate is shown in Figure A2.2.

$$\text{Relative peak area ratio (formate)} = \frac{\text{Singlet peak area at 8.36 ppm (formate)}}{\text{Triplet peak area at 7.24 ppm (phenol)}}$$

The equation of calibration curve (Figure A2.1) is found to be y = 0.1603x, R^2 = 0.995) to determine the formate concentration in electrolyte.

Relative peak area ratio (formate)= 0.46

Therefore, the formate concentration = 2.9×10^{-3} mol L^{-1}]

RESEARCH OUTCOMES

Journal Publications

- **A. Chowdhury,** N. R. Peela, A. K. Golder, Synthesis of Cu_2O NPs using bioanalytes present in *Sechium edule*: Mechanistic insights and application in electrocatalytic CO_2 reduction to formate, Journal of CO_2 Utilization 51 (2021) 101622.
- **A. Chowdhury**, , C. Bhan, N. R. Peela, A. K. Golder, A tunable bioinspired process of SnO_2 NPs synthesis for electrochemical CO_2-into-formate conversion, Journal of CO_2 Utilization 66 (2022) 102263.
- **A. Chowdhury**, C. Bhan, N. R. Peela, A. K. Golder, A simple template-free bioinspired route of 1D Bi_2S_3 nanorods synthesis for electrochemical CO_2 reduction to formate (**Communicated**).
- **A. Chowdhury**, N. R. Peela, A. K. Golder, Environmentally benign synthesis of shape-controlled 2D Co_3O_4 spinel nanodisc using gallic acid for electrochemical N_2 reduction (**Communicated**).

International Conferences and Workshops

- **A. Chowdhury**, N. R. Peela, A. K. Golder, Bio-inspired Synthesis of Cu NPs and Its Application Towards Electrochemical CO_2 Reduction to Single Carbon Oxygenated Product. 2nd International Conference on Bioprocess for Sustainable Environment and Energy (ICBSEE-India-2020). 5-7th March, 2020. Held at NIT Rourkela, Odissa, India.
- **A. Chowdhury**, N. R. Peela, A. K. Golder, Synthesis of AgNPs using bio-active compounds present in *E. serratus L.* extract: A proposed mechanistic pathway of synthesis. ChemCon-2021. 26-30th December, 2021. Held at CSIR- Institute of Minerals and Materials Technology, Bhubaneswar, India.
- "**Recent Advances on Bio-inspired Nanomaterials for Environmental Applications**". UKIERI. Department of Science & Technology. Held on 18th December, 2018 at Indian Institute of Technology Guwahati.

National Conferences and Workshops

- **A. Chowdhury**, N. R. Peela, A. K. Golder, A Facile Bioinspired Route of Spinel type Co_3O_4 NPs Synthesis using *Elaeocarpus Serratus L. Leaves Extract.* NERC-2022. 20-22th May, 2022. Held at IIT Guwahati, Guwahati, Assam, India.
- **A. Chowdhury**, N. R. Peela, A. K. Golder, A One-pot Bioinspired Route of Synthesis of SnO_2 NPs for Electrochemical CO_2-into-Formate Conversion. NERC-2022. 20-22th May, 2022. Held at IIT Guwahati, Guwahati, Assam, India.

- **A. Chowdhury**, N. R. Peela, A. K. Golder, A Facile Bio-inspired Route for the Synthesis of Cu_2O Nanoparticles for Electrocatalytic CO_2 Reduction to Formate. Reflux 7.0, 28-29th September, 2019 at Indian Institute of Technology Guwahati.
- **A. Chowdhury**, N. R. Peela, A. K. Golder, Bio-inspired Cu_2O Nanoparticles for Photocatalytic CO_2 Reduction to Methanol. Research Conclave'19, 14-17th March, 2019. Indian Institute of Technology Guwahati.
- Workshop on **'Advances in Separation Techniques'**, Conducted under the TEQIP. Sponsored by MHRD, Government of India. Held on 15th March, 2019. Indian Institute of Technology Guwahati.